

**Investigations of Carbon Dioxide Electrolysis on Perovskite with Exsolved Nanoparticles in
Solid Oxide Electrolysis Cell**

by

Bowen Zhang

A thesis submitted in partial fulfillment of the requirements for the degree of

Doctor of Philosophy

in

Materials Engineering

Department of Chemical and Materials Engineering

University of Alberta

© Bowen Zhang, 2023

Abstract

Carbon dioxide (CO₂) electrolysis, when combined with renewable energy sources, has emerged as a promising technology for reducing CO₂ emissions. Integrating CO₂ electrolysis into solid oxide electrolysis cell (SOEC) technology has become one of the main ways to reduce carbon emissions in the future due to its advantages of high efficiency, high selectivity, long lifespan and scalability. In recent years, significant efforts have been dedicated to developing promising electrode materials and gaining insight into the reaction mechanisms for CO₂ electrolysis in SOEC, leading to the prospect of a sustainable and low-carbon future. Perovskites with exsolved nanoparticles (P-eNs) have become the most promising electrode materials, thanks to the coupling of multifunctionality of perovskite and the high activity and thermal stability of the exsolved nanoparticles. However, several challenges remain with regards to their practical applications, such as enhancing the stability performances of P-eNs and a more comprehensive understanding of CO₂ electrolysis mechanisms on P-eNs based cathodes. Addressing these issues will facilitate the commercialization of CO₂ electrolysis using P-eNs based materials, bringing us one step closer to a greener future.

Although many efforts have been devoted to enhancing the catalytic activity of perovskite by promoting the exsolution, the remarkable degradation of P-eNs based materials, particularly at high voltages, still remains as a major challenge. In my first work, using Sr₂Fe_{1.3}Ni_{0.2}Mo_{0.5}O_{6-δ} as a model example, I have demonstrated that the B-site vacancies left on the perovskite scaffold after exsolution have a great influence on the stability of P-eN-based catalysts. Through ion exchange between foreign Fe cations and bulk Ni cations in the parent perovskite, the

resistance to reduction of the perovskite substrate with B-site supplement has been significantly enhanced, resulting in the improved stability performance at high voltages compared to the P-eNs without B-site supplement. Furthermore, I have put forward the degradation mechanisms based on the structural evolution of perovskite substrate to shed lights on the origin of performance deterioration of P-eNs based cathodes.

In addition, the full exploitation of the heterogeneous architecture on exsolution-facilitated perovskites is still limited due to the absence of fine-regulation over the phase evolution of host perovskite during exsolution. Consequently, our current understanding on how the phase transformation of the perovskite scaffold affects the catalytic performances of P-eNs remains inadequate, leading to a lack of design guidance for exsolution-promoted P-eNs materials. In the second work, I identified a set of strategies for controlling the phase evolution of the perovskite scaffold without compromising exsolution on $\text{Sr}_2\text{Fe}_{1.2}\text{Ni}_{0.3}\text{Mo}_{0.5}\text{O}_{6-\delta}$. In particular, the trade-off between the promoted exsolution of nanoparticles and well-preserved phase structure of host perovskite has been broken by a B-site supplement strategy. Using CO_2 electrolysis as an illustrative case study, we have experimentally and theoretically demonstrated that the carbon monoxide production and operating stability of P-eNs can be selectively enhanced by regulating the phase evolution of host perovskites while facilitating exsolution. My findings shed light on the significance of the phase structure of the host perovskite in catalytic reactions occurring on P-eNs. Furthermore, the effective implementation of B-site supplement strategy could potentially pave the way for ground-breaking advance in the field of catalytic chemistry.

In my latest research, I have presented another novel and ingenious method involving F-doping, aimed at effectively suppressing the phase transition of $\text{Sr}_2\text{Fe}_{1.2}\text{Ni}_{0.3}\text{Mo}_{0.5}\text{O}_{6.6}$ (SFN₃M) during exsolution and enhancing the stability performances of exsolved SFN₃M in CO₂ electrolysis. The experimental characterizations combined with density functional theory calculations reveal that the incorporation of fluorine into SFN₃M lattice is beneficial for preserving the high oxidation states of B-site cations and inhibiting the lattice oxygen loss, resulting in a robust BO₆ octahedron in host perovskite. It is found that the well-preserved double perovskite structure exhibits a stronger interaction with CO₂, thus enhancing the catalytic activity of F-doped exsolved SFN₃M (F-SFN₃M-red). Furthermore, the robust BO₆ octahedron of host perovskite significantly enhances the resistance of F-SFN₃M-red to decomposition under high-voltage CO₂ electrolysis, leading to the significantly increased carbon monoxide productivity over a broad voltage range. These findings highlight that F doping strategy has great potential to aid the development of exsolved perovskites with high catalytic activity and stability for a wider range of electrocatalysis applications.

Preface

This thesis is an original work by Bowen Zhang (Bo-Wen Zhang) under the supervision of Dr. Jing-Li Luo and Dr. Hongbo Zeng.

Chapter 1 is the introduction of the background knowledge and principles of carbon dioxide electrolysis in solid oxide electrolysis cell.

Chapter 2 displays the literature review of metal-based, metal oxide-based and perovskite-based electrocatalysts for CO₂ electrolysis in solid oxide electrolysis cell based on the previous studies.

Chapter 3 briefly introduces the methodologies and characterizations employed in this thesis.

Chapter 4 of this thesis has been published as Bo-Wen Zhang, Meng-Nan Zhu, Min-Rui Gao, Xiuan Xi, Nanqi Duan, Zhou Chen, Renfei Feng, Hongbo Zeng, Jing-Li Luo, Boosting the stability of perovskites with exsolved nanoparticles by B-site supplement mechanism. *Nat. Commun.* 2022, 13 (1), 4618.

B.W.Z. conceived the idea and performed the experiments, and wrote the manuscript. M.N.Z. contributed to the DFT calculations, TEM analysis and Raman analysis. M.R.G. performed the DFT calculations. X.X. contributed to ECR experiments and temperature-dependent electrical conductivity data. R.F.F. contributed to XANES data. N.D., Z.C. and H.Z. gave constructive comments. J.L.L. supervised the project and edited the manuscript.

Chapter 5 of this thesis has been published as Bo-Wen Zhang, Meng-Nan Zhu, Min-Rui Gao, Jian Chen, Xiuan Xi, Jing Shen, Ren-Fei Feng, Natalia Semagina, Nan-qi Duan Hongbo Zeng, Jing-Li Luo, Phase transition engineering of host perovskite toward optimal exsolution-facilitated catalysts for carbon dioxide electrolysis. *Angew. Chem. Int. Ed.* 2023, e202305552.

B.W.Z. conceived the work, performed experimental work, data analysis and interpretation, and wrote the manuscript draft. M.N.Z. contributed to the DFT calculation section of this manuscript, participated in the experimental design and data analysis, TEM analysis, Raman analysis and edited the manuscript. M.R.G. participated in the data discussion of experiments and theoretical calculations. J.C. contributed to TEM analyses and the writing of the TEM part. X.X. contributed to temperature-dependent electrical conductivity data and gave suggestions on manuscript writing. J.S. contributed to CO₂-TPD data. R.F.F. performed the synchrotron X-ray spectroscopy measurements. N.S. and N.D. participated in the data discussions and gave constructive comments of this work. H.Z. supervised this project. J.L.L. supervised and directed the study, contributed to the funding acquisition, edited and revised the manuscript, helped to discuss the data of the manuscript.

Chapter 6 of this thesis has been submitted to ACS Catalysis for publication as Bo-Wen Zhang, Meng-Nan Zhu, Min-Rui Gao, Jing Shen, Nanqi Duan, Natalia Semagina, Hongbo Zeng, and Jing-Li Luo, Fluorine-stabilized BO₆ octahedron of host perovskites for robust carbon dioxide electrolysis on exsolved catalysts.

B.W.Z. conceived the work, performed experimental work, data analysis and interpretation, and wrote the manuscript draft. M.N.Z. contributed to DFT calculations, TEM analysis, Raman

analysis and edited the manuscript. M.R.G. participated in the data discussion of experiments and theoretical calculations. J.S. contributed to CO₂-TPD data. N.S. and N.D. participated in the data discussions and gave constructive comments of this work. H.Z. supervised this project. J.L.L. supervised this project, contributed to the funding acquisition, revised the manuscript.

Chapter 7 includes the summary and prospects.

Acknowledgements

First and foremost, I would like to express my sincere gratitude to my supervisor, Dr. Jing-Li Luo, for her support throughout the past four years. She not only provided me with academic and financial assistance but also taught me how to approach scientific questions in an effective and meaningful manner. Her patient guidance, insightful criticism, and expert instruction have been invaluable in helping me complete this thesis. More importantly, she helped me develop good research habits and provided direction for my future career plans. At the same time, I would like to express my gratitude to my co-supervisor, Dr. Hongbo Zeng, for his invaluable guidance and support throughout my doctoral studies. His expertise and encouragement have been essential to the completion of this thesis. To my supervisory committee members Dr. Hao Zhang for his valuable suggestions and guidance during my research progress.

To my colleague Meng-Nan Zhu, who provided me with valuable advice and guidance throughout my scientific journey. Her wisdom, hard work, and rigorous research attitude have been a source of inspiration and motivation for me to continue on the path of scientific discovery. I am deeply grateful for her help.

To my colleagues Min-Rui Gao, Dr. Nanqi Duan, Dr. Xiuan Xi, Dr. Jian Chen, Dr. Jing Shen who spent many hours not only teaching me to get into this field, but also addressing my questions. To my other colleagues, Pengfei Sui, Shaoqing Liu, Jing Xiao, Yuanyuan Hong, Dr. Chenyu Xu and Yicheng Wang, for their help during the past four years.

I extend my heartfelt gratitude to my closest friends, basketball, Hanyu Zhang, Daowei Wang, Dong Wang, Shengli Zhai, Keren Jiang, Xuehai Tan, for the many moments of laughter and joy that have kept me going.

Lastly, I would like to extend my deepest gratitude to my parents and grandparents for their unwavering understanding, encouragement, support, and love throughout my Ph.D. studies. I particularly want to dedicate this achievement to my grandmother, who is now in heaven, and I hope that she is at peace and free from suffering. Your love and support have been a constant source of motivation and strength, and I will always cherish your role in my life.

Table of Contents

| | |
|--|--------|
| Abstract..... | ii |
| Preface | v |
| Acknowledgements..... | viii |
| Table of Contents..... | x |
| List of Tables | xiii |
| List of Figures | xv |
| List of Symbols | xxviii |
| List of Abbreviations | xxxii |
| Chapter 1. Introduction | 1 |
| 1.1 CO ₂ capture and conversion: Closing the cycle..... | 1 |
| 1.2 Basic principles of CO ₂ electrolysis in solid oxide electrolysis cell (SOEC) | 3 |
| 1.2.1 Introduction and application of CO ₂ electrolysis in SOEC | 4 |
| 1.2.2 Thermodynamics and kinetics of CO ₂ electrolysis in SOEC | 7 |
| 1.2.3 Metrics for evaluating SOEC performances | 10 |
| 1.3 Scope of the thesis | 14 |
| Chapter 2. Literature review of cathode candidates for CO ₂ electrolysis in SOEC..... | 15 |
| 2.1 Metal, metal oxide-based cathode materials | 15 |
| 2.2 Perovskite-based cathode materials..... | 16 |

| | |
|---|----|
| 2.3 Strategy to enhance the electrochemical performances of perovskites | 20 |
| 2.3.1 Composite materials..... | 20 |
| 2.3.2 Doping..... | 21 |
| 2.3.3 Exsolution | 25 |
| 2.4 Current status and challenges..... | 35 |
| Chapter 3. Experimental methodologies..... | 38 |
| 3.1 Materials synthesis..... | 38 |
| 3.1.1 Synthesis of SFNM+xFe-red ($x=0.0, 0.5, 0.8, 1.2, 1.5$)..... | 38 |
| 3.1.2 Synthesis of SFN ₃ M+xFe-red-2h ($x=0.5, 0.8, 1.2$), SFN ₃ M-red-2h and SFN ₃ M-red-10h | 39 |
| 3.1.3 Synthesis of Sr ₂ Fe _{1.2} Ni _{0.3} Mo _{0.5} O _{6-δ} , F doped Sr ₂ Fe _{1.2} Ni _{0.3} Mo _{0.5} O _{6-δ} F _{0.1} | 40 |
| 3.2 Physicochemical characterizations | 41 |
| 3.3 Cell fabrications and electrochemical characterizations | 43 |
| 3.3.1 Cell fabrications | 43 |
| 3.3.2 Electrochemical characterizations..... | 44 |
| 3.4 Density functional theory (DFT) calculations..... | 45 |
| Chapter 4. Boosting the stability of perovskites with exsolved nanoparticles by B-site supplement mechanism..... | 50 |
| 4.1 Introduction..... | 50 |

| | |
|---|-----|
| 4.2 Results and Discussion | 52 |
| 4.3 Conclusions..... | 74 |
| 4.4 Supporting information..... | 75 |
| Chapter 5. Phase transition engineering of host perovskite toward optimal exsolution-facilitated catalysts for CO ₂ electrolysis..... | 90 |
| 5.1 Introduction..... | 90 |
| 5.2 Results and discussion..... | 92 |
| 5.3 Conclusions..... | 108 |
| 5.4 Supporting information..... | 109 |
| Chapter 6. Fluorine-stabilized BO ₆ octahedron of host perovskites for robust CO ₂ electrolysis on exsolved catalysts | 124 |
| 6.1 Introduction..... | 124 |
| 6.2 Results and discussion..... | 127 |
| 6.3 Conclusions..... | 140 |
| 6.4 Supporting information..... | 141 |
| Chapter 7. Summary and prospects | 147 |
| Bibliography | 151 |

List of Tables

| | |
|--|-----|
| Table 1.1 Reversible voltage E_{rev} at 800 °C for CO ₂ electrolysis when anode is exposed to air and cathode is fed using different CO/CO ₂ atmospheres [55]. | 9 |
| Table S4.1 Fe and Ni content in randomly selected nanoparticles on SFNM+0.0Fe-red and SFNM+1.2Fe-red. | 77 |
| Table S4.2 EIS fitting values (R_s , R_H , R_L). | 79 |
| Table S4.3 EIS fitting values (R_s , R_H , R_L) of SFNM+1.2Fe-red-GDC at 800 °C (Equivalent circuit model: LR(Q _H R _H)(Q _L R _L)). | 80 |
| Table S4.4 Comparison of the polarization resistance, CO productivity with other state-of-art exsolved SOECs for CO ₂ electrocatalysis..... | 81 |
| Table S4.5 The corresponded energies of three defective configurations and perfect SFM. | 84 |
| Table S4.6 Comparison of the short-term stability with the state-of-art P-eNs for pure CO ₂ electrocatalysis in SOEC. | 86 |
| Table S5.1 Fe and Ni content in randomly selected nanoparticles on DLP-NPs, SFN ₃ M+1.2Fe-red-2h and SFN ₃ M-red-10h..... | 111 |
| Table S5.2 Relative composition of Sr and O on DLP-NPs, DP-NPs, LP-NPs and SFN ₃ M calculated from respective XPS spectra. | 113 |
| Table S5.3 EIS fitting values of R_p ($=R_H+R_L$) for DLP-NPs-GDC, DP-NPs-GDC and LP-NPs-GDC. ... | 117 |
| Table S5.4 Electronic conductivities ($S\ cm^{-1}$) of DLP-NPs, DP-NPs and LP-NPs under 1:1 CO–CO ₂ and 2:1 CO–CO ₂ at 850 °C. | 119 |
| Table S5.5 Relative composition of Fe and Mo on DLP-NPs, DP-NPs and LP-NPs calculated from respective XPS spectra. | 120 |

| | |
|--|-----|
| Table S5.6 Formation energy of oxygen vacancy (E_{VO}) on models DP-SFM, DP-SFNM, LP-SFM and LP-SFNM..... | 123 |
| Table S5.7 Co-segregation energy of Fe and Ni (EM_{co-seg} , where M is donated as B-site cations such as Ni, Fe) on slabs DP-SFM (001), LP-SFM-1 (001), LP-SFM-2 (001), DP-SFNM (001), LP-SFNM-1 (001) and LP-SFNM-2 (001)..... | 123 |
| Table S6.1 Relative composition of Fe, Ni and Mo on SFN ₃ M-red and F-SFN ₃ M-red calculated from respective XPS spectra. | 142 |
| Table S6.2 Calculated B-O bond length in SFN ₃ M and F-SFN ₃ M models. | 143 |
| Table S6.3 Local Bader charge analysis on SFN ₃ M and F-SFN ₃ M models. | 144 |
| Table S6.4 Relative composition of O on SFN ₃ M-red and F-SFN ₃ M-red calculated from respective XPS spectra..... | 144 |
| Table S6.5 EIS fitting values of R_s , $R_p (=R_H+R_L)$ for SOECs with SFN ₃ M-red-GDC and F-SFN ₃ M-red-GDC as cathodes. | 145 |

List of Figures

| | |
|--|----|
| Figure 1.1 The concentration of CO ₂ in the atmosphere from 1958-2021. Reprinted with permission from Reference. [1] Copyright (2022) Earth System Science Data. | 2 |
| Figure 1.2 Illustration of CO ₂ conversion and utilization through popular pathways, including chemical reformation, mineralization, enzymatic catalysis and photochemical/electrochemical methods. [18] Copyright (2018) Elsevier. | 3 |
| Figure 1.3 Schematic diagram of CO ₂ electroreduction at (a) room temperature and (b) high temperature. | 4 |
| Figure 1.4 Illustration of the practical application of the CO ₂ electrolysis in SOEC technology in a future energy system with increased share of intermittent electricity from renewable sources such as wind and solar. [38] Copyright (2020) American Association for the Advancement of Science. | 5 |
| Figure 1.5 SOEC schematics and the CO ₂ electrolysis reaction paths in SOEC with an oxygen-ion conductor electrolyte. | 6 |
| Figure 1.6 Total energy demanded (ΔH) and electrical energy demanded (ΔG) for conversion of CO ₂ into CO as a function of temperature. [34] Copyright 2014 American Chemical Society. | 7 |
| Figure 2.1 Schematic diagrams of TPB in the (a) metallic Ni, (b) Ni-YSZ and (c) perovskite-based catalysts. | 16 |
| Figure 2.2 The structure illustration of idea perovskite ABO _{3±δ} . (a) Corner-sharing (BO ₆) octahedral with A ions located in 12-coordinated interstices. (b) B-site cation at the center of the cell. [83] Copyright (2017) Elsevier. | 17 |

Figure 2.3 Stacking structures of (a) simple perovskite $ABO_{3\pm\delta}$, (b) double perovskite $AA'B_2O_{5+\delta}$ and (c) Ruddlesden-Popper typed perovskite-oxides ($A_2BO_{4\pm\delta}$). [96] Copyright (2014) RSC Publishing..... 18

Figure 2.4 (a) Current density-voltage curves of SOEC with the SFM and GDC-SFM cathodes. [125] Copyright (2019) Elsevier. (b) Current density-voltage curves of LST and Cr, Mn doped LST ($LSTCo_+$ and $LSTMo_+$) for CO_2 electrolysis at 800 °C. [89] Copyright (2017) Springer Nature. (c) Current density-voltage curves of LSF and LSF doped with different concentrations of vanadium for CO_2 electrolysis at 800 °C. [127] (d) TPD- CO_2 curves of $LSFV_x/GDC$ with MS of CO_2 ($m/z = 44$). [127] Copyright (2018) Elsevier. 21

Figure 2.5 (a) Electrochemical performances of LFO, LCFO82, LSFO82 and LBFO82 for CO_2 electrolysis at 800 °C. [130] (b) CO_2 -TPD of LFO, LCFO82, LSFO82 and LBFO82. [130] Copyright (2019) Elsevier. (c) D_{chem} versus $1000/T$ and (d) k_{chem} versus $1000/T$ of F-SFM and SFM. [139] Copyright (2018) John Wiley and Sons. 24

Figure 2.6 Schematic of the comparison of perovskite with nanoparticles by conventional impregnation and exsolution processes. [157] Copyright (2020) American Chemical Society. .. 26

Figure 2.7 Schematic of exsolution approach for the synthesis of perovskite with exsolved nanoparticles. [161] Copyright (2020) American Chemical Society. 26

Figure 2.8 (a) Illustration of the exsolution process. (b) Gibbs free energy change during the nucleation and growth. Copyright (2016) Elsevier. 28

Figure 2.9 (a) Selected areas of the $La_{0.4}Sr_{0.4}Sc_{0.9}Ni_{0.1}O_{3-\delta}$ particles reduced in pure H_2 (left) and 20% H_2 (right) at 900 °C for 5, 10, 15, 20, and 30 h (from top to down) with the scale bar being 100 nm. (b) The average particle size and the fitting curves with strain-limited model (solid line),

reactant-limited model (dashed line), and diffusion-limit model (dotted line). Copyright (2016) Elsevier. 29

Figure 2.10 (a) Schematic representation of the exsolution of B-site cations from A-site-deficient perovskites. Copyright (2013) Springer Nature. (b) Co exsolution of double perovskites without and with crystal reconstruction. Copyright (2016) American Chemical Society. (c) Effects of the substrate on three important physical parameters related to the exsolved thin films. Copyright (2019) Springer Nature. (d) Exsolution process with and without topotactic ion exchange. Copyright (2019) Springer Nature. (e) Comparison of the physical parameters of exsolved nanoparticles and (f) SEM micrographs for $\text{La}_{0.43}\text{Ca}_{0.37}\text{Ni}_{0.06}\text{Ti}_{0.94}\text{O}_{3-\gamma}$ electrodes after conventional reduction and after electrochemical switching. Copyright (2016) Springer Nature. 30

Figure 2.11 (a) Schematic illustration of model used for the calculations of co-segregation energy and the comparison of the co-segregation energy of dopant T (Co, Ni, Mn and Fe) in $\text{PrBaMn}_{1.7}\text{T}_{0.3}\text{O}_{5+6}$. Copyright (2017) Springer Nature. (b) Comparison of current–voltage curves for CO_2 electrolysis using the Fe–Ni-LSFN, LSFN, GDC and Fe–Ni as cathode catalysts at 850 °C. Copyright (2016) American Chemical Society. (c) Comparison of co-segregation energy of Fe and Ni in LCFO and LCFNO. Copyright (2017) Elsevier. 35

Figure 2.12 The landmark studies of the exsolution on perovskites in the past decade. 37

Figure 4.1 (a) Co-segregation energy and schematic illustrations of the DFT models for co-segregation by conventional exsolution. (b) Exchange energy comparison of B-site cations of SFNM with guest Fe. 53

Figure 4.2 Schematic illustration of exsolution with and without B-site supplement on SFNM. 54

| | |
|--|----|
| Figure 4.3 (a ₁) XRD patterns of SFNM+xFe (x=0.0, 0.5, 0.8, 1.2) reduced at 800 °C for 2 h in 5% H ₂ /N ₂ from 20 to 80°. Amplified XRD patterns in the range of (a ₂) 41-45° and (a ₃) 31.5-33°..... | 56 |
| Figure 4.4 (a ₁) XRD patterns of re-oxidized SFNM+xFe-red at 1000 °C in air for 10 h. Amplified XRD patterns in the range of (a ₂) 35-45° and (a ₃) 26-31°..... | 58 |
| Figure 4.5 <i>j</i> -V curves of SFNM+0.0Fe-red-GDC and SFNM+1.2Fe-red-GDC for pure CO ₂ electrolysis at 850 °C..... | 58 |
| Figure 4.6 (a) EIS of SFNM+0.0Fe-red-GDC and SFNM+1.2Fe-red-GDC for pure CO ₂ electrolysis at 850 °C. (b) DRT analyses of the EIS for SFNM+0.0Fe-red-GDC and SFNM+1.2Fe-red-GDC at 1.6 and 1.8 V. | 61 |
| Figure 4.7 FTIR spectra of CO ₂ chemisorption and physisorption for SFNM+0.0Fe-red and SFNM+1.2Fe-red at 600 °C..... | 62 |
| Figure 4.8 (a) Normalized electrical conductivity relaxation curves for SFNM+0.0Fe-red and SFNM+1.2Fe-red at 850 °C with switching of the gas stream from 2:1 CO-CO ₂ to 1:1 CO-CO ₂ . XPS of (b) Temperature-dependent electrical conductivities of SFNM+0.0Fe-red and SFNM+1.2Fe-red under 50% CO ₂ /50% CO atmosphere. | 65 |
| Figure 4.9 (a) The current density response curves for the 15 min potential step chronoamperometry and (b) corresponded CO productivity and <i>FECO</i> for SFNM+0.0Fe-red-GDC and SFNM+ 1.2Fe-red-GDC at 850 °C with pure CO ₂ | 67 |
| Figure 4.10 (a) 100h long term stability testing for SFNM+0.0Fe-red-GDC and SFNM+ 1.2Fe-red-GDC at 1.6V and 850 °C in pure CO ₂ . SEM images of cathode surface microstructure of (b ₁ -b ₂) SFNM+0.0Fe-red-GDC and (c ₁ -c ₂) SFNM+1.2Fe-red-GDC after long-term stability at 1.6 V and | |

850 °C. SE-STEM and STEM-EDS images of cathode on (d) SFNM+0.0Fe-red-GDC, (e) SFNM+1.2Fe-red-GDC after long-term stability at 1.6 V and 850 °C..... 70

Figure 4.11 (a) Raman spectra collected from cathode surface of SFNM+0.0Fe-red-GDC and SFNM+1.2Fe-red-GDC after the long-term stability test. (b) Raman spectra collected from cathode surface of SFNM+0.0Fe-red-GDC whose stability test was interrupted before entering the Phase II..... 71

Figure 4.12 Structure evolution driven degradation mechanisms for SFNM+0.0Fe-red-GDC and SFNM+1.2Fe-red-GDC at high negative potentials..... 72

Figure S4.1 Synthesis route of guest Fe deposition on the surface of SFNM for TIE-assisted exsolution process. 75

Figure S4.2 XRD pattern of SFNM+1.5Fe-red. 75

Figure S4.3 XRD pattern of SFNM+0.0Fe-red. 76

Figure S4.4 TEM with EDS of randomly selected nanoparticles on (a-c) SFNM+0.0Fe-red and (d-e) SFNM+1.2Fe-red. 76

Figure S4.5 (a₁, a₂-d₁, d₂) SEM images of microstructures and (a₃-d₃) size distribution histograms of the exsolved nanoparticles on SFNM+xFe-red (x=0.0, 0.5, 0.8, 1.2)..... 77

Figure S4.6 Population of exsolved nanoparticles in 1µm² area..... 78

Figure S4.7 XPS O 1s spectra for SFNM+xFe-red (x=0.0, 0.5, 0.8, 1.2)..... 78

Figure S4.8 *j* – *V* curves for SFNM+ *x* Fe-red (x =0.0, 0.5, 0.8, 1.2) at 800 and 850 °C. 79

Figure S4.9 Nyquist plots of SFNM+1.2Fe-red-GDC at 800 °C (Equivalent circuit model: LR(Q_HR_H)(Q_LR_L)). 80

Figure S4.10 Comparison of deconvoluted results of EIS on SFNM+0.0Fe-red and SFNM+1.2Fe-red at applied potentials and 850 °C by DRT analysis. 82

Figure S4.11 FTIR spectra of CO₂ (a) chemisorption and (b) physisorption for SFNM+0.0Fe-red and SFNM+1.2Fe-red at 400 °C. Time dimensioned FTIR spectra for (c, e) SFNM+0.0Fe-red and (d, f) SFNM+1.2Fe-red at 400 and 600 °C. 82

Figure S4.12 Overlap of Sr- and O- EDS signals for SFNM+0.0Fe-red and SFNM+1.2Fe-red. 83

Figure S4.13 TGA of SFNM+xFe-red (x=0.0, 0.5, 0.8, 1.2) in the 5% H₂/95% N₂ atmosphere. 83

Figure S4.14 Three defective configurations of (a) $VFe'' - VO \cdot\cdot$, (b) VFe'' and (c) $VO \cdot\cdot$ in SFM. The gray balls represent Sr atoms, the red balls represent Fe atoms, the pink balls represent Mo atoms, the blue balls represent O atoms. 84

Figure S4.15 XPS of (a) Fe 2p and (b) Mo 3d for SFNM+0.0Fe-red and SFNM+1.2Fe-red. 85

Figure S4.16 (a) Fe K-edge and (b) Ni K-edge X-ray absorption near-edge structure (XANES) spectra of SFNM-oxi, SFNM+0.0Fe-red and SFNM+1.2Fe-red, together with reference samples Fe-foil, FeO, Fe₂O₃, Ni-foil, and NiO. Fourier-transformed (c) Fe K-edge and (d) Ni K-edge extended X-ray absorption fine structure (EXAFS) spectra of SFNM-oxi, SFNM+0.0Fe-red and SFNM+1.2Fe-red, together with reference samples Fe-foil, FeO, Fe₂O₃, Ni-foil, and NiO. 85

Figure S4.17 Temperature-dependent electrical conductivities of SFNM+0.0Fe-red and SFNM+1.2Fe-red under 5% H₂/95% Ar atmosphere. 86

Figure S4.18 High resolution TEM results for (a) SFNM+0.0Fe-red and (b) SFNM+1.2Fe-red. 87

Figure S4.19 I-V curves of SFNM-oxi-GDC with that of SFNM+0.0Fe-red-GDC and SFNM+1.2Fe-red-GDC at (a) 800 °C and (b) 850 °C. Comparison of (c) Short-term stability and (d) long-term

stability performances at 850 °C of SFNM-oxi-GDC with that of SFNM+0.0Fe-red-GDC and SFNM+1.2Fe-red-GDC..... 87

Figure S4.20 SEM images of cathode surface microstructures of SFNM-oxi-GDC after long-term stability at 1.6 V and 850 °C..... 88

Figure S4.21 TEM images of cathode surface microstructures of SFNM-oxi-GDC after long-term stability at 1.6 V and 850 °C..... 88

Figure S4.22 Raman spectrum collected from cathode surface of SFNM-oxi-GDC after the long-term stability test..... 89

Figure S4.23 SEM images of cross section of (a) SFNM+0.0Fe-red-GDC and (b) SFNM+1.2Fe-red-GDC after long-term stability tests at 1.6 V and 850 °C. 89

Figure 5.1 Design scheme of the exsolution-facilitated P-eNs with different perovskite compositions as scaffold. (In the 3D models, the red area represents DP structure, the blue area represents LP structure, the light green area represents Fe-Ni nanoparticles. In the 2D models, the purple spheres represent A-site atoms Sr, the pink spheres represent B-site atoms Fe/Ni/Mo, the gray spheres represent oxygen atoms, and the green spheres represent exsolved Fe-Ni alloy nanoparticles). 92

Figure 5.2 Secondary electron-scanning transmission electron microscopy (SE-STEM) and STEM with energy-dispersive X-ray spectroscopy (STEM-EDS) results results of SFN₃M-red-2h. 94

Figure 5.3 a, XRD patterns of three P-eNs (DLP-NPs, SFN₃M+1.2Fe-red-2h, SFN₃M-red-10h). **b**, Ex situ XRD patterns of SFN₃M+1.2Fe after reduction at different temperatures and time. 94

Figure 5.4 SEM images of microstructures and size distribution histograms of the exsolved nanoparticles on SFN₃M-red (black color), SFN₃M+1.2Fe-red (pink color) and SFN₃M-red-10h (blue color)..... 95

Figure 5.5 High resolution Environmental transmission electron microscope (HRTEM) images and the corresponding electron diffraction patterns of (e) SFN₃M+1.2Fe-red-2h, (f) SFN₃M-red-2h and (g) SFN₃M-red-10h, respectively..... 96

Figure 5.6 FTIR spectra of CO₂ chemisorption and physisorption for DP-NPs, DLP-NPs and LP-NPs at 400 and 600 °C. **b**, CO₂-TPD results of DP-NPs, DLP-NPs and LP-NPs up to 850 °C. 98

Figure 5.7 (a) DFT-based CO₂ surface adsorption configurations and energies (*E_{ad.}*) on DP-VO ··, LP-VO ··, DP-VO ··-F2N3, DP-VO ··-F3N1, LP-VO ··-F2N3 and LP-VO ··-F3N2 models, and the Fe/Ni ratio in exsolved nanoparticles. In these DFT models, the grey balls represent Sr atoms, the red balls represent Fe atoms, the dark blue balls represent Ni atoms, the pink balls represent Mo atoms, the light blue balls represent O atoms. Change in *E_{ad.}* with model evolution toward (b) DP-VO ··-F3N1 and (c) LP-VO ··-F3N2..... 99

Figure 5.8 (a) Comparison of catalytic activity among all P-eNs-GDC. (a) Current density-voltage curves and (b) EIS results of DP-NPs-GDC, DLP-NPs-GDC and LP-NPs-GDC for pure CO₂ electrolysis at 850 °C. The inset is the equivalent circuit used to simulate the EIS data. (c) DRT results of DP-NPs-GDC, DLP-NPs-GDC and LP-NPs-GDC at 1.4 and 1.6 V..... 101

Figure 5.9 Index characterization of charge conduction capability of DP-NPs, DLP-NPs and LP-NPs. 102

Figure 5.10 Gibbs free energy diagram for CO₂ electrolysis over models DP-VO ··-F2N3, DP-VO ··-F3N1, LP-VO ··-F2N3 and LP-VO ··-F3N2. 103

Figure 5.11 Stability performances of all SOECs and indicators of stability of P-eNs. a,b, Short-term stability tests. **(a)** The current density response curves for the 20 min potential step chronoamperometry and **(b)** the corresponded CO productivity (histogram) and FE_{CO} (markers) for DP-NPs-GDC, DLP-NPs-GDC and LP-NPs-GDC. **c,** Long-term stability performances of DP-NPs-GDC, DLP-NPs-GDC and LP-NPs-GDC at 1.4 V and 850 °C. 104

Figure 5.12 (a) Formation energy of first three oxygen vacancies on models DP-SFM, Ni-DP-SFM, LP-SFM and Ni-LP-SFM calculated by DFT. **(b)** Co-segregation energies of Fe and Ni on slabs DP-SFM (001), Ni-DP-SFM (001), LP-SFM-1 (001), LP-SFM-2 (001), Ni-LP-SFM-1 (001) and Ni-LP-SFM-2 (001) calculated by DFT..... 106

Figure S5.1 XRD results of $SrFe_{0.3}Ni_{0.7}O_{3-\delta}$ before and after reduction ($SrFe_{0.3}Ni_{0.7}O_{3-\delta}$ and $SrFe_{0.3}Ni_{0.7}O_{3-\delta}$ -red-2h) at 850 °C for 2h. 109

Figure S5.2 Ex situ XRD patterns of $SrFe_{0.3}Ni_{0.7}O_{3-\delta}$ after reduction at different temperatures and time. 109

Figure S5.3 XRD patterns of $SrFe_{0.3}Ni_{0.7}O_{3-\delta} + xFe$ -red-2h, ($x=0.0, 0.5, 0.8, 1.2$, where x is the molar ratio of guest Fe/host Ni). 110

Figure S5.4 Distribution density of the exsolved nanoparticles (number/ μm^2) on **(a)** DLP-NPs, **(b)** $SrFe_{0.3}Ni_{0.7}O_{3-\delta} + 1.2Fe$ -red-2h and **(c)** $SrFe_{0.3}Ni_{0.7}O_{3-\delta}$ -red-10h (It is 1 μm^2 in one yellow box). 110

Figure S5.5 STEM-EDS results of **(a)** $SrFe_{0.3}Ni_{0.7}O_{3-\delta} + 1.2Fe$ -red-2h and **(b)** $SrFe_{0.3}Ni_{0.7}O_{3-\delta}$ -red-10h. 111

Figure S5.6 Low resolution TEM image of DLP-NPs..... 112

Figure S5.7 XPS of Sr and O of air sintered $SrFe_{0.3}Ni_{0.7}O_{3-\delta}$ 112

Figure S5.8 CO_2 adsorption configuration on SFM-based DP with existence of one oxygen vacancy on the surface. In these DFT models, the grey balls represent Sr atoms, the red balls

represent Fe atoms, the dark blue balls represent Ni atoms, the pink balls represent Mo atoms, the light blue balls represent O atoms. 113

Figure S5.9 CO₂ adsorption configuration on SFM-based LP with existence of one oxygen vacancy on the surface. In these DFT models, the grey balls represent Sr atoms, the red balls represent Fe atoms, the dark blue balls represent Ni atoms, the pink balls represent Mo atoms, the light blue balls represent O atoms. 114

Figure S5.10 DFT-based CO₂ surface adsorption configuration and energies, energetic analysis of CO₂ electrolysis. Most stable CO₂ adsorption configuration on (a) DP-VO --F2N3, (b) DP-VO --F3N1, (c) LP-VO --F2N3 and (d) LP-VO --F3N2. In these DFT models, the grey balls represent Sr atoms, the red balls represent Fe atoms, the dark blue balls represent Ni atoms, the pink balls represent Mo atoms, the light blue balls represent O atoms..... 115

Figure S5.11 (a-c) The cross-sectional button cells (a₁-a₃: DLP-NPs-GDC, b₁-b₃: DP-NPs-GDC, c₁-c₃: LP-NPs-GDC). (d) Electrochemical impedance spectra with subtracting the ohmic resistance part for DP-NPs-GDC, DLP-NPs-GDC and LP-NPs-GDC. 116

Figure S5.12 DRT results of DP-NPs-GDC, DLP-NPs-GDC and LP-NPs-GDC at 1.0, 1.2, 1.4, 1.6 and 1.8 V (P₁: oxygen ion transfer through electrolyte and oxygen evolution at anode, P₂: charge transfer, P₃: surface CO₂ adsorption and activation, P₄: gas diffusion process at cathode from high to low frequency)..... 118

Figure S5.13 XPS of Fe and Mo of DLP-NPs, DP-NPs and LP-NPs. 119

Figure S5.14 (a) TGA profiles of DP-NPs, DLP-NPs and LP-NPs. (b) Long-term stability performances (first hour) of DP-NPs-GDC, DLP-NPs-GDC and LP-NPs-GDC at 1.4 V and 850 °C. (c) SEM images of cathode surface microstructure of (c₁) DLP-NPs-GDC, (c₂) DP-NPs-GDC and (c₃)

LP-NPs-GDC after long-term stability. **(d)** Repeated Raman results and **(e)** XRD results of cathode of **(i)** DLP-NPs-GDC, **(ii)** DP-NPs-GDC and **(iii)** LP-NPs-GDC after long-term stability... 120

Figure S5.15 The most stable oxygen vacancy formation sites during the sequential formations of oxygen vacancy in the DP-SFM, Ni-DP-SFM, LP-SFM and Ni-LP-SFM models. In these DFT models, grey balls represent Sr atoms, red balls represent Fe atoms, dark blue balls represent Ni atoms, pink balls represent Mo atoms, light blue balls represent O atoms, the white balls represent oxygen vacancies, the 1st, 2nd, 3rd in the white balls represent the order in which the three oxygen vacancies are formed in these models. 121

Figure S5.16 DP-based models and LP-based models for calculation of co-segregation energy.

The eight-layer metal-terminated **(a)** DP-SFM (001) and **(b)** Ni-DP-SFM (001) slabs based on the DP-Sr₈Fe₆Mo₂O₂₄ and DP-Sr₈Fe₅Ni₁Mo₂O₂₄ unit cells. The metal-terminated **(c)** LP-SFM-1 (001), **(d)** LP-SFM-2 (001), **(e)** Ni-LP-SFM-1 (001) and **(f)** Ni-LP-SFM-2 (001) slabs based on the LP-Sr₂₄Fe₁₂Mo₄O₅₆ and LP-Sr₂₄Fe₁₁Ni₁Mo₄O₅₆ unit cells. In these DFT models, the grey balls represent Sr atoms, the red balls represent Fe atoms, the dark blue balls represent Ni atoms, the pink balls represent Mo atoms, the light blue balls represent O atoms..... 122

Figure S5.17 XANES results of DP-NPs, DLP-NPs and LP-NPs. 123

Figure 6.1 **(a)** Secondary electron-scanning transmission electron microscopy (SE-STEM) and STEM with energy-dispersive X-ray spectroscopy (STEM-EDS) results of F-SFN₃M. **(b₁-b₂)** XRD patterns of air-sintered SFN₃M and F-SFN₃M. **(c)** XRD patterns of SFN₃M-red and F-SFN₃M-red. (In the 2D models, the grey balls represent Sr/F atoms, the red balls represent Fe/Ni/Mo atoms, the blue balls represent O atoms, the light blue balls represent Fe-Ni nanoparticles). 127

Figure 6.2 SEM images and size distribution histograms of the exsolved nanoparticles on **(a₁-a₃)** SFN₃M-red and **(b₁-b₃)** F-SFN₃M-red. STEM-EDS results of **(c)** SFN₃M-red and **(d)** F-SFN₃M-red. 128

Figure 6.3 XPS of **(a)** Ni _{2p}, **(b)** Fe _{2p}, **(c)** Mo _{3d} for SFN₃M-red and F-SFN₃M-red. **(d)** TGA profiles of SFN₃M-red and F-SFN₃M-red in the 5% H₂/95% N₂ atmosphere. 130

Figure 6.4 **(a)** Change of bond length of B-O after F doping in SFN₃M. Bader charge transfers on **(b)** SFN₃M and **(c)** F-SFN₃M models (In the DFT models, the grey balls represent Sr atoms, the red balls represent Fe atoms, the dark blue balls represent Ni atoms, the pink balls represent Mo atoms, the light blue balls represent O atoms, the orange balls represent F atoms). **(d-e)** Partial density of states analyses depicting the interaction between Fe/Ni 3d orbitals adjacent to F/O anions and the 2p orbitals of surrounding oxygen atoms. 131

Figure 6.5 **(a)** CO₂-TPD results of SFN₃M-red and F-SFN₃M-red up to 800 °C. **(b)** XPS of O _{1s} for SFN₃M-red and F-SFN₃M-red. **(c)** Current density-voltage curves of SFN₃M-red-GDC and F-SFN₃M-red-GDC for pure CO₂ electrolysis at 850 °C. **(d)** Comparison of simulated polarization resistance of SFN₃M-red-GDC and F-SFN₃M-red-GDC using the equivalent circuit LR(CR)(QR). 135

Figure 6.6 **(a)** The current density response curves for the 20 min potential step chronoamperometry and **(b)** the corresponding CO productivity (histogram) and FE_{CO} (markers) for SFN₃M-red-GDC and F-SFN₃M-red-GDC. **(c)** Long-term stability performances of SFN₃M-red and F-SFN₃M-red at 1.4 V and 850 °C. **(d)** Raman results of SFN₃M-red and F-SFN₃M-red after 100 h long-term stability tests. 139

Figure S6.1 Ex situ XRD patterns of **(a)** SFN₃M and **(b)** F-SFN₃M after reduction at different temperatures and time. 141

Figure S6.2 Secondary electron-scanning transmission electron microscopy (SE-STEM) and STEM with energy-dispersive X-ray spectroscopy (STEM-EDS) results of (a) SFN₃M-red (b) F-SFN₃M-red..... 141

Figure S6.3 Possible configurations and corresponding free energies of F-SFN₃M based DFT-models. (In the DFT models, the grey balls represent Sr atoms, the red balls represent Fe atoms, the dark blue balls represent Ni atoms, the pink balls represent Mo atoms, the light blue balls represent O atoms, the orange balls represent F atoms) 142

Figure S6.4 DFT models of SFN₃M and F-SFN₃M. (In the DFT models, the grey balls represent Sr atoms, the red balls represent Fe atoms, the dark blue balls represent Ni atoms, the pink balls represent Mo atoms, the light blue balls represent O atoms, the orange balls represent F atoms). 143

Figure S6.5 Simulated electrochemical impedance spectra of SFN₃M-red-GDC and F-SFN₃M-red-GDC with removing the ohmic resistance part..... 145

Figure S6.6 0-4 h long-term stability performances of SFN₃M-red and F-SFN₃M-red at 1.4 V and 850 °C. 146

List of Symbols

| | |
|---------------|--|
| ΔG | Gibbs free energy |
| $T\Delta S$ | Entropy term |
| ΔH | Enthalpy of reaction |
| E^0 | Standard-state reversible cell voltage |
| n | Number of moles of electrons transferred |
| F | Faraday's constant |
| E_{rev} | Reversible voltage |
| i_{CO_2} | Electrolysis current |
| i_{0,CO_2} | Exchange current |
| α | Charge transfer coefficient |
| η_c | Activation overpotential |
| V_{oc} | Theoretical open-circuit voltage |
| $p_{O_2,C}$ | Oxygen partial pressure at cathode |
| $p_{O_2,A}$ | Oxygen partial pressure at anode |
| $V_{oc,real}$ | Experimentally measured open-circuit voltage |
| FE_{CO} | Faraday efficiency |
| F_m | Molar flow rate in mol/s |
| I_{total} | Total current |
| v | Mole fraction of the product gas in the |

| | |
|------------------------|--|
| | gaseous mixture analyzed |
| p_0 | Atmospheric pressure |
| R | Gas constant |
| j | Current density |
| T | Temperature in K |
| V | Flow rate in mL/min |
| t | Electrolysis time |
| S | Geometric area of the electrode |
| r_A | Ionic radii of the A-site cation |
| r_B | Ionic radii of the B-site cation |
| r_C | Ionic radii of the C-site cation |
| t' | Tolerance factor |
| $V_O^{\bullet\bullet}$ | Oxygen vacancy |
| k_{chem} | Surface exchange coefficient |
| D_{chem} | Bulk diffusion constant |
| ΔG_V | Volume free energy |
| γ | Surface/interface energy |
| ΔG_n | Free energy of formation for a spherical crystalline nucleus |
| ΔG_n^* | Critical free energy barrier |
| r^* | Critical radius |

| | |
|--|--|
| r_{s-lim} | Strain-limited characteristic radius |
| $\tau_{s-lim}, \tau_{r-lim}, \tau_{d-lim}$ | Timescale |
| r_{r-lim} | Reactant-limited characteristic radius |
| r_{d-lim} | Diffusion-limited characteristic radius |
| P_{O_2} | Oxygen partial pressure |
| FE_{CO} | Faraday efficiency |
| $E_{ad.}$ | CO ₂ adsorption energy |
| ΔG_1 | Free energy of CO ₂ adsorption |
| ΔG_2 | Free energy of *CO ₂ dissociation |
| $E_{V\ddot{O}}$ | Formation energy of oxygen vacancy |
| $E_{M_{co-seg}}$ | Co-segregation energy of reducible cation M |

List of Abbreviations

| | |
|-------------------|---|
| CO ₂ | Carbon oxide |
| CCS | Carbon capture and storage |
| CO | Carbon monoxide |
| SOEC | Solid oxide electrolysis cell |
| SOFC | Solid oxide fuel cell |
| LSGM | La _{0.8} Sr _{0.2} Ga _{0.8} Mg _{0.2} O _{3-δ} |
| YSZ | 8 mol% Y ₂ O ₃ stabilized zirconia |
| GDC | Gadolinia-doped ceria |
| SDC | Ce _{0.8} Sm _{0.2} O _{1.9} |
| <i>j</i> -V | Current density-voltage |
| EIS | Electrochemical impedance spectra |
| P-eNs | Perovskite with exsolved nanoparticles |
| TPB | Triple phase boundary |
| MIEC | Mixed ionic and electronic conductivity |
| LSCM | (La _{0.75} Sr _{0.25}) _{0.97} Cr _{0.5} Mn _{0.5} O _{3-δ} |
| TIE | Topotactic ion exchange |
| SFM | Sr ₂ Fe _{1.5} Mo _{0.5} O _{6-δ} |
| LST | La _{0.2} Sr _{0.8} TiO _{3+δ} |
| LSFV _x | La _{0.5} Sr _{0.5} Fe _{1-x} V _x O _{3-δ} |

| | |
|-----------------------------------|---|
| LSCrF | $\text{La}_{0.75}\text{Sr}_{0.25}\text{Cr}_{0.5}\text{Fe}_{0.5}\text{O}_{3-\delta}$ |
| DFT | Density functional theory |
| LSNT | $\text{La}_{0.2}\text{Sr}_{0.7}\text{Ni}_{0.1}\text{Ti}_{0.9}\text{O}_{3-\delta}$ |
| SFNM | $\text{Sr}_2\text{Fe}_{1.3}\text{Ni}_{0.2}\text{Mo}_{0.5}\text{O}_{6-\delta}$ |
| SFN ₃ M | $\text{Sr}_2\text{Fe}_{1.2}\text{Ni}_{0.3}\text{Mo}_{0.5}\text{O}_{6-\delta}$ |
| XRD | X-ray diffraction |
| TEM | Transmission electron microscopy |
| EDS | Energy dispersive X-ray spectroscopy |
| FESEM | Field emission-scanning electron microscopy |
| XPS | X-ray photoelectron spectroscopy |
| HRTEM | High resolution transmission electron microscopy |
| TGA | Thermogravimetric analysis |
| FTIR | Fourier Transform Infrared Spectroscopy |
| XANES | X-ray absorption near edge structure spectra |
| EXAFS | Extended X-ray absorption fine structure spectra |
| ECR | Electrical conductivity relaxation |
| GC | Gas chromatography |
| R _S | Ohmic resistance |
| R _H and R _L | Polarization resistances at high and low frequencies |
| R _P | Total polarization resistances |
| DRT | Distribution of relaxation times |

| | |
|---|--|
| P ₁ | Oxygen ion transfer through electrolyte and oxygen evolution at anode |
| P ₂ | Charge transfer |
| P ₃ | Surface CO ₂ adsorption and activation |
| P ₄ | Gas diffusion process |
| DP-NPs | Double perovskite structure with exsolved Fe-Ni nanoparticles |
| LP-NPs | Layered perovskite structure with exsolved Fe-Ni nanoparticles |
| DLP-NPs | Composite perovskite structure with exsolved Fe-Ni nanoparticles |
| CO ₂ -TPD | CO ₂ temperature programmed desorption |
| DP-V _O ^{••} and LP-V _O ^{••} | SFM-based DP and LP with presence of one oxygen vacancy on the surface |
| DP-V _O ^{••} -F3N1 | DP-NPs model with Fe/Ni ratio of 3:1 |
| DP-V _O ^{••} -F2N3 | DP-NPs model with Fe/Ni ratio of 2:3 |
| LP-V _O ^{••} -F3N2 | LP-NPs model with Fe/Ni ratio of 3:2 |
| LP-V _O ^{••} -F2N3 | LP-NPs model with Fe/Ni ratio of 2:3 |
| F-SFN ₃ M-red | Reduced SFN ₃ M with F doping |
| PDOS | Partial density of states |

Chapter 1. Introduction

1.1 CO₂ capture and conversion: Closing the cycle

As one of the most notorious greenhouse gases, the atmospheric carbon dioxide (CO₂) has undergone an unprecedented increase over the past few decades (Figure 1.1), [1] primarily caused by the frequent anthropogenic activities such as excessive consumption of fossil fuels and deforestation. [2-4] Consequently, the accumulation of CO₂ and other greenhouse gases in atmosphere has accelerated the global warming, resulting in the melting of the polar ice caps, sea level rise, increasingly intense heatwaves, floods, and tropical storms. Such natural disasters have seriously threatened the environment and human existence on Earth. [5] To address the global warming and the impacts of climate change, member states of the United Nations signed the Paris Agreement in 2015, which established comprehensive international framework to reduce greenhouse gas emissions. [6] Policymakers worldwide have taken active measures to reduce carbon footprint by issuing decrees on energy conservation and emission reduction, as well as vigorously encouraging the research and development of CO₂ emission reduction and renewable energy utilization technologies. [7, 8]

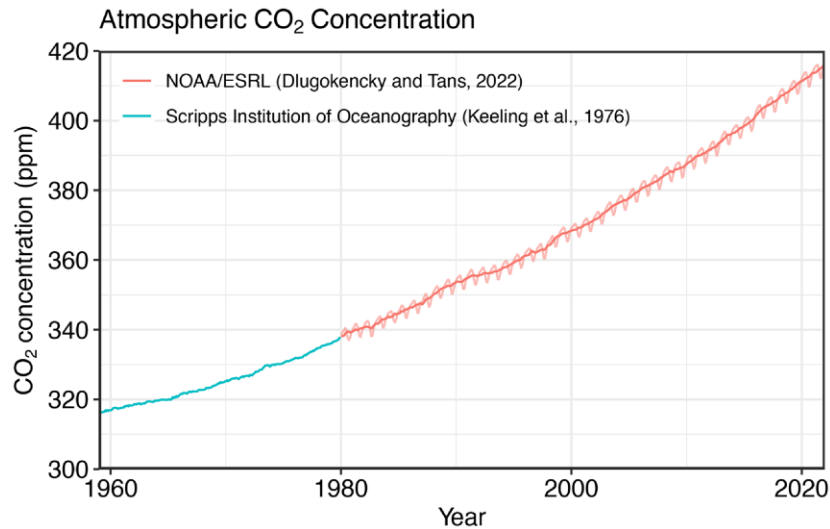


Figure 1.1 The concentration of CO₂ in the atmosphere from 1958-2021. Reprinted with permission from Reference. [1] Copyright (2022) Earth System Science Data.

The major technologies utilized to mitigate CO₂ emissions primarily include carbon capture and storage (CCS) and the conversion and utilization of CO₂. [9-11] However, the widespread implementation of CCS has been impeded by its strict geological requirements and high energy consumption.[12, 13] In contrast, the conversion of CO₂ into chemical products by chemical reformation, mineralization, enzymatic catalysis, and photochemical/electrochemical methods presents a more compelling avenue towards achieving carbon neutrality (Figure 1.2). [14-18] In particular, the electrochemical conversion of CO₂ has significant potential for practical applications due to the following reasons: (1) it is more efficient and requires less energy, (2) the production can be more readily controlled by adjusting the applied voltage and temperature, (3) the system can flexibly incorporate renewable energies such as wind, solar, nuclear, and geothermal power to drive CO₂ conversion. [19-23]

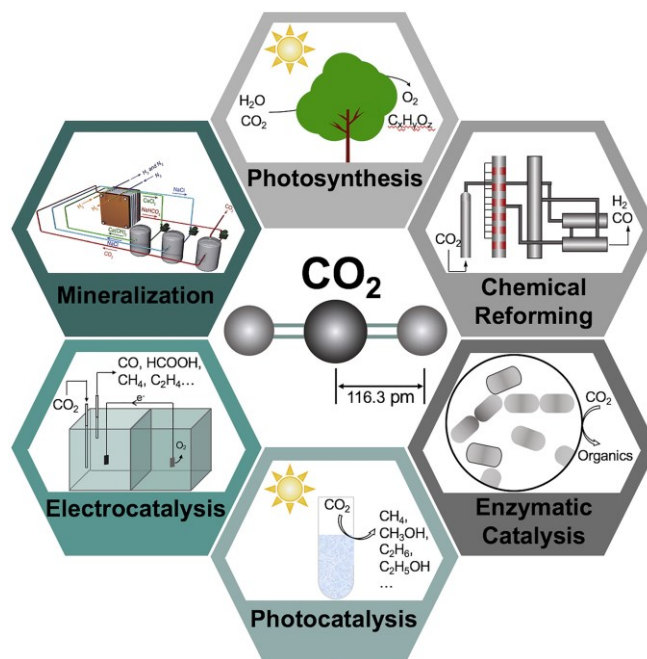


Figure 1.2 Illustration of CO₂ conversion and utilization through popular pathways, including chemical reformation, mineralization, enzymatic catalysis and photochemical/electrochemical methods. [18] Copyright (2018) Elsevier.

1.2 Basic principles of CO₂ electrolysis in solid oxide electrolysis cell (SOEC)

There are two typical approaches to achieving the CO₂ electroreduction: CO₂ reduction at room temperature and CO₂ electrocatalysis at elevated temperatures (Figure 1.3). [12, 24-26] Room-temperature electrolysis of CO₂ occurs in an aqueous environment, usually in an H-typed electrolysis cell or flow cell. [24, 27] The apparent advantage of this method is its broad range of product types, which includes carbon monoxide (CO), formic acid, methane, methanol, ethanol, and more. [18, 28, 29] However, its low current density, insufficient stability performance, poor energy efficiency, and additional cost in product separation impede its path to industrialization. [30, 31]

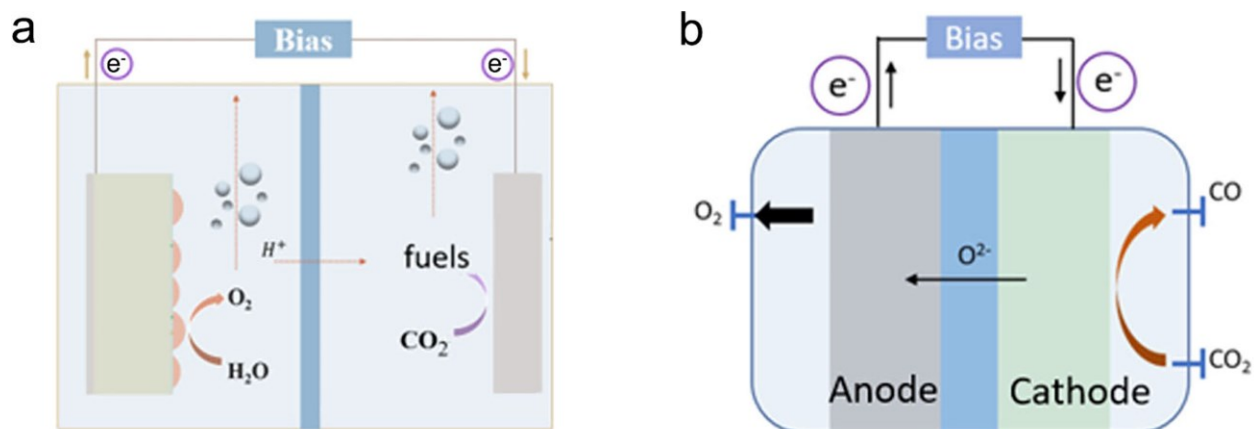


Figure 1.3 Schematic diagram of CO₂ electroreduction at (a) room temperature and (b) high temperature.

1.2.1 Introduction and application of CO₂ electrolysis in SOEC

Compared to CO₂ electroreduction at room temperature, high-temperature CO₂ electrocatalysis (700-1000 °C) in SOEC has shown great potential for reducing carbon footprint and eventually achieving carbon neutrality due to its following advantages. [26, 31-33] Firstly, the CO₂ electrocatalysis at elevated temperatures results in the facilitated reaction kinetics and enhanced electrochemical efficiency, thus leading to reduced energy consumption. [34, 35] Secondly, the primary cathode product of high-temperature CO₂ electrocatalysis is CO, which avoids the requirement for product separation that commonly happens in the case of CO₂ electroreduction at room temperature. [28, 33] The CO produced can react with H₂ in a precise ratio to generate the highly promising energy carrier known as synthesis gas. This can be further processed via Fischer-Tropsch synthesis to produce a variety of chemicals or liquid fuels. [36, 37] Thirdly, the SOEC can be flexibly integrated with the intermittent renewable energy from solar, wind, geothermal, tidal, etc, to optimize energy systems (Figure 1.4). [38] Moreover,

the reversible operation of SOEC and solid oxide fuel cell (SOFC) modes enables the mutual conversion of electricity and fuel, overcoming the shortcomings of intermittent renewable energy. [39-42]

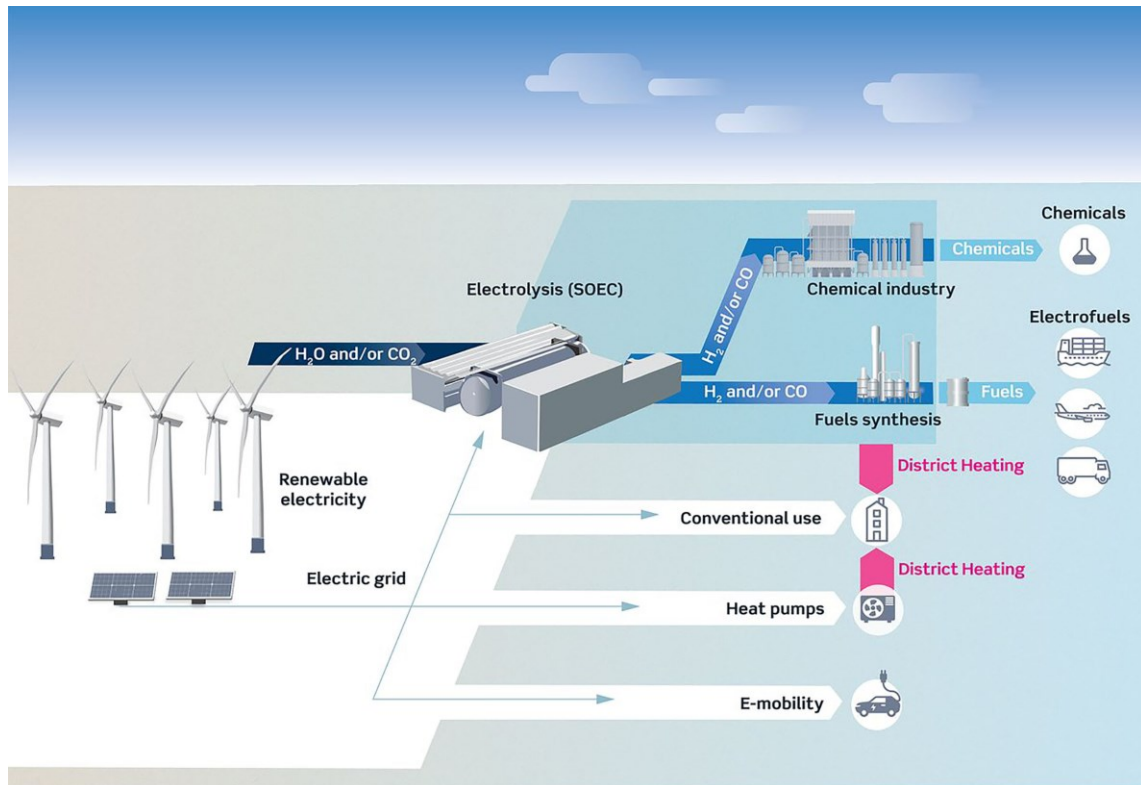


Figure 1.4 Illustration of the practical application of the CO₂ electrolysis in SOEC technology in a future energy system with increased share of intermittent electricity from renewable sources such as wind and solar. [38] Copyright (2020) American Association for the Advancement of Science.

It is worth noting that CO₂ electrolysis in SOEC also shows great promise in space exploration. In fact, the concept of CO₂ electrolysis in SOEC was initially proposed in the 1960s-70s for producing oxygen and fuel for rocket thrusters from the Martian atmosphere. [43-46] The Mars

2020 rover mission has recently achieved a significant breakthrough by successfully converting CO₂ into breathable oxygen for the first time ever, [47] thus opening up a large number of possibilities for future applications.

The general SOEC for CO₂ electrolysis is comprised of three essential components: electrolyte, anode and cathode, as depicted in Figure 1.5. [31] The porous cathode and anode compartments are separated by a dense solid electrolyte such as La_{0.8}Sr_{0.2}Ga_{0.8}Mg_{0.2}O_{3-δ} (LSGM), 8 mol% Y₂O₃ stabilized zirconia (YSZ), gadolinia-doped ceria (GDC) and Ce_{0.8}Sm_{0.2}O_{1.9} (SDC). [48-51] These materials allow only the transportation of oxygen ions and impede the conduction of electrons. During CO₂ electrolysis, the gaseous CO₂ is fed to the cathode where it is converted to CO and oxygen ions. These oxygen ions subsequently diffuse through the dense electrolyte towards the anode side and are ultimately converted to O₂ at the anode side. [52, 53] The reactions on the cathode and anode can be expressed by the following equations.

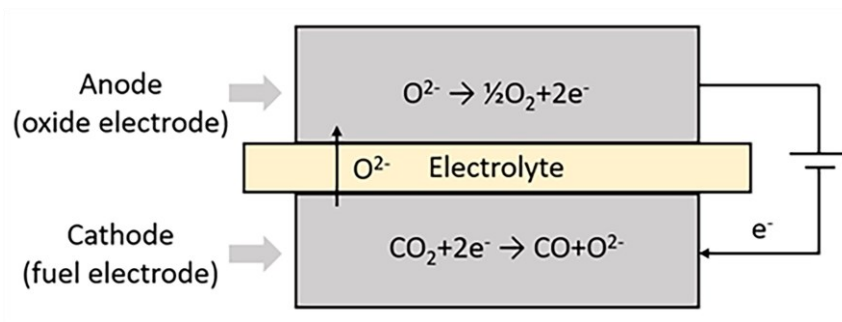
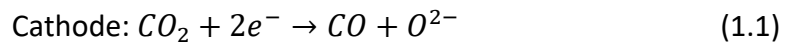


Figure 1.5 SOEC schematics and the CO₂ electrolysis reaction paths in SOEC with an oxygen-ion conductor electrolyte.

1.2.2 Thermodynamics and kinetics of CO₂ electrolysis in SOEC

Figure 1.6 illustrates the total energy required for the conversion of CO₂ into CO, as represented by the enthalpy of reaction (ΔH), as a function of temperature. Remarkably, the ΔH remains nearly constant as temperature increases, while the demand for electrical energy (ΔG , Gibbs free energy) can be significantly offset by heat ($T\Delta S$, entropy term) (equation 1.3). [54] Therefore, the CO₂ reduction at room temperature requires considerably more electric energy, making the process much less efficient. By contrast, the CO₂ electrolysis in SOECs at 800 °C can reduce electric energy consumption from 90% to 67%, resulting in a substantial improvement in energy efficiency. [33]

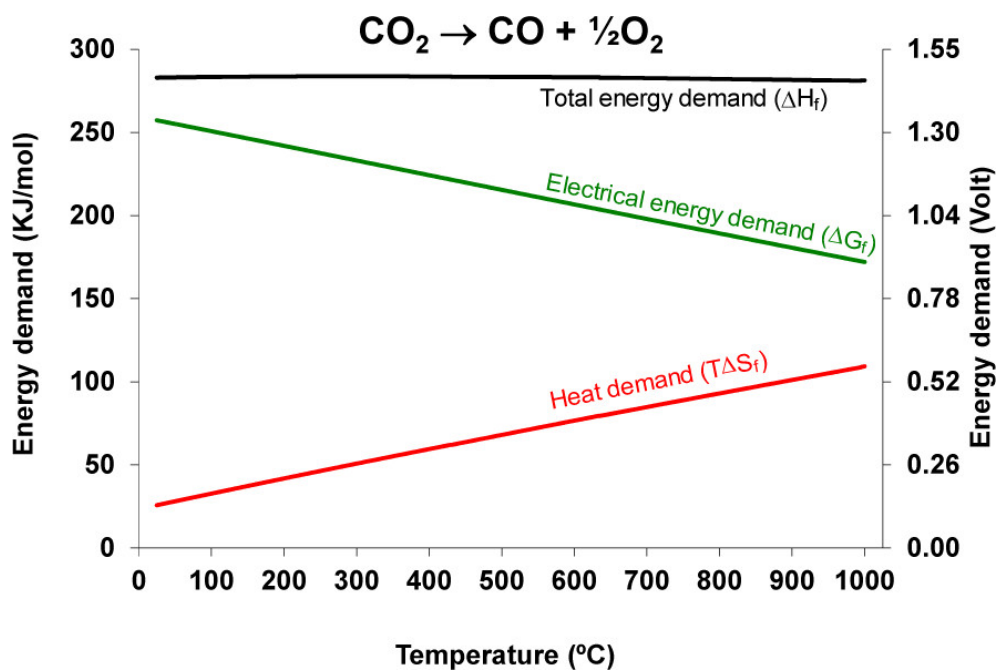


Figure 1.6 Total energy demanded (ΔH) and electrical energy demanded (ΔG) for conversion of CO₂ into CO as a function of temperature. [34] Copyright 2014 American Chemical Society.

The electromotive force to drive CO₂ reduction without the heat exchange with environment can be mathematically expressed by Equation 1.4:

$$\Delta_r H^\ominus = \Delta_r G^\ominus + T\Delta_r S^\ominus \quad (1.3)$$

$$E^0 = -\frac{\Delta_r G^\ominus}{nF} \quad (1.4)$$

Where E^0 is the standard-state reversible cell voltage, n is the number of moles of electrons transferred (n is equal to 2 in case of 1 mol CO₂ splitting), F is Faraday's constant (96485 C mol⁻¹). E^0 at the standard-state conditions (25 °C and 1 atm) is 1.33 V and decreases with increased temperature.

In addition, the reversible voltage E_{rev} is also affected by the partial pressure of CO₂ and CO at cathode side and the oxygen partial pressure at anode side, which can be expressed by the Nernst equation: [54]

$$E_{rev} = E^0 - \frac{RT}{2F} \ln \frac{p_{CO_2}}{p_{CO} p_{O_2}^{1/2}} \quad (1.5)$$

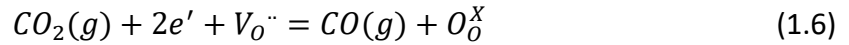
Where R is universal gas constant, T is absolute temperature, p_{CO_2} and p_{CO} are the partial pressure of CO₂ and CO at cathode, respectively, while p_{O_2} is the oxygen partial pressure at anode. Assuming the CO₂/CO is equal to 1 at the cathode side and 1 atm oxygen at the anode, the calculated $E_{rev} = E^0 = 0.97$ V at 800 °C. During the practical CO₂ electrolysis, the anode is usually exposed to air, the oxygen partial pressure is only 0.21 atm, which causes the further decrease of E_{rev} to 0.947 V. Table 1.1 lists the values of E_{rev} at 800 °C when anode is exposed

to air and cathode is fed using different CO/CO₂ atmospheres, it is clear that E_{rev} shows a decreasing trend with decreasing CO concentration. [55]

Table 1.1 Reversible voltage E_{rev} at 800 °C for CO₂ electrolysis when anode is exposed to air and cathode is fed using different CO/CO₂ atmospheres [55].

| CO/CO ₂ | 2:1 | 1:1 | 1:2 | 1:4 | 1:9 | 1:19 | Pure CO ₂ |
|--------------------|-------|-------|-------|-------|-------|-------|----------------------|
| E_{rev} (V) | 0.979 | 0.947 | 0.915 | 0.883 | 0.845 | 0.811 | 0.364 |

In terms of kinetics, this thesis prioritizes the cathode side where CO₂ reduction occurs, and the cathode reaction can be represented by Kröger-Vink notation:



Where e^- refers to free electron from external circuit, $V_{O''}$ represents oxygen vacancy in cathode, and O_O^X is the lattice oxygen. In details, it involves the adsorption and activation of the non-polarized CO₂, charge transfer, and CO desorption. These sub-processes play an important role in determining the performance of CO₂ electrolysis by influencing the activation polarization, ohmic polarization, and concentration polarization of SOEC.

The activation polarization of the cathode is highly related to the reactivity of the catalysts. The Butler-Volmer equation is a fundamental equation to describes the interplay between the current density and applied voltage associated with the cathodic activation polarization, (Equation 1.7) providing the insights into the underlying mechanism of this process:

$$i_{CO_2} = i_{0,CO_2} \left[\exp\left(\frac{\alpha F \eta_c}{RT}\right) - \exp\left(-\frac{(1+\alpha) F \eta_c}{RT}\right) \right] \quad (1.7)$$

Where i_{CO_2} is the electrolysis current, i_{0,CO_2} is the exchange current, α is the charge transfer coefficient, F is Faraday constant, η_c is the activation overpotential, R is gas constant. It is noted that the forward reaction dominates when i_{0,CO_2} is small and η_c is large, and the Butler-Volmer equation can be simplified into Tafel equations.

$$\eta_c = a + b \log i_{CO_2} \quad (1.8)$$

$$a = -\frac{RT}{2\alpha F} \ln i_{0,CO_2} \quad (1.9)$$

$$b = \frac{RT}{2\alpha F} \quad (1.10)$$

Where b is called the Tafel slope. Once the activation polarization region has been surpassed (i.e., the energy barrier that hinders the reaction has been overcome), the current density-voltage curve is primarily dominated by ohmic polarization, encompassing the transfer of oxygen ions and electrons. As the voltage is further increased, the reaction rate also rises, leading to rapid reactant consumption. This, in turn, results in a decline in reactant concentration at the cathode surface. Consequently, the current density no longer increases with increasing applied voltage, but instead remains constant at the limiting current density.

1.2.3 Metrics for evaluating SOEC performances

To evaluate the performance of the state-of-the-art SOEC, various fundamental metrics have been introduced.

Open-circuit voltage. The theoretical open-circuit voltage (V_{oc}) is dependent on the difference of oxygen partial pressures at cathode ($p_{O_2,C}$) and anode ($p_{O_2,A}$), [55] which can be expressed by the Nernst equation for oxygen reduction reaction.

$$V_{oc} = \frac{RT}{4F} \ln \frac{p_{O_2,A}}{p_{O_2,C}} \quad (1.11)$$

The experimentally measured open-circuit voltage ($V_{oc,real}$) is expected to be slightly lower than the theoretical V_{oc} due to the inevitable leakage, internal short circuit and polarization of the cell. Generally, $V_{oc,real}$ is used to evaluate the tightness of cell before CO₂ electrolysis. Upon exceeding the $V_{oc,real}$, a non-zero current density arises, which drives the CO₂ reduction at cathode and oxygen evolution reaction at the anode.

Current density-voltage curve ($j - V$). $j - V$ curve is used to quantitatively evaluate the overall CO₂ electrocatalysis performance of a SOEC. This metric allows for a preliminary judgment of the catalytic activity of cathodic catalyst by comparing the j under the same conditions.

Electrochemical impedance spectroscopy (EIS). Once the current response of the SOEC has been recorded through the application of a small sinusoidal voltage perturbation (a maximum 20 mV alternating current signal is applied to keep a pseudolinear segment of the $j - V$ curve), the resulted Nyquist plot provides a clear visualization of the real and imaginary components of impedance, allowing for an in-depth analysis of the electrode reaction in SOEC. The EIS results can be further interpreted through the use of equivalent circuit modeling, which can extract valuable electrode kinetic information, thus revealing the underlying processes occurring on the electrodes. In this way, EIS serves as a powerful in-situ diagnostic tool that can help distinguish the major sources of polarization loss and uncover the electrode dynamic process of the SOEC.

Faraday efficiency (FE_{CO}) and CO productivity. FE_{CO} and CO productivity are another two important indexes that can be determined through a series of potential step

chronoamperometry. Faraday efficiency is a measure of the efficiency with which charge (electrons) is transferred during an electrochemical reaction, and is described by the general formula in Equation 1.12:

$$FE_j = \frac{nFvF_m}{I_{total}} \times 100\% \quad (1.12)$$

Where n is the number of electrons exchanged, F is Faraday's constant ($F = 96487 \text{ C/mol}$), v is the mole fraction of the product gas in the gaseous mixture analyzed (also equals to the volume fraction if gases are assumed to be ideal), F_m is the molar flow rate in mol/s, and I_{total} is the total current. For CO_2 electrolysis in SOEC, the only product at cathode side is CO. The specific Faraday efficiency formula for producing CO can be derived from the general Faraday efficiency formula. As shown in Equation 1.13, the molar flow rate is derived from the volume flow rate V by the relation $F_m = p_0V/RT$, with p_0 the atmospheric pressure (Pa), R the ideal gas constant ($R = 8.314 \text{ J/mol K}$), and T the temperature in K. Therefore, the Faraday efficiency for producing CO (FE_{CO}) can be expressed as Equation 1.16:

$$FE_{CO} = \frac{2Fvp_0V}{RT_0I_{total}} \times 100\% \quad (1.13)$$

$$FE_{CO} = \frac{2 \times 96485 \left(\frac{\text{C}}{\text{mol}}\right) \times V \left(\frac{\text{m}^3}{\text{s}}\right) \times v(\text{vol}\%) \times 1.01 \times 10^5 \left(\frac{\text{N}}{\text{m}^2}\right)}{8.314 \left(\frac{\text{N}\cdot\text{m}}{\text{mol}\cdot\text{K}}\right) \times 298.15(\text{K}) \times I_{total} \left(\frac{\text{C}}{\text{s}}\right)} \times 100\% \quad (1.14)$$

$$FE_{CO} = \frac{2 \times 96485 \left(\frac{\text{C}}{\text{mol}}\right) \times V \left(\frac{\text{mL}}{\text{min}}\right) \times 10^{-6} \left(\frac{\text{m}^3}{\text{mL}}\right) \times v(\text{vol}\%) \times 1.01 \times 10^5 \left(\frac{\text{N}}{\text{m}^2}\right)}{8.314 \left(\frac{\text{N}\cdot\text{m}}{\text{mol}\cdot\text{K}}\right) \times 298.15(\text{K}) \times I_{total} \left(\frac{\text{C}}{\text{s}}\right) \times 60 \left(\frac{\text{s}}{\text{min}}\right)} \times 100\% \quad (1.15)$$

Where the unit of V is mL/min. Then,

$$FE_{CO} = \frac{0.1315 \times V\left(\frac{mL}{min}\right) \times v(vol\%)}{I_{total}(A)} \times 100\% \quad (1.16)$$

Where $V\left(\frac{mL}{min}\right)$ = Gas flow rate measured by a flow meter at the exit of the cell at room temperature and under ambient pressure.

$v(vol\%)$ = Volume concentration of CO in the exhaust gas from the cell (obtained by gas chromatography).

$I_{total}(A)$ = cell current during short-term stability experiments.

CO productivity, on the other hand, measures the amount of CO produced per unit time, which can be described by the following equation: [56]

$$Production\ rate\ of\ CO = \frac{q_{total} \times FE_{CO} \times 22.4(L/mol) \times 1000 \times 60\left(\frac{h}{min}\right)}{FntS \times 100} \quad (1.17)$$

Where q_{total} = total charge passed.

FE_{CO} = Faradaic efficiency of CO.

F = Faraday constant.

n = the number of exchanged electrons to produce CO from CO₂.

t = electrolysis time (h).

S = the geometric area of the electrode (cm²).

Both of these two parameters provide important information about the efficiency and effectiveness of the electrocatalytic system in converting CO₂ to CO.

1.3 Scope of the thesis

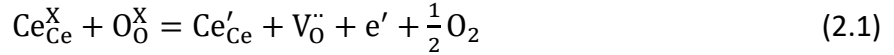
CO₂ electrolysis in SOEC represents a promising technology for converting CO₂ to valuable chemicals with the potential to reduce carbon emissions at commercial scale and promote a low-carbon economy. [38] Despite its promising future, CO₂ electrolysis in SOEC remains at the laboratory research and development stage. Advanced electrode materials are crucial to the transition of this technology from laboratory to industrialization, and perovskite-based materials have emerged as a particularly promising candidate due to their low cost, abundance, and ease of synthesis. [57] However, the catalytic activity of perovskite is still inferior to that of commonly used Ni-based ceramics. [31] Fortunately, the use of in-situ exsolution techniques can enhance the catalytic activity of perovskites. Nonetheless, employment of perovskite materials with exsolved nanoparticles for practical application still presents many challenges. This thesis places its primary emphasis on the advancement of perovskite with exsolved nanoparticles (P-eNs) based electrode materials that exhibit both high catalytic activity and stability; the thesis also investigates the CO₂ electrolysis mechanism on P-eNs to direct the creation of P-eNs based catalysts suitable for a broad range of applications in energy storage and conversion.

Chapter 2. Literature review of cathode candidates for CO₂ electrolysis in SOEC

In consideration of the cathode reaction, it is imperative that cathode materials fulfill several prerequisites, including high ionic and electronic conductivities, superior catalytic activity, robust stability under operating conditions, and high compatibility with electrolyte. [31, 54] Over time, many cathode materials have been developed to meet these requirements, ranging from metals and metal-ceramic materials to perovskite-based materials. [26, 35, 58-60]

2.1 Metal, metal oxide-based cathode materials

Metals, such as Ni and Pt, have demonstrated high catalytic activities towards CO₂ electrocatalysis in SOEC. [61, 62] However, the cathode reaction occurs only at the interface between metal and electrolyte due to the poor oxygen ion conductivity of metal, which restricts the length of the triple phase boundary (TPB) composed of gaseous CO₂, oxygen ion conductor and electronic conductor (Figure 2.1a). [63] The introduction of a pure oxygen ion conductor like YSZ and GDC can expand the TPB across the entire cathode layer, thereby increasing the number of reactive sites for CO₂ electrocatalysis (as depicted in Figure 2.1b). Typically, Ni-YSZ has been extensively studied as the cathode owing to its excellent ionic and electronic conductivities. [53, 64] Furthermore, the catalytic performance further improves by replacing YSZ with GDC due to the mixed ionic and electronic conductivity of ceria in the reducing environment. [65-69] The reduction of GDC ($\text{Ce}^{4+} \rightarrow \text{Ce}^{3+}$) in the composite electrodes under cathodic polarization would offer additional electrical conduction paths (Equation 2.1). [70-72]



Nevertheless, a major issue for the Ni-cermet is the easy oxidation of Ni at high CO₂ concentration, which significantly decreases the reactivity of electrode. [73-75] To address this issue, a small amount of reductive gases such as CO or H₂ have been introduced into the cathode side along with the CO₂ flow. [76] Yue et al. found the polarization resistance of Ni-YSZ cathode initially reduced but then increased with increasing the CO concentration in the cathodic reaction gas flow. [77] The reduced polarization resistance of Ni-YSZ at low concentration of CO can be ascribed to the suppressed oxidation of Ni, while the incorporation of high concentration of CO would lead to the undesired coking near Ni active sites. [53, 78] In addition, other metal-cermets like Cu-GDC, Ni-Ru-GDC have also been investigated as cathode materials for CO₂ electrolysis due to the relatively cheap price of Cu and higher resistance to carbon deposition of Cu and Ru than Ni. [79, 80]

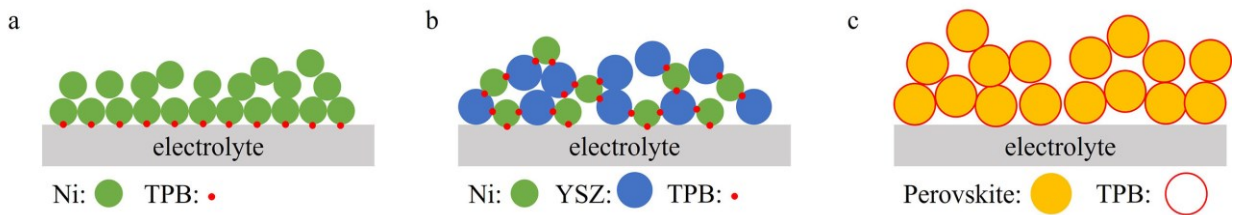


Figure 2.1 Schematic diagrams of TPB in the (a) metallic Ni, (b) Ni-YSZ and (c) perovskite-based catalysts.

2.2 Perovskite-based cathode materials

Perovskites have shown great potentials as the alternative cathode materials for CO₂ electrocatalysis due to their unique mixed ionic and electronic conductivity (MIEC) (Figure 2.1c),

[57, 81-83] high redox stability and high resistance to coking at elevated temperatures. [84, 85] Typically, a simple perovskite has a general formula of $ABO_{3\pm\delta}$, where A-site is occupied by the large-sized alkaline earth ions coordinated with twelve oxygen ions, [83, 86] such as lanthanides, while B-site is occupied by the small-sized transition cations coordinated with six oxygen ions (Figure 2.2).

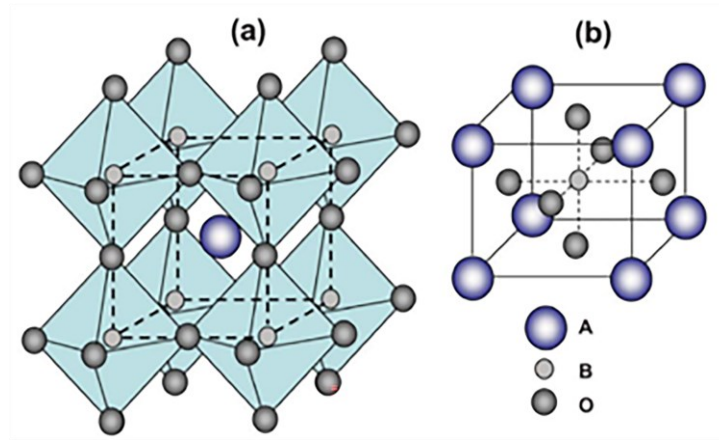


Figure 2.2 The structure illustration of ideal perovskite $ABO_{3\pm\delta}$. **(a)** Corner-sharing (BO_6) octahedral with A ions located in 12-coordinated interstices. **(b)** B-site cation at the center of the cell. [83] Copyright (2017) Elsevier.

Due to the remarkable electronic structural versatility and compositional flexibility, the abundant defect sites and feasible cation substitution with similar ionic radii are allowed on A-site, B-site and O-site of perovskite. [87-89] The tolerance factor t' , [90] first introduced by Goldschmidt in the early 1920s, provides a preliminary means of assessing the structural characteristics of perovskites: [91]

$$t' = \frac{(r_A + r_O)}{\sqrt{2}(r_B + r_O)} \quad (2.2)$$

Where r_A , r_B and r_O are the ionic radii of the A-site cation, B-site cation and O-site anion, respectively. The range of t for most developed perovskites lies between 0.75-1.00. When $t' = 1$, a perfect cubic structure can be obtained, whereas the crystalline structure of perovskite will undergo distortion and transformation when the t deviates from 1, resulting in orthorhombic, tetragonal, or rhombohedral structures. This endows the perovskites with the versatile physicochemical properties. Besides the simple perovskite structure, there are two other representative perovskite-derivatives: double perovskite ($AA'B_2O_{5+\delta}$ or $A_2BB'O_{5+\delta}$) and Ruddlesden-Popper typed perovskite-oxides ($A_{n+1}B_nO_{3n+1}$, R-P typed perovskite). [92-95]

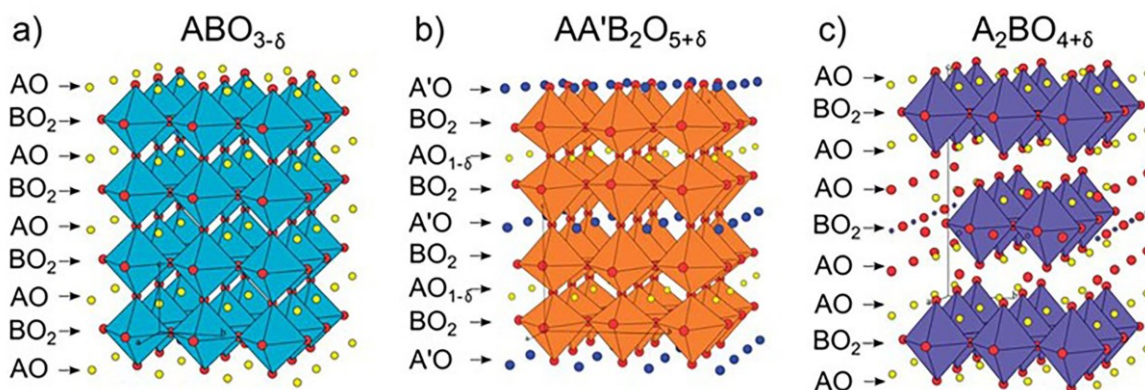


Figure 2.3 Stacking structures of (a) simple perovskite $ABO_{3\pm\delta}$, (b) double perovskite $AA'B_2O_{5+\delta}$ and (c) Ruddlesden-Popper typed perovskite-oxides ($A_2BO_{4\pm\delta}$). [96] Copyright (2014) RSC Publishing.

A comprehensive understanding of the structural characteristics and the CO_2 electrolysis mechanism on various perovskite derivatives can help us deliberately design the multifunctional composite catalysts. [97] The crystal structure of the simple perovskite with a formula of $ABO_{3-\delta}$ can be envisioned as a stack of alternating AO and BO_2 sheets (Figure 2.3a).

[96] When the aliovalent dopant A' or B' alternately occupy the A-site or B-site with the hosts A and B in an atomic ratio close to unit, the crystal structure could be transformed into a double perovskite structure (Figure 2.3b), the common double perovskite involves $\text{PrBaMn}_2\text{O}_{5+\delta}$ and $\text{Sr}_2\text{FeMoO}_{5+\delta}$ systems. [98-101] It results in the alternating differences in the oxygen ion binding capacity between host cation and aliovalent dopant in adjacent alternating layers due to the difference in charge, which leads to the lower formation energy of oxygen vacancy for the layers with weak oxygen binding capacity. [102, 103] The alternating layers with more open oxygen ion channels contribute to the increased oxygen ion conductivity of double perovskites. [104-106] The crystal structure of another intriguing family of R-P typed perovskite is constructed in a sandwich-like stacking with n ABO_3 perovskite blocks inserted between AO rock salt planes ($\text{AO}-(\text{BO}_2-\text{AO})_n-$). [95, 107-109] $\text{La}_2\text{NiO}_{4+\delta}$, one of the most popular R-P typed structures with $n=1$ (Figure 2.3c), displays the superior oxygen surface exchange rate and oxygen bulk diffusion rate. It can be ascribed to a large amount of interstitial oxygen in the LaO layers, which provides the additional interstitial oxygen transfer pathways. [110, 111] With increasing n up to 2, $\text{Sr}_3\text{FeMoO}_{7+\delta}$, another R-P typed oxide, exhibits excellent surface exchange rate and bulk diffusion rate as well, but through an accelerated vacancy hopping mechanism. [112-114] Therefore, the diverse perovskite oxides with versatile crystal structures possess unique physical and chemical properties, thus presenting more possibilities and greater application prospects for CO_2 electrocatalysis.

Thus far, the perovskites of an extensive range have been employed for high temperature CO_2 electrocatalysis in SOEC. [115-118] Given that the catalytic activity of perovskites is mainly derived from the B-site cations, the perovskite-based cathode candidates primarily include

chromate-based perovskite oxides, titanates, Mn-based, and Fe-based perovskites. [31, 119-121] However, the catalytic activities of these perovskites are still inferior to those of conventional Ni-cermet cathode materials. As a result, various strategies have been investigated to boost the reactivity of perovskite-based materials for CO₂ electrocatalysis.

2.3 Strategy to enhance the electrochemical performances of perovskites

2.3.1 Composite materials

Like metal-based electrodes mixed with pure oxygen ions, constructing the perovskite-based composite electrodes by blending with an oxygen ion conductor is one effective means of prolonging the TPB and enhancing the electrocatalytic performance relative to that of their pure perovskite cathode counterparts [60, 77, 122-125]. Yue et al. developed a composite cathode consisted of $(\text{La}_{0.75}\text{Sr}_{0.25})_{0.97}\text{Cr}_{0.5}\text{Mn}_{0.5}\text{O}_{3-\delta}$ and YSZ (LSCM-YSZ), [77] the current density reached 0.45 A cm⁻² at 2 V and 900 °C, which is lower than a current density of 0.70 A cm⁻² for Ni-YSZ cathode with the same electrolyte and anode. The current density increased to 0.49 A cm⁻² by replacing YSZ with GDC, where the reduction of Ce⁴⁺ to Ce³⁺ contributed to the enhanced oxygen ion and electronic conductivities. [77, 126] In addition, by infiltrating 12.8 wt.% GDC nanoparticles, Lv et al. found that the current density for Sr₂Fe_{1.5}Mo_{0.5}O_{6-δ} (SFM) cathode increased from 0.283 to 0.446 A cm⁻² at 1.6 V and 800 °C (Figure 2.4a). [125] Based on this advantage, the perovskite-based composite electrodes have been widely used in CO₂ electrolysis and other reactions.

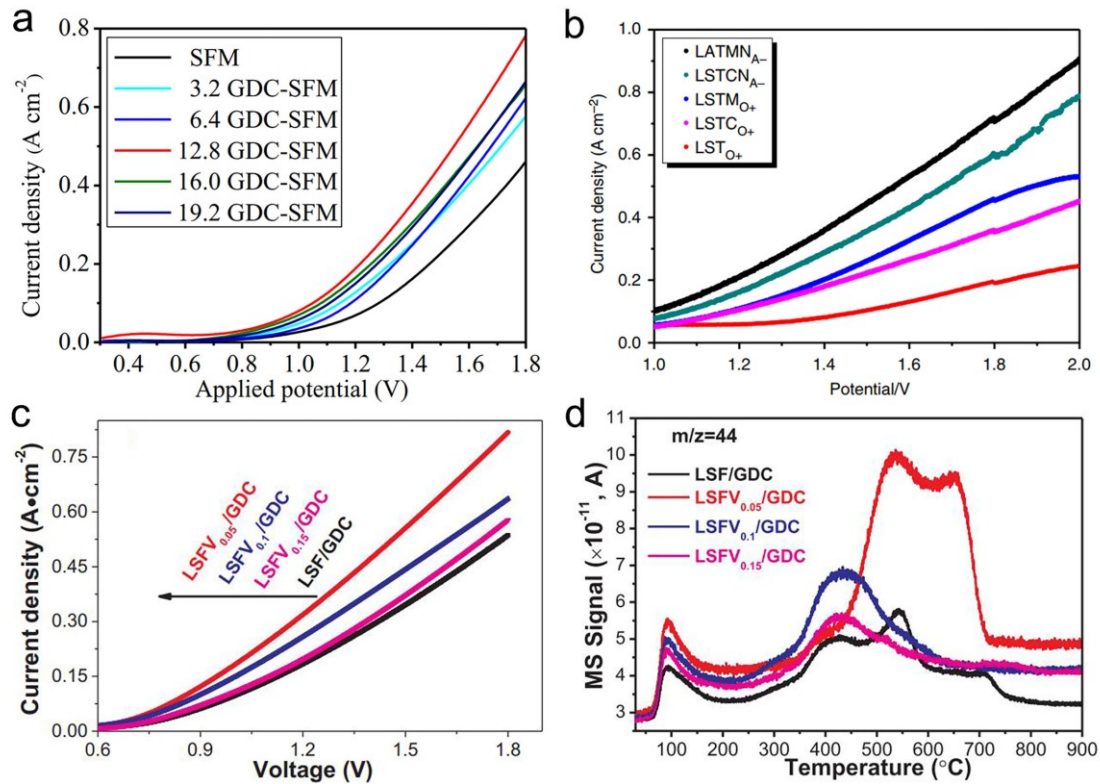


Figure 2.4 (a) Current density-voltage curves of SOEC with the SFM and GDC-SFM cathodes. [125] Copyright (2019) Elsevier. (b) Current density-voltage curves of LST and Cr, Mn doped LST (LSTC_{O+} and LSTM_{O+}) for CO₂ electrolysis at 800 °C. [89] Copyright (2017) Springer Nature. (c) Current density-voltage curves of LSF and LSF doped with different concentrations of vanadium for CO₂ electrolysis at 800 °C. [127] (d) TPD-CO₂ curves of LSFV_x/GDC with MS of CO₂ (m/z = 44). [127] Copyright (2018) Elsevier.

2.3.2 Doping

The exceptional structural adaptability and broad compositional range of perovskites have provided an avenue for employing doping techniques to further improve their intrinsic physical and chemical properties. [128-132] Intentionally manipulating the surface electronic structure

by B-site doping has been widely employed and has led to great enhancement of CO₂ electrocatalytic activity. [133-135] Ye et al. demonstrated that the catalytic activities of La_{0.2}Sr_{0.8}TiO_{3+δ} (LST) can be enhanced by partially replacing Ti with Cr/Mn. At 2 V and 800 °C, LST-based SOEC displayed a current density of 0.23 A cm⁻², while Cr-doped LST and Mn-doped LST exhibited higher current density of 0.44 and 0.51 A cm⁻², respectively (Figure 2.4b) [89] It found that, by introducing the redox-active dopants Cr and Mn, the concentration of oxygen vacancies was significantly increased under the reducing conditions (Cr³⁺→Cr²⁺ and Mn⁴⁺→Mn³⁺) due to the charge compensation, thereby boosting the surface CO₂ adsorption and bulk oxygen ion conductivity. In another work, Zhou *et al.* observed that the catalytic activities of La_{0.5}Sr_{0.5}Fe_{1-x}V_xO_{3-δ} (LSFV_x) exhibited a volcano-type profile with increasing vanadium doping concentration at Fe-site in the range of x=0-0.15, peaking at x=0.05 (LSFV_{0.05}) (Figure 2.4c). [127] From the structural characterization, the surface reactivity and bulk charge transfer seem to be highly dependent on the average oxidation state of B-site cations, and LSFV_{0.05} with the most positive charge amount at B-site exhibits the strongest CO₂ adsorption ability and the highest oxygen vacancy concentration (Figure 2.4d). Similarly, Xi et al. disclosed that the increased oxidation state of Fe in Sr₂Fe_{1+x}Mo_{1-x}O_{6-δ} by increasing the Fe concentration significantly enhanced the metal–oxygen hybridization and shifted up the O p band energy closer to Fermi level, thus accelerating the CO₂ adsorption and oxygen ion conductivity. [136]

Additionally, it should be noted that the A-site cations of perovskites also play a critical role in the CO₂ electrolysis process. [130, 137, 138] The size, valence state, and electronic configuration of A-site cations significantly influence the structural and electronic properties of perovskites. Therefore, modifying the A-site cations presents an alternative approach to

enhancing the electrocatalytic performance of perovskites without altering the active B-site. Considering the additional electronic and ionic paths delivered by Ce at the reducing condition, Zhang *et al.* doped small amount of Ce into A-site of $\text{La}_{0.75}\text{Sr}_{0.25}\text{Cr}_{0.5}\text{Fe}_{0.5}\text{O}_{3-\delta}$ (LSCrF), the current density significantly increased from 0.56 to 0.84 A cm^{-2} at 0.7 V (vs OCV), demonstrating the remarkable improvement in electrochemical performance by A-site doping. [137] Hu *et al.* systematically investigated the effect of the divalent alkaline earth cation (Ca, Sr and Ba) doping at the La-site of $\text{LaFeO}_{3-\delta}$ on the CO_2 electrocatalysis. [130] The authors clarified that the alkaline-earth elements have a major influence on the surface reactivity of the pristine perovskites. All alkaline-earth cation doped samples performed the higher catalytic activities compared to the A-site doping-free counterpart, which can be attributed to the higher concentration of the oxygen vacancies and higher CO_2 chemisorption capacity compared to the bare $\text{LaFeO}_{3-\delta}$ (Figures 2.5a and 2.5b). From the point of view of charge compensation, the negatively charged Ca'_{La} , Sr'_{La} , Ba'_{La} are well-balanced by the formation of the positively charged oxygen vacancies ($V_{\text{O}}^{\bullet\bullet}$), thus strengthening the CO_2 chemisorption. Furthermore, the divalent cation doping at La-site also contributes to the improvement of the electronic density of Fe, which facilitates the subsequent activation of the surface-adsorbed CO_2 . Nevertheless, the detrimental influence of alkaline-earth cations is also significant, for instance, the stronger sintering ability of Ca-doped LFO can lead to the easy formation of coarse powders of the perovskite. A-site segregation and surface reorganization occur on the surface of Ba- and Sr-doped LFO, which cause the formation of insulated phases BaCO_3 and SrCO_3 , respectively.

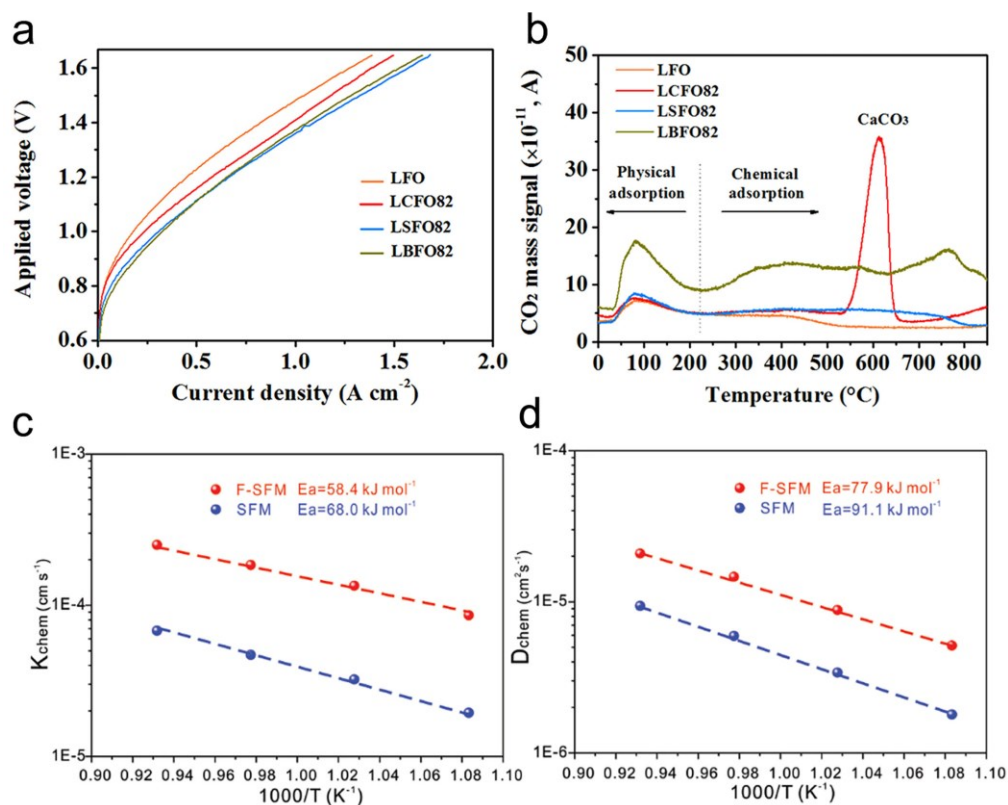


Figure 2.5 (a) Electrochemical performances of LFO, LCFO82, LSFO82 and LBFO82 for CO_2 electrolysis at 800 °C. [130] (b) CO_2 -TPD of LFO, LCFO82, LSFO82 and LBFO82. [130] Copyright (2019) Elsevier. (c) D_{chem} versus $1000/T$ and (d) k_{chem} versus $1000/T$ of F-SFM and SFM. [139] Copyright (2018) John Wiley and Sons.

In addition to A-site and B-site doping, some studies have focused on the O-site doping using F^- , Cl^- , N^{3-} . [140-145] Zhu et al. found the large electronegativity of F would weaken the binding of A-/B-site cations and O ions, which enhances the mobility of lattice oxygen and results in a higher oxygen ion diffusion in perovskite bulk. [140] Therefore, F-doped perovskites have become appealing electrocatalysts for oxygen evolution reaction and oxygen reduction reaction. [131, 146] Likewise, Li et al. have demonstrated that F doping in SFM significantly improved the

CO₂ adsorption by a factor of 2 and the chemical bulk diffusion coefficient by factors of 2–3 at 800 °C (Figures 2.5c and 2.5d), thus leading to a lower polarization resistance of 0.656 Ω cm² for F-doped SFM compared to 1.130 Ω cm² for SFM at 800 °C in the symmetrical cells. These studies suggest that anion doping at O-site of perovskites is a feasible way to facilitate the surface chemical exchange rate and oxygen ion bulk diffusion rate. It is worth noting that cation and anion co-doping strategy may have great potentials for developing the perovskites with high catalytic activity for CO₂ electrocatalysis. [132, 144]

2.3.3 Exsolution

Due to the high activity of metal particles, introducing metal nanoparticles onto perovskite significantly enhances the catalytic activity of perovskite for CO₂ reduction in SOEC. However, traditional methods such as deposition and impregnation have limitations in controlling the size and population of nanoparticles, leading to uneven dispersion on the perovskite surface. [147, 148] Moreover, the formed nanoparticles tend to agglomerate at high operating temperatures due to their weak interaction with perovskite substrates, thus causing the deactivation of active sites and degradation of electrodes. [35, 148] Alternatively, the exsolution technique has gained extensive attentions for in-situ growing nanoparticles from perovskites due to several advantages: (1) Exsolved nanoparticles are socked on the surface of perovskites, the locked interface leads to the high resistance to agglomeration at elevated temperatures (Figure 2.6). [149] (2) Exsolved nanoparticles exhibit the high resistance to hydrocarbon coking, preserving the surface reactivity of perovskites. [150, 151] (3) Exsolved nanoparticles can be re-generated by a redox treatment. [83, 148, 152-156] (4) Exsolved nanoparticles by the facile one-step reduction show smaller size, large population and more even distribution compared to the

counterparts prepared by the traditional deposition and infiltration methods, demonstrating that exsolution is more efficient, cost-saving and timesaving than the traditional methods. [147]

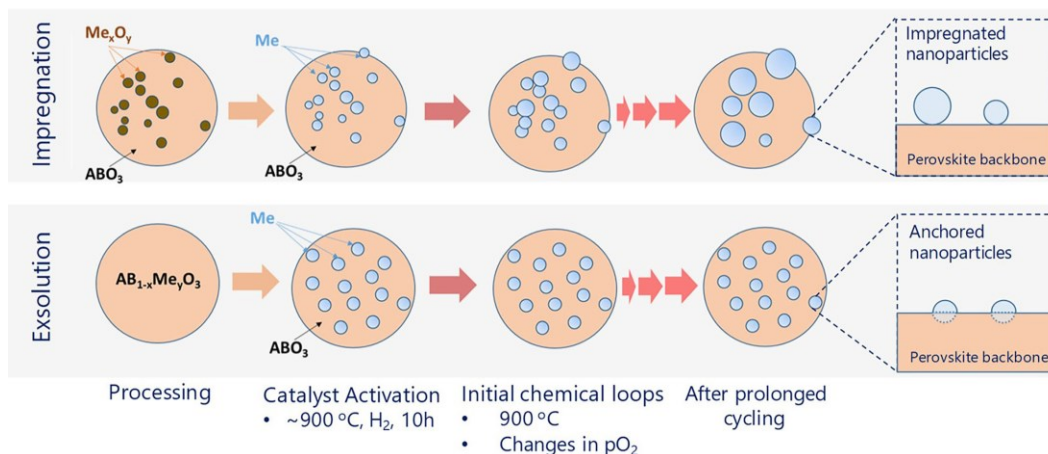


Figure 2.6 Schematic of the comparison of perovskite with nanoparticles by conventional impregnation and exsolution processes. [157] Copyright (2020) American Chemical Society.

This approach involves introducing a catalytically active cation into the B-site of the perovskite substrate during sintering in air, stripping the reducible cation from the perovskite by heating in a reducing gas flow, and finally dispersing the resulting nanoparticles on the surface of the parent perovskites (Figure 2.7). [158-160]

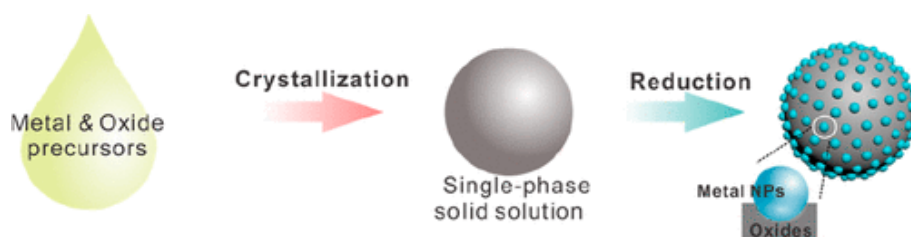


Figure 2.7 Schematic of exsolution approach for the synthesis of perovskite with exsolved nanoparticles. [161] Copyright (2020) American Chemical Society.

A comprehensive understanding of the exsolution mechanism not only can help to optimize the exsolution parameters, but also can tune the properties of the exsolved nanoparticles such as size, population and composition, thereby improving the electrochemical performance of P-eNs based catalysts. Gao et al. proposed that exsolution may involve four physical processes: diffusion of reducible cations, reduction of cations on the surface, nucleation and growth of nanoparticles on the surface (Figure 2.8a). [162] Obviously, the exsolution of nanoparticles from perovskite substrate can be considered as a phase transition process of the parent perovskite as it interacts with the reducing environment. From the classical isothermal nucleation theory, the heterogeneous nucleation of nanoparticles on the surface of perovskite is highly dependent on two opposing components (Figure 2.8b): a decrease in the volume free energy (ΔG_V) and an increase in generated surface/interface energy between nanoparticles and substrate (γ). The free energy of formation for a spherical crystalline nucleus with radius of r (ΔG_n) can be expressed by the following Equation:

$$\Delta G_n = \frac{4}{3}\pi r^3 \Delta G_V + 4\pi r^2 \gamma \quad (2.3)$$

Accordingly, only after a critical free energy barrier (ΔG_n^*) is overcome can the formation of a thermodynamically stable nuclei with the critical radius (r^*) be triggered, the relation between r^* and ΔG_n^* can be written as:

$$\Delta G_n^* = \frac{4}{3}\pi r^2 (r^*)^2 = \frac{16\pi\gamma^3}{3\Delta G_V^2} \quad (2.4)$$

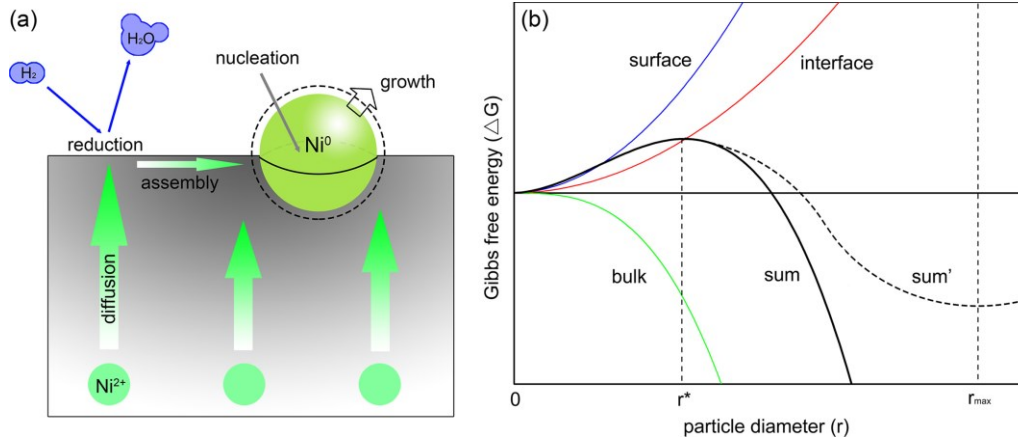


Figure 2.8 (a) Illustration of the exsolution process. (b) Gibbs free energy change during the nucleation and growth. Copyright (2016) Elsevier.

After that, ΔG_n will decrease with the increase of the crystal nucleus size, thus driving the further growth of nanoparticles. However, the experimental observation found that the growth of the exsolved nanoparticles slows down after nucleation (Figure 2.9). Considering the sluggish kinetics of B-site reducible cation diffusion and the subsequent reduction into metal processes, three major limiting models were proposed to explain the discrepancy between the experimental phenomenon and the nucleation theory, and to depict the growth of exsolved nanoparticles, including strain-limited exsolution model, reactant-limited exsolution model and diffusion-limited exsolution model (Equations 2.5-2.7). [162]

$$\text{Strain-limited: } r = r_{s-lim} \left(\ln \left(1 + \frac{t}{\tau_{s-lim}} \right) \right)^{\frac{1}{3}} \quad (2.5)$$

Where t is time, r_{s-lim} is the strain-limited characteristic radius, which is dependent on the strain energy term as a function of r . [163] The timescale τ_{s-lim} is dependent on the oxygen partial pressure in the reducing atmosphere.

$$\text{Reactant-limited: } r = r_{r-lim} \left(1 - \exp\left(-\frac{t}{\tau_{r-lim}}\right)\right)^{\frac{1}{3}} \quad (2.6)$$

Where r_{r-lim} is the reactant-limited characteristic radius, which is dependent on the total amount of reducible atoms in the bulk. The time scale τ_{r-lim} is dependent on the oxygen partial pressure in the reducing atmosphere.

$$\text{Diffusion-limited: } r = r_{d-lim} \left(\frac{t}{\tau_{d-lim}}\right)^{\frac{1}{6}} \quad (2.7)$$

Where r_{d-lim} is the diffusion-limited characteristic radius, which is dependent on the total amount of reducible atoms in the bulk. The timescale τ_{d-lim} is dependent on the diffusion coefficient.

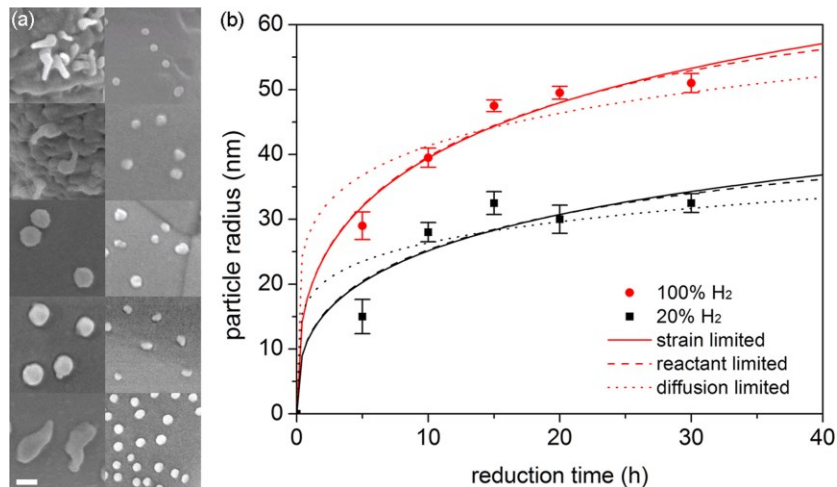


Figure 2.9 (a) Selected areas of the $\text{La}_{0.4}\text{Sr}_{0.4}\text{Sc}_{0.9}\text{Ni}_{0.1}\text{O}_{3-\delta}$ particles reduced in pure H_2 (left) and 20% H_2 (right) at 900 °C for 5, 10, 15, 20, and 30 h (from top to down) with the scale bar being 100 nm. (b) The average particle size and the fitting curves with strain-limited model (solid line), reactant-limited model (dashed line), and diffusion-limit model (dotted line). Copyright (2016) Elsevier.

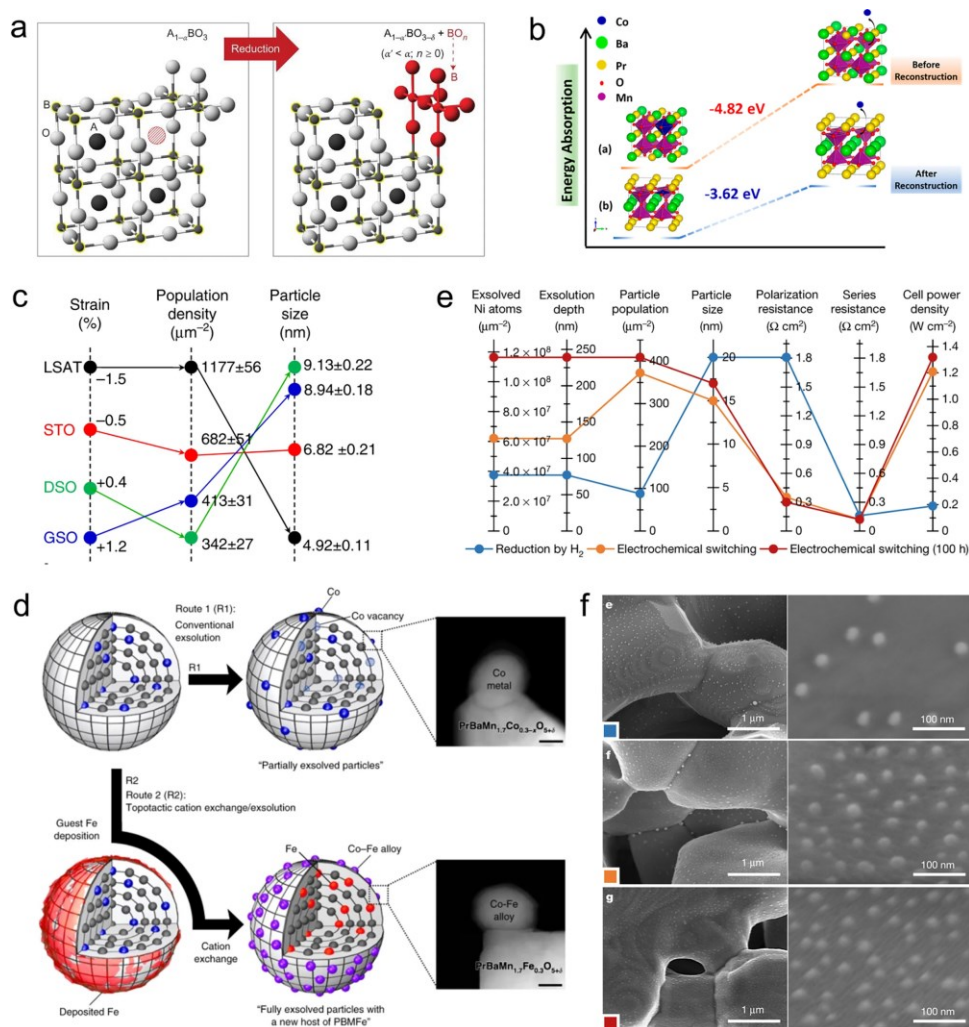
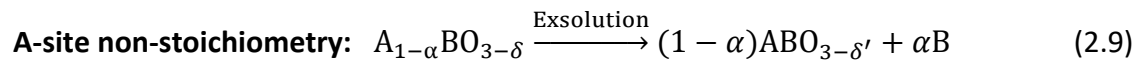
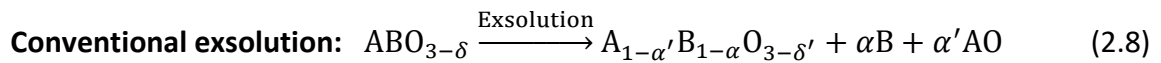


Figure 2.10 (a) Schematic representation of the exsolution of B-site cations from A-site-deficient perovskites. Copyright (2013) Springer Nature. (b) Co exsolution of double perovskites without and with crystal reconstruction. Copyright (2016) American Chemical Society. (c) Effects of the substrate on three important physical parameters related to the exsolved thin films. Copyright (2019) Springer Nature. (d) Exsolution process with and without topotactic ion exchange. Copyright (2019) Springer Nature. (e) Comparison of the physical parameters of exsolved nanoparticles and (f) SEM micrographs for $\text{La}_{0.43}\text{Ca}_{0.37}\text{Ni}_{0.06}\text{Ti}_{0.94}\text{O}_{3-y}$ electrodes after conventional reduction and after electrochemical switching. Copyright (2016) Springer Nature.

Generally, the well-dispersion of the exsolved nanoparticles on the surface of perovskite typically requires above 900 K for a long-time reduction. To facilitate this process, the additional driving forces such as A-site non-stoichiometry, phase transition, lattice strain, electrochemical force, cation exchange and solar energy have been developed to promote exsolution process. [107, 164-170]

Compared to the A-site stoichiometry, creating A-site deficiency of perovskites would destabilize the perovskite lattice, thus resulting in spontaneous B-site exsolution to revert stoichiometric perovskite with A/B=1 (Equations 2.8 and 2.9, Figure 2.10a). [164, 171, 172] Furthermore, the undesired A-site segregation can be significantly relieved, which increases the exposure opportunity of B-site elements to reaction gas. [173]

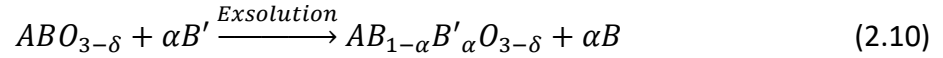


It is worth to note that a wide variety of defects would be formed through the conventional exsolution. Due to the structural flexibility of perovskite, the accumulation of the defects in perovskite bulk until a critical point would result in the phase transition of host perovskite during the exsolution. Sun et al. found that the phase transition from simple perovskite $Pr_{0.5}Ba_{0.5}Mn_{0.9}Co_{0.1}O_{3-\delta}$ (PBMCo) to double perovskite $PrBaMn_{1.8}Co_{0.2}O_5$ is thermodynamically favorable for exsolution of Co nanoparticles, indicating that phase transition of perovskite with a negative free energy can facilitate the exsolution of nanoparticles (Figure 2.10b). [167] Taking this advantage, the P-eNs with an optimized perovskite scaffold can be obtained by one-step in-

situ reducing the pristine perovskite. Similarly, Han et al. put their focus on the lattice regulation of perovskite substrate and found that the lattice strain plays a critical role in decorating the size and population of exsolved nanoparticles (Figure 2.10c). [166] By the epitaxial film grown technique, they deposited the perovskite $\text{La}_{0.2}\text{Sr}_{0.7}\text{Ni}_{0.1}\text{Ti}_{0.9}\text{O}_{3-\delta}$ (LSNT) on the substrates with different lattice parameters and as a result, the lattice misfit strains with both compressive strains and tensile strains can be implemented on LSNT. The results reveal that a compressive strain employed on LSNT could help to release the nanoparticles. Further structural analysis shows that the compressive-strained LSNT films tend to return to a stable cubic-like structure, while the tensile-strained LSNT films evolve into an unstable structure after exsolution. This in turn confirms that the structural evolution of host perovskite with a negative free energy change would result in a facilitated exsolution process.

In addition, with the help of phase evolution in repeated redox treatment, Lv et al. demonstrated that the exsolved nanoparticles with smaller size and large population can be obtained, which can be used to expand the active sites. [174] Another intelligent strategy of topotactic ion exchange assisted exsolution has been developed to regulate the population and composition of exsolved nanoparticles (Figure 2.10d). [169, 175, 176] In this concept, a suitable guest ion is firstly introduced on the surface of perovskite, the guest ion and reducible B-site cations would exchange, driven by the difference in segregation energy under reduction conditions, leading to the accelerated exsolution and replenish of B-site vacancies (Equation 2.10). To achieve this bidirectional ion diffusion process, the following requirements need to be met: 1) Higher co-segregation energy of exsolved cations than that of guest ions; 2)

Accommodation of guest ions into B-site of perovskite lattice; 3) heat treatment under reducing conditions. [177]



Although these approaches to regulating the phase structures of perovskite would significantly promote exsolution of nanoparticles, the cost and time-consuming nature of the conventional exsolution process are not changing. Alternatively, the input of external energy provides the possibility of optimizing the properties of exsolved nanoparticles more efficiently. For instance, by applying external voltage, more intensively dispersed nanoparticles anchored on the surface of perovskite backbone could be achieved in a few minutes in the absence of hydrogen atmosphere (Figures 2.10e-f). [178] Chen et al. introduced a method of using photo-illumination to drive electron donation and promote electron collection on perovskite with the help of trialkyl amine as hole acceptors, this enabled the exsolution of nanoparticles at room temperature. [179]

Thanks to many researches conducted so far on the exploration and development of exsolution technology on perovskites, a wide range of B-site cations have been investigated as the active sites on the surface of perovskites. Since the exsolution of B-site cations is closely related to the ease with which these cations can reduce to metals, the reducible cations Ni²⁺, Cu²⁺, Ru²⁺, Rh⁴⁺, Pd⁴⁺ and Pt⁴⁺ are more easily stripped out from perovskite compared to the relatively redox-stable cations Fe³⁺, Mn³⁺, Cr³⁺ and Ti⁴⁺ after reducing treatment at high temperatures. [61, 164, 180-182] Kwon et al. suggested that the exsolution ability of B-site cations can be preliminarily judged by calculating the co-segregation energy of B-site transition metal accompanying oxygen

vacancies (Figure 2.11a). [183] Up to now, the perovskites with exsolved Ni, Co, Cu, Fe nanoparticles and their alloys have been extensively explored in Ti-, Cr-, Mn- and Fe-based perovskite substrates for CO₂ electrocatalysis, [159, 184-186] and their catalytic activities have been remarkably enhanced compared to their exsolution-free counterparts. [187, 188] For example, Ye et al. showed that the current densities of SOECs with (La_{0.2}Sr_{0.8})_{0.95}Ti_{0.85}Cr_{0.1}Ni_{0.05}O_{3-δ} and (La_{0.2}Sr_{0.8})_{0.95}Ti_{0.85}Mn_{0.1}Ni_{0.05}O_{3-δ} as cathode materials increased from 0.32 to 0.42 A cm⁻² and from 0.36 to 0.54 A cm⁻² after Ni exsolution, respectively. [89] Liu et al. fabricated La_{0.6}Sr_{0.4}Fe_{0.8}Ni_{0.2}O_{3-δ} with exsolved Fe-Ni alloy nanoparticles, which achieves a remarkably enhanced current density of 1.78 A cm⁻² at 1.6 V and 850 °C (Figure 2.11b). Ding et al. found the Ni doped into LaCr_{0.5}Fe_{0.5}O₃ could significantly reduce the co-segregation energy of Fe, [171] which promotes the formation of Fe-Ni alloy in reducing environment (Figure 2.11c). Furthermore, the Fe-Ni alloy in-situ grown from (La_{0.3}Ca_{0.7})_{0.95}Fe_{0.7}Cr_{0.25}Ni_{0.05}O_{3-δ} undergoes a compositional evolution from an initially Ni-rich phase to an Fe-rich phase during the heat treatment. [189] It indicates that the composition of exsolved Fe-Ni alloy is able to be regulated by controlling the reducing conditions. In addition to Fe-Ni alloy, Fe-Cu, Co-Fe and Ru-Fe alloys have also been investigated for enhancing the catalytic activity of perovskites by exsolution, which have shown great potentials for CO₂ electroreduction due to their excellent catalytic activity and coking resistance. [189]

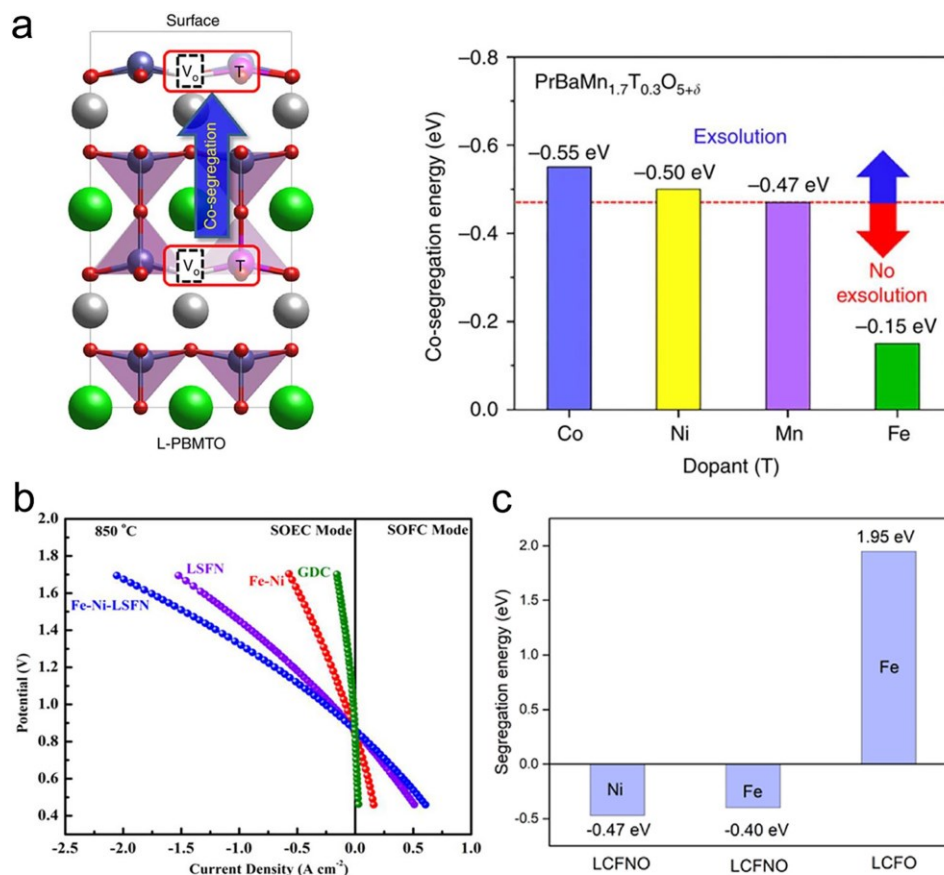


Figure 2.11 (a) Schematic illustration of model used for the calculations of co-segregation energy and the comparison of the co-segregation energy of dopant T (Co, Ni, Mn and Fe) in PrBaMn_{1.7}T_{0.3}O_{5+δ}. Copyright (2017) Springer Nature. (b) Comparison of current–voltage curves for CO₂ electrolysis using the Fe–Ni-LSFN, LSFN, GDC and Fe–Ni as cathode catalysts at 850 °C. Copyright (2016) American Chemical Society. (c) Comparison of co-segregation energy of Fe and Ni in LCFO and LCFNO. Copyright (2017) Elsevier.

2.4 Current status and challenges

Over the last few decades, exsolution has emerged as a promising technique to improve the widespread applications of perovskites (Figure 2.12). [150, 164-166, 168, 169, 174, 190-192]

Most studies have focused on the enhancement of catalytic activity by promoting the exsolution of the nanoparticles and tuning the features of exsolved nanoparticles, however, relatively few studies focus on manipulating the structure of perovskite substrates. It is worth noting that exsolution is a decomposition process in which the formation of nanoparticles on the surface is at the expense of the structural stability of the parent perovskite, especially in the case of promoting exsolution, it would result in the unintentional phase evolution of host perovskite. [191, 193] Although the structural configurations of perovskite substrates after exsolution are diverse, including simple perovskite, double perovskite, layered perovskite and their composite structures, we still have an insufficient comprehension of the effects of the host perovskite's phase evolution on the catalytic activity and stability of P-eNs based catalysts for CO₂ electrolysis. Therefore, it is necessary to shift our attention from the exsolved nanoparticles to perovskite substrates. A thorough understanding of the role of perovskite substrates in the CO₂ electrolysis process is essential to enhance the electrochemical performances of P-eNs based materials, and to gain insights into the reaction mechanism of CO₂ electrolysis on P-eNs. Herein, the research objectives of my thesis include:

- 1) To develop advanced strategies to regulate the phase structure of perovskite scaffolds.
- 2) To enhance both catalytic activity and stability performances of P-eNs by regulating the structures of perovskite substrates.
- 3) To investigate the reaction mechanisms and degradation mechanisms of CO₂ electrolysis on P-eNs.

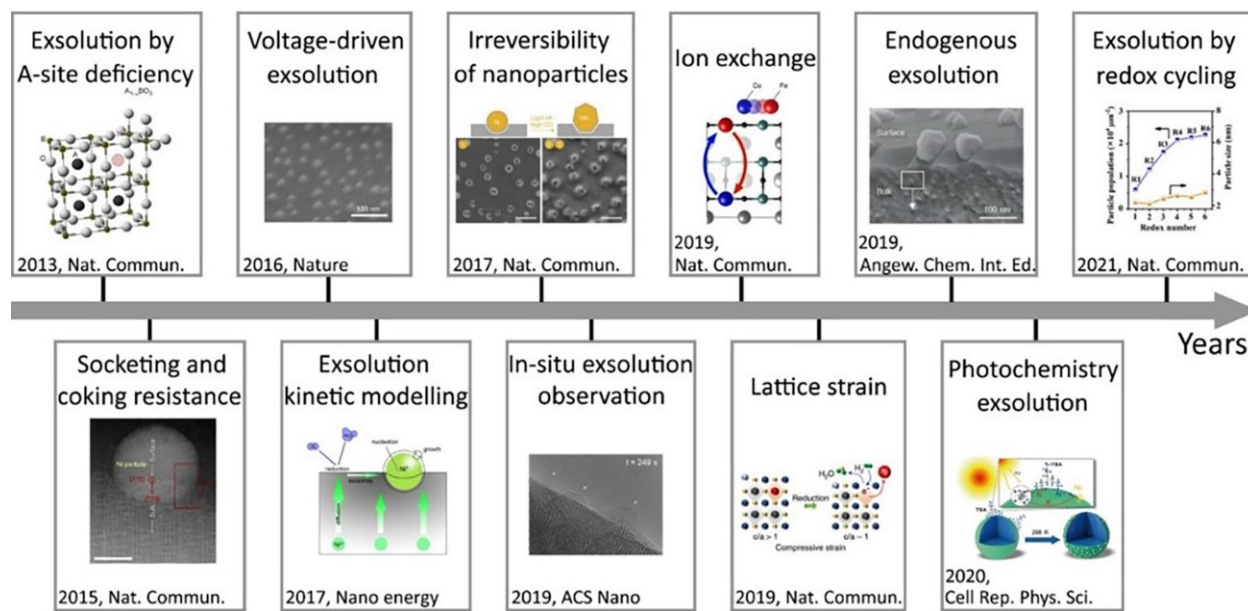


Figure 2.12 The landmark studies of the exsolution on perovskites in the past decade.

Chapter 3. Experimental methodologies

3.1 Materials synthesis

3.1.1 Synthesis of SFNM+ x Fe-red ($x=0.0, 0.5, 0.8, 1.2, 1.5$)

Polycrystalline perovskite $\text{Sr}_2\text{Fe}_{1.3}\text{Ni}_{0.2}\text{Mo}_{0.5}\text{O}_{6-\delta}$ (SFNM) powder was synthesized by a modified sol-gel method.[159] Stoichiometric amounts of $\text{Sr}(\text{NO}_3)_2$, $\text{Fe}(\text{NO}_3)_3 \cdot 9\text{H}_2\text{O}$, $\text{Ni}(\text{NO}_3)_2 \cdot 6\text{H}_2\text{O}$ and $(\text{NH}_4)_6\text{Mo}_7\text{O}_{24} \cdot 4\text{H}_2\text{O}$ were dissolved in EDTA-28% $\text{NH}_3 \cdot \text{H}_2\text{O}$ mixture under continuous stirring, followed by the addition of citric acid. The molar ratio of total metal ions: EDTA: citric acid was 1: 1: 1.5. Subsequently, 28% $\text{NH}_3 \cdot \text{H}_2\text{O}$ was added dropwise to maintain a pH at around 8. The solution was slowly evaporated at 80 °C until a homogeneous organic/cation resin was achieved. The as-obtained gel was further decomposed at 300 °C for 4 h to remove the organic components and remnant nitrates, then the obtained powder was finally fired at 1000 °C for 5 h in air to yield pristine SFNM (SFNM-oxi).

SFNM+0.0Fe-red was obtained by heating SFNM-oxi in a tubular furnace at 800 °C for 2 h with a 5% H_2/N_2 balanced reducing gas flow. For SFNM+ x Fe-red ($x=0.5, 0.8, 1.2, 1.5$), the external Fe ion was introduced on the surface of as-prepared SFNM-oxi porous support by an immerse-freeze drying process (Figure 3.1). Certain amount of $\text{Fe}(\text{NO}_3)_3 \cdot 9\text{H}_2\text{O}$ was firstly dissolved in 10 mL deionized water at room temperature and stirred for 2 h. Then, the pre-prepared SFNM-oxi powders were added to the Fe-containing solutions and ultrasound-treated for 3 h. The suspension precursor was then rapidly frozen with liquid nitrogen and freeze dried overnight to achieve the homogeneous Fe-SFNM complex with Fe seeds uniformly coated on perovskite scaffold. The fluffy powder was collected and heated in a tube furnace at 800 °C for 2 h in 5%

H₂/N₂, yielding the final catalysts SFN₃M+xFe-red ($x=0.5, 0.8, 1.2$, referring to the molar ratio of guest Fe to host Ni).

3.1.2 Synthesis of SFN₃M+xFe-red-2h ($x=0.5, 0.8, 1.2$), SFN₃M-red-2h and SFN₃M-red-10h

Pristine perovskite Sr₂Fe_{1.2}Ni_{0.3}Mo_{0.5}O_{6- δ} (SFN₃M) powder was synthesized by a modified sol-gel method.[159] Stoichiometric amounts of Sr(NO₃)₂, Fe(NO₃)₃·9H₂O, Ni(NO₃)₂·6H₂O and (NH₄)₆Mo₇O₂₄·4H₂O were dissolved in EDTA-28% NH₃·H₂O mixture under continuous stirring and heating on a hot plate at 80 °C. A certain amount of citric acid was added into the solution, the molar ratio of total cations in SFN₃M: EDTA: citric acid was 1: 1: 1.5. Subsequently, 28% NH₃·H₂O was added into the mixture to keep the pH=8. The solution was evaporated on the hot plate with continuous stirring. Until the solution evaporated to a viscous sol, it was transferred to a muffle furnace and heated at 300 °C for 4 h, which helped to remove the organic components and remnant nitrates. The obtained fluffy powder was further calcined at 1000 °C for 5 h to yield the double perovskite SFN₃M.

The reduced perovskite SFN₃M-red-850-2h was obtained by heating the air-sintered SFN₃M in a tubular at 850 °C for 2 h with a 5% H₂/N₂ gas flow. Similarly, SFN₃M-red-850-10h was obtained by deeply reducing SFN₃M in a tubular at 850 °C for 10 h. To get SFN₃M+xFe-red ($x=0.5, 0.8, 1.2$), the guest Fe ion was firstly deposited on the surface of air-sintered SFN₃M support by an immerse-freeze drying process.

Fe(NO₃)₃·9H₂O was selected as the precursor of guest Fe ion and dissolved into a beaker with 10 mL deionized water followed by ultrasound for 2h. Subsequently, the air-sintered SFN₃M powder was added into the Fe(NO₃)₃ solution for another 3 h-ultrasound treatment. The

suspension precursor was then rapidly transferred to the prepared liquid nitrogen and then freeze dried overnight. The obtained fluffy powder was subsequently reduced in the tubular furnace at 850 °C for 2 h with a 5% H₂/N₂ gas flow, thus forming SFN₃M+xFe-red ($x=0.5, 0.8, 1.2$, which refers to the molar ratio of guest Fe to host Ni).

3.1.3 Synthesis of Sr₂Fe_{1.2}Ni_{0.3}Mo_{0.5}O_{6-δ}, F doped Sr₂Fe_{1.2}Ni_{0.3}Mo_{0.5}O_{6-δ}F_{0.1}.

Powders of perovskite Sr₂Fe_{1.2}Ni_{0.3}Mo_{0.5}O_{6-δ} (SFN₃M) and F doped SFN₃M (Sr₂Fe_{1.2}Ni_{0.3}Mo_{0.5}O_{6-δ}F_{0.1}, F-SFN₃M) was obtained by a modified sol-gel method. [159, 194] Iron(III) fluoride trihydrate (FeF₃·3H₂O) was selected as the F-containing precursor for synthesizing SFN₃MF_{0.1}. To prepare SFN₃MF_{0.1}, Sr(NO₃)₂, Fe(NO₃)₃·9H₂O, Ni(NO₃)₂·6H₂O, FeF₃·3H₂O and (NH₄)₆Mo₇O₂₄·4H₂O were dissolved in EDTA-28% NH₃·H₂O mixture under continuous stirring and heating on a hot plate at 80 °C. Citric acid was dropped into the mixture, the molar ratio of total cations: EDTA: citric acid was 1: 1: 1.5. Subsequently, 28% NH₃·H₂O was added to adjust the pH of the solution to be around 8. The solution gradually evaporated under stirring and heating, eventually forming a condensate. The condensate was transferred to a muffle furnace and calcined at 300 °C for 4 h, the fluffy powders were obtained and then grinded. The raw materials were further calcined at 1100 °C for 5 h, thus forming the final perovskite F-SFN₃M. The oxidized SFN₃M and F-SFN₃M were then heated in the tubular furnace at 850 °C with a 5% H₂/N₂ balanced gas flow, yielding the final SFN₃M-red and F-SFN₃M-red.

3.2 Physicochemical characterizations

X-ray Diffraction (XRD): The crystalline structures of synthesized perovskite materials were identified by XRD examination on Rigaku Ultima IV with a Cu K α source at 40 kV and 44 mA and Bruker D8 XRD. The XRD spectra were analyzed by Software Jade 6.0.

Field Emission Scanning Electron Microscopy (FESEM): The surface microstructures of prepared perovskite materials were probed by a Zeiss Sigma 300 VP FESEM.

Transmission electron microscopy (TEM): The TEM-EDS images of perovskite materials were obtained on a JEOL JEM-ARM200CF electron microscopy equipped with an energy dispersive X-ray spectroscopy (EDS) detector. The high resolution transmission electron microscopy (HRTEM) characterization was conducted on the 300kV Hitachi H-9500 TEM.

X-ray photoelectron spectroscopy (XPS): The surface chemistry of perovskite materials was examined by XPS, performed on a Krato AXIS Ultra Spectrometer. The obtained XPS spectra were analyzed on the CASAXPS software with C 1s at binding energy of 284.8 eV as the reference.

Thermogravimetric analysis (TGA): The weight loss of perovskite materials in the reducing environment (5% H₂/N₂ balance) was performed on TA SDT Q500 and TA SDT Q600 at a heating/cooling rate of 20 °C min⁻¹ to characterize the lattice oxygen loss.

Fourier Transform Infrared Spectroscopy (FTIR): The FTIR spectra at the elevated temperatures (400 and 600 °C) of perovskite materials were obtained on Nicolet 8700 Fourier transform infrared spectrometer and Thermo Nicolet iS50 Fourier transform infrared spectrometer. The

spectra were obtained by subtracting the corresponding background peaks from the overall absorption and then normalizing it with respect to the noise peaks.

X-ray absorption measurements: The X-ray absorption near edge structure (XANES) and extended X-ray absorption fine structure (EXAFS) spectra in this thesis were conducted at Canadian Light Source. Fe K-edge and Ni K-edge XANES spectra were collected using the Very Sensitive Elemental and Structural Probe Employing Radiation from a Synchrotron (VESPERS, 07B2-1) beamline.

CO₂ temperature programmed desorption (CO₂-TPD): CO₂-TPD were performed using an AutoChem 2950HP instrument (Micromeritics) equipped with a quartz U-tube reactor and a thermal conductivity detector (TCD). The samples with approximately 50 mg loading were pretreated at 400 °C in He for 1 h to eliminate the adsorbed species on surface, followed by purged adsorption of CO₂ with 5% CO₂/He flow at 100 °C for 1 h. Then, CO₂-TPD was performed from 50 to 850 °C at 10 °C min⁻¹ with He flow of 20 mL min⁻¹.

Electrical conductivity relaxation (ECR) experiments: ECR experiments were implemented at elevated temperatures with switching of the gas stream from 2:1 CO-CO₂ ($P_{O_2} = 1.246 \times 10^{-18} \text{ atm}$ at 850 °C) to 1:1 CO-CO₂ ($P_{O_2} = 4.985 \times 10^{-18} \text{ atm}$ at 850 °C).

Temperature-dependent electrical conductivity test: The temperature-dependent electrical conductivities of perovskite materials were measured in the 50% CO₂/50% CO and 5% H₂/95% Ar atmospheres.

Raman spectra: Raman spectroscopy of perovskite materials was carried out on the enishaw inVia Qontor Confocal Raman Microscope with a laser wavelength of 532 nm.

For the post-mortem characterizations (Raman, XRD, SEM), pure Argon gas was purged the cathode sides of all SOECs to maintain an inert atmosphere, a slower cooling rate ($3^{\circ}/\text{min}$) was applied to avoid the cracking of cells and exposure of the cathode side to air.

3.3 Cell fabrications and electrochemical characterizations

3.3.1 Cell fabrications

The developed SOECs in this thesis were YSZ electrolyte supported (. In particular, the YSZ electrolytes utilized in this thesis were purchased from Fuel Cell Materials Company, with a thickness ranging from 250-300 μm). Since the electrodes in this thesis are chemically incompatible with YSZ electrolyte, the GDC slurry was screen-printed/spin-coated on both sides of the YSZ electrolyte and then sintered at 1300 $^{\circ}\text{C}$ for 5 h to form dense GDC buffer layer between electrode and electrolyte.

Cathode materials were prepared by mixing perovskite materials and pure oxygen ion conductor GDC with a weight ratio of 3:2. The cathode slurry was prepared by mixing the perovskite-GDC mixture with a glue containing 1-butanol, benzyl butyl phthalate, ethyl cellulose, and α -terpineol in a weight ratio of 1.7:1, followed by ball milling for 3 h. Anode slurry was prepared using the same method as the cathode slurry. Both cathode and anode slurries were printed on both GDC sides to form the configuration of “anode| GDC buffer layer| YSZ electrolyte| GDC buffer layer| cathode”. In particular, the SOECs in Chapter 5 have a cathode thickness that falls between 17-20 μm , while the anode thickness measures around 10-12 μm .

The GDC barrier layers have an approximate thickness of 2.5 μm . The assembled cell was finally sintered at 1100 $^{\circ}\text{C}$ for 2 h. Gold paste was painted onto the surfaces of both anode and cathode to serve as current collectors. The cell was built by fixing the cell between coaxial pairs of alumina tubes with a high temperature-resistant sealant, which was fastened in a vertical tubular furnace.

3.3.2 Electrochemical characterizations

Prior to electrochemical test, the 5% H_2/N_2 reducing gas flow was continuously pumped into the cathode compartment during the temperature ramping of SOEC for testing the reduced perovskite-based cathode, the cathode underwent re-reduction to complete the further reduction and exsolution. The reducing gas flow was not required for the cell with the oxidized perovskite cathode during the temperature ramping. During the electrolysis, pure CO_2 was fed to the cell via the cathode compartment located at the bottom, while the anode was placed on the top and exposed to air. The current density-voltage ($j - V$) curves, potential step chronoamperometry and long-term stability test under a constantly applied voltage of SOECs were measured using a four-probe method with Ag wires as the leads on a Solartron 1255 frequency response analyzer and a Solartron 1286 electrochemical interface instrument. The ohmic resistance and polarization resistance of SOEC were determined by electrochemical impedance spectroscopy (EIS) under an ac potential with a frequency range of 1 MHz to 0.1 Hz and an amplitude of 10-20 mV at the applied potentials. The outlet gas from the cathode compartment was analyzed using a Hewlett-Packard model HP5890 gas chromatograph (GC) equipped with a packed column (Porapak QS) operated at 80 $^{\circ}\text{C}$ with a thermal conductivity detector and a flame ionization detector.

3.4 Density functional theory (DFT) calculations.

Density functional theory calculations (DFT) in Chapter 4 were performed by Vienna Ab initio Simulation Package (VASP). [195, 196] Perdew-Burke-Ernzer (PBE) function and projector-augmented plane-wave (PAW) method were employed in order to treat the exchange-interaction effect and electron-ion interaction, respectively. [197] For plane-wave expansion, the cutoff energy was set at 520 eV. A Gaussian smearing with a width of 0.2 eV was used to determine partial occupancies. A 4*2*4 supercell was built based on the optimized unit cell and a vacuum layer of 15 Angstroms was added in order to avoid the interaction between neighbouring slabs. Monkhorst-Pack (3×6 × 1) was set for Brillouin zone sampling. [198] During geometry optimization, the top four atomic layers were fully relaxed while the other atomic layers were fixed. Relaxation of degree of ions was not terminated until a maximum force component of 0.05 eV/Angstrom was achieved. In order to describe the formation of SFNM perovskite, we replaced one Fe atom with one Ni atom in SFM. A PBE+U strategy was used to take the exchange and on-site Coulomb interaction in Fe, Ni into consideration. The values of U were set at 6.2 eV and 5.3 eV for Ni and Fe, respectively. Spin polarization was considered during all calculations. The (001) plane was chosen for the calculation of co-segregation by conventional exsolution and exchange energy between guest Fe and host B-site cations since the (001) lattice plane had been used as the active surface of SFNM in the previous work. [199, 200] Vesta software was employed for model construction and visualization. [201]

The co-segregation energy is defined as the energy difference between the total energies of the supercell with exsolved metal ion plus its nearest oxygen vacancy in the 1st and 3rd atomic layers of perovskite, as following equation (Taking M as the exsolved metal):

$$E_{\text{co-segregation}}(M) = E_{(M-V_{\text{O}}^{\cdot\cdot})@1\text{st layer}} - E_{(M-V_{\text{O}}^{\cdot\cdot})@3\text{rd layer}}$$

where $E_{\text{co-segregation}}(M)$, $E_{(M-V_{\text{O}}^{\cdot\cdot})@1\text{st layer}}$, $E_{(M-V_{\text{O}}^{\cdot\cdot})@3\text{rd layer}}$ are the co-segregation energy, the total energy of the supercell with exsolved ion plus its nearest oxygen vacancy in the 1st atomic layer, and the total energy of the supercell with exsolved ion plus its nearest oxygen vacancy in the 3rd atomic layer, respectively.

The exchange energy is defined as the difference between the co-segregation energies of the two metal ions involved in exchanging, as shown in following equation:

$$E_{\text{exchange}}(M_1-M_2) = E_{\text{co-segregation}}(M_1) - E_{\text{co-segregation}}(M_2)$$

The DFT calculations in Chapter 5 were performed by Vienna Ab initio Simulation Package (VASP). Perdew-Burke-Ernzer (PBE) function and projector-augmented plane-wave (PAW) method were employed to describe the exchange-interaction effect and electron-ion interaction, respectively. The cut-off Energy was set as 520 eV for plane-wave expansion. Gaussian smearing with a smear width of 0.2 eV was used to determine the partial occupancies. The “PBE+U” was employed during calculations to take the exchange and on-site Coulomb interaction in Fe, and Ni into consideration, and the values of U were set at 5.3 and 6.2 eV for Fe and Ni, respectively. [177, 202] Spin calculation was adopted throughout calculations. DFT-D3 was employed to treat the Vdw interactions. [203] Relaxation of degree of ions was terminated once a maximum force component of 0.02 eV/Angstrom was achieved. For slab models, a vacuum layer with 15 Angstrom was placed along the Z direction. VESTA was used for model construction and visualization. [201] Vaspkit was employed to generate the input files. [204]

1. Formation energy of oxygen vacancy (E_{V_O}): The E_{V_O} is defined as the total energy difference between the defect-free stoichiometric and V_O -contained non-stoichiometric structure, as shown in Equation 1.

$$E_{V_O} = \left(E_{def} + \frac{1}{2} E_{O_2(g)} \right) - E_{perfect} \quad (1)$$

Where the E_{def} , $E_{O_2(g)}$ and $E_{perfect}$ represent the total energy of V_O -contained supercell, free oxygen molecule, and perfect supercell, respectively.

Calculations were performed on the DP-Sr₈Fe₆Mo₂O₂₄ and LP-Sr₁₂Fe₆Mo₂O₂₈ cell with a Fe:Mo ratio of 3:1. The DP-Sr₈Fe₆Mo₂O₂₄ structure has been proposed by many previous studies[200, 205]. For LP-Sr₁₂Fe₆Mo₂O₂₈, all possible sites for Mo substitution have been considered and the one configuration with the lowest total energy was used for further calculations. Following the same protocol, the optimal Ni-doped structures of DP-Sr₈Fe₅Ni₁Mo₂O₂₄ and LP-Sr₁₂Fe₅Ni₁Mo₂O₂₈ can be determined. The models of DP-Sr₈Fe₆Mo₂O₂₄, DP-Sr₈Fe₅Ni₁Mo₂O₂₄, LP-Sr₁₂Fe₆Mo₂O₂₈ and LP-Sr₁₂Fe₅Ni₁Mo₂O₂₈ are denoted as models DP-SFM, DP-SFNM, LP-SFM and LP-SFNM in the Manuscript and Supplementary information.

2. Co-segregation energy of reducible cations ($E_{M_{co-seg}}$, where M is donated as B-site cations such as Ni, Fe): The $E_{M_{co-seg}}$ is defined as the energy difference between the total energies of the supercell with exsolved metal ion plus its nearest V_O in the 1st and 3rd atomic layer of perovskite, as shown in Equation 2 (Taking M as the exsolved metal).

$$E_{M_{co-seg}} = E_{M-V_O@1st\ layer} - E_{M-V_O@3rd\ layer} \quad (2)$$

where $E_{M-V_O^{\ddot{}}@1st\ layer}$ and $E_{M-V_O^{\ddot{}}@3rd\ layer}$ are the total energy of the supercell with exsolved ion plus its nearest $V_O^{\ddot{}}$ in the 1st atomic layer and the total energy of the supercell with exsolved ion plus its nearest $V_O^{\ddot{}}$ in the 3rd atomic layer, respectively.

The $E_{Ni_{co-seg}}$ and $E_{Fe_{co-seg}}$ in different models were calculated based on the (001) surface of the perovskite due to its higher stability[200]. For DP-based modes, the eight-layer metal-terminated DP-SFM (001) and DP-SFNM (001) slabs were constructed based on the DP- $Sr_8Fe_6Mo_2O_{24}$ unit cell, and the bottom three layers were frozen during geometric optimizations. The determination of Ni doping positions in DP-SFNM (001) follows the same protocol as described above. For the construction of metal-terminated LP-SFM (001) and LP-SFNM (001) slabs, there are two general considerations: 1) the symmetry in pristine LP-SFM cell should be preserved and thus only the doping positions that do not affect this symmetry shall be considered. 2) all metal layers should contain Mo atoms and the Fe:Mo ratio should be fixed at 3:1. The as-obtained LP-SFM (001) and LP-SFNM (001) slabs contain a total layer of ten, which is the minimum layer required for a complete RP structure and the bottom five layers are frozen during optimizations. Based on the results of surface energy proposed by Takamatsu et al.[206], two LP-SFM (001) surfaces and two LP-SFNM (001) surfaces with lower surface energies have been considered, denoted as LP-SFM-1 (001), LP-SFM-2 (001), LP-SFNM-1 (001) and LP-SFNM-2 (001).

3. Gibbs free energy change towards CO_2 -to-CO conversion: To examine the Gibbs free energy of reaction on DP-NPs-GDC, DLP-NPs-GDC and LP-NPs-GDC, the models DP- $V_O^{\ddot{}}$ -F2N3, DP- $V_O^{\ddot{}}$ -F3N1, LP- $V_O^{\ddot{}}$ -F2N3 and LP- $V_O^{\ddot{}}$ -F3N2 were constructed. Considering the total number of atoms

involved, the cut-off Energy was set as 450 eV for plane-wave expansion and maximum force component was set as 0.05 eV/Angstrom for the systems to converge. The individual Fe₂Ni₃, Fe₃Ni₂ and Fe₃Ni clusters were firstly optimized and the resultant structures obtained in this study are in good agreement with previous studies[207]. The clusters were then placed on top of Sr-terminated surface DP-SFM (001) (Sr₃₂Fe₂₄Mo₈O₉₆) and LP-SFM (001) (Sr₉₆Fe₄₈Mo₁₆O₂₂₄) supercells adjacent to one $V_O^{\bullet\bullet}$ with two and eight bottom layers frozen during geometric optimizations, respectively. Based on the methods proposed by Takamatsu et al.[206], we adopted two Sr-terminated LP-SFM (001) (Sr₉₆Fe₄₈Mo₁₆O₂₂₄) surfaces (LP-SFM-Sr-1 (001) and LP-SFM-Sr-2 (001)) and further compared their surface energy (E_{sur}). The results showed that the E_{sur} of LP-SFM-Sr-1 (001) is 0.48 J m⁻², much lower than 1.15 J m⁻² of LP-SFM-Sr-2 (001). Therefore, the clusters were placed on LP-SFM-Sr-1 (001) surface to further examine the CO₂ adsorption and conversion behaviours.

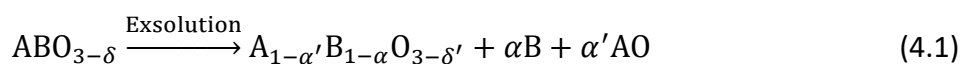
The DFT calculations in Chapter 6 were performed using Vienna Ab initio Simulation Package (VASP). Perdew-Burke-Ernzer (PBE) function and projector-augmented plane-wave (PAW) method was employed to describe the exchange interaction effect and electron-ion interaction, respectively. The maximum force component for the termination of the relaxation of degree of ions was set as 0.02 eV/Angstrom. The cut-off Energy was 520 eV for plane-wave expansion. The smear width of the Gaussian smearing was set as 0.1 eV. A (2 x 2 x 1) Sr₁₆Fe₁₀Mo₄Ni₂O₄₈ supercell was constructed based on the optimized unit cell Sr₂FeMoO₆ obtained from Materials Project. One O atom in the supercell was replaced with one F atom to model the F-doped SFNM. VESTA software and VASPKIT was used for model constructions and input files generation, respectively. [201, 204]

Chapter 4. Boosting the stability of perovskites with exsolved nanoparticles by B-site supplement mechanism

4.1 Introduction

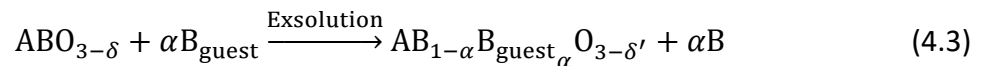
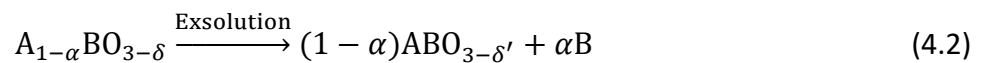
Perovskites are attractive candidates for high temperature SOEC/SOFC. [12, 31, 35, 208] Benefiting from the excellent catalytic activities of well-exposed metallic nanoparticles, alongside the unique nanoparticle-perovskite interface with high resistance to agglomeration, P-eNs provide an appealing platform for the large-scale energy storage and conversion technique compared to their nanoparticle-free counterparts. [150, 156, 191, 209, 210] Over the past decades, there have been significant advances in promoting exsolution via additional driving forces. [164, 166, 168] However, challenges remain concerning the stability of P-eNs, especially when being used as a cathode for CO₂ electrolysis in SOEC. [89, 120] Although the thermal stability of nanoparticles has been literally enhanced by exsolution process, the rapid degradation issue still exists at high voltages, which results in a lower energy efficiency. [185, 211, 212] Since steady high-voltage CO₂ electrolysis can lead to higher CO yields, [213] new strategies are urgently required to enhance the stability of P-eNs at high voltages while promoting nanoparticle exsolution.

To tackle this challenge, we started by examining the fundamental process of nanoparticle exsolution on the perovskite, [164] as shown in Equation 4.1.



It is noteworthy that the exsolution of B-site reducible cations inevitably leaves behind many B-site vacancies within the perovskite bulk, thus causing the detrimental A-site segregation and slowdown of the electron transfer rate via the $B^{(n-1)+}-O-B^{n+}$ pathway. [99, 214, 215] The external potentials would drive the continuous exsolution during CO₂ electrolysis, especially at higher voltages, which could potentially hamper the stability of P-eNs. [151, 178] However, the B-site vacancy-dictated stability issues are often veiled by the reactivity enhancement brought by concurrent B-site exsolution. Very few studies have attempted to correlate the perovskite structure evolution dominated by B-site vacancy to the stability of P-eNs.

In this study, the promising double perovskite Sr₂Fe_{1.3}Ni_{0.2}Mo_{0.5}O_{6-δ} (SFNM) was selected as a prototype example to elaborate the effects of the structure evolution of the perovskite scaffold on the stability of P-eNs. [185] Either controlling the A-site deficiency or implementing the topotactic ion exchange (TIE) is expected to be a pathway to regulate the concentration of the B-site vacancies in the reduced SFNM (Equations 4.2 and 4.3). [164, 169, 176, 216] However, the limited Sr-site deficiency (less than 5% mol) in the SFNM makes it fail to refill the B-site vacancies after the exsolution by controlling the A-site deficiency. [217] Therefore, the TIE-assisted exsolution was employed to fine-tune the B-site occupation of perovskite scaffold while promoting the formation of nanoparticles.



To initiate the TIE-assisted exsolution, the foreign Fe ion is a good choice as the B-site filling agent due to its relatively high redox stability. [218] Our density functional theory (DFT) results demonstrated the feasibility of swapping of guest Fe with host Ni in SFNM driven by the difference in co-segregation energy. Therefore, uniform guest Fe overlayer was introduced on the surface of SFNM scaffold by a facile lyophilization method, followed by the supplement of Fe into B-site vacancies in the reduced SFNM bulk. Consequently, a robust $\text{Sr}_2\text{Fe}_{1.5}\text{Mo}_{0.5}\text{O}_{6-\delta}$ (SFM) scaffold with decreased B-site vacancies and Ni incorporation has been implemented, accompanied by the exsolution of Fe-Ni alloy nanoparticles. [219] The extensive electrochemical and structural characterizations confirm that the incorporation of the guest Fe into B-site vacancies of the reduced SFNM scaffold delivers higher catalytic activity and stability of the reduced perovskite scaffold, especially when external voltages ≥ 1.6 V. Furthermore, from the short/long term stability performances and post characterizations, we have uncovered the degradation mechanism of the reduced SFNM with/without B-site supplement at high potentials from the perspective of structure stability. These results highlight the indispensable contribution of structurally robust mother perovskite to the higher stability of P-eNs for CO_2 reduction in SOEC, and also provide the extensive prospects towards the rational design of advanced heterogeneous P-eNs and other catalytic systems.

4.2 Results and Discussion

DFT calculations and B-site supplement. To reoccupy the B-site vacancies of reduced SFNM scaffold during exsolution, the appropriate filling agent should be selected to initiate the TIE process. For this purpose, the co-segregation energies of Ni, Fe and Mo at B-site of SFNM were calculated by DFT simulation, which are -2.26 eV, -1.46 eV and -1.06 eV, respectively (Figure

4.1a). It indicates that Fe exsolves more favourably than Mo but less favourably than Ni. [183] Considering that TIE is driven by the difference in co-segregation between guest ion and host ion, [216] the exchanges of guest Fe \leftrightarrow host Ni (-0.79 eV) and guest Fe \leftrightarrow host Fe (0 eV) are thermodynamically more favorable than that of guest Fe \leftrightarrow host Mo (0.40 eV) when external Fe ion is introduced on the surface of SFNM substrate (Figure 4.1b), suggesting the feasibility of refilling of guest Fe into the B-site vacancies and exsolution of Fe-Ni alloy.

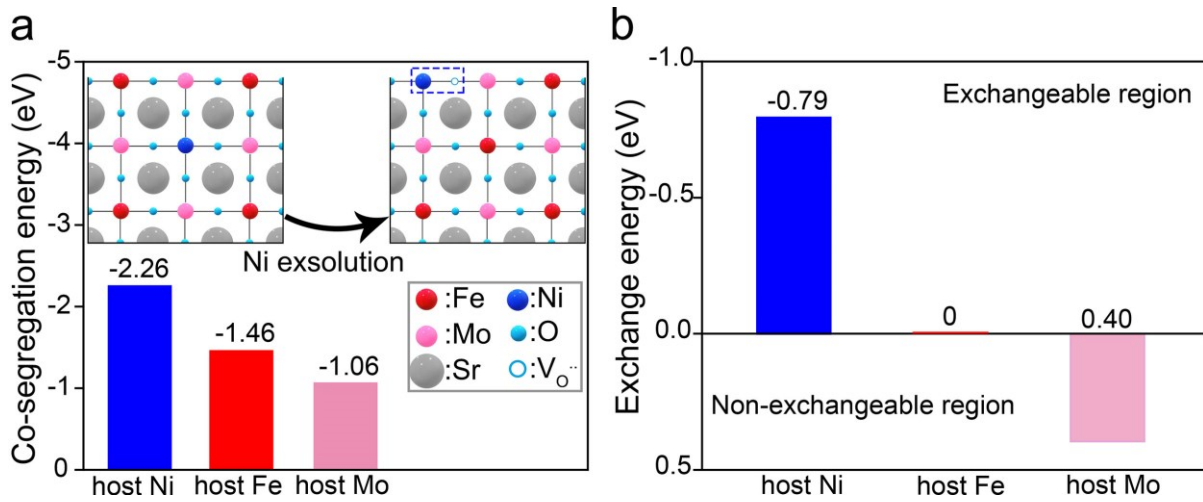
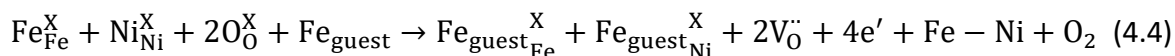


Figure 4.1 (a) Co-segregation energy and schematic illustrations of the DFT models for co-segregation by conventional exsolution. (b) Exchange energy comparison of B-site cations of SFNM with guest Fe.

With the guidance of DFT calculations, two different exsolution routes are recapitulated in Figure 4.2 for schematic illustrations. Route i depicts the TIE-assisted exsolution initiated on the guest Fe-SFNM complex while the conventional counterpart is shown as route ii. In TIE-assisted approach, the foreign Fe ions are initially deposited on the surface of perovskite by freeze

drying (Figure S4.1), which will then be incorporated into the remaining B-site vacancies, accompanied with the egression of host Ni and Fe upon reduction (Equation 4.4).

TIE-assisted exsolution:



For the conventional exsolution, Fe- and Ni-site vacancies emerge in perovskite matrix with the formation of Fe-Ni alloy nanoparticles at the surface (Equation 4.5).

Conventional exsolution:

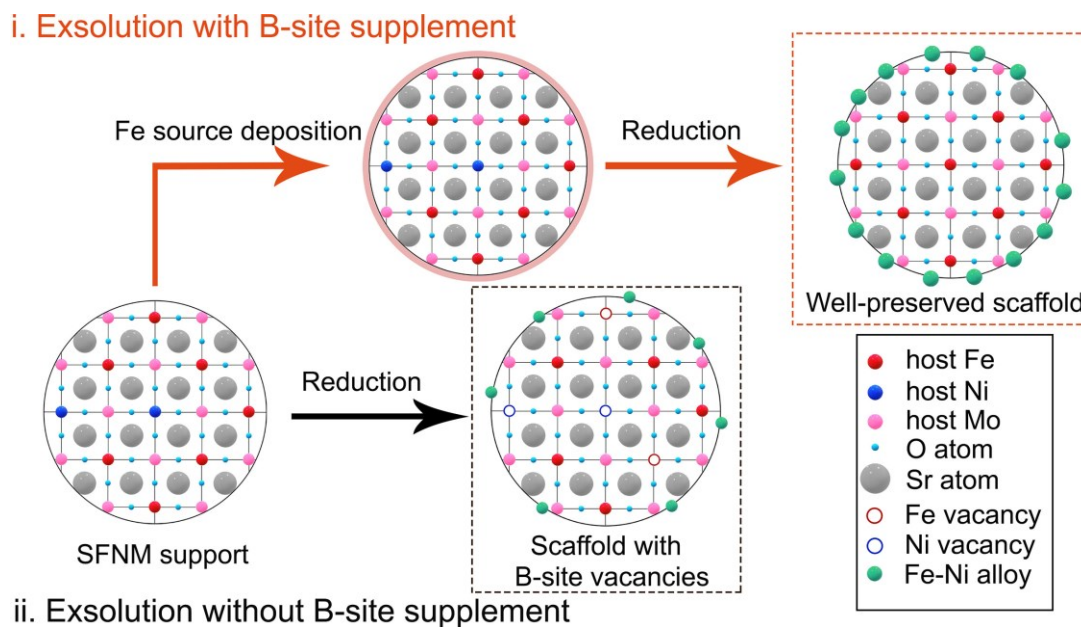


Figure 4.2 Schematic illustration of exsolution with and without B-site supplement on SFNM.

Examination of the exsolved nanoparticles and perovskite scaffold. To determine the optimal

Fe loading amount on surface of SFNM, a series of SFNM+xFe-red samples ($x=0.0, 0.5, 0.8, 1.2,$

which refer to the molar ratios of guest Fe to host Ni) were prepared. X-ray diffraction (XRD) analysis confirms that the Fe-Ni alloy phases have emerged in all SFNM+ x Fe-red samples with the well-preserved perovskite phase (Figure 4.3a₁). Nevertheless, further increasing x to 1.5 gives rise to metallic Fe phase (PDF# 06-0696) (Figure S4.2), suggesting that the excessive surface Fe seeds trigger the formation of Fe clusters at this deposition level. Therefore, the interplay between the nanoparticle formation and perovskite structure evolution among SFNM+ x Fe-red ($x=0.0, 0.5, 0.8, 1.2$) are further elucidated. The characteristic Fe-Ni alloy peaks in SFNM+0.0Fe-red can be well indexed to FeNi₃ phase (PDF#03-065-3244) (Figure S4.3), while the peak located at 44.1° among SFNM+ x Fe-red ($x=0.5, 0.8, 1.2$) slightly shifts leftward (Figure 4.3a₂). Transmission electron microscopy (TEM) with energy dispersive X-ray spectroscopy (EDS) element mappings on randomly selected nanoparticles of SFNM+0.0Fe-red and SFNM+1.2Fe-red reveal the significant increase of Fe proportion in the exsolved nanoparticles of SFNM+1.2Fe-red (Figure S4.4 and Table S4.1). It may be presumably explained by the involvement of guest Fe in the nanoparticle growth, and the slightly smaller electronegativity of Fe than that of Ni causes the lattice expansion of Fe-Ni alloy. [220-222] More importantly, distinct peak-shifting of parent perovskites can be observed from the XRD patterns of SFNM+ x Fe-red. As shown in Figure 4.3a₃, the magnified diffraction peak at about 32° of SFNM+0.5Fe-red shifts slightly to a higher angle with regards to SFNM+0.0Fe-red, which may be ascribed to the partial filling of B-site vacancies with the guest Fe. Oppositely, the peak shifts leftward when further increasing the deposited Fe content to $x=0.8$ and 1.2, mainly due to the loss of lattice oxygen after the accelerated exsolution. [159] It in turn indicates the promotion

of exsolution and substantial occupation of B-site vacancies by the guest Fe in SFNM+0.8Fe-red and SFNM+1.2Fe-red.

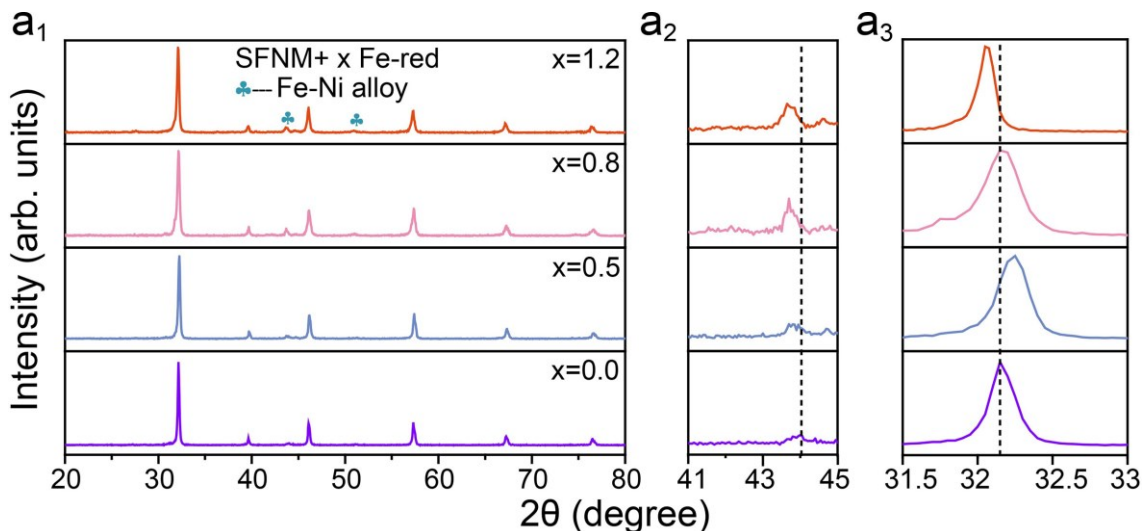


Figure 4.3 (a₁) XRD patterns of SFNM+xFe ($x=0.0, 0.5, 0.8, 1.2$) reduced at 800 °C for 2 h in 5% H₂/N₂ from 20 to 80°. Amplified XRD patterns in the range of (a₂) 41-45° and (a₃) 31.5-33°.

Field emission-scanning electron microscopy (FE-SEM) results demonstrate that the nanoparticle exsolution among SFNM+xFe-red ($x=0.5, 0.8, 1.2$) is more efficient compared with that on SFNM+0.0Fe-red, as illustrated by the larger average size, wider size distribution and larger population (Figures S4.5a-d, S4.6). SFNM+xFe-red samples ($x=0.0, 0.5, 0.8, 1.2$) were subsequently subjected to O 1s X-ray photoelectron spectroscopy (XPS) analysis to inspect the surface oxygen species. As shown in Figure S4.7, the concentration of surface-adsorbed oxygen gradually increases as the surface Fe deposition increases, which is consistent with the promoted exsolution observed by SEM.

To further verify the reoccupation of B-site by the guest Fe, SFNM+ x Fe-red samples ($x=0.0, 0.5, 0.8, 1.2$) were re-oxidized to inspect the ability of exsolved nanoparticles to reintegrate into the parent perovskite lattice. [152, 174, 188] After reoxidation at 1000 °C for 10 h, XRD analysis shows that the additional NiO peaks have clearly emerged in re-oxidized SFNM+0.0Fe-red, while NiFe₂O₄ or SrMoO₄ can be detected on re-oxidized SFNM+ x Fe-red ($x=0.5, 0.8, 1.2$) (Figures 4.4a₁-a₃). It can be concluded that the redissolution of the exsolved FeNi₃ nanoparticles is partially reversible on the SFNM+0.0Fe-red. Moreover, Fe atoms in FeNi₃ nanoparticles preferentially dissolve into perovskite compared to Ni atoms, which is in accord with the fact that Ni exsolves more favourably than Fe (Figure 4.1a). As a result, the residual Ni on the surface transforms into NiO after heating in air. [190] However, for SFNM+ x Fe-red ($x=0.5, 0.8, 1.2$), the B-site vacancies of parent perovskite have been occupied by the guest Fe partially/entirely; the exsolved Fe and Ni on surface are prone to self-assembly into binary oxide NiFe₂O₄ in air rather than dissolve into perovskite lattice. In addition, the secondary phase SrMoO₄ detected on re-oxidized SFNM+0.8Fe-red and SFNM+1.2Fe-red is due to the fact that B-sites were almost completely occupied by the high-valence Fe and Mo, exceeding the tolerance of perovskite structure. This is consistent with the emergence of SrMoO₄ in the air-sintered SFM. [223] Therefore, it suggests that the target P-eNs have been successfully synthesized where Fe-Ni alloy nanoparticles are on the SFM substrate with decreased B-site vacancies and Ni incorporation.

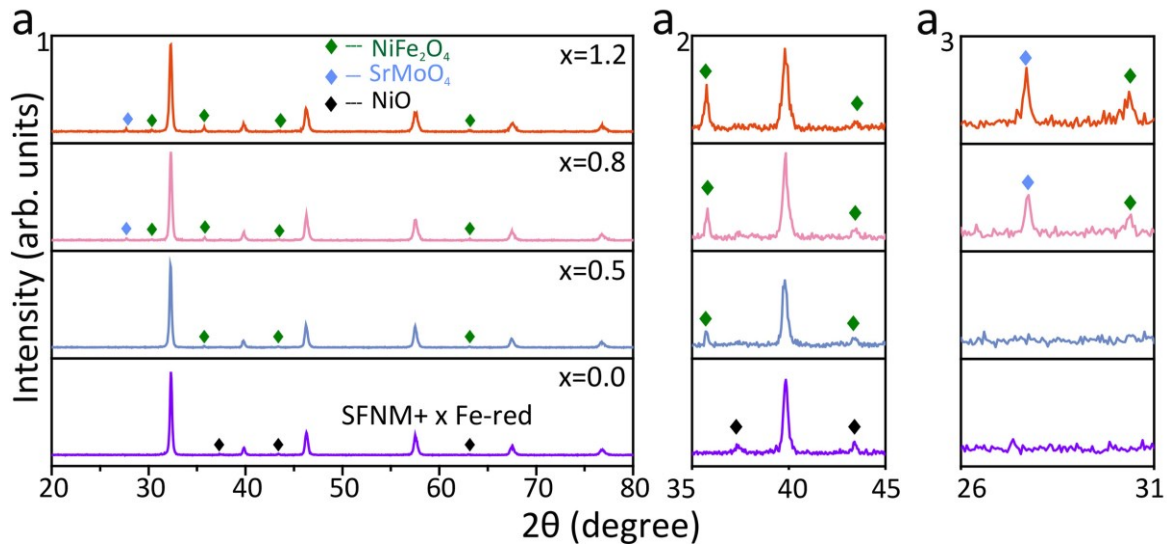


Figure 4.4 (a₁) XRD patterns of re-oxidized SFNM+xFe-red at 1000 °C in air for 10 h. Amplified XRD patterns in the range of (a₂) 35-45° and (a₃) 26-31°.

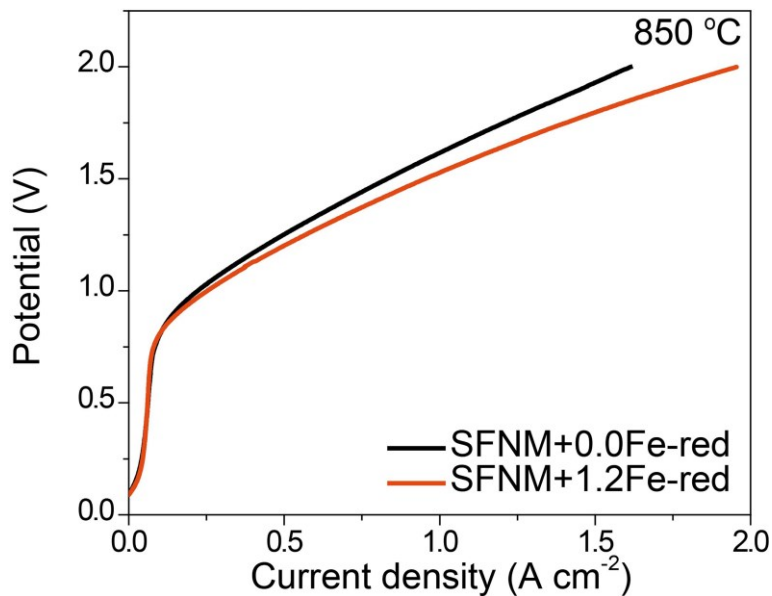


Figure 4.5 *j*-*V* curves of SFNM+0.0Fe-red-GDC and SFNM+1.2Fe-red-GDC for pure CO₂ electrolysis at 850 °C.

Electrocatalytic performance. The electrocatalytic capacities of SFNM+ x Fe-red for CO₂ reduction were subsequently examined by current density-voltage (j -V) curves at 800 and 850 °C, as shown in Figure S4.8. The cathode electrodes were prepared by mixing SFNM+ x Fe-red with gadolinium doped ceria (GDC), and the full cells for the measurements of ((La_{0.6}Sr_{0.4})_{0.95}Co_{0.2}Fe_{0.8}O_{3- δ} -GDC|GDC|YSZ|GDC|SFNM+ x Fe-red-GDC) are denoted as SFNM+ x Fe-red-GDC for simplicity. Apparently, SFNM+1.2Fe-red-GDC exhibits superior electrocatalysis performance compared with others, indicative of its better catalytic activity towards CO₂ conversion. Specifically, the j reaches 0.97 and 1.13 A cm⁻² for SFNM+0.0Fe-red-GDC and SFNM+1.2Fe-red-GDC, respectively, at 1.6 V and 850 °C (Figure 4.5).

To further gain insights into the CO₂ electrolysis in SOEC, SFNM+0.0Fe-red-GDC and SFNM+1.2Fe-red-GDC were subjected to the electrochemical impedance spectra (EIS) analysis. Figure 4.6a shows the Nyquist plots of both cells at the applied potentials of 1.0, 1.2, 1.4, 1.6 and 1.8 V at 850 °C and the corresponding equivalent circuit model LR(Q_HR_H)(Q_LR_L) (inserted image). The simulated ohmic resistance (R_s), polarization resistances at high and low frequencies (R_H and R_L) are summarized in Table S4.2. Both cells show the similar R_s due to their identical cell assembly, while the R_p values of SFNM+1.2Fe-red-GDC are comparably smaller than that of the SFNM+0.0Fe-red-GDC at all the monitored potentials, suggesting the faster cathode kinetics for CO₂ reduction over SFNM+1.2Fe-red-GDC. Interestingly, R_p of SFNM+0.0Fe-red-GDC firstly drops with the increase of voltage (from 1.0 to 1.6 V), following an increase at 1.8 V, while R_p drops monotonously as the voltage increases over SFNM+1.2Fe-red-GDC. This confirms that the exceptional kinetic performance of SFNM+1.2Fe-red-GDC is well maintained even under harsh poling conditions. Remarkably, the R_p at 1.8 V for SFNM+1.2Fe-red-GDC

reaches an appreciably low value of $0.09 \Omega \text{ cm}^2$, almost half the value of that for SFNM+0.0Fe-red-GDC ($0.17 \Omega \text{ cm}^2$). In addition, the Nyquist plots and the fitted R_p of SFNM+1.2Fe-red-GDC at $800 \text{ }^\circ\text{C}$ are obtained (Figure S4.9 and Table S4.3). It shows the lowest R_p at high voltages ($\geq 1.6 \text{ V}$) among the state-of-art P-eNs-based cathode candidates as listed in Table S4.4, indicative of the higher catalytic activities of SFNM+1.2Fe-red-GDC at higher negative potentials.

In conjunction with the EIS data, distribution of relaxation times (DRT) analysis was used to discern the contributions of underlying kinetic processes to the polarization resistances over these two cells. [224] As shown in Figure S4.10, the electrode process can be deconvoluted into four peaks, which are denoted as 1) oxygen ion transfer through electrolyte and oxygen evolution at anode (P_1), 2) charge transfer (P_2), 3) surface CO_2 adsorption and activation (P_3), 4) gas diffusion process (P_4) at cathode from high to low frequency. [139, 174] Notably, the integral areas of P_2 and P_3 peaks on SFNM+0.0Fe-red increase as voltage rises from 1.6 to 1.8 V, as opposite to that on the SFNM+1.2Fe-red (Figure 4.6b). It can be inferred that the higher surface reactivity, the faster charge transfer on SFNM+1.2Fe-red, whereas the passivated surface would deteriorate the charge transfer on SFNM+0.0Fe-red at 1.8 V.

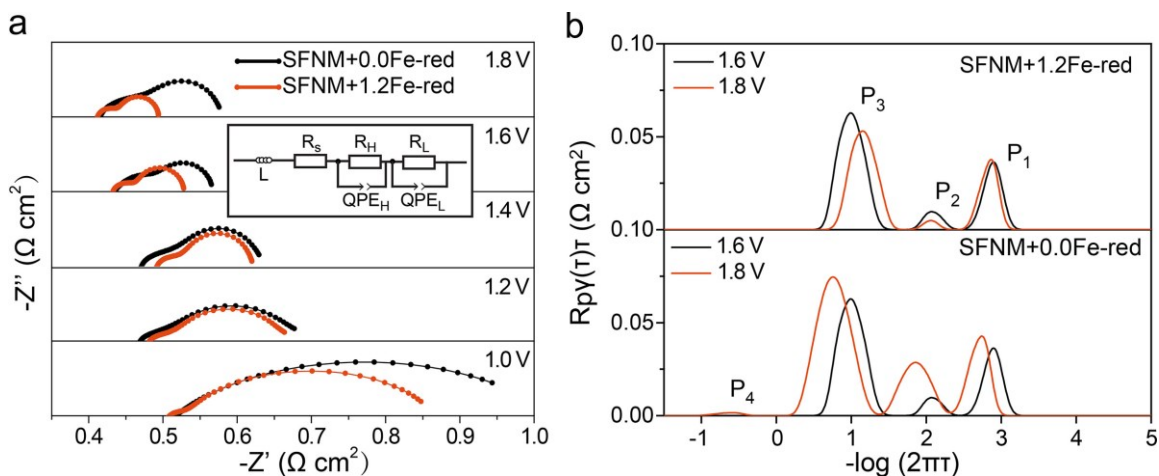


Figure 4.6 (a) EIS of SFNM+0.0Fe-red-GDC and SFNM+1.2Fe-red-GDC for pure CO_2 electrolysis at 850 °C. (b) DRT analyses of the EIS for SFNM+0.0Fe-red-GDC and SFNM+1.2Fe-red-GDC at 1.6 and 1.8 V.

The origin of the enhanced catalytic activity. To understand the origin of the difference in catalytic performances between these two cells for CO_2 reduction at high voltages, further characterizations were carried out on SFNM+0.0Fe-red and SFNM+1.2Fe-red. Firstly, Fourier Transform Infrared Spectroscopy (FTIR) measurement was performed to compare their CO_2 adsorption capacities. [89, 225] As shown in Figure 4.7 and Figures S4.11, SFNM+1.2Fe-red exhibits a higher chemical CO_2 adsorption signal with a quicker response time at 600 °C than the SFNM+0.0Fe-red, implying the superiority of SFNM+1.2Fe-red in terms of surface CO_2 adsorption and reactivity. However, SFNM+0.0Fe-red presents more intensive physical adsorption peaks compared with SFNM+1.2Fe-red at all the examined temperatures (Figure S4.11). It may be ascribed to its higher surface alkalinity caused by more severe Sr-segregation. As shown in Equation 4.6, the Fe-Ni nanoparticle exsolution, together with exhaustion of B-site

cations and lattice oxygen, in a conventional way would trigger the stripping out of Sr cations to re-establish stoichiometry.

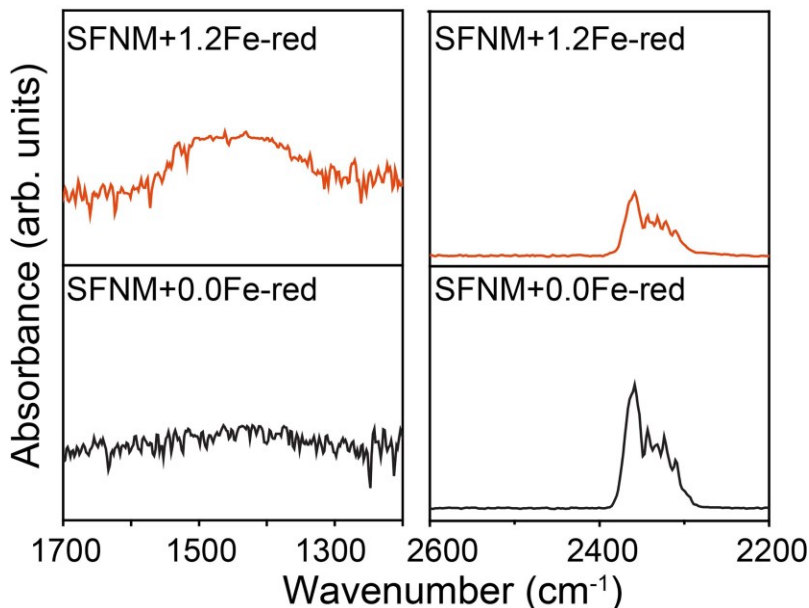
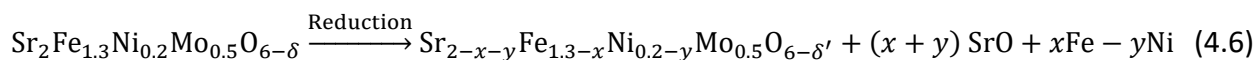


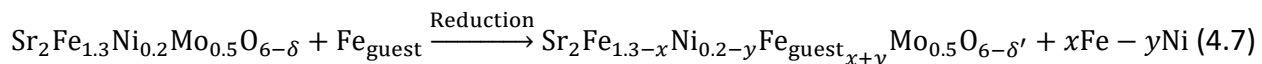
Figure 4.7 FTIR spectra of CO₂ chemisorption and physisorption for SFNM+0.0Fe-red and SFNM+1.2Fe-red at 600 °C.

Conventional exsolution:



The Sr-rich surface would reorganize into SrCO₃ at a high CO₂ concentration, which has a detrimental effect on the surface catalytic activity for CO₂ reduction. [130] Furthermore, high voltages would impose high reducing potentials at the cathode, the concomitant exsolution and Sr segregation would be sustained by the voltage driving force. On the contrary, the undesired Sr segregation could be efficiently alleviated when the B-site vacancies are occupied by the guest Fe; the active sites can be well exposed even at high potentials (Equation 4.7).

TIE-assisted exsolution:



The difference in Sr segregation between SFNM+0.0Fe-red and SFNM+1.2Fe-red has also been verified by comparable EDS signal intensity of Sr in the form of thin shell around the exsolved nanoparticles (Figure S4.12). [214] Combined with the facilitated formation of Fe-Ni alloy nanoparticles and surface-active oxygen vacancies, it in turn persuasively confirms the evolution of initial surface of SFNM+1.2Fe-red into a more catalytically active surface by B-site filling, which contributes to enhanced CO₂ adsorption and activation at high operating voltages. [89]

Thermogravimetric analysis (TGA) reveals that the lattice oxygen loss increases with the guest Fe deposition amount among SFNM+xFe-red ($x=0.0, 0.5, 0.8, 1.2$), indicative of higher oxygen vacancy concentration within perovskite scaffold of SFNM+1.2Fe-red than that of SFNM+0.0Fe-red (Figure S4.13). Since the oxygen ion transfer in perovskite is realized by reverse jumping of oxygen vacancies, the oxygen ion conductivity is also dependent on the mobility of oxygen vacancies in addition to oxygen vacancy concentration. [215] Apparently, the association between neighbouring B-site vacancy and oxygen vacancy on SFNM+0.0Fe-red is likely to trap the oxygen vacancy. The calculated binding energy of the $V_{Fe}'' - V_O''$ defect pair is -1.73 eV (Figure S4.14 and Table S4.5), indicating that the additional association barrier needs to be overcome to achieve the jumping of oxygen vacancies. [215] In contrast, the full occupation of B-sites on SFNM+1.2Fe-red allows the elimination of constraint of B-site defect to surrounding oxygen vacancies. The electrical conductivity relaxation (ECR) experiments for SFNM+0.0Fe-red

and SFNM+1.2Fe-red were carried out to study the oxygen ion bulk diffusion (Figure 4.8a). [116, 200] The bulk diffusion constant (D_{chem}) of SFNM+1.2Fe-red obtained by fitting the ECR curve is $3.747 \times 10^{-4} \text{ cm}^2 \text{ s}^{-1}$, much higher than $1.439 \times 10^{-5} \text{ cm}^2 \text{ s}^{-1}$ of the SFNM+0.0Fe-red. [226] It suggests that there are more available oxygen ion transfer pathways in SFNM+1.2Fe-red, which lead to the higher oxygen ion conductivity and lower charge transport resistance.

Since the valence states of B-site cations have a great influence on the electronic transfer within perovskite bulk, the electronic environments of B-site cations on SFNM+0.0Fe-red and SFNM+1.2Fe-red were examined by the XPS, X-ray absorption near edge structure (XANES) and extended X-ray absorption fine structure (EXAFS) spectra (Figures S4.15 and S4.16). [227-229] As shown in Figure S4.15, higher proportion of Fe^{3+} (23.30%) in SFNM+1.2Fe-red can be observed than that in SFNM+0.0Fe-red (16.29%). In parallel, there is a distinct reduction in the average oxidation state of the Mo atom in SFNM+1.2Fe-red (+5.67) with respect to that in SFNM+0.0Fe-red (+5.89), which was derived from partial reduction of Mo^{6+} to Mo^{5+} (Figures S4.15), indicating the coexistence of $\text{Fe}^{3+}\text{-Mo}^{5+}$ and $\text{Fe}^{2+}\text{-Mo}^{6+}$ electronic configurations to achieve charge neutrality ($\text{Fe}^{3+} + \text{Mo}^{5+} = \text{Fe}^{2+} + \text{Mo}^{6+}$). [230] More $\text{Fe}^{2+}\text{-Fe}^{3+}$ and $\text{Mo}^{5+}\text{-Mo}^{6+}$ charge pairs should endow SFNM+1.2Fe-red with the improved electronic conductivity owing to the sufficient $\text{B}^{(n-1)+}\text{-O-B}^{n+}$ conduction pathways in SFNM+1.2Fe-red. The temperature-dependent electrical conductivity results show that SFNM+1.2Fe-red performs better than SFNM+0.0Fe-red in the 50% CO_2 /50% CO and 5% H_2 /95% Ar atmospheres (Figure 4.8b and Figure S4.17). In the 50% CO_2 /50% CO atmosphere, the electrical conductivities of SFNM+0.0Fe-red and SFNM+1.2Fe-red increase as the temperature increases, reaching 16.5 and 24.6 S cm^{-1} at 850 °C,

respectively (Figure 4.8b). SFNM+1.2Fe-red shows the higher conductivity in the prospective operation atmosphere of CO₂ electrolysis.

In summary, the B-site supplement of the reduced SFNM by external Fe source plays a crucial role in preserving the high surface activity, high oxygen ion conductivity and electronic conductivity at high voltages, thus leading to the faster cathode reaction kinetics.

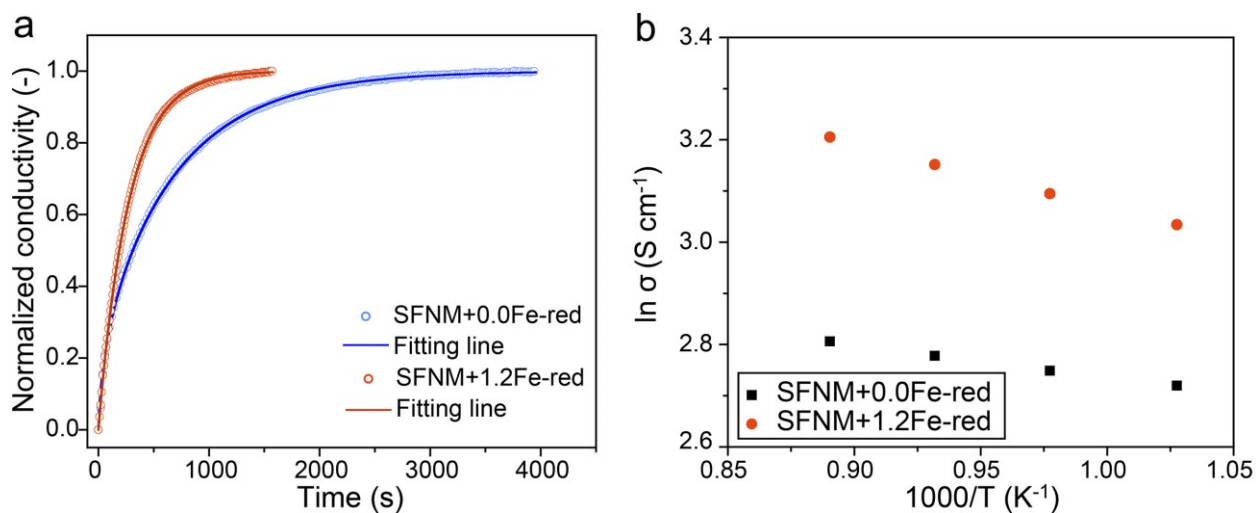


Figure 4.8 (a) Normalized electrical conductivity relaxation curves for SFNM+0.0Fe-red and SFNM+1.2Fe-red at 850 °C with switching of the gas stream from 2:1 CO–CO₂ to 1:1 CO–CO₂. XPS of (b) Temperature-dependent electrical conductivities of SFNM+0.0Fe-red and SFNM+1.2Fe-red under 50% CO₂/50% CO atmosphere.

Short-term/long-term stability performances. The cathode stability under operational conditions is a vital criterion to evaluate the CO₂ electrocatalysis performances in SOEC. The 15 min potential step chronoamperometry was firstly performed at 850 °C to gain initial indication of the stability of SFNM+0.0Fe-red-GDC and SFNM+1.2Fe-red-GDC. Online gas chromatography

(GC) was employed to monitor the CO formation during the short-term stability tests. These two cells deliver quite similar j at negative potentials of 1.0, 1.2 and 1.4 V (Figure 4.9a). Upon increasing the potential to 1.6 V and then to 1.8 V stepwise, stark differences in j have emerged. The significant decay of j can be observed over SFNM+0.0Fe-red-GDC, whereas there is negligible j decline over SFNM+1.2Fe-red-GDC under both polarization conditions. SFNM+1.2Fe-red-GDC shows the competitive short-term stability at the voltages ≥ 1.6 V in comparison with the SFNM+0.0Fe-red-GDC and other state-of-art P-eNs-based SOECs (Table S4.6). Additionally, both cells could steadily generate CO with appreciable Faraday efficiency (FE_{CO}) (around 90%) at all the potentials (Figure 4.9b). As expected, the CO production rate for SFNM+1.2Fe-red-GDC gradually increased with increasing the external voltages, while the production rate for SFNM+0.0Fe-red-GDC peaked at 1.6 V and then decreased upon further raising the potential to 1.8 V. Considering that the nanoparticles closely socketed on the surface of SFNM+0.0Fe-red and SFNM+1.2Fe-red can retain the virtue of high resistance to agglomeration (Figure S4.18), [231] the discrepancies in j decay and CO productivity appear to be raising from the differences in the structure evolution of perovskite matrix at higher negative potentials.

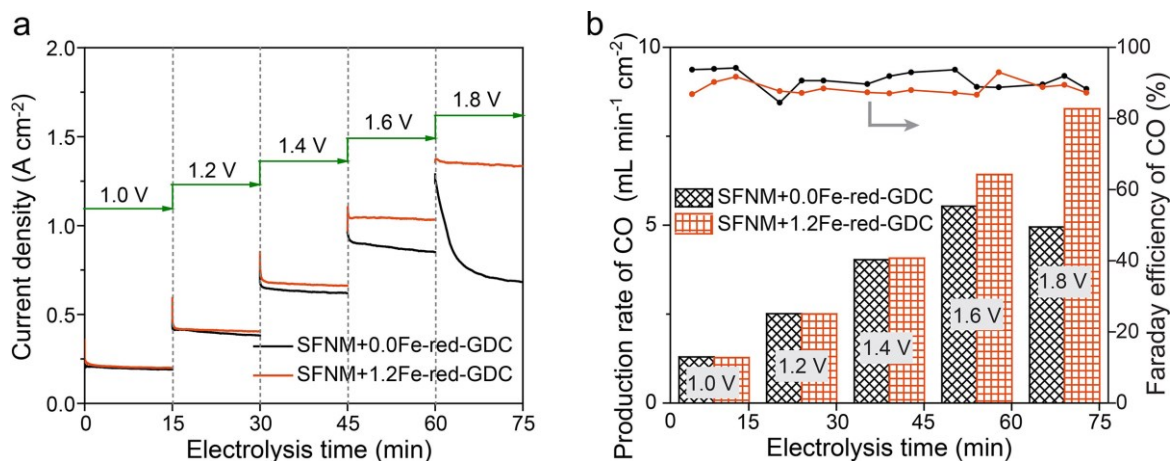


Figure 4.9 (a) The current density response curves for the 15 min potential step chronoamperometry and (b) corresponded CO productivity and FE_{CO} for SFNM+0.0Fe-red-GDC and SFNM+ 1.2Fe-red-GDC at 850 °C with pure CO₂.

It should be worth noting that the stable SOEC operation at high voltages has significant implications on improving the energy efficiency and industrial scale of applications. [213] Furthermore, high cathode potentials are applied to intentionally accelerate electrode degradation to help us understand the cathode evolution and further shed lights on the degradation mechanisms. This in turn is of great significance for designing P-eNs materials in line with the goal for industrialization. Figure 4.10a presents the prolonged stability performances of SFNM+0.0Fe-red-GDC and SFNM+1.2Fe-red-GDC at 850 °C and 1.6 V. Interestingly, SFNM+0.0Fe-red-GDC experiences the current density output instability at around 55 h. Moreover, despite the apparent j decrease over the entire operation, a trend of “degradation–reactivation–degradation” emerges that can be roughly categorized to Phase I (0–8 h), Phase II (8–35 h) and Phase III (35–55 h). Within Phase I, j experiences dramatic decrease with a degradation rate of 44 mA cm⁻² h⁻¹. As the reaction proceeds and enters Phase II, the j

slowly climbs up, peaking at 35 h with a maximum j of 0.47 A cm^{-2} . In the following Phase III, the j drops again until it becomes unstable at around 55 h. Especially, j declines at an attenuation rate of $6 \text{ mA cm}^{-2} \text{ h}^{-1}$ from 50 to 55 h. In sharp contrast to the complicated $j - t$ profile on SFNM+0.0Fe-red-GDC, SFNM+1.2Fe-red-GDC manifests a rather simple and mild degradation profile throughout the long-term stability measurement without observable j fluctuations, only having an average degradation rate of $3 \text{ mA cm}^{-2} \text{ h}^{-1}$. The j remains at a high value of 0.75 A cm^{-2} at 100 h. In addition, the recorded FE_{CO} profiles show that SFNM+0.0Fe-red-GDC experienced a significant FE_{CO} decline, only having 75% at 48 h. In contrast, the FE_{CO} of SFNM+1.2Fe-red-GDC has remained at above 90% throughout the 100-h stability test, indicating its superiority in preventing the yielding of by-products.

Post-mortem characterization and degradation mechanism. After the long-term stability tests, the significant morphology changes and coarsening of exsolved particles can be observed on the both cathode surfaces, and the coarsening of surface nanoparticles on SFNM+1.2Fe-red-GDC is less severe than that on SFNM+0.0Fe-red-GDC (Figures 4.10b-c). Both cathodes were scratched from the cells for the element distribution detection by secondary electron-scanning TEM (SE-STEM) and STEM-EDS. More pronounced Sr- and Mo-derived phase separation in the form of irregular particles appear on the surfaces of SFNM+0.0Fe-red-GDC, (Figures 4.10d-e), suggesting that SFNM+0.0Fe-red-GDC undergoes the more significant phase decomposition than SFNM+1.2Fe-red-GDC under the synergistic effect of the high voltage and CO_2/CO mixed atmosphere during the CO_2 electrolysis. The Raman spectra from cathode surface of both cells were collected (Figure 4.11a). As shown, the distinct Raman feature peaks of SrCO_3 (located at 701 cm^{-1}), SrMoO_4 (located at $795, 842$ and 887 cm^{-1}), carbon with lattice defect (D band,

located at 1319 cm^{-1}) can be found on the cathode surface of SFNM+0.0Fe-red-GDC, [223, 232, 233] whereas only trace amounts of SrMoO_4 peaks were detected on the cathode surface of SFNM+1.2Fe-red-GDC. The emergence of Sr-containing impurities on both spectra confirms the structure decomposition and surface reconstruction on SFNM+0.0Fe-red and SFNM+1.2Fe-red. Obviously, the phase decomposition of SFNM+0.0Fe-red is more thorough. Furthermore, a small amount of carbon deposition on SFNM+0.0Fe-red-GDC may be ascribed to the newly born Ni nanoparticles driven by the applied voltage. Subsequently, SFNM+0.0Fe-red-GDC was subjected to the stability test again and was interrupted before entering the Phase II, and the Raman spectrum of the cathode surface was collected. As shown in Figure 4.11b, only the Raman feature peaks of SrCO_3 and SrMoO_4 were detected but no peaks of carbon, which confirms that the perovskite scaffold of SFNM+0.0Fe-red primarily underwent the bulk structural decomposition before the exposure of newly grown nanoparticles and carbon deposition. This also explains the j evolution over SFNM+0.0Fe-red-GDC.

To verify the exsolution scenario and the structural decomposition during the electrolysis process, the SFNM without pre-reduction treatment was fabricated as the composite cathode material (SFNM-oxi-GDC) for the electrochemical testing (Figure S4.19) and the post-mortem characterizations (Figures S4.20-22). As shown in Supplementary Fig. 20d, the SFNM-oxi-GDC shows the similar long-term stability profile as the SFNM+0.0Fe-red-GDC. The SEM, SE-STEM and STEM-EDS results confirm that partial Ni elements segregate from the SFNM bulk and the newly born fibrous phases appear on the cathode surface (Figures S4.20-21). Meanwhile, the Raman feature peaks of SrCO_3 , carbon with lattice defect (D band) can be observed (Figure S4.22), suggesting that the Ni element in-situ exsolves from the SFNM bulk and subsequently

results in the carbon fiber growth during CO₂ electrolysis. This can be ascribed to the lower co-segregation energy of Ni in SFNM, which causes the structural decomposition under the synergistic effect of 1.6 V and 850 °C.

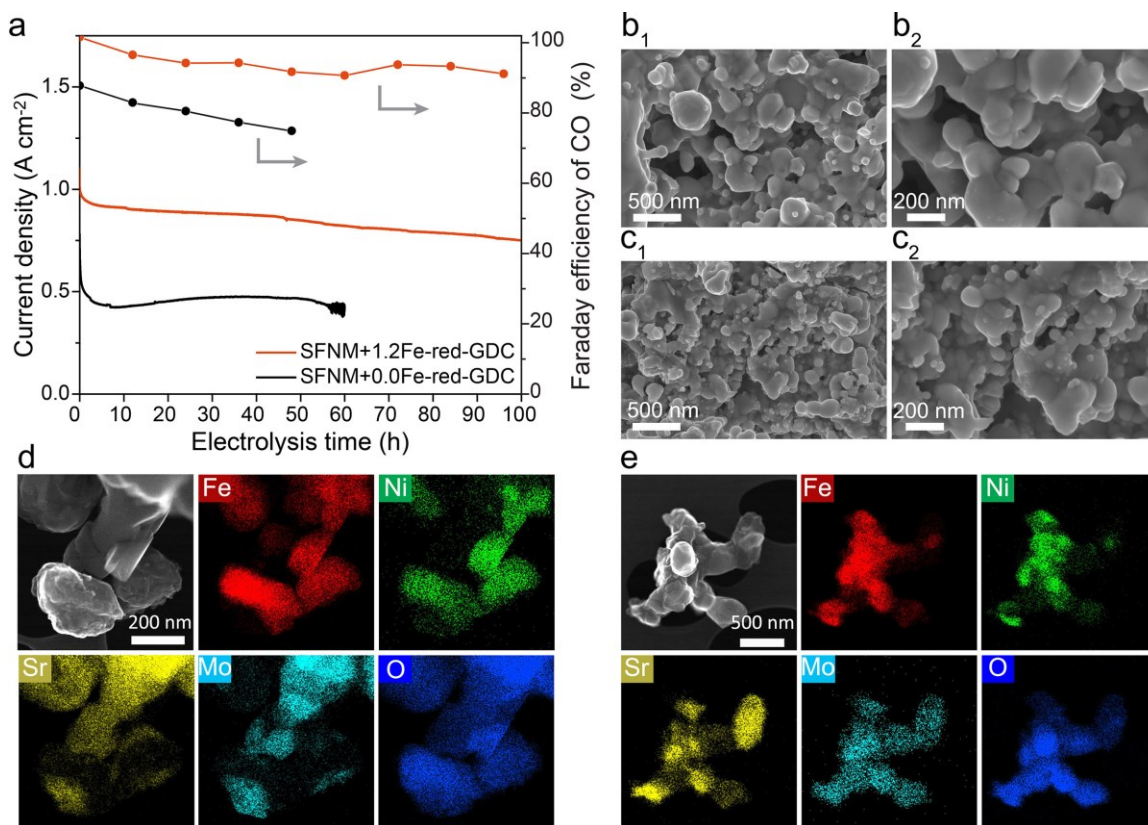


Figure 4.10 (a) 100h long term stability testing for SFNM+0.0Fe-red-GDC and SFNM+ 1.2Fe-red-GDC at 1.6V and 850 °C in pure CO₂. SEM images of cathode surface microstructure of (b₁-b₂) SFNM+0.0Fe-red-GDC and (c₁-c₂) SFNM+1.2Fe-red-GDC after long-term stability at 1.6 V and 850 °C. SE-STEM and STEM-EDS images of cathode on (d) SFNM+0.0Fe-red-GDC, (e) SFNM+1.2Fe-red-GDC after long-term stability at 1.6 V and 850 °C.

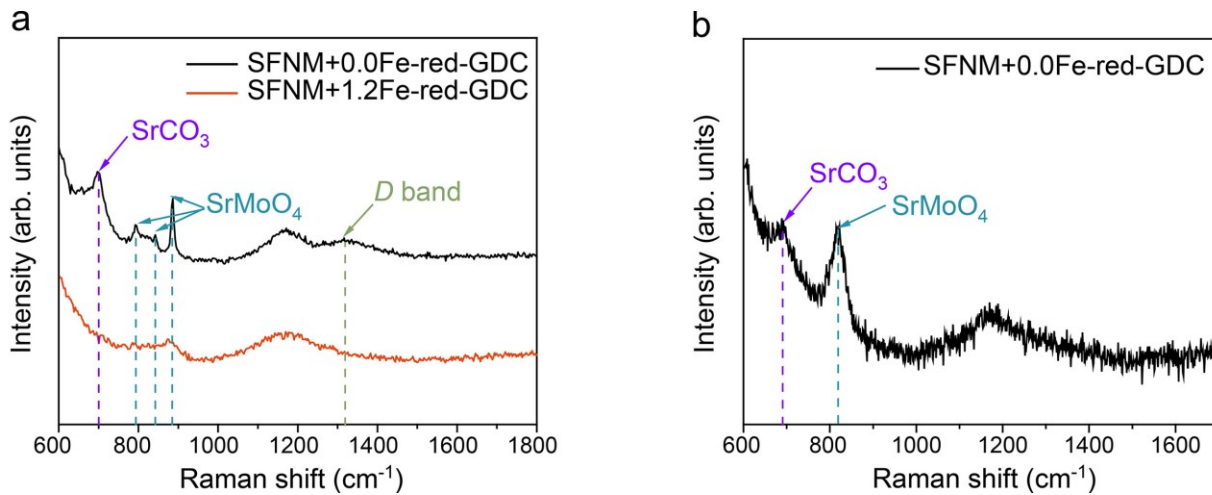


Figure 4.11 (a) Raman spectra collected from cathode surface of SFNM+0.0Fe-red-GDC and SFNM+1.2Fe-red-GDC after the long-term stability test. (b) Raman spectra collected from cathode surface of SFNM+0.0Fe-red-GDC whose stability test was interrupted before entering the Phase II.

Accordingly, the severe degradation may be effectively mitigated by preserving the structural integrity and enhancing the resistance to exsolution of perovskite scaffold of SFNM+0.0Fe-red. In SFNM+1.2Fe-red, the robustness of perovskite scaffold has been significantly enhanced by B-site supplement using redox-stable Fe ions, which postpones the decomposition of perovskite bulk and reassembly of Sr-based insulators on surface. Furthermore, the continuous exsolution has been greatly suppressed due to the decreased Ni content in perovskite bulk. This also well accounts for the mild degradation rate, high FE_{CO} , no intuitive reactivation process, decreased Sr-based matters and negligible deposited carbon over SFNM+1.2Fe-red-GDC.

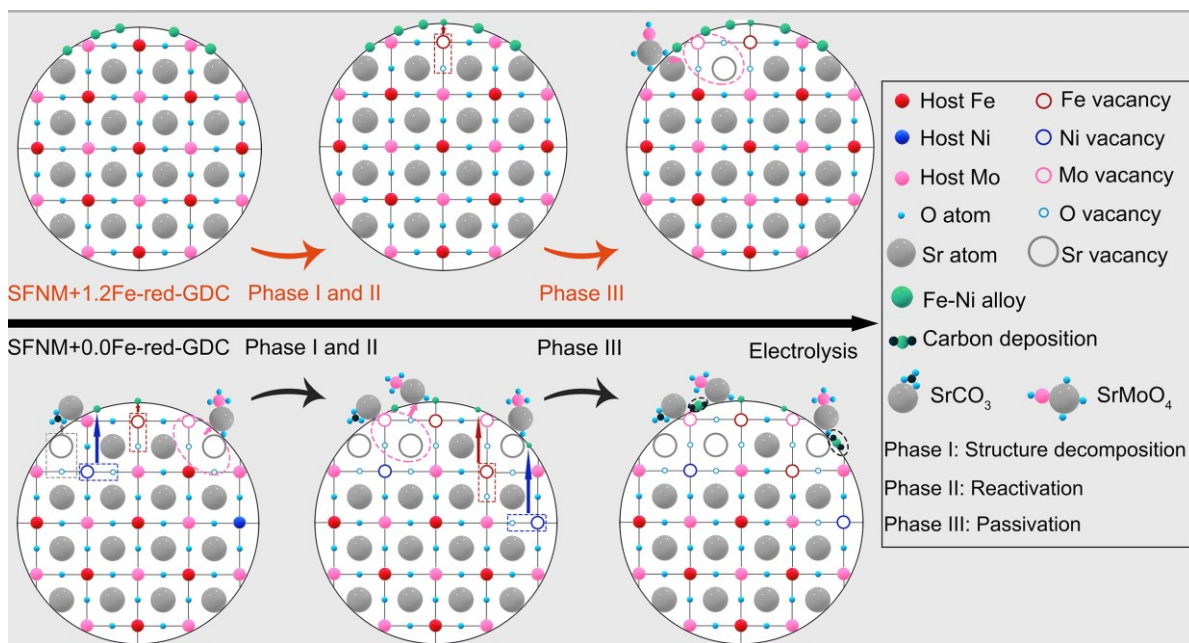


Figure 4.12 Structure evolution driven degradation mechanisms for SFNM+0.0Fe-red-GDC and SFNM+1.2Fe-red-GDC at high negative potentials.

In view of the above analyses, a perspective on the degradation mechanism of P-eNs from the structure stability of perovskite substrate can be proposed. Since the proper negative potential acts as the driving force to drain out B-site reducible cations from perovskite, the high voltage on cathode will not only accelerate CO_2 reduction reaction, but also give rise to the continuous and slow exsolution during the electrolysis, [178] starting from breaking of weak B-O bonds, diffusion of B-site cations, followed by nucleation and growth of nanoparticles. [162] In parallel, A-site segregation occurs, leading to surface reassembly and perovskite bulk reconstruction. As below, we can tentatively discuss the differences in structure evolutions of SFNM+0Fe-red-GDC and SFNM+1.2Fe-red-GDC in light of their degradation processes (Figure 4.12). For SFNM+0Fe-red-GDC, the profile presents a high j but a faster decay rate in the Phase I (Figure 4.10a). This is presumably ascribed to the breaking of B-O bonds and subsequent diffusion of ions from bulk

to surface driven by the external voltage, [165] which causes deteriorated charge transfer capability of perovskite scaffold and surface assembly of detrimental Sr-based matters (Figure 4.11b). This stage is named as “Structure decomposition” regime. However, such a declining profile has been gradually counterbalanced by the newly exposed active nanoparticles derived from diffusion of active cations in the deeper region of perovskite (Phase II in Figure 4.10a). It can be seen that this process is very mild, which means that exsolution is limited by the concentration of exsolved cations in the perovskite and proceeds slowly. [162] This stage is termed as the “Reactivation” regime. As electrolysis proceeds, the structural decomposition progresses slowly, and a balance between surface reorganization and bulk reconstruction has gradually reached. Meanwhile, carbon deposition around the nanoparticles becomes increasingly distinct (Figure 4.11a). Consequently, j drops again or even becomes unstable (Phase III in Figure 4.10a), this period can be named as the “Passivation” zone. Nevertheless, for SFNM+1.2Fe-red-GDC, the “structure decomposition” has been significantly alleviated by the reoccupation of relatively redox-stable Fe ions at B-site vacancies of perovskite. The high applied potential offers a higher initial transient j , however, the amplitude of j attenuation has been remarkably reduced at the initial stage compared with that for SFNM+0.0Fe-red-GDC, which proves that the structural decomposition has been greatly alleviated (Figure 4.10a). Although the “reactivation” stage is not visible from the j curve, the change in FE_{CO} and phase analysis from Raman results suggest the existence of a small amount of exsolution and surface reconstruction (Figures 4.10a and 4.11a). Moreover, carbon deposition near active sites has been circumvented (Figure 4.11a), resulting in a moderate degradation process in the following reaction and a longer operating life. In addition, the deteriorations of the electrolyte and the

anode under the harsh conditions seem to be inevitable (Figure S4.23), which are also responsible for the significant attenuation of the current density during CO₂ electrocatalysis at 1.6 V and 850 °C.

4.3 Conclusions

In summary, this study has highlighted that the B-site supplement should be an alternative strategy to boost the stability of P-eNs for CO₂ electrocatalysis in SOEC. By incorporating the guest Fe ions into the residual B-site vacancies of perovskite scaffold, SFNM+1.2Fe-red exhibits the higher surface activity, charge conductivities and structural robustness compared to SFNM+0.0Fe-red, thus leading to both the high catalytic activity and the high stability performances, especially at high voltages (i.e., ≥ 1.6 V). Furthermore, the degradation mechanisms of the reduced SFNM with/without B-site supplement have been clarified from the perspective of structure stability of perovskite scaffold, revealing the important role of the robust perovskite scaffold in enhancing the stability of P-eNs. This work provides an approach to rational design of the P-eNs with improved activity and stability and also paves the way toward their wide industrial applications as the efficient electrocatalysts for various energy storage and conversion systems.

4.4 Supporting information

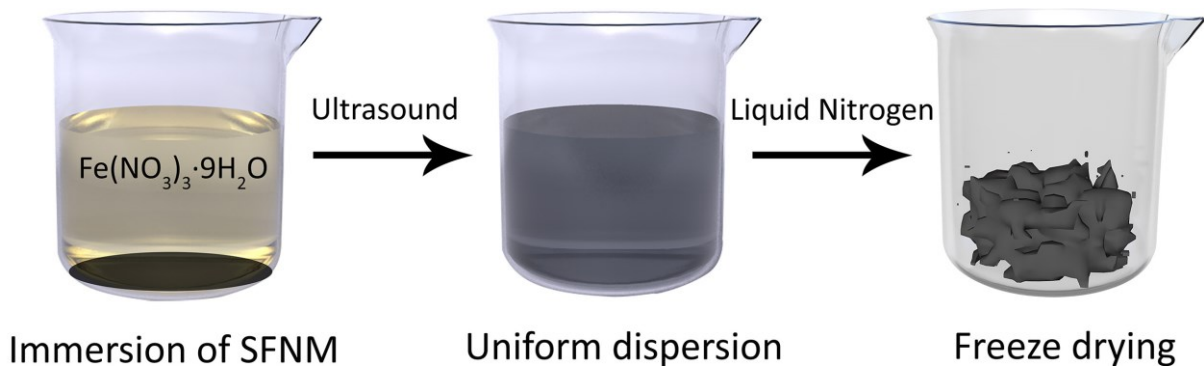


Figure S4.1 Synthesis route of guest Fe deposition on the surface of SFNM for TIE-assisted exsolution process.

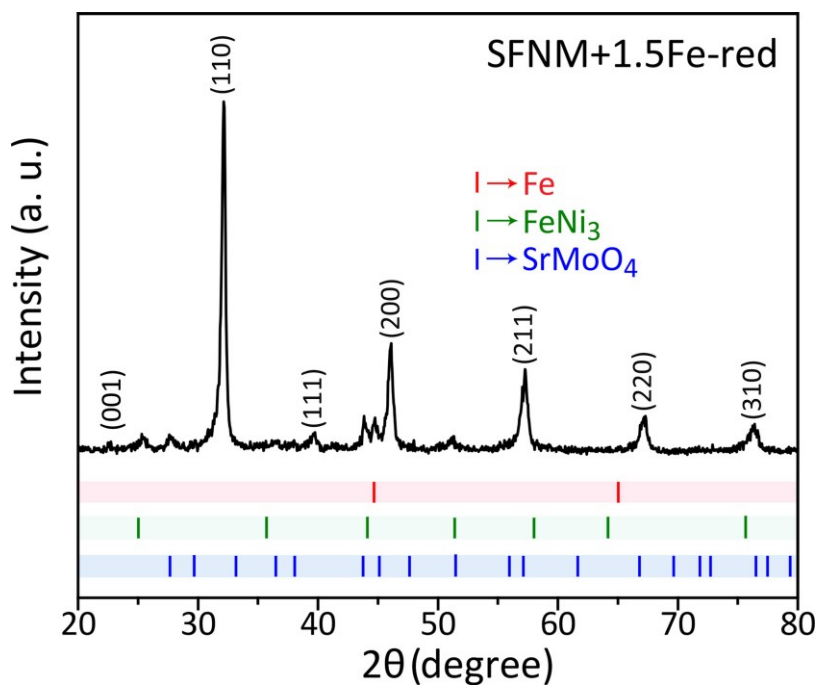


Figure S4.2 XRD pattern of SFNM+1.5Fe-red.

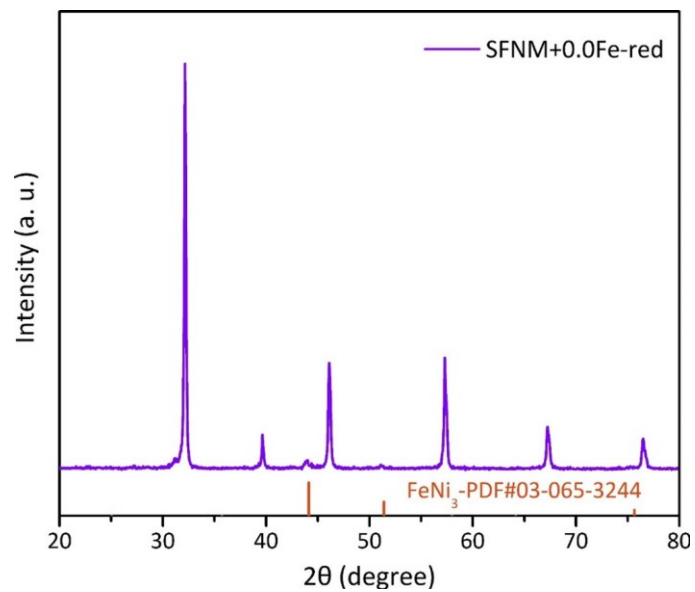


Figure S4.3 XRD pattern of SFNM+0.0Fe-red.

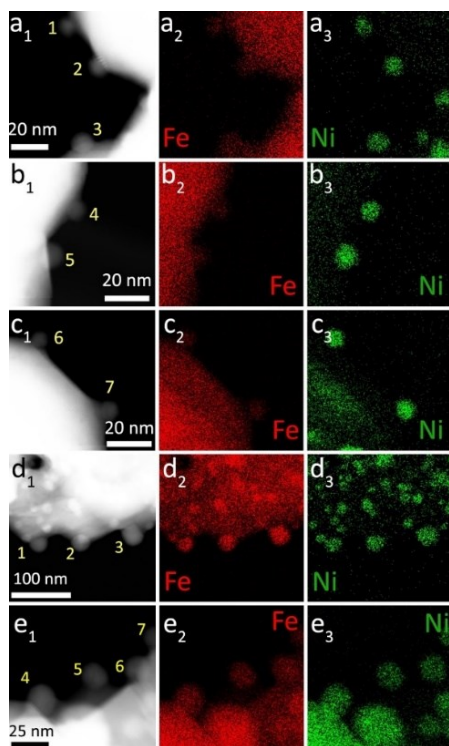


Figure S4.4 TEM with EDS of randomly selected nanoparticles on (a-c) SFNM+0.0Fe-red and (d-e) SFNM+1.2Fe-red.

Table S4.1 Fe and Ni content in randomly selected nanoparticles on SFNM+0.0Fe-red and SFNM+1.2Fe-red.

| Exsolved nanoparticles | | Atom ratio (Fe/Ni, Ni as reference that Ni=1) | |
|------------------------|--|---|----------------|
| Number | | SFNM+0.0Fe-red | SFNM+1.2Fe-red |
| Site 1 | | 0.36 | 3.05 |
| Site 2 | | 0.34 | 2.90 |
| Site 3 | | 0.32 | 3.45 |
| Site 4 | | 0.36 | 1.98 |
| Site 5 | | 0.44 | 2.27 |
| Site 6 | | 0.41 | 2.65 |
| Site 7 | | 0.35 | 2.70 |
| Average | | 0.37 | 2.71 |

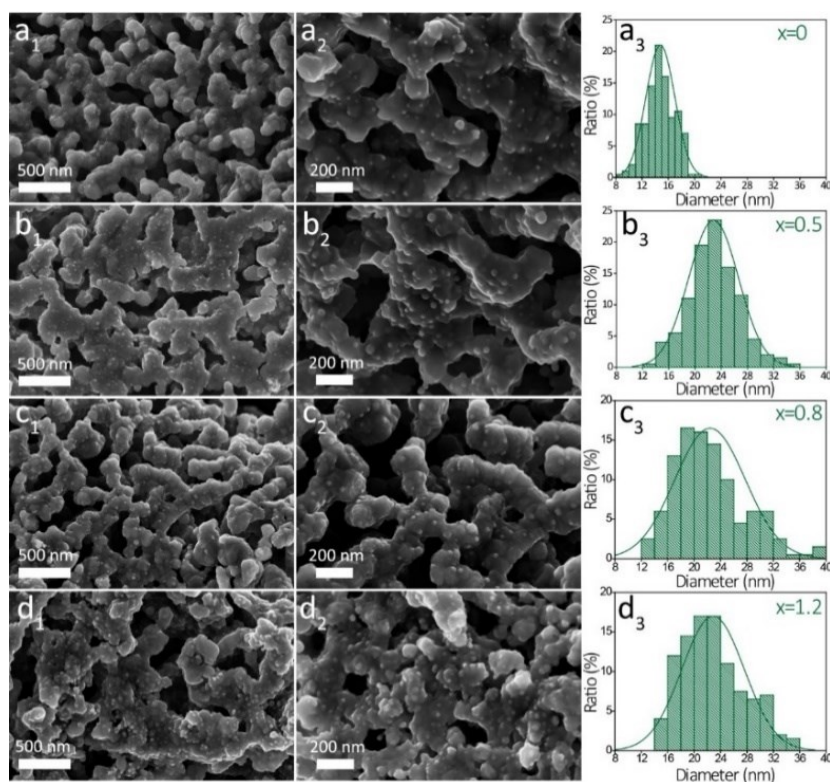


Figure S4.5 (a₁, a₂-d₁, d₂) SEM images of microstructures and (a₃-d₃) size distribution histograms of the exsolved nanoparticles on SFNM+xFe-red (x=0.0, 0.5, 0.8, 1.2).

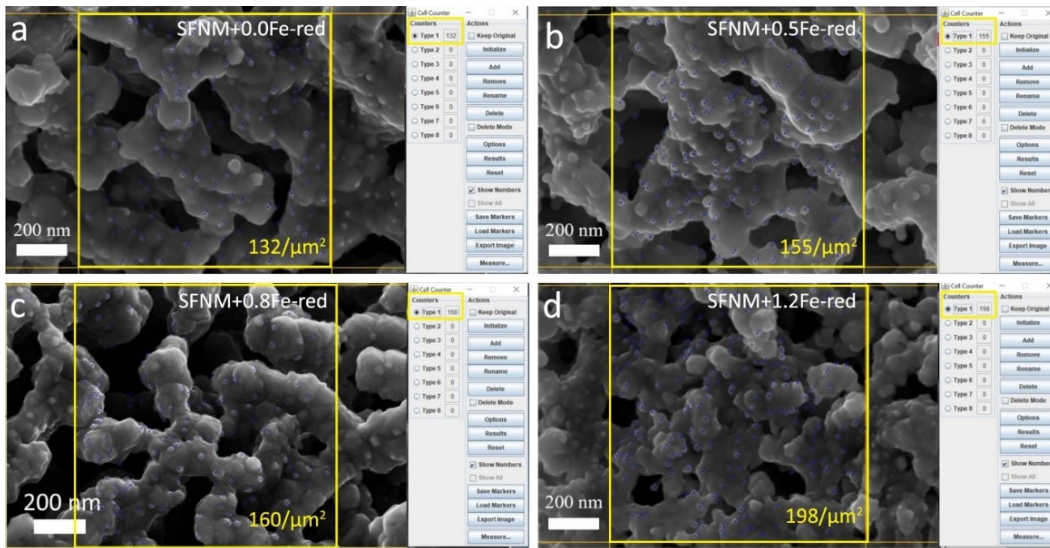


Figure S4.6 Population of exsolved nanoparticles in $1\mu\text{m}^2$ area.

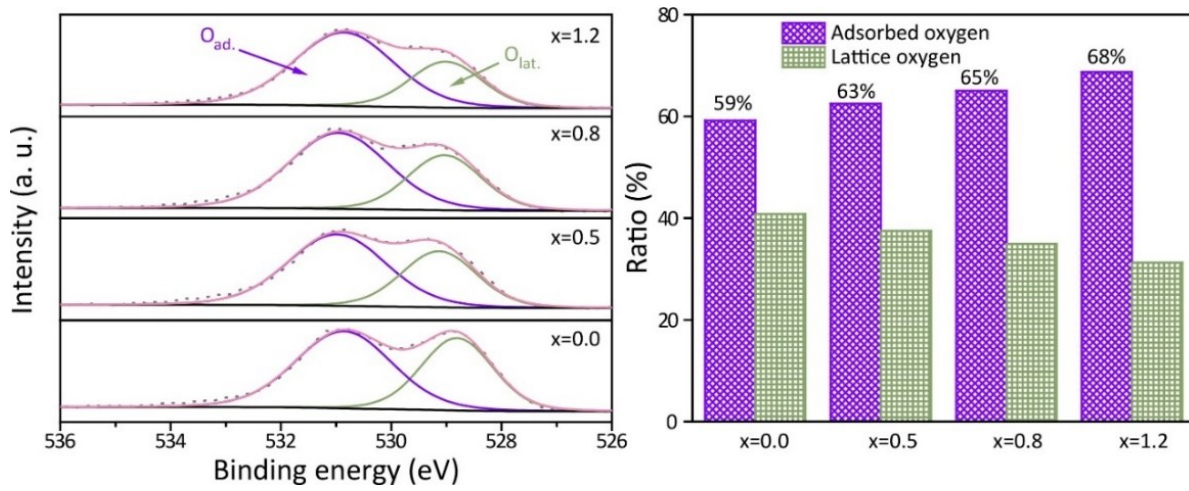


Figure S4.7 XPS O 1s spectra for SFNM+xFe-red ($x=0.0, 0.5, 0.8, 1.2$).

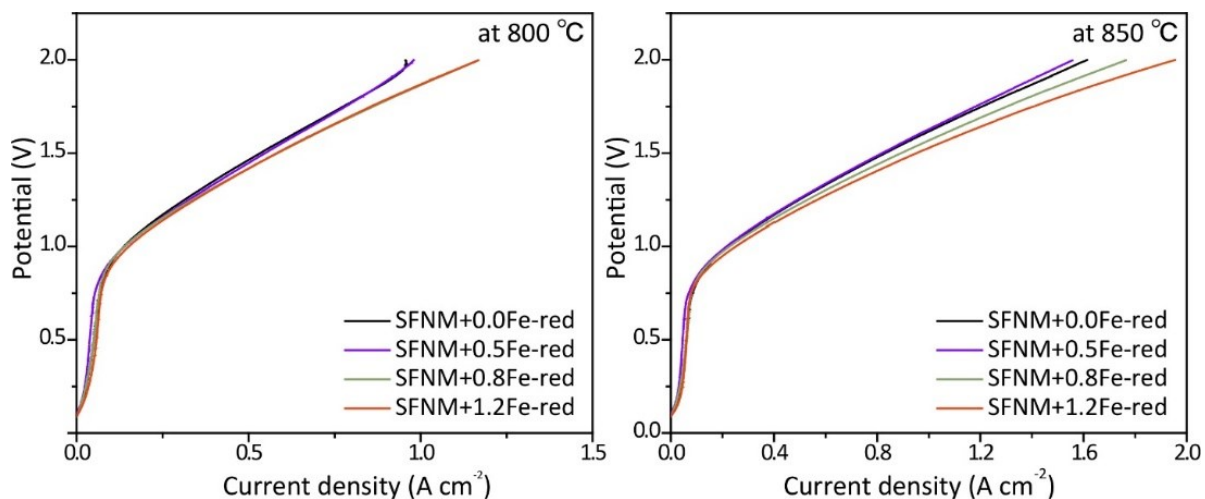


Figure S4.8 $j - V$ curves for SFNM+ x Fe-red ($x = 0.0, 0.5, 0.8, 1.2$) at 800 and 850 °C.

Table S4.2 EIS fitting values (R_s , R_H , R_L).

| Potential (V) | Samples | R_s ($\Omega \text{ cm}^2$) | R_H ($\Omega \text{ cm}^2$) | R_L ($\Omega \text{ cm}^2$) | R_p ($\Omega \text{ cm}^2$) |
|---------------|----------------|---------------------------------|---------------------------------|---------------------------------|---------------------------------|
| 1 | SFNM+0.0Fe-red | 0.4992 | 0.01906 | 0.5066 | 0.52566 |
| | SFNM+1.2Fe-red | 0.4901 | 0.3306 | 0.04527 | 0.37587 |
| 1.2 | SFNM+0.0Fe-red | 0.453 | 0.09258 | 0.1726 | 0.26518 |
| | SFNM+1.2Fe-red | 0.4563 | 0.0974 | 0.1479 | 0.2453 |
| 1.4 | SFNM+0.0Fe-red | 0.4555 | 0.07313 | 0.1142 | 0.18733 |
| | SFNM+1.2Fe-red | 0.4741 | 0.07575 | 0.07375 | 0.1495 |
| 1.6 | SFNM+0.0Fe-red | 0.4259 | 0.05786 | 0.08628 | 0.14414 |
| | SFNM+1.2Fe-red | 0.4239 | 0.05847 | 0.04617 | 0.10464 |
| 1.8 | SFNM+0.0Fe-red | 0.4063 | 0.07069 | 0.1046 | 0.17529 |
| | SFNM+1.2Fe-red | 0.4054 | 0.04964 | 0.03924 | 0.08888 |

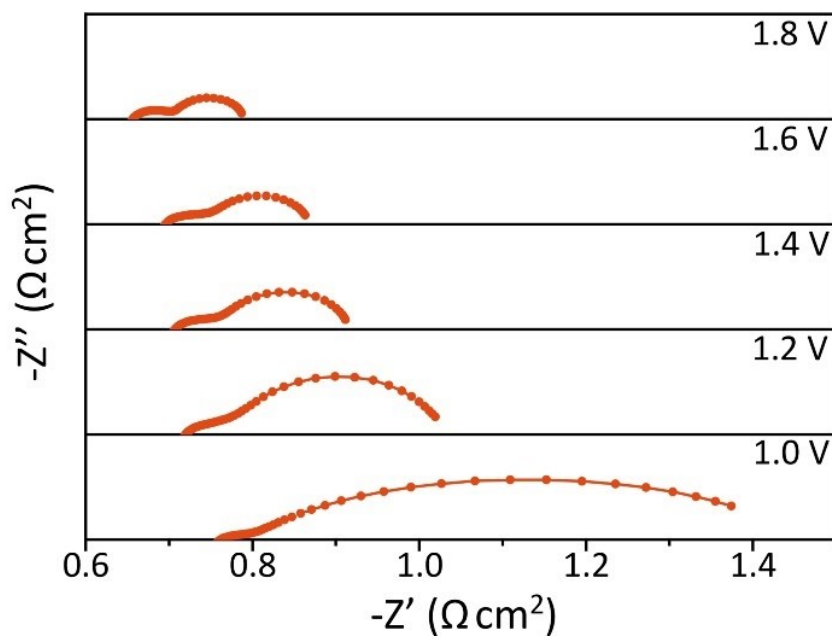


Figure S4.9 Nyquist plots of SFNM+1.2Fe-red-GDC at 800 °C (Equivalent circuit model: LR(Q_HR_H)(Q_LR_L)).

Table S4.3 EIS fitting values (R_s , R_H , R_L) of SFNM+1.2Fe-red-GDC at 800 °C (Equivalent circuit model: LR(Q_HR_H)(Q_LR_L)).

| Potential (V) | R_s (Ω cm ²) | R_H (Ω cm ²) | R_L (Ω cm ²) | R_p (Ω cm ²) |
|---------------|------------------------------------|------------------------------------|------------------------------------|------------------------------------|
| 1 | 0.7375 | 0.0714 | 0.6480 | 0.7194 |
| 1.2 | 0.6901 | 0.1796 | 0.1871 | 0.3667 |
| 1.4 | 0.6847 | 0.1254 | 0.1090 | 0.2344 |
| 1.6 | 0.6743 | 0.0910 | 0.1064 | 0.1974 |
| 1.8 | 0.6441 | 0.0751 | 0.0700 | 0.1451 |

Table S4.4 Comparison of the polarization resistance, CO productivity with other state-of-art exsolved SOECs for CO₂ electrocatalysis.

| Perovskite cathode | Rp (Ω cm ²) | CO productivity (mL min ⁻¹ cm ⁻²) | Ref. |
|---|--------------------------------|---|------------------|
| SFNM+1.2Fe-red (Fe-Ni alloy) | 0.10 (1.6V, 850 °C) | 6.43 (1.6 V and 850 °C) | This work |
| Sr ₂ Fe _{1.58} Mo _{0.5} O _{6-δ} (Fe) | 0.29 (1.8 V, 850 °C) | - | [234] |
| (La _{0.2} Sr _{0.8}) _{0.85} Ti _{0.8} Cr _{0.1} Ni _{0.1} O _{3-δ} (Ni) | 0.43 (1.6 V, 850 °C) | 3.27 (1.6 V, 850 °C) | [235] |
| Sr ₂ Fe _{1.35} Mo _{0.45} Co _{0.2} O _{6-δ} (Co-Fe) | 0.28 (1.6 V, 800 °C) | 8.50 (1.6 V, 800 °C) | [218] |
| (La _{0.2} Sr _{0.8}) _{0.95} Ti _{0.85} Mn _{0.1} Ni _{0.05} O _{3-δ} (Ni) | 0.51 (1.6 V, 800 °C) | 3.67 (1.6 V, 800 °C) | [89] |
| Sr ₂ Fe _{1.35} Mo _{0.45} Ni _{0.2} O _{6-δ} (FeNi ₃) | 0.20 (1.6 V, 800 °C) | ca. 7.50 (1.6 V, 800 °C) | [185] |
| La _{1.2} Sr _{0.8} Mn _{0.4} Fe _{0.6} O _{4-a} (Fe) | 0.326 (1.5 V, 800 °C) | - | [236] |
| La _{0.6} Ca _{0.4} Fe _{0.8} Ni _{0.2} O _{3-δ} (Fe-Ni) | 0.399 (1.3 V, 800 °C) | - | [237] |
| Sr ₂ Fe _{1.25} Cu _{0.25} Mo _{0.5} O _{6-δ} (Fe-Cu) | 0.46 (ca. 0.92 V, 850 °C) | 12.80 (1.4 V, 800 °C) | [238] |

Note: Some values of the current density at 1.6 V of the cited literatures are determined by the Digitizer function of Origin software.

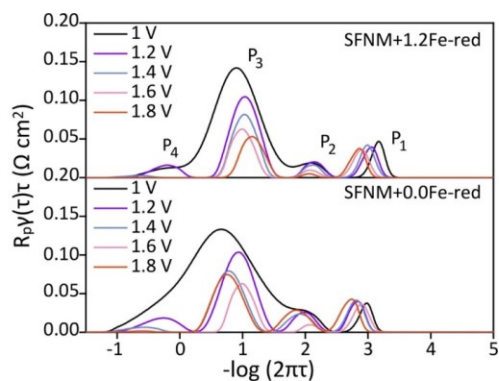


Figure S4.10 Comparison of deconvoluted results of EIS on SFNM+0.0Fe-red and SFNM+1.2Fe-red at applied potentials and 850 °C by DRT analysis.

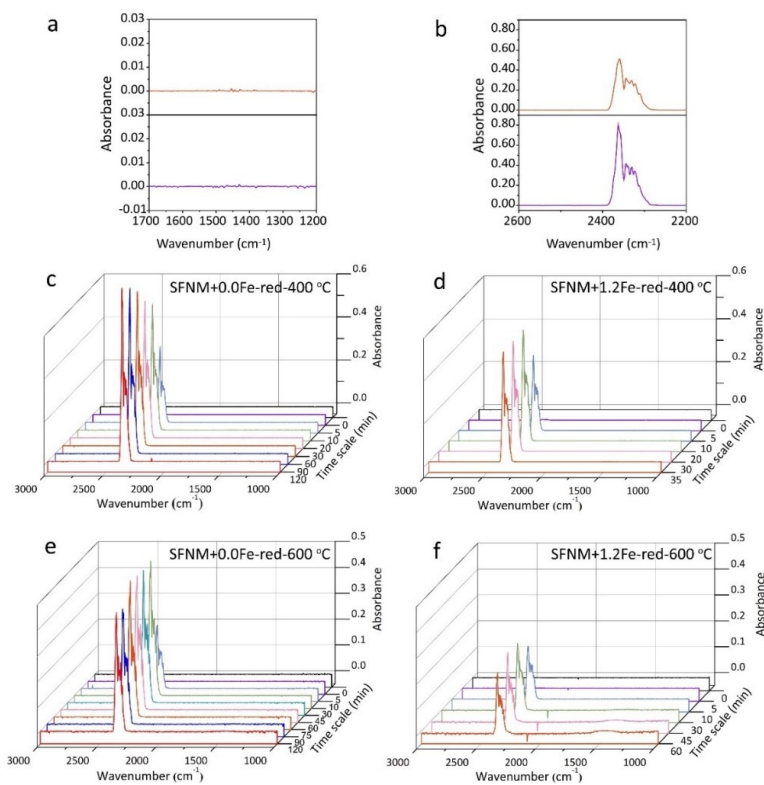


Figure S4.11 FTIR spectra of CO₂ (a) chemisorption and (b) physisorption for SFNM+0.0Fe-red and SFNM+1.2Fe-red at 400 °C. Time dimensioned FTIR spectra for (c, e) SFNM+0.0Fe-red and (d, f) SFNM+1.2Fe-red at 400 and 600 °C.

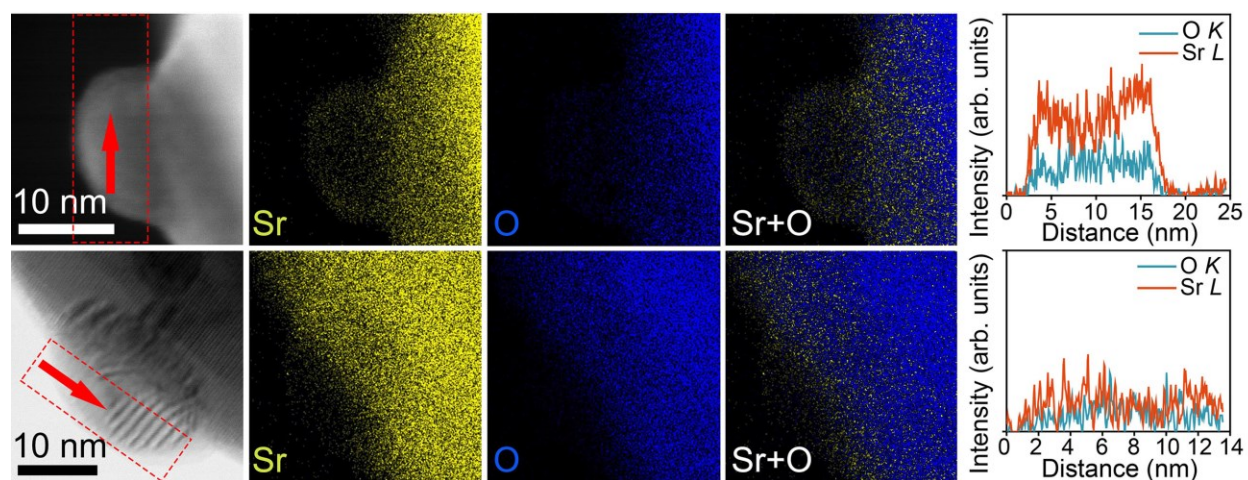


Figure S4.12 Overlap of Sr- and O- EDS signals for SFNM+0.0Fe-red and SFNM+1.2Fe-red.

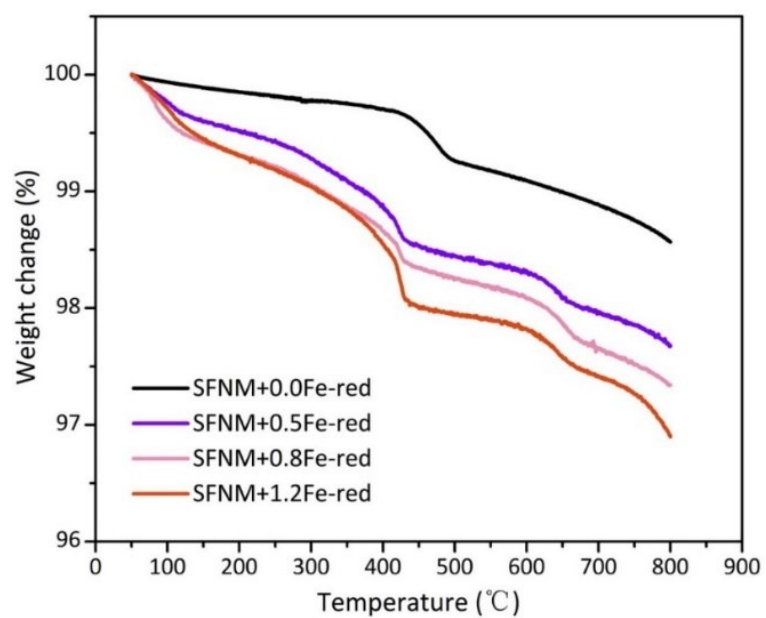


Figure S4.13 TGA of SFNM+ x Fe-red ($x=0.0, 0.5, 0.8, 1.2$) in the 5% H₂/95% N₂ atmosphere.

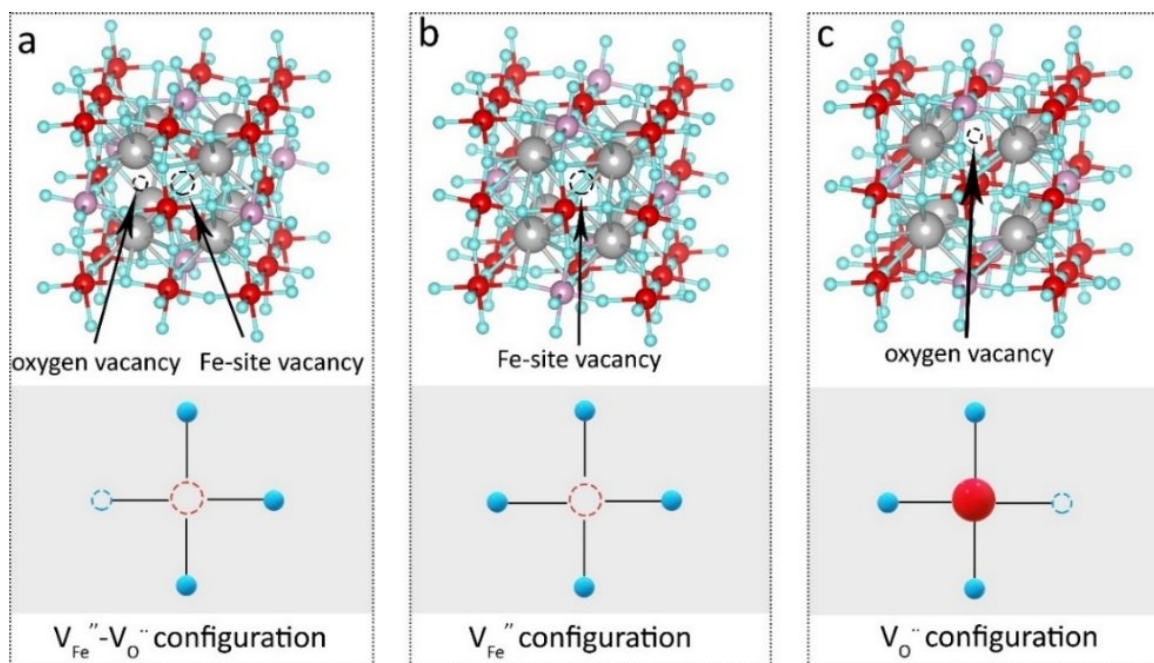


Figure S4.14 Three defective configurations of (a) $V_{Fe}'' - V_{O}''$, (b) V_{Fe}'' and (c) V_{O}'' in SFM. The gray balls represent Sr atoms, the red balls represent Fe atoms, the pink balls represent Mo atoms, the blue balls represent O atoms.

Table S4.5 The corresponded energies of three defective configurations and perfect SFM.

| Configuration | Energy (eV) |
|-----------------------------|-------------|
| $V_{Fe}'' - V_{O}''$ in SFM | -258.45 |
| V_{Fe}'' in SFM | -262.85 |
| V_{O}'' in SFM | -268.81 |
| Perfect SFM | -274.94 |

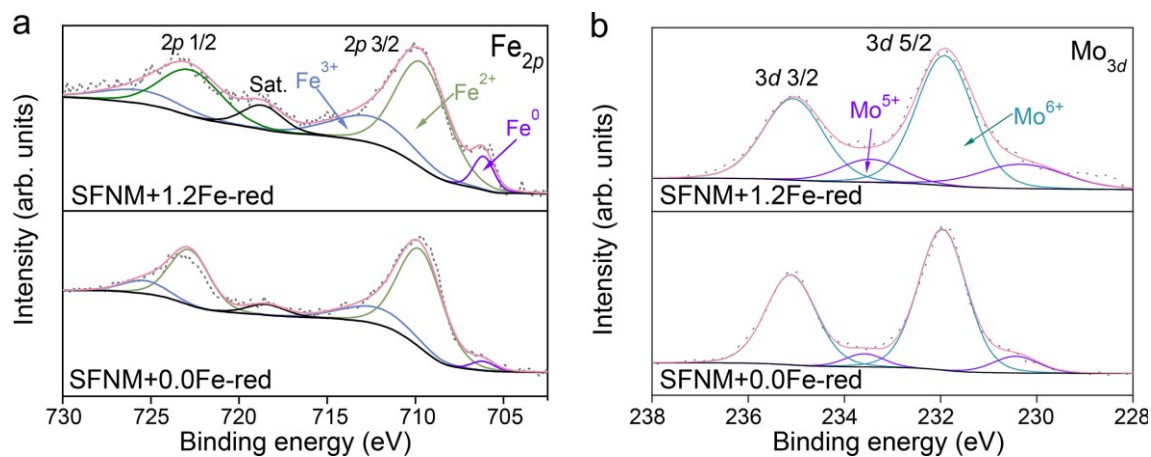


Figure S4.15 XPS of (a) Fe 2p and (b) Mo 3d for SFNM+0.0Fe-red and SFNM+1.2Fe-red.

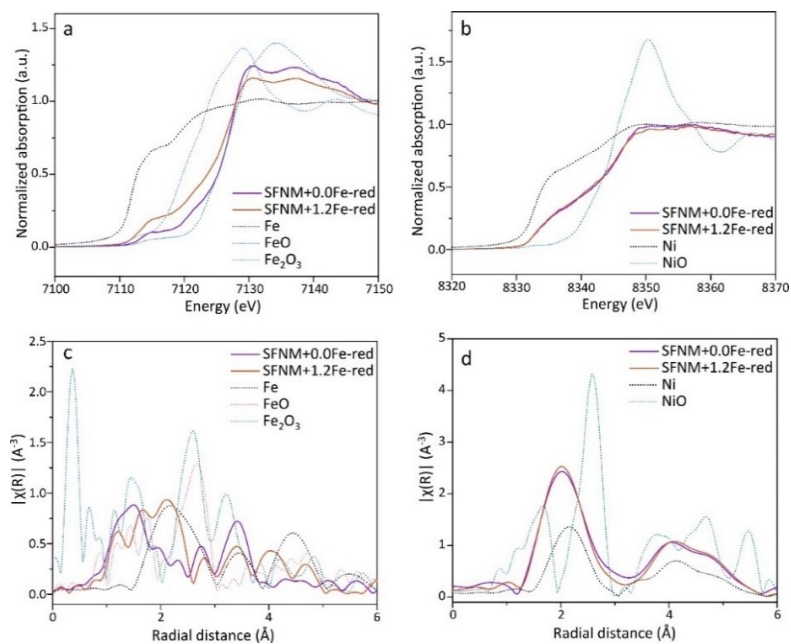


Figure S4.16 (a) Fe K-edge and (b) Ni K-edge X-ray absorption near-edge structure (XANES) spectra of SFNM-oxi, SFNM+0.0Fe-red and SFNM+1.2Fe-red, together with reference samples Fe-foil, FeO, Fe₂O₃, Ni-foil, and NiO. Fourier-transformed (c) Fe K-edge and (d) Ni K-edge extended X-ray absorption fine structure (EXAFS) spectra of SFNM-oxi, SFNM+0.0Fe-red and SFNM+1.2Fe-red, together with reference samples Fe-foil, FeO, Fe₂O₃, Ni-foil, and NiO.

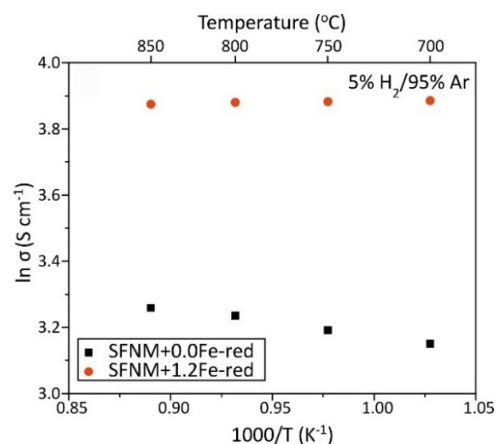


Figure S4.17 Temperature-dependent electrical conductivities of SFNM+0.0Fe-red and SFNM+1.2Fe-red under 5% H₂/95% Ar atmosphere.

Table S4.6 Comparison of the short-term stability with the state-of-art P-eNs for pure CO₂ electrocatalysis in SOEC.

| Perovskite cathode (Exsolved nanoparticles) | <i>j</i> loss rate at 1.6 V (A cm ⁻² min ⁻¹) | <i>j</i> loss rate at 1.8 V (A cm ⁻² min ⁻¹) | Ref. |
|--|--|--|-----------|
| SFNM+1.2Fe-red (Fe-Ni alloy) | 0.003 (850 °C, 15min) | 0.001 (850 °C, 15min) | This work |
| SFNM+0.0Fe-red (Fe-Ni alloy) | 0.008 (850 °C, 15min) | 0.040 (850 °C, 15min) | This work |
| Sr ₂ Fe _{1.58} Mo _{0.5} O _{6-δ} (Metallic Fe) | 0.002 (850 °C, 15min) | 0.002 (850 °C, 15min) | [234] |
| (La _{0.65} Sr _{0.3} Ce _{0.05}) _{0.9} (Cr _{0.5} Fe _{0.5}) _{0.1} ₈₅ Ni _{0.15} O _{3-δ} (Fe-Ni alloy) | 0.022 (850 °C, 15min) | 0.030 (850 °C, 15min) | [171] |
| Sr ₂ Fe _{1.35} Mo _{0.45} Ni _{0.2} O _{6-δ} (FeNi ₃ alloy) | 0.005 (800 °C, 20min) | - | [185] |
| (La _{0.2} Sr _{0.8}) _{0.95} Ti _{0.85} Mn _{0.1} Ni _{0.05} O _{3-δ} (Metallic Ni) | 0.004 (800 °C, 15min) | 0.005 (800 °C, 15min) | [89] |

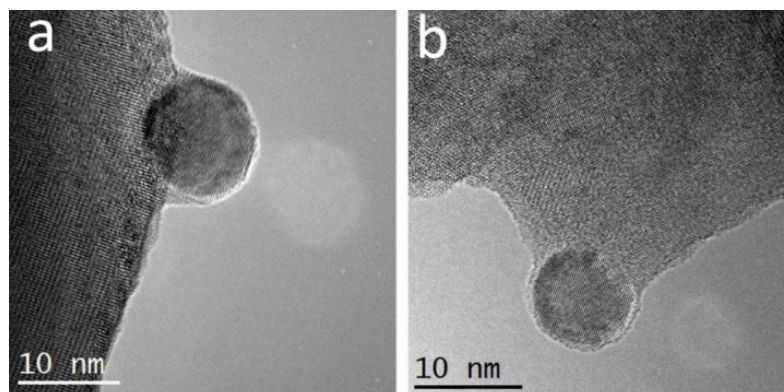


Figure S4.18 High resolution TEM results for (a) SFNM+0.0Fe-red and (b) SFNM+1.2Fe-red.

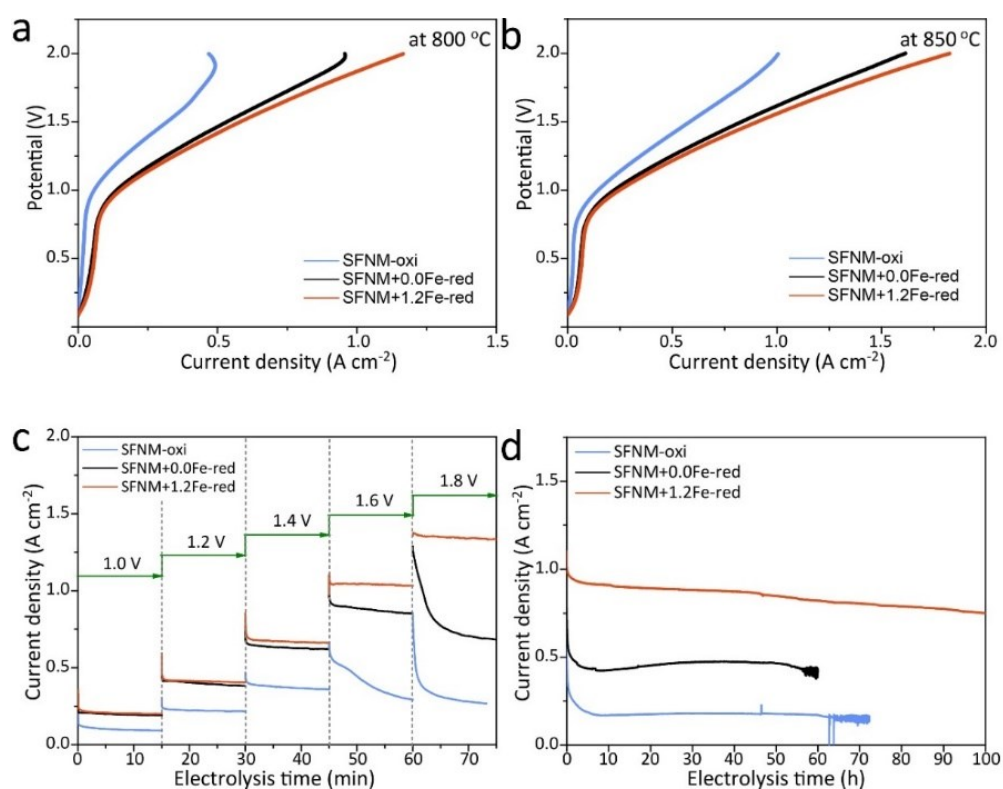


Figure S4.19 I-V curves of SFNM-oxi-GDC with that of SFNM+0.0Fe-red-GDC and SFNM+1.2Fe-red-GDC at (a) 800 °C and (b) 850 °C. Comparison of (c) Short-term stability and (d) long-term stability performances at 850 °C of SFNM-oxi-GDC with that of SFNM+0.0Fe-red-GDC and SFNM+1.2Fe-red-GDC.

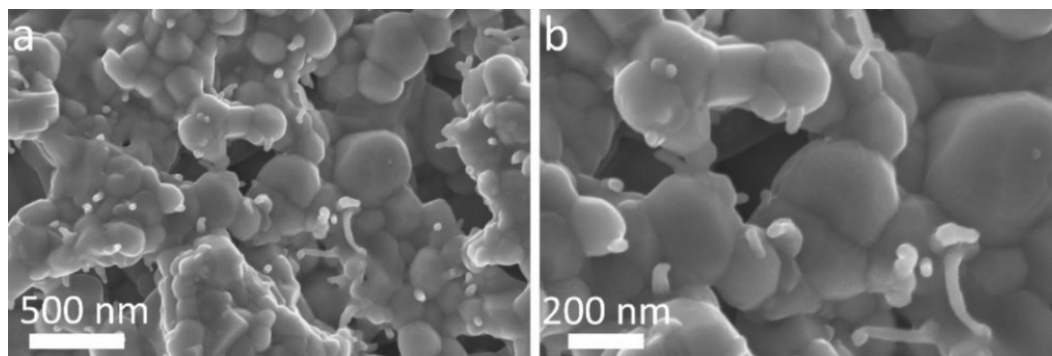


Figure S4.20 SEM images of cathode surface microstructures of SFNM-oxi-GDC after long-term stability at 1.6 V and 850 °C.

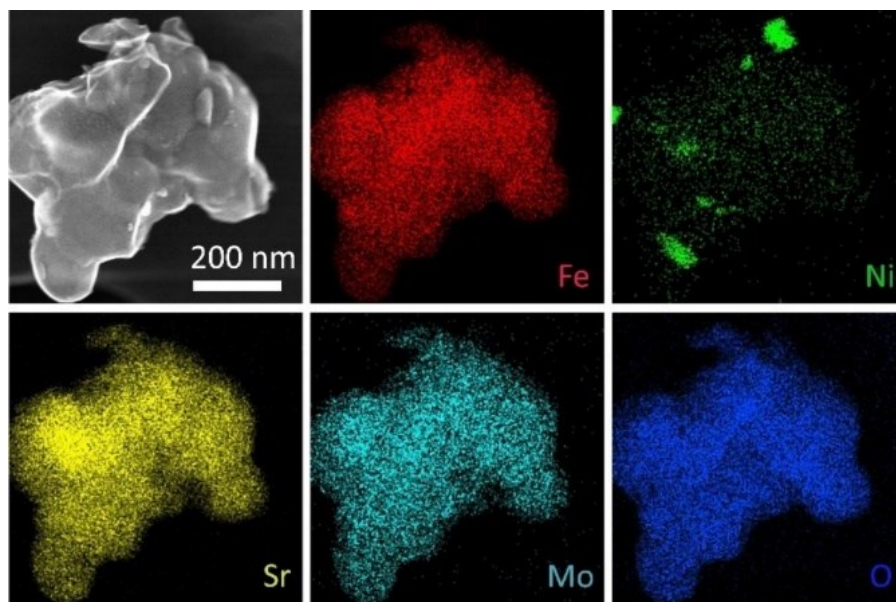


Figure S4.21 TEM images of cathode surface microstructures of SFNM-oxi-GDC after long-term stability at 1.6 V and 850 °C.

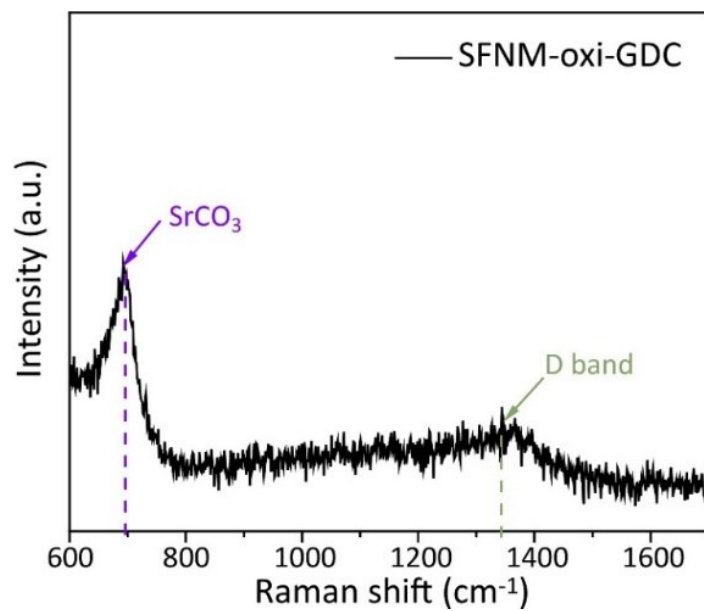


Figure S4.22 Raman spectrum collected from cathode surface of SFNM-oxi-GDC after the long-term stability test.

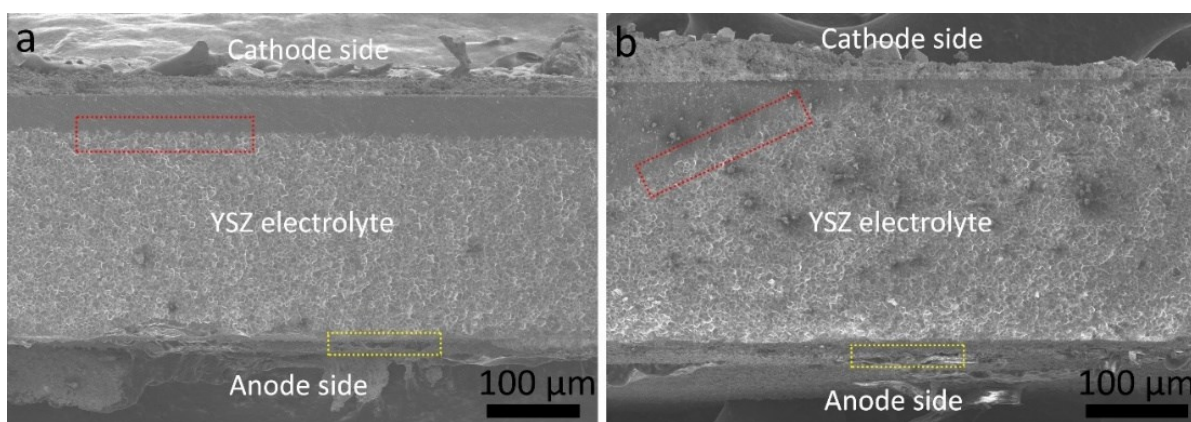


Figure S4.23 SEM images of cross section of (a) SFNM+0.0Fe-red-GDC and (b) SFNM+1.2Fe-red-GDC after long-term stability tests at 1.6 V and 850 °C.

Chapter 5. Phase transition engineering of host perovskite toward optimal exsolution-facilitated catalysts for CO₂ electrolysis

5.1 Introduction

P-eNs have been extensively used as the electrocatalysts in solid oxide cells (SOCs) for energy conversion and storage. [165, 192, 218, 239] In recent years, significant efforts have been made to modify the size, density and composition of exsolved nanoparticles, [148, 164, 166, 174, 187] thereby improving the catalytic activity of P-eNs. [175] However, the perovskite scaffold, which plays a crucial role in extending the surface TPB and preserving the highly active sites, has received relatively little attention. [177, 193] It is worth noting that the promoted exsolution of nanoparticles is at the cost of consuming the perovskite scaffold, the continuous stripping of reducible B-site cations and lattice oxygen from the host perovskites would result in an inadvertent structural reconstruction, [230, 238, 240, 241] even lead to the unintentional phase transformation in cases where the exsolution exceeds a critical threshold. [102, 103, 242] This limits the full exploitation of the heterogeneous architectures on exsolution-facilitated perovskites and also, limits our current understanding on how the phase transformation of the perovskite scaffold affects the catalytic performances of P-eNs.

One of the key points in addressing the aforementioned concerns is controlling the phase evolution of perovskite substrate while facilitating exsolution, [177, 243] however, there remains a scarcity of effective and straightforward methods to suppress phase transition without compromising exsolution. [244] In addition, the lack of systematic investigation on the

electrolysis processes on P-eNs with diverse nanoparticle support hinders the in-depth understanding of the role of perovskite scaffold in electrocatalysis. [242, 245] Only by overcoming these two challenges can we more effectively design P-eNs materials for a wide range of reactions.

In this study, we have identified a set of strategies for controlling the phase evolution of the host perovskite without compromising exsolution on the perovskite $\text{Sr}_2\text{Fe}_{1.2}\text{Ni}_{0.3}\text{Mo}_{0.5}\text{O}_{6-\delta}$ (SFN₃M). In particular, the trade-off between promoting exsolution of Fe-Ni nanoparticles and preserving phase structure of host perovskite has been broken by a B-site supplement strategy (Scheme 1), thus broadening the scope of exsolution-facilitated perovskite. Using CO₂ electrolysis in SOEC as an illustrative case study, we have demonstrated that the catalytic activity and stability of P-eNs can be selectively enhanced by controlling the phase evolution of host perovskites from double perovskite (DP) to layered perovskite (LP) structure. Combining the experimental and theoretical results, we reveal that the intentional manipulation of perovskite architectures can optimize the surface chemical environment and strengthen the surface-bulk interactions, thus dominating the cathode kinetics in response to the applied voltages and even altering the rate-limiting step. In addition, we propose two structural factors: structural stability of host perovskite itself and the concentration of the reducible B-site cations for predicting the robustness of P-eNs for CO₂ electrolysis. The methodology of precisely regulating the architectures of host perovskite can offer the insights into the exsolution-facilitated P-eNs design for various electrocatalytic reactions and contribute to the comprehensive understanding of catalytic mechanisms occurring on P-eNs-based materials.

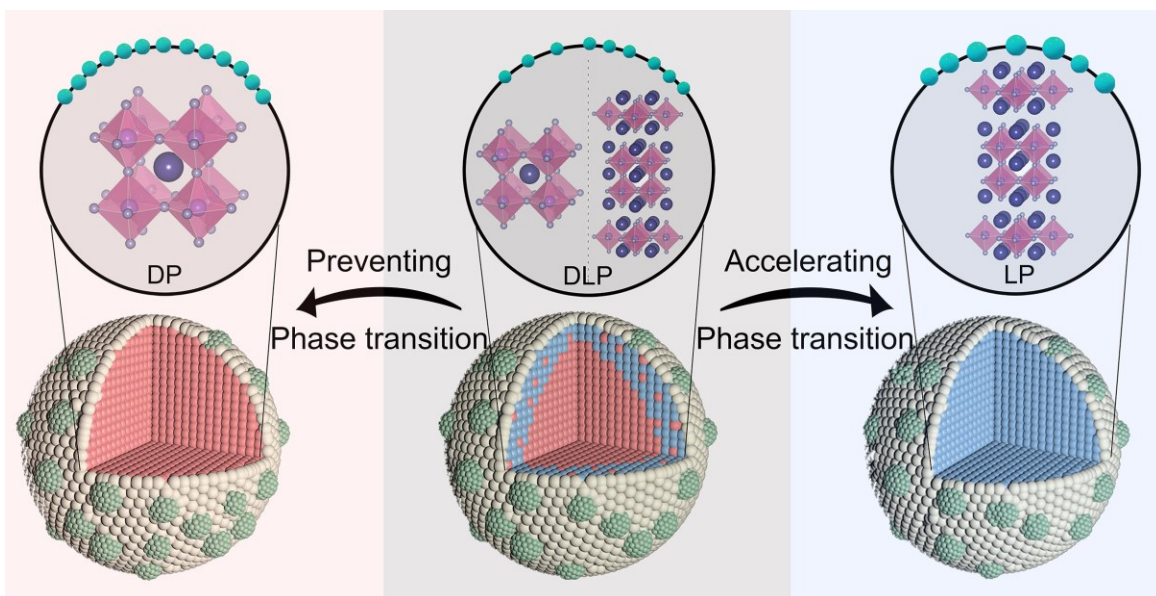


Figure 5.1 Design scheme of the exsolution-facilitated P-eNs with different perovskite compositions as scaffold. (In the 3D models, the red area represents DP structure, the blue area represents LP structure, the light green area represents Fe-Ni nanoparticles. In the 2D models, the purple spheres represent A-site atoms Sr, the pink spheres represent B-site atoms Fe/Ni/Mo, the gray spheres represent oxygen atoms, and the green spheres represent exsolved Fe-Ni alloy nanoparticles).

5.2 Results and discussion

Construction of heterogeneous P-eNs by fine-tuning the structure of perovskite scaffold.

Figure S5.1 shows that the crystalline structure of SFN₃M presents a pattern corresponding to DP-typed Sr₂FeMoO₆ (PDF#00-060-0459), while the LP-typed Sr₃FeMoO_{6.5} (PDF#00-052-1715) as an emerging phase can be probed after reduction at 850 °C for 2 h (SFN₃M-red-2h). [230, 246] Secondary electron-scanning transmission electron microscopy (SE-STEM) and STEM with energy-dispersive X-ray spectroscopy (STEM-EDS) results confirm the formation of Fe-Ni alloy

on the surface of SFN₃M-red-2h (Figure 5.2), demonstrating that a composite substrate composed of DP and LP with exsolved Fe-Ni alloy nanoparticles (DLP-NPs) has been well-constructed (Figure 5.3a i). By prolonging the reduction duration of SFN₃M to 10 h at 850°C (SFN₃M-red-10h), the stripping of reducing cations continued, and a state of near-complete phase transition has thus been attained. (Figure 5.3a iii and Figure S5.2). On the contrary, to eliminate the trade-off between the inhibition of phase transition and promotion of exsolution, we incorporated the redox-stable Fe ions into the host perovskite by ion exchange assisted exsolution, to enhance the structural stability of perovskite scaffold. [177] X-ray diffraction (XRD) spectra of SFN₃M loaded with various amounts of guest Fe (SFN₃M+xFe-red-2h, $x=0.5, 0.8, 1.2$, where x is the molar ratio of guest Fe/host Ni) after reduction reveal that the phase evolution into the LP has been gradually mitigated with increased Fe loading (Figure S5.3), and the DP structure is well preserved without any indication of the LP phase when $x=1.2$ (Figure 5.3a ii). By tracking the phase evolution of parent perovskite throughout the reduction process of SFN₃M+1.2Fe-red-2h (Figure 5.3b), we probed SrMoO₄ phase at 400 °C. It implies that the ion exchange has initiated at this temperature because the incorporation of foreign Fe ions into the B-site vacancies of perovskite substrate would result in the formation of Sr₂Fe_{1.5}Mo_{0.5}O₆ (SFM) in the local area, which leads to the detachment of SrMoO₄ phase at the relatively lower reducing temperatures. Further temperature ramping would cause the harsher reducing conditions where SrMoO₄ could completely redissolve back into the SFM lattice at 800 °C. Therefore, the well-preserved pure double perovskite substrate on SFN₃M+1.2Fe-red-2h can be ascribed to the structural reinforcement of perovskite scaffold by B-site supplement with external Fe source.

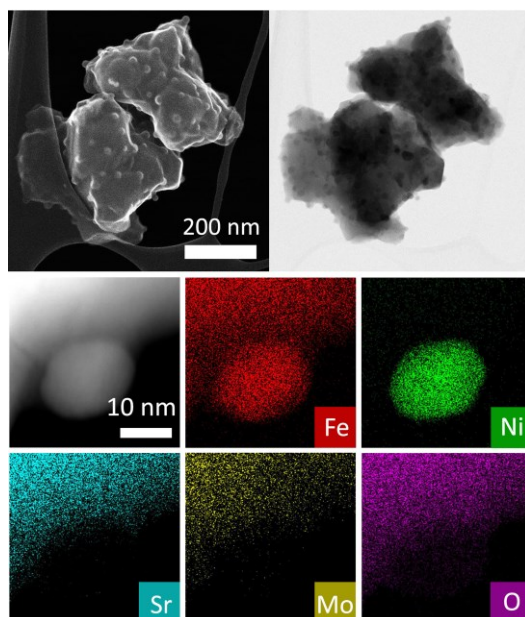


Figure 5.2 Secondary electron-scanning transmission electron microscopy (SE-STEM) and STEM with energy-dispersive X-ray spectroscopy (STEM-EDS) results results of SFN₃M-red-2h.

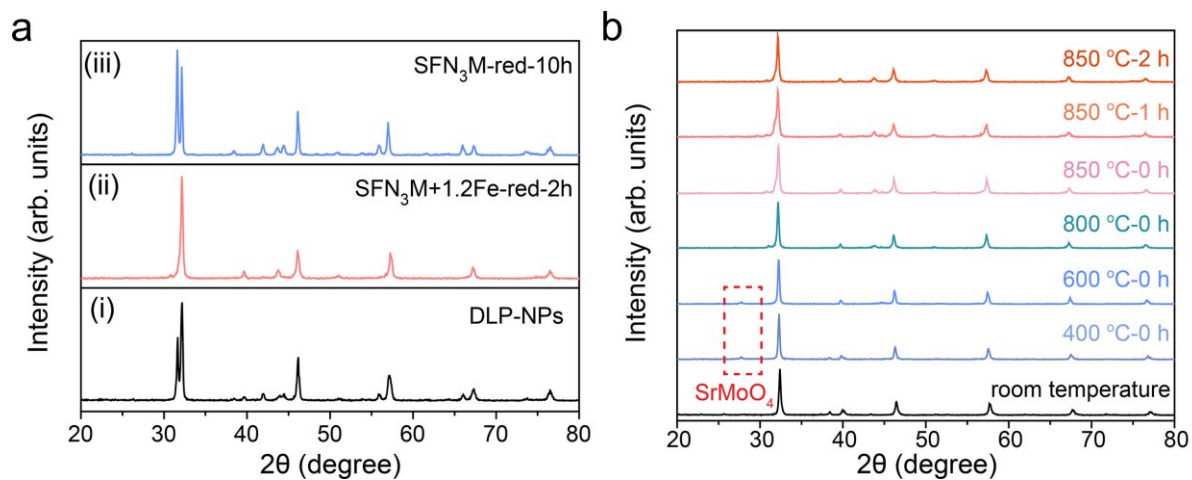


Figure 5.3 a, XRD patterns of three P-eNs (DLP-NPs, SFN₃M+1.2Fe-red-2h, SFN₃M-red-10h). **b**, Ex situ XRD patterns of SFN₃M+1.2Fe after reduction at different temperatures and time.

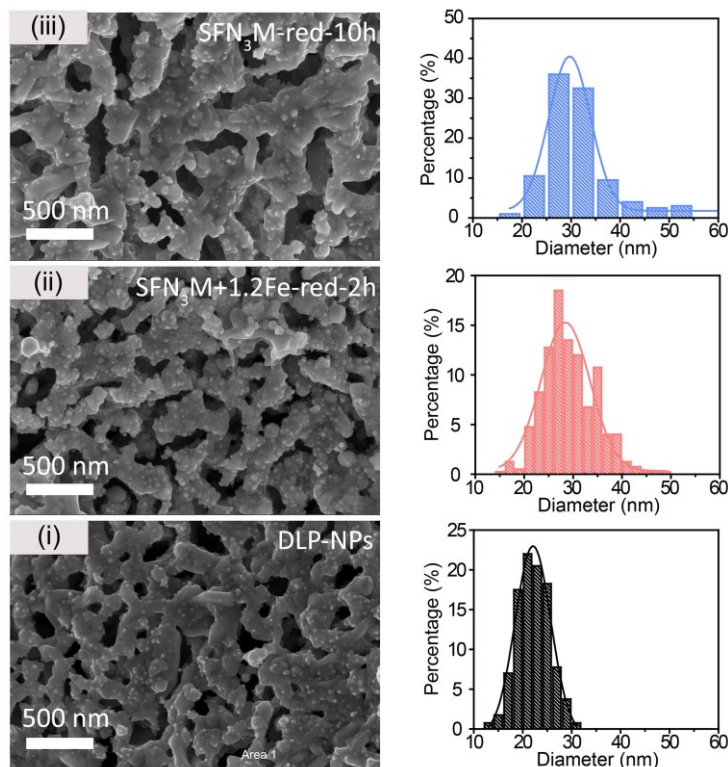


Figure 5.4 SEM images of microstructures and size distribution histograms of the exsolved nanoparticles on SFN₃M-red (black color), SFN₃M+1.2Fe-red (pink color) and SFN₃M-red-10h (blue color).

Field emission-scanning electron microscopy (FE-SEM) and STEM-EDS results substantiate that the Fe-Ni alloy nanoparticles, characterized by a larger size and increased population, have been evenly anchored on the surface of SFN₃M+1.2Fe-red-2h via a thermodynamically favorable ion-swapping process (Figure 5.4 ii, Figure S5.4b). [177] However, as a result of the extended exsolution and Ostwald ripening, the exsolved Fe-Ni nanoparticles exhibit the larger size and less population on the surface of SFN₃M-red-10h (Figure 5.4 iii, Figure S5.4c)[152, 162]. Furthermore, Fe/Ni ratio of exsolved nanoparticles on SFN₃M+1.2Fe-red-2h and SFN₃M-red-10h are 2.72 and 1.29, respectively, higher than 0.67 on DLP-NPs (Figure 5.2, Figure S5.5, Table S5.1).

Based on the characterization presented thus far, we can draw the conclusion that DP-NPs (simplified from SFN₃M+1.2Fe-red-2h) and LP-NPs (simplified from SFN₃M-red-10h) have been successfully constructed.

Upon the examination of perovskite matrix using the high resolution TEM (HRTEM), only DP-typed Sr₂FeMoO₆ structure can be captured from the indexation of the diffractograms of DP-NPs (Figure 5.5a). However, for DLP-NPs, the HRTEM images of the randomly selected substrate reveal that the lattice structures of Areas 1 and 3 correspond to the DP structure, while that of Area 2 belongs to the LP-typed Sr₃FeMoO_{6.5} structure (Figure 5.5b), where the existence of a streak in this diffractogram along c* indicates the formation of a stacking superstructure along the c axis. Close check of Area 3 reveals that LP-typed structure can be found as well (Figure 5.5c). Judging by the sizes of these streaks, we postulate that they are at an early growth stage and by contrast, the LP-dominated areas are readily observed on the substrate of LP-NPs from the HRTEM image (Figure 5.5c).

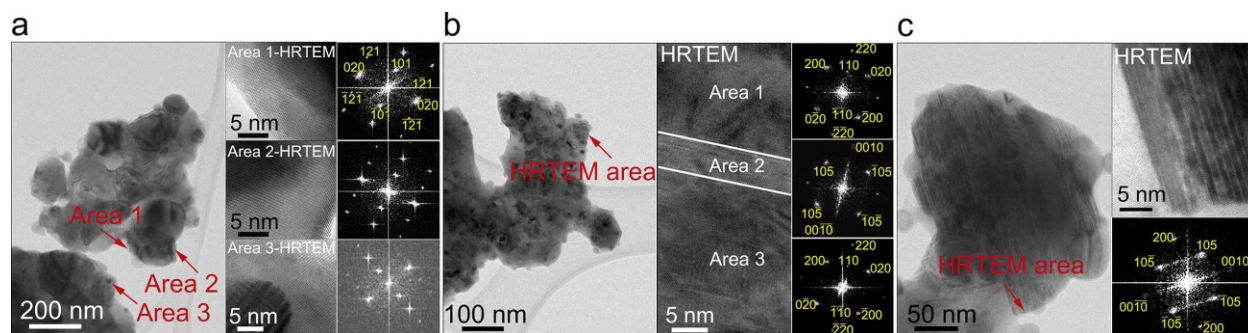


Figure 5.5 High resolution Environmental transmission electron microscope (HRTEM) images and the corresponding electron diffraction patterns of (e) SFN₃M+1.2Fe-red-2h, (f) SFN₃M-red-2h and (g) SFN₃M-red-10h, respectively.

CO₂ surface adsorption on P-eNs with various surface chemical environments.

To validate the significance of structural regulation on the electrocatalytic performance manifestation of P-eNs, we applied all P-eNs in the CO₂ electrolysis process, where CO₂ adsorption is the first and crucial step. We firstly conducted Fourier transforming infrared spectroscopy (FTIR) and CO₂ temperature programmed desorption (CO₂-TPD) experiments on all P-eNs to understand the effect of the phase architecture of perovskite substrate on the surface CO₂ adsorption capacity. [89, 127, 225] The FTIR spectra of all P-eNs at 600 °C show that LP-NPs display the strongest CO₂ chemisorption with a bandwidth of 1300-1550 cm⁻¹ at 600 °C (Figure 5.6a). [89] It is in good agreement with the results from the CO₂-TPD experiments, where LP-NPs exhibit the strongest chemical desorption peak at 550 °C (Figure 5.6b). As the temperature of the CO₂-TPD experiment increases to 850 °C, a more intensive chemical desorption peak with the onset temperature of 760, 655 and 687 °C appears for DP-NPs, DLP-NPs and LP-NPs. It indicates that the surface of DP-NPs is the most favorable for CO₂ adsorption at the operating temperatures above 800 °C. The X-ray photoelectron spectroscopy (XPS) results of O 1s illustrates that the concentration of chemisorbed oxygen species (O₂²⁻/O⁻, at the binding energy of ~531 eV) is the highest for LP-NPs, [185, 247] reaching 72%, followed by DP-NPs with 59% and DLP-NPs with 55% (Figure S5.7 and Table S5.2). It demonstrates that the surface of the LP-NPs features the highest concentration of CO₂ chemisorption sites, which is inconsistent with the CO₂-TPD results. Given the existence of two distinct chemical desorption peaks observed in all CO₂-TPD profiles, we suggested that two CO₂ adsorption scenarios occur on the surface of P-eNs, either on the isolated oxygen vacancies (V_{O}^{\bullet}) or on the V_{O}^{\bullet} adjacent to the exsolved nanoparticles, which have a substantial influence on the CO₂ chemisorption.

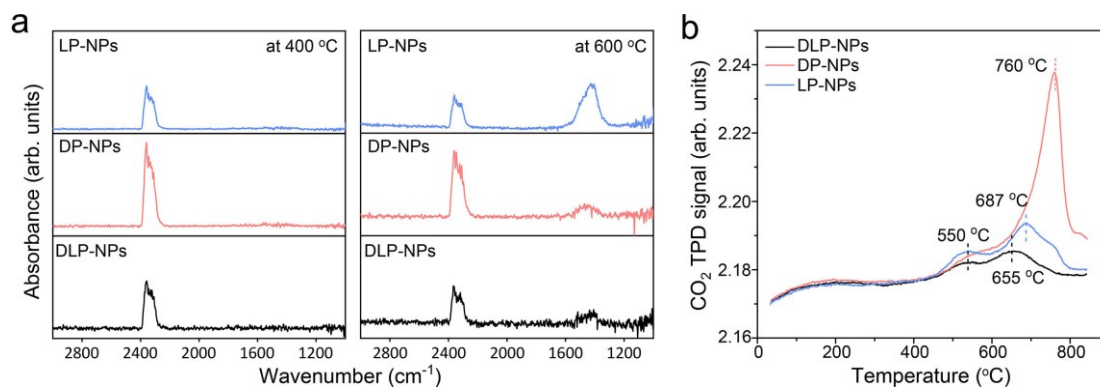


Figure 5.6 FTIR spectra of CO₂ chemisorption and physisorption for DP-NPs, DLP-NPs and LP-NPs at 400 and 600 °C. **b**, CO₂-TPD results of DP-NPs, DLP-NPs and LP-NPs up to 850 °C.

Density functional theory (DFT) was performed to investigate the various CO₂ adsorption scenarios by calculating the CO₂ adsorption energies ($E_{ad.}$). (Figure 5.7a) In the cases of SFM-based DP and LP with the presence of one V_{O}^{\bullet} on the surface (DP- V_{O}^{\bullet} and LP- V_{O}^{\bullet}), the CO₂ adsorption with a bidentate carbonate configuration at the V_{O}^{\bullet} of DP- V_{O}^{\bullet} and LP- V_{O}^{\bullet} is the most stable, the calculated $E_{ad.}$ were -0.64 and -1.12 eV (Figures S5.8 and S5.9), demonstrating that SFN₃M-based LP structure is more favorable for CO₂ chemisorption without exsolution. For the other cases involving exsolved nanoparticles, it shows that the most stable configurations for CO₂ adsorption on all the models exist in the form of the C atom of CO₂ bound with a Fe atom from the Fe-Ni cluster, with an O ion attached to an adjacent V_{O}^{\bullet} of the perovskite substrate (Figure 5.7a and Figure S5.10). DP-NPs model (DP- V_{O}^{\bullet} -F3N1) displays the most robust adsorption, with an $E_{ad.}$ of -2.81 eV, followed by -1.47 eV for LP-NPs model (LP- V_{O}^{\bullet} -F3N2) and finally, -1.04 and 0.54 eV for DLP-NPs models. We can find that the well-preserved DP structure results in a boosted CO₂ adsorption during the evolution of the model from DP- V_{O}^{\bullet} to DP- V_{O}^{\bullet} -F3N1 with increasing Fe content in the nanoparticles (Figure 5.7b). Conversely, during the model evolution

towards LP- $V_{\text{O}}^{\bullet\bullet}$ -F3N2, the phase transition on the DLP-NPs models leads to an increase in $E_{ad.}$ from -1.04 to 0.54 eV, until the Fe/Ni ratio reaches 3:2, where the $E_{ad.}$ of LP- $V_{\text{O}}^{\bullet\bullet}$ -F3N2 becomes slightly negative compared to that of LP- $V_{\text{O}}^{\bullet\bullet}$ (Figure 5.7c). These findings indicate that DP-typed substrate is more favorable for CO₂ adsorption at the $V_{\text{O}}^{\bullet\bullet}$ adjacent to the exsolved nanoparticles compared to the LP-typed substrate.

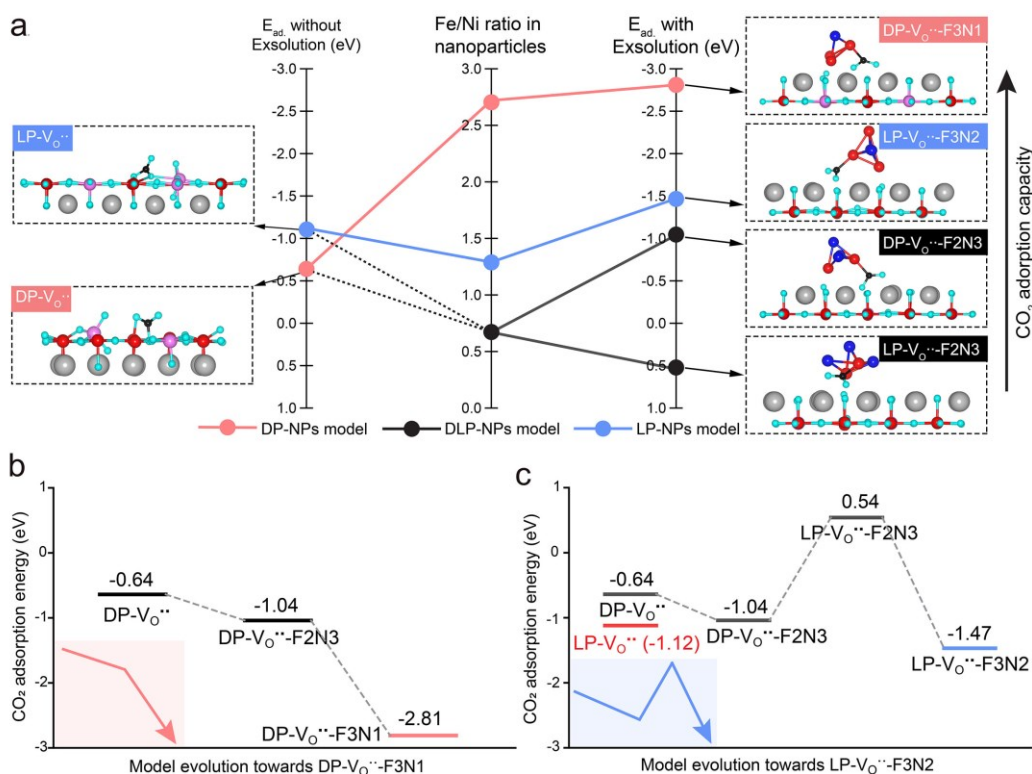


Figure 5.7 (a) DFT-based CO₂ surface adsorption configurations and energies ($E_{ad.}$) on DP- $V_{\text{O}}^{\bullet\bullet}$, LP- $V_{\text{O}}^{\bullet\bullet}$, DP- $V_{\text{O}}^{\bullet\bullet}$ -F2N3, DP- $V_{\text{O}}^{\bullet\bullet}$ -F3N1, LP- $V_{\text{O}}^{\bullet\bullet}$ -F2N3 and LP- $V_{\text{O}}^{\bullet\bullet}$ -F3N2 models, and the Fe/Ni ratio in exsolved nanoparticles. In these DFT models, the grey balls represent Sr atoms, the red balls represent Fe atoms, the dark blue balls represent Ni atoms, the pink balls represent Mo atoms, the light blue balls represent O atoms. Change in $E_{ad.}$ with model evolution toward (b) DP- $V_{\text{O}}^{\bullet\bullet}$ -F3N1 and (c) LP- $V_{\text{O}}^{\bullet\bullet}$ -F3N2.

Unveiling the effects of phase evolution on the electrochemical performances of P-eNs for CO₂ electrolysis over a broad range of voltages.

All P-eNs were mixed with pure oxygen ion conductor Gd-doped ceria (GDC) to fabricate the cathode materials to evaluate their catalytic activities for CO₂ electrolysis at 850 °C. The well-assembled SOECs (P-eNs-GDC|GDC|YSZ|GDC|(La_{0.6}Sr_{0.4})_{0.95}Co_{0.2}Fe_{0.8}O_{3-δ}-GDC) were denoted as P-eNs-GDC for simplicity (Figures S5.11a-c). Figure 5.8a presents the current density-voltage (*j*-V) curves of all SOECs, the order of *j* under identical conditions is as follows: DP-NPs-GDC>DLP-NPs-GDC>LP-NPs-GDC. To track the electrode kinetics as a function of voltage, we extract the polarization resistance (*R_p*) of all SOECs from the electrochemical impedance spectroscopy (EIS) with the equivalent circuit LR(Q_HR_H)(Q_LR_L) (Figure 5.8b, Figure S5.11d and Table S5.3). [248] The smallest *R_p* of DP-NPs-GDC at all monitored voltages confirm that DP-NPs-GDC exhibits the highest catalytic activity over a broad range of voltages. For DLP-NPs-GDC and LP-NPs-GDC with the nearly overlapping EIS curves, 1.4 V appears to be a turning point, where LP-NPs-GDC exhibits the larger *R_p* at or below 1.4 V, while DLP-NPs-GDC demonstrates the larger *R_p* above 1.4 V. It implies that phase evolution regulation also has an impact on other sub-step processes in addition to CO₂ adsorption. The simulated distribution of relaxation times (DRT) results from EIS data illustrate that LP-NPs-GDC exhibits a slightly large integral area of P₂ peak (charge transfer) than DLP-NPs-GDC at all tracked voltages, while the sizes of P₃ peak (CO₂ adsorption and activation) areas switch from DLP-NPs-GDC<LP-NPs-GDC to DLP-NPs-GDC>LP-NPs-GDC when the voltage increases from 1.4 to 1.6 V (Figure 5.8c and Figure S5.12). [139, 224] Considering the better adsorption behavior of LP-NPs than that of DLP-NPs, the smaller P₃ peak of DLP-NPs-GDC below 1.6 V can be ascribed to its superior CO₂ activation performance. Since

electrons are involved in the activation of the surface-absorbed CO₂ during electrolysis, [52] all P-eNs were then subjected to the electronic conductivity tests at 850 °C. As listed in Figure 5.9 and Table S5.4, the electronic conductivities of all P-eNs follow an order of DP-NPs>DLP-NPs>LP-NPs in the atmospheres of 1:1 CO–CO₂ and 2:1 CO–CO₂, substantiating that CO₂ activation on DLP-NPs is easier to proceed than that on LP-NPs. [116, 139] XPS analysis of Fe 2*p* and Mo 3*d* with redox charge couples reveals that the higher electron conductivity of DLP-NPs than that of LP-NPs can be attributed to the more concentrated Fe²⁺-Fe³⁺ charge couples, which acts as the primary electronic pathways bridging the surface-adsorbed CO₂ and SFN₃M perovskite substrate (Figure 5.9, Figure S5.13, Table S5.5). [136, 249] The highest electronic conductivities of DP-NPs can thus be ascribed to both the most concentrated Fe and Mo-related redox charge couples and B-site supplement in the perovskite substrate.

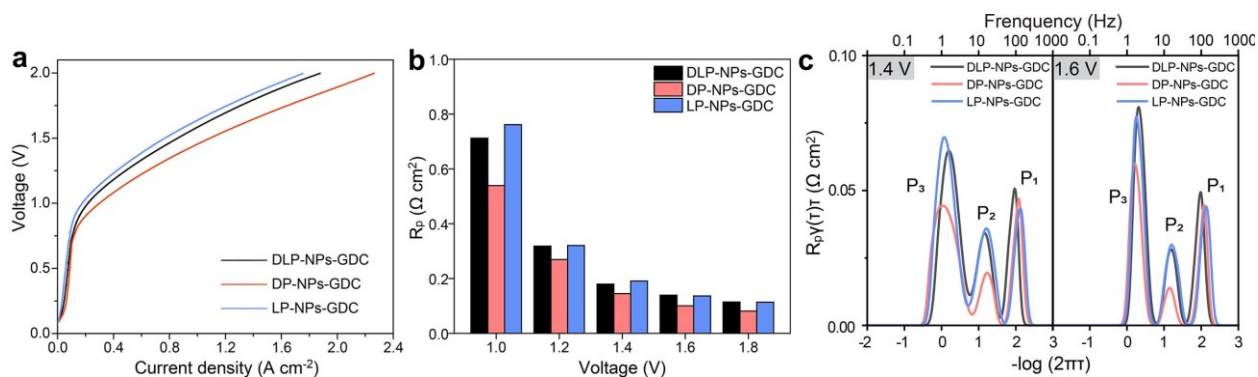


Figure 5.8 (a) Comparison of catalytic activity among all P-eNs-GDC. (a) Current density-voltage curves and (b) EIS results of DP-NPs-GDC, DLP-NPs-GDC and LP-NPs-GDC for pure CO₂ electrolysis at 850 °C. The inset is the equivalent circuit used to simulate the EIS data. (c) DRT results of DP-NPs-GDC, DLP-NPs-GDC and LP-NPs-GDC at 1.4 and 1.6 V.

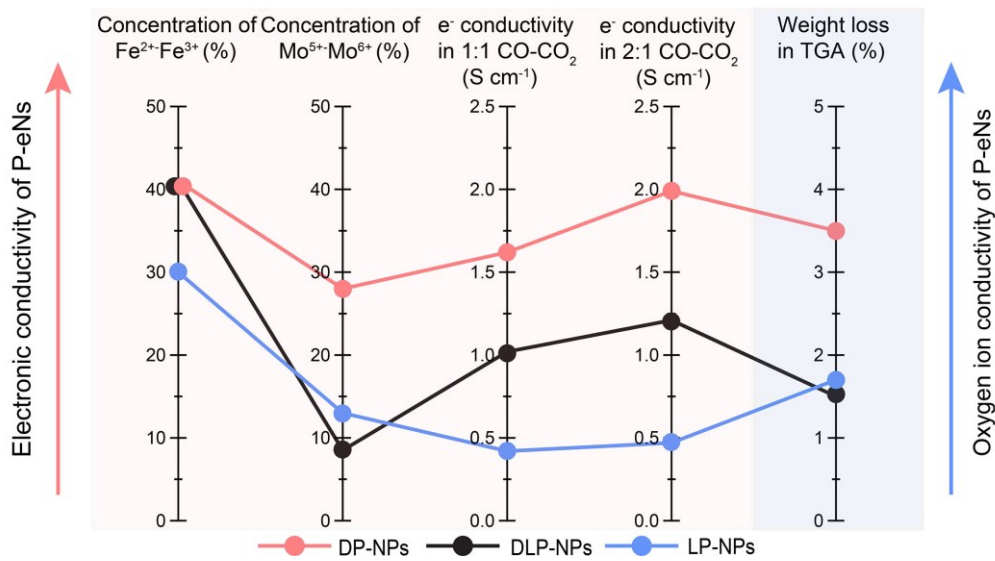


Figure 5.9 Index characterization of charge conduction capability of DP-NPs, DLP-NPs and LP-NPs.

In addition to activating the surface-absorbed CO₂, [52, 145] electrons also participate in the reduction of the surface intermediate to *CO and *O. [52] The resulted CO is then desorbed from the surface, and the oxygen ions occupying $V_{O}^{\bullet\bullet}$ are transported to the anode through a hopping mechanism. [145] This process leaves new $V_{O}^{\bullet\bullet}$ and electrons available to participate in a subsequent round reaction. It is noteworthy that the transfer of oxygen ions, which is more difficult than electron transfer, may have a more pronounced impact on surface relaxation, [250] especially at high voltages. It has been reported that there is negligible difference in oxygen ion migration between SFM-based DP and LP counterpart, [218] the oxygen ion conductivities of all P-eNs catalysts are highly dependent on the concentration of $V_{O}^{\bullet\bullet}$. The thermogravimetric profiles of all P-eNs in a reducing atmosphere containing 5% H₂/95% N₂ reveal that the weight losses of DP-NPs, LP-NPs reach 3.5 wt. % and 1.7 wt. % after heating treatment up to 850 °C, which is higher than the weight loss of 1.5 wt. % observed in DLP-NPs

(Figures 5.9 and S5.14a). It suggests that the perovskite substrate of DLP-NPs has the fewest oxygen ion transfer pathways, which may lead to the slow oxygen penetration, thus resulting in the sluggish surface exchange when a high voltage (≥ 1.6 V) is applied. It well explains the inferior CO_2 surface adsorption and activation behavior of DLP-NPs compared to that of LP-NPs observed in DRT results when a voltage at and above 1.6 V is employed.

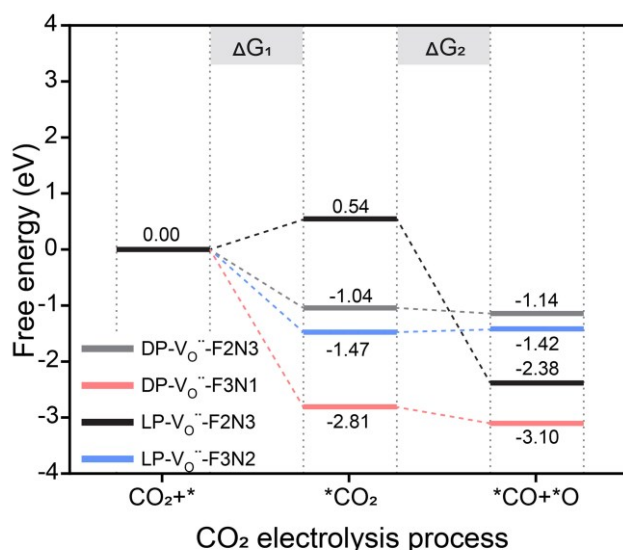


Figure 5.10 Gibbs free energy diagram for CO_2 electrolysis over models DP- V_{O} -F2N3, DP- V_{O} -F3N1, LP- V_{O} -F2N3 and LP- V_{O} -F3N2.

DFT was further performed to elaborate the effects of phase transition on the CO_2 electrolysis on all P-eNs. As depicted in Figure 5.10, the $^*\text{CO}_2$ dissociation proved to be the rate-limiting step for DP- V_{O} -F3N1 and LP- V_{O} -F3N2, with the dissociation energies (ΔG_2) of -0.29 and 0.05 eV, respectively. For DLP-NPs models, we can find that the energy barrier of rate-determining step of DLP-NPs changes from ΔG_2 of -0.1 eV to CO_2 adsorption energy (ΔG_1) of 0.54 eV as the model evolves from DP- V_{O} -F2N3 into LP- V_{O} -F2N3, indicating that the poor CO_2 adsorption resulted

from the phase transition is the thermodynamic limiting factor for CO₂ electrolysis taking place on DLP-NPs. And the DFT results align well with the electrochemical experimental results, demonstrating that DP-NPs exhibit a highest catalytic activity.

Structural stability and degradation mechanism.

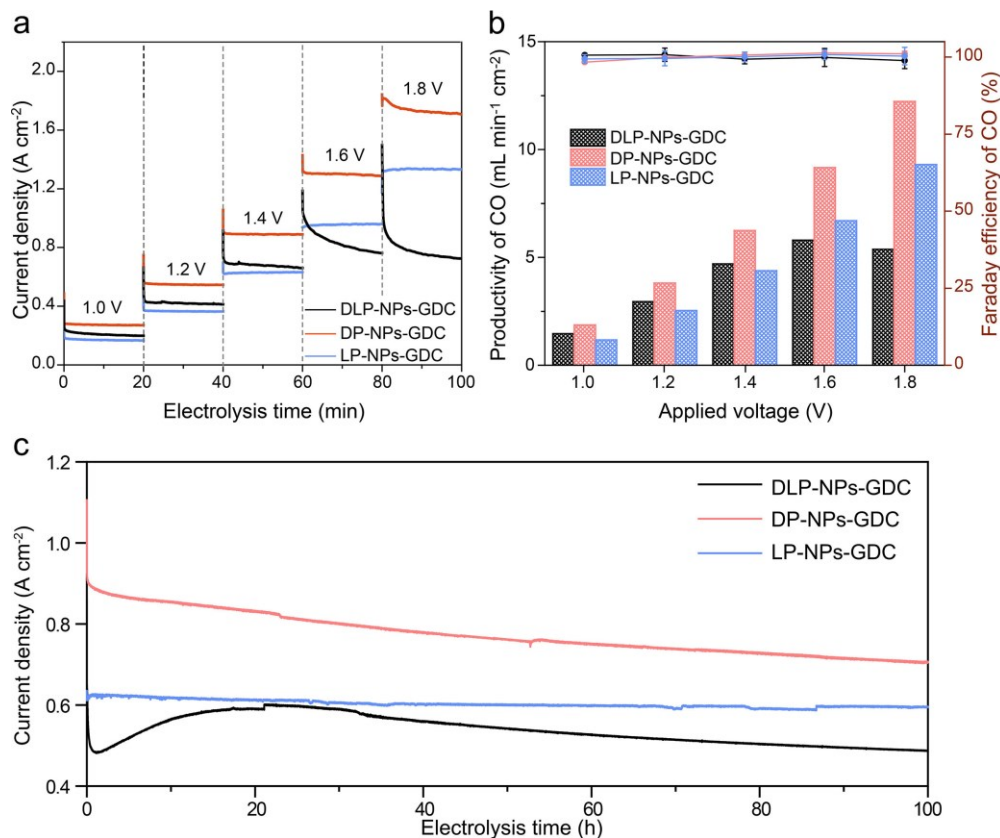


Figure 5.11 Stability performances of all SOECs and indicators of stability of P-eNs. **a,b**, Short-term stability tests. **(a)** The current density response curves for the 20 min potential step chronoamperometry and **(b)** the corresponded CO productivity (histogram) and FE_{CO} (markers) for DP-NPs-GDC, DLP-NPs-GDC and LP-NPs-GDC. **c**, Long-term stability performances of DP-NPs-GDC, DLP-NPs-GDC and LP-NPs-GDC at 1.4 V and 850 °C.

With a comprehensive understanding of the CO₂ electrolysis on various P-eNs, we then delved into the robustness of these P-eNs for CO₂ electrolysis. The 20 min short-term stability test results show that all SOECs display the satisfactory stability at 1.4 V or below (Figure 5.11a), after that, DLP-NPs-GDC undergoes a remarkable decay of j , as opposed to the excellent stability with little attenuation of LP-NPs-GDC and the slight j decay of DP-NPs-GDC. Due to the close-to-100% Faraday efficiency of CO (FE_{CO}) for all SOECs at all examined voltages, the CO productivity of DLP-NPs-GDC reaches its peak at 1.6 V with 5.80 mL min⁻¹ cm⁻², which is lower than 9.17 and 6.71 mL min⁻¹ cm⁻² for DP-NPs-GDC and LP-NPs-GDC under the same conditions (Figure 5.11b). This highlights that a stable operation plays an important role in maintaining high CO yields at high voltages. We continued to investigate the robustness of all SOECs by 100 h long-term CO₂ electrolysis tests at 1.4 V and 850 °C (Figure 5.11c). After excluding the first momentary data points of j obtained from all SOECs, the j of DLP-NPs-GDC, DP-NPs-GDC and LP-NPs-GDC decreased by 32%, 27%, and 7%, with values dropping from 0.7, 0.95, and 0.63 A cm⁻² to 0.48, 0.7, and 0.59 A cm⁻², respectively. Unlike the monotonic decrease in the j -V curves of DP-NPs-GDC and LP-NPs-GDC, DLP-NPs-GDC underwent a “degradation-activation-degradation” process. [177] In particular, the j of DLP-NPs-GDC experiences dramatic decrease in the first hour with a degradation rate of 220 mA cm⁻² h⁻¹, which is remarkably higher than 70 and 10 mA cm⁻² h⁻¹ of DP-NPs-GDC and LP-NPs-GDC (Figure S5.14b). The post-characterization results of the cathode morphology demonstrate that severe coarsening has occurred in the exsolved nanoparticles on all perovskite substrates (Figure S5.14c), thereby ruling out the possibility of exsolved nanoparticle thermal stability dominating the degradation. Meanwhile, repeated local Raman analysis and XRD results reveal the detection of SrMoO₄ and SrCO₃

phases on both DLP and DP electrodes, while only SrMoO₄ phase is present on the LP electrode (Figures S5.14d-e). This observation suggests that perovskite scaffolds undergo varying degrees of decomposition under the synergistic effects of CO₂/CO atmosphere and external voltage. As a result, diverse structural evolution occurs among the three P-eNs, including phase transition and the formation of secondary phases.

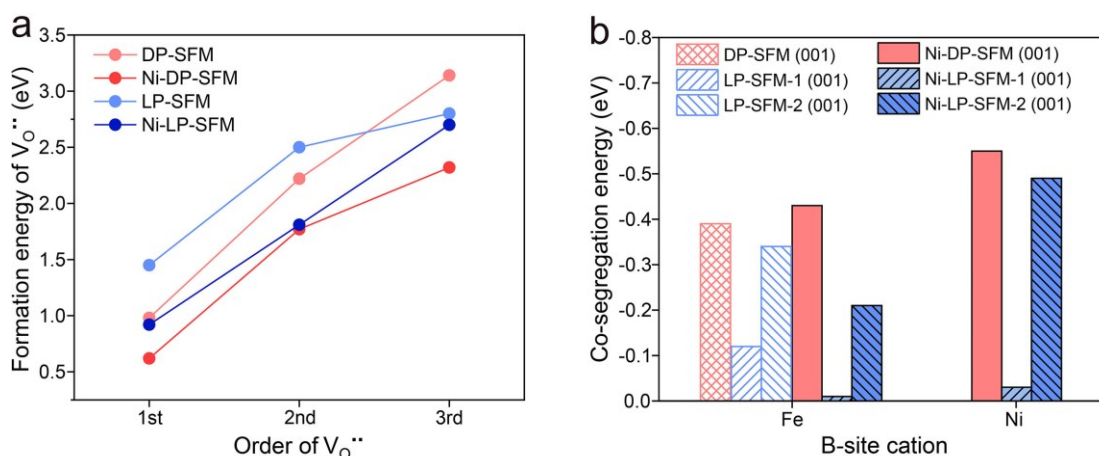


Figure 5.12 (a) Formation energy of first three oxygen vacancies on models DP-SFM, Ni-DP-SFM, LP-SFM and Ni-LP-SFM calculated by DFT. (b) Co-segregation energies of Fe and Ni on slabs DP-SFM (001), Ni-DP-SFM (001), LP-SFM-1 (001), LP-SFM-2 (001), Ni-LP-SFM-1 (001) and Ni-LP-SFM-2 (001) calculated by DFT.

Given the ongoing depletion of lattice oxygen and subsequent removal of reducible cations from the perovskite substrate during the electrolysis, [177, 251] DFT was adopted to examine the structural stability of different perovskite substrates by calculating the formation energy of $V_O^{..}$ ($E_{V_O^{..}}$) and co-segregation energy of reducible cations ($E_{M_{co-seg}}$, where M is donated as B-site cations such as Ni, Fe) (Figures 5.12 and 5.13, Figures S5.15 and S5.16, Tables S5.6 and S5.7).

[102] Based on different structures of substrate and different degrees of reducible Ni exsolution (Figures S5.17), we constructed the DP models with/without Ni doping (Ni-DP-SFM/ DP-SFM) and LP models with/without Ni doping (Ni-LP-SFM/ LP-SFM). Figure 5.12a illustrates that the $E_{V_O^{\bullet}}$ of the first three V_O^{\bullet} of the DP and LP models all show a downward trend after Ni doping, indicative of the detrimental effect of Ni doping on the stability of DP-SFM and LP-SFM. [219] This is also confirmed by the lower $E_{Ni_{co-seg}}$ than $E_{Fe_{co-seg}}$ in Ni-DP-SFM (001) (-0.55 eV < -0.43 eV), Ni-LP-SFM-1 (001) (-0.03 eV < -0.01 eV) and Ni-LP-SFM-2 (001) (-0.49 eV < -0.21 eV) (Figure 5.12b). Furthermore, the $E_{Fe_{co-seg}}$ and $E_{Ni_{co-seg}}$ in Ni-DP-SFM (001) are more negative than that in Ni-LP-SFM-1 (001) and Ni-LP-SFM-2 (001) (Table S5.7). Likewise, the $E_{Fe_{co-seg}}$ in DP-SFM is -0.39 eV, which is more negative than -0.12 eV of LP-SFM-1 and -0.34 eV of LP-SFM-2, demonstrating that the LP structure has the higher resistance to reduction compared to the DP structure. It well elucidates the excellent stability performance of LP at high voltages owing to the perovskite scaffold's predominant composition of LP structure and relatively less residual Ni. However, in DLP-NPs with a composite substrate, the DP part still retains a relatively higher amount of reducible Ni, which can be readily released under the harsh reduction conditions during CO₂ electrolysis, thereby leading to the rapid degradation in the initial stage of the long-term stability test. When the newly born nanoparticles emerge on the surface, the catalytic performance initially shows a recovery, but eventually deteriorates once the surface chemistry reaches equilibrium with the electrolytic environments. In contrast, although DP-NPs still retain almost intact DP structure, the relatively redox-stable Fe cations occupying B-sites significantly reduce the rate of lattice oxygen loss and B-site cation exsolution, resulting in a relatively

milder decline during the initial stages. The agreement between experimental and theoretical calculations suggests that the structural stability of host perovskite itself and the reducibility of B-site cations can serve as the indicators to predict the stability performance of P-eNs under CO₂ electrolysis conditions.

5.3 Conclusions

We have fine-regulated the phase structures of host perovskite and elucidated the effects of phase evolution of perovskite on the CO₂ electrolysis performances of exsolution-facilitated P-eNs by establishing the structural characteristics-electrochemical performances on the SFN₃M-based P-eNs with diverse host perovskite composition. In particular, by implementing B-site supplement strategy, we have broken the trade-off between suppressed phase transition and facilitated exsolution, resulting in the P-eNs with the completely preserved DP structure and promoted exsolution of Fe-Ni nanoparticles. During CO₂ electrolysis, DP-NPs exhibits the highest catalytic activity, whereas LP-NPs demonstrates remarkable stability performance over a broad range of operating voltages. Our experimental and theoretical findings have discovered that the structural regulation of host perovskite plays a crucial role in optimizing the surface chemical environments, strengthening the surface-bulk interaction, thus dominating the cathode kinetics in response to applied voltages and even altering the rate-limiting step. The outputs of this study also emphasize the importance of phase structure and reducibility of the perovskite substrate in preventing P-eNs from decomposing during CO₂ electrolysis, these two factors determine the CO productivity and lifespan across a wide range of voltages. Our approach employs the unique regulation strategies of the perovskite structure and a combined experimental-theoretic method and therefore, is able to offer a roadmap for the rational design

and evaluation of novel exsolution-promoted P-eNs catalysts for a variety of applications and to gain a comprehensive understanding of the reaction mechanisms in P-eNs based catalysts.

5.4 Supporting information

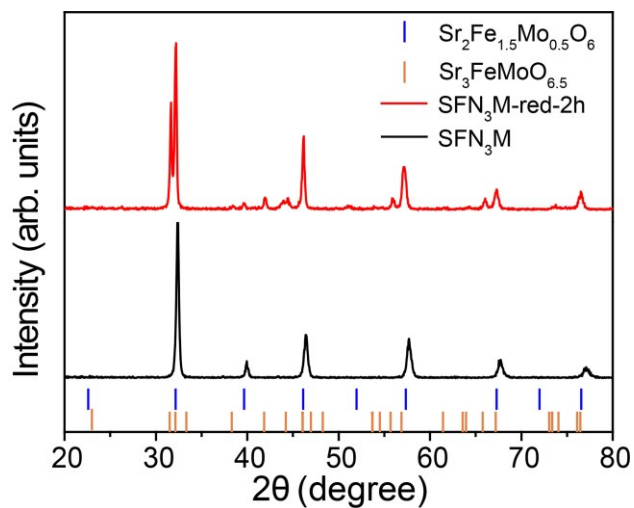


Figure S5.1 XRD results of SFN_3M before and after reduction (SFN_3M and $\text{SFN}_3\text{M-red-2h}$) at 850 °C for 2h.

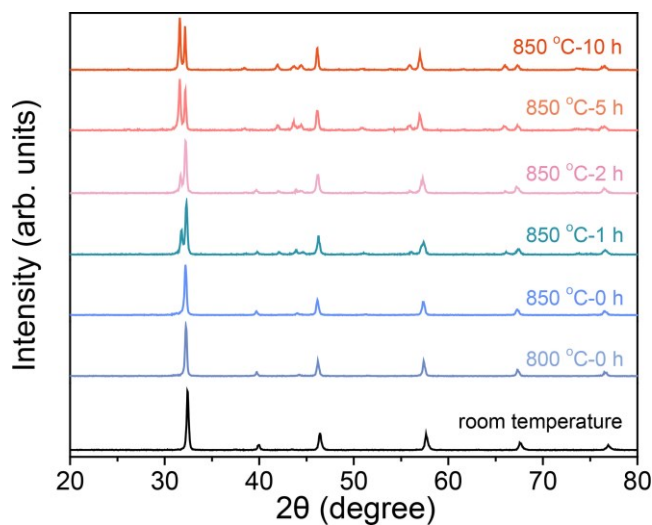


Figure S5.2 Ex situ XRD patterns of SFN_3M after reduction at different temperatures and time.

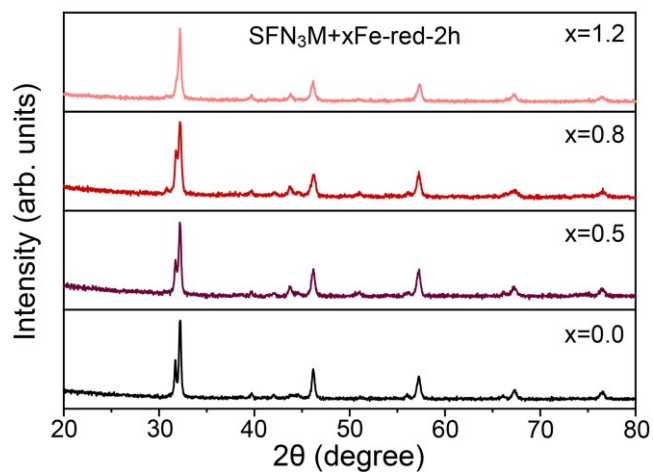


Figure S5.3 XRD patterns of SFN₃M+ x Fe-red-2h, ($x=0.0, 0.5, 0.8, 1.2$, where x is the molar ratio of guest Fe/host Ni).

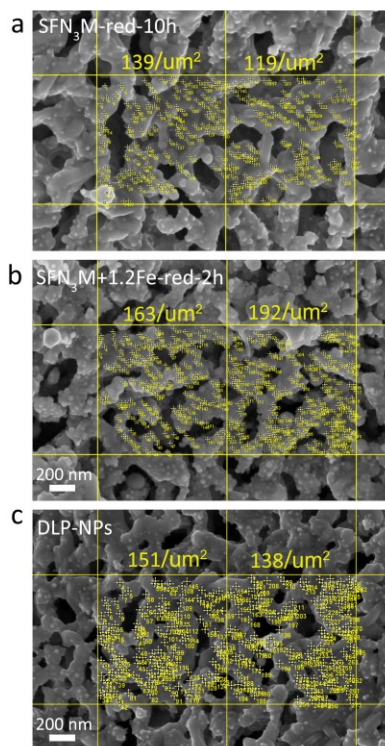


Figure S5.4 Distribution density of the exsolved nanoparticles (number/ μm^2) on (a) DLP-NPs, (b) SFN₃M+1.2Fe-red-2h and (c) SFN₃M-red-10h (It is 1 μm^2 in one yellow box).

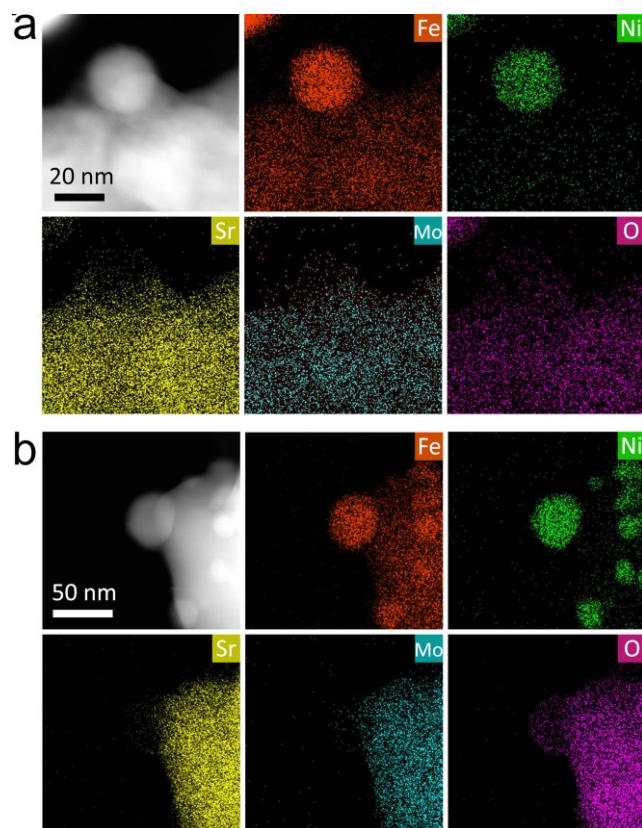


Figure S5.5 STEM-EDS results of (a) SFN₃M+1.2Fe-red-2h and (b) SFN₃M-red-10h.

Table S5.1 Fe and Ni content in randomly selected nanoparticles on DLP-NPs, SFN₃M+1.2Fe-red-2h and SFN₃M-red-10h.

| P-eNs | DLP-NPs | SFN ₃ M+1.2Fe-red | SFN ₃ M-red-10h |
|-------------|---------|------------------------------|----------------------------|
| Fe/Ni ratio | 0.67 | 2.72 | 1.29 |

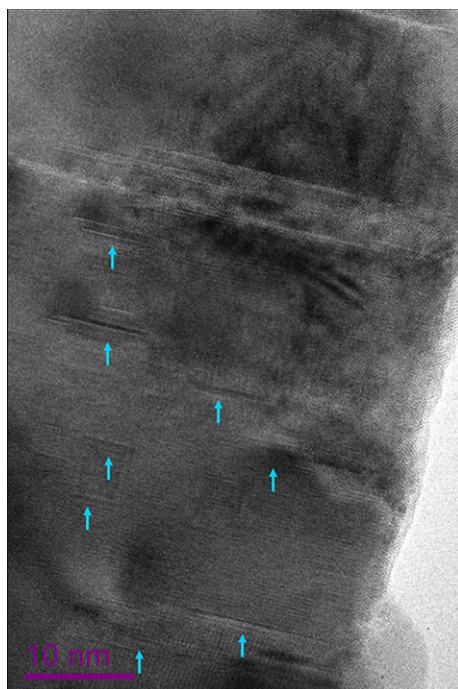


Figure S5.6 Low resolution TEM image of DLP-NPs.

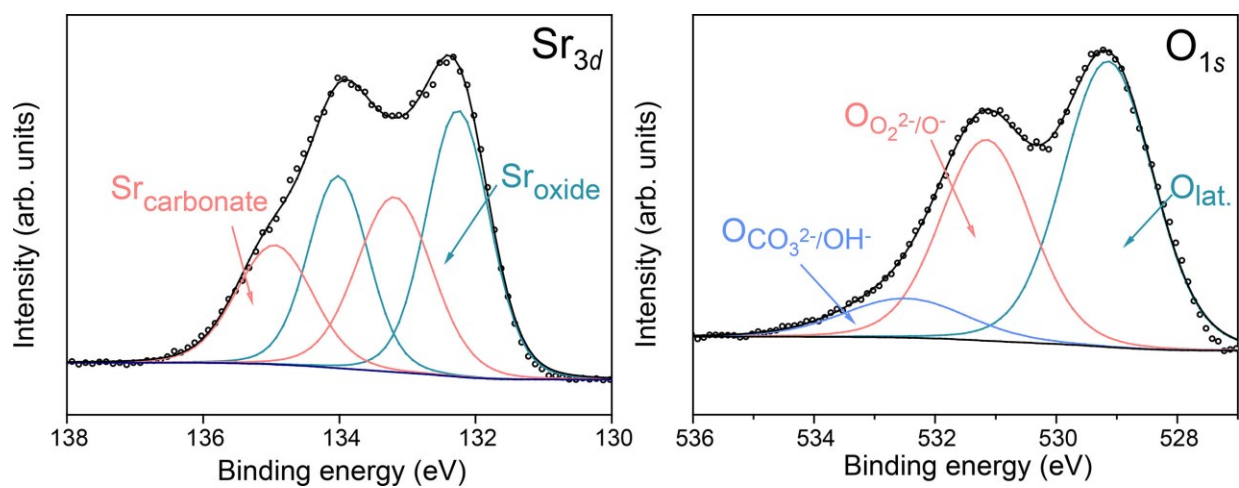


Figure S5.7 XPS of Sr and O of air sintered SFN₃M.

Table S5.2 Relative composition of Sr and O on DLP-NPs, DP-NPs, LP-NPs and SFN₃M calculated from respective XPS spectra.

| Samples | B-site cations | | Sr | | O | |
|--------------------|----------------|------|------|--|--|-----------------|
| | Types | Car. | Oxi. | CO ₃ ²⁻ /OH ⁻ | O ₂ ²⁻ /O ⁻ | O ²⁻ |
| DLP-NPs | | 60% | 40% | 9% | 59% | 32% |
| DP-NPs | | 65% | 35% | 12% | 55% | 33% |
| LP-NPs | | 34% | 66% | 5% | 72% | 23% |
| SFN ₃ M | | 44% | 56% | 10% | 37% | 53% |

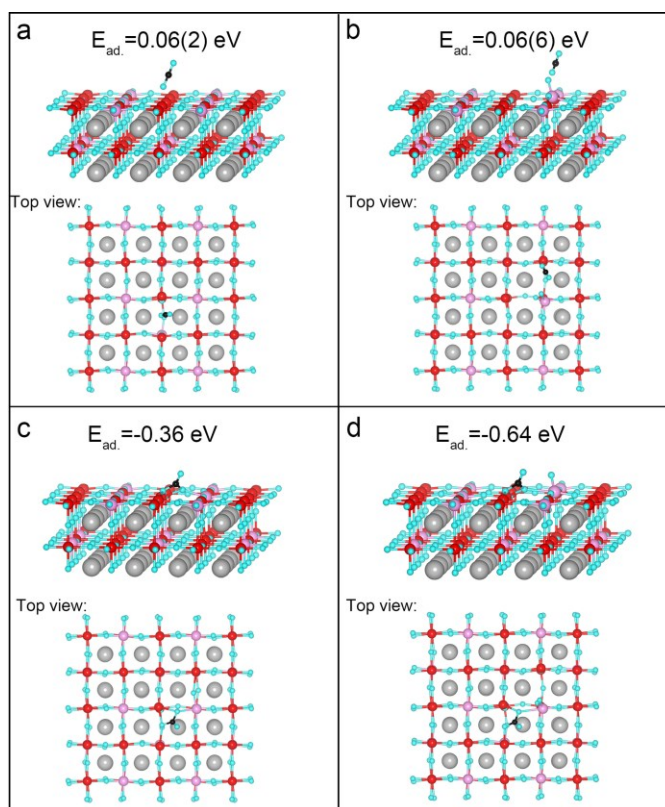


Figure S5.8 CO₂ adsorption configuration on SFM-based DP with existence of one oxygen vacancy on the surface. In these DFT models, the grey balls represent Sr atoms, the red balls represent Fe atoms, the dark blue balls represent Ni atoms, the pink balls represent Mo atoms, the light blue balls represent O atoms.

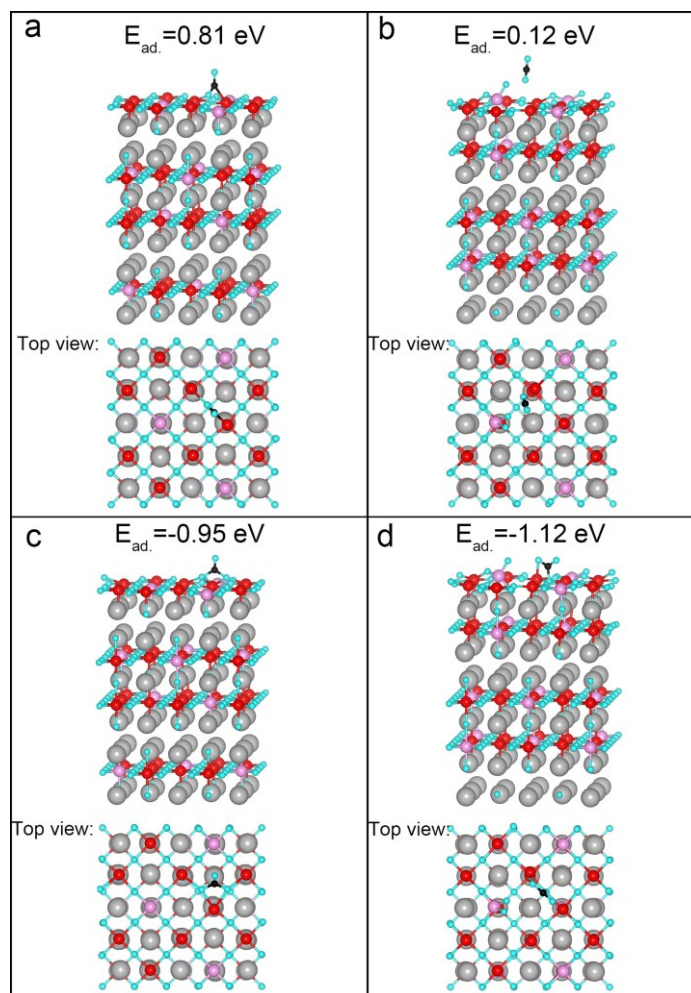


Figure S5.9 CO₂ adsorption configuration on SFM-based LP with existence of one oxygen vacancy on the surface. In these DFT models, the grey balls represent Sr atoms, the red balls represent Fe atoms, the dark blue balls represent Ni atoms, the pink balls represent Mo atoms, the light blue balls represent O atoms.

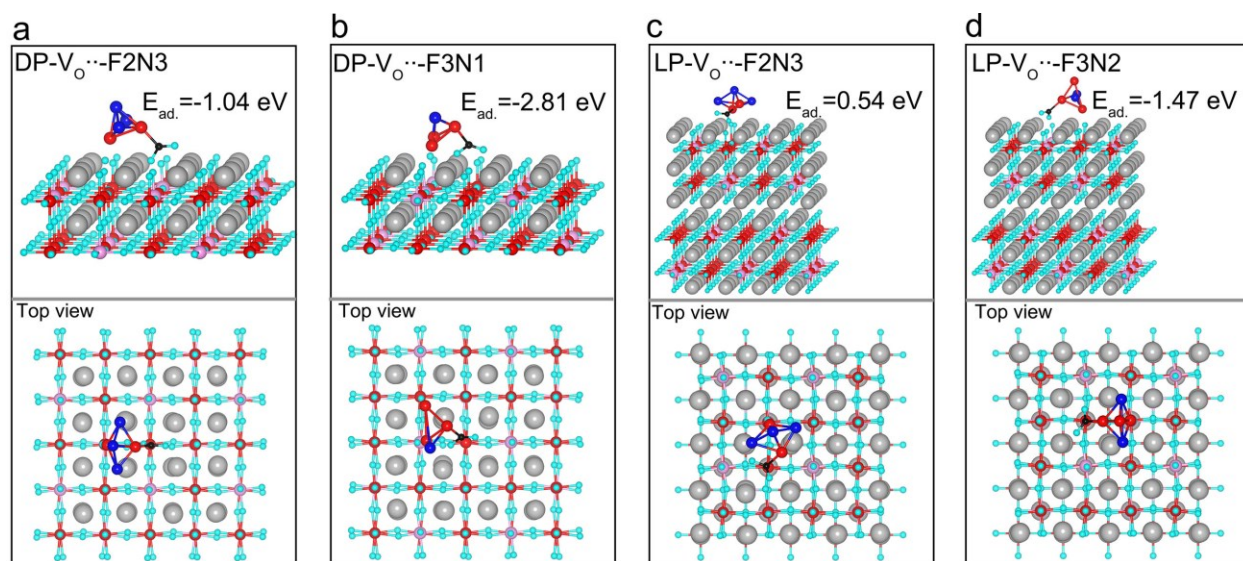


Figure S5.10 DFT-based CO₂ surface adsorption configuration and energies, energetic analysis of CO₂ electrolysis. Most stable CO₂ adsorption configuration on (a) DP-V_O-F2N3, (b) DP-V_O-F3N1, (c) LP-V_O-F2N3 and (d) LP-V_O-F3N2. In these DFT models, the grey balls represent Sr atoms, the red balls represent Fe atoms, the dark blue balls represent Ni atoms, the pink balls represent Mo atoms, the light blue balls represent O atoms.

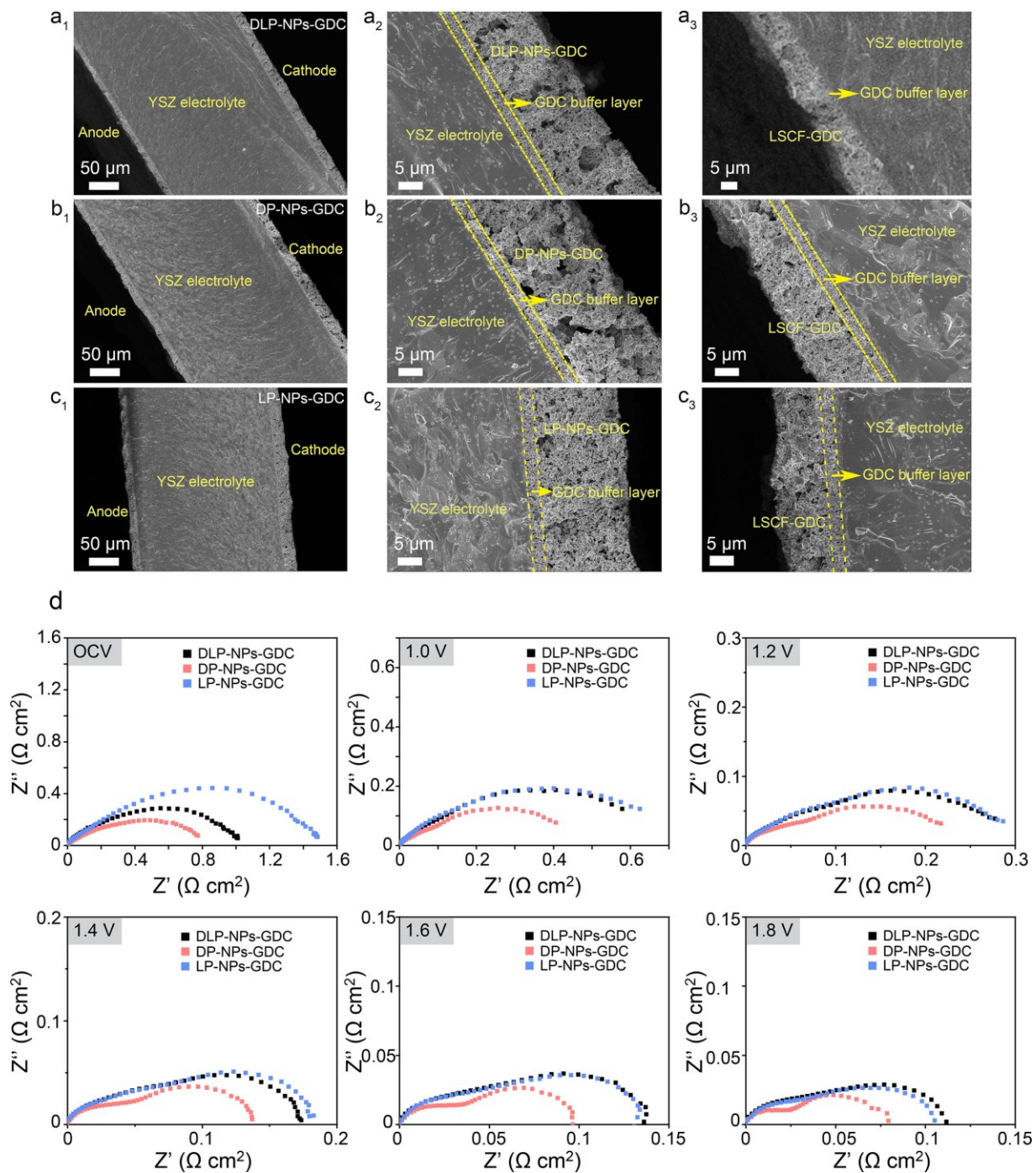


Figure S5.11 (a-c) The cross-sectional button cells (a₁-a₃: DLP-NPs-GDC, b₁-b₃: DP-NPs-GDC, c₁-c₃: LP-NPs-GDC). (d) Electrochemical impedance spectra with subtracting the ohmic resistance part for DP-NPs-GDC, DLP-NPs-GDC and LP-NPs-GDC.

Table S5.3 EIS fitting values of $R_p (=R_H+R_L)$ for DLP-NPs-GDC, DP-NPs-GDC and LP-NPs-GDC.

| Potential (V) | Samples | R_H ($\Omega \text{ cm}^2$) | R_L ($\Omega \text{ cm}^2$) | R_p ($\Omega \text{ cm}^2$) |
|---------------|-------------|---------------------------------|---------------------------------|---------------------------------|
| 1 | DLP-NPs-GDC | 0.02372 | 0.6882 | 0.71192 |
| | DP-NPs-GDC | 0.107 | 0.4324 | 0.5394 |
| | LP-NPs-GDC | 0.04971 | 0.7114 | 0.76111 |
| 1.2 | DLP-NPs-GDC | 0.01823 | 0.3001 | 0.31833 |
| | DP-NPs-GDC | 0.04578 | 0.2236 | 0.26938 |
| | LP-NPs-GDC | 0.05758 | 0.2631 | 0.32068 |
| 1.4 | DLP-NPs-GDC | 0.069 | 0.1106 | 0.1796 |
| | DP-NPs-GDC | 0.06367 | 0.08148 | 0.14515 |
| | LP-NPs-GDC | 0.07214 | 0.119 | 0.19114 |
| 1.6 | DLP-NPs-GDC | 0.06628 | 0.07313 | 0.13941 |
| | DP-NPs-GDC | 0.05156 | 0.04906 | 0.10062 |
| | LP-NPs-GDC | 0.06089 | 0.0754 | 0.13629 |
| 1.8 | DLP-NPs-GDC | 0.05117 | 0.06324 | 0.11441 |
| | DP-NPs-GDC | 0.04538 | 0.03572 | 0.0811 |
| | LP-NPs-GDC | 0.02316 | 0.09059 | 0.11375 |

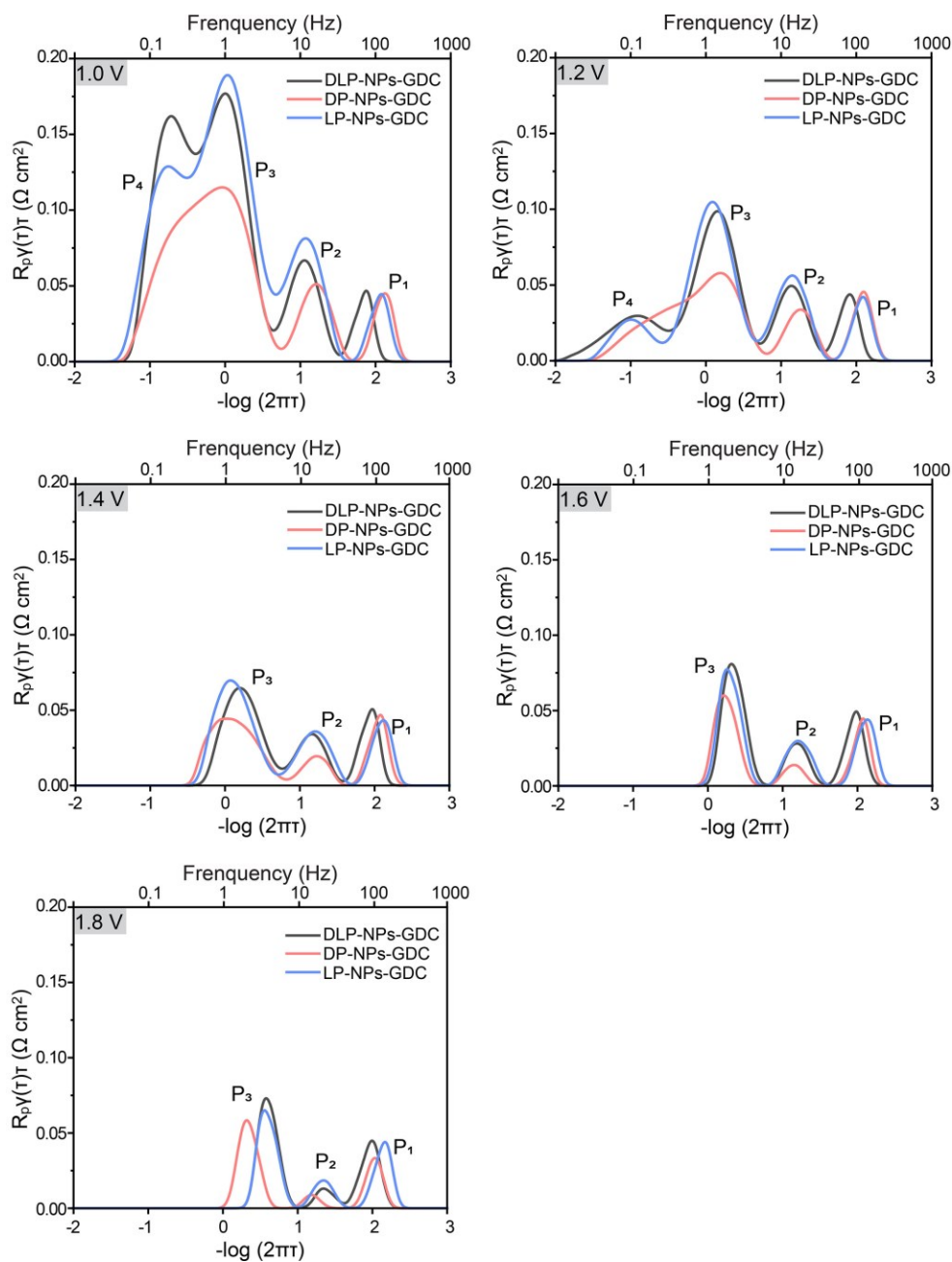


Figure S5.12 DRT results of DP-NPs-GDC, DLP-NPs-GDC and LP-NPs-GDC at 1.0, 1.2, 1.4, 1.6 and 1.8 V (P₁: oxygen ion transfer through electrolyte and oxygen evolution at anode, P₂: charge transfer, P₃: surface CO₂ adsorption and activation, P₄: gas diffusion process at cathode from high to low frequency).

Table S5.4 Electronic conductivities ($S\text{ cm}^{-1}$) of DLP-NPs, DP-NPs and LP-NPs under 1:1 CO–CO₂ and 2:1 CO–CO₂ at 850 °C.

| Atmosphere | DLP-NPs | DP-NPs | LP-NPs |
|------------------------|---------|--------|--------|
| 1:1 CO–CO ₂ | 1.02 | 1.62 | 0.42 |
| 2:1 CO–CO ₂ | 1.21 | 1.99 | 0.47 |

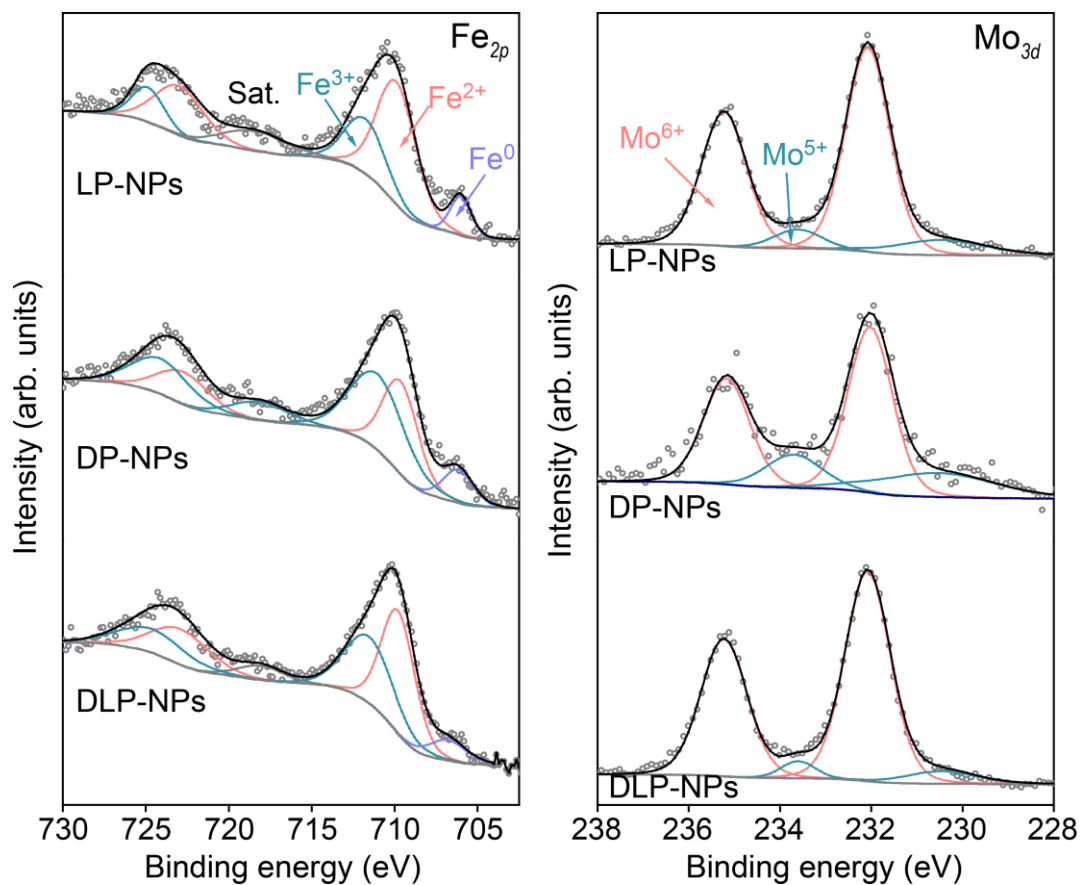


Figure S5.13 XPS of Fe and Mo of DLP-NPs, DP-NPs and LP-NPs.

Table S5.5 Relative composition of Fe and Mo on DLP-NPs, DP-NPs and LP-NPs calculated from respective XPS spectra.

| B-site cations | | Fe | | | Mo | |
|----------------|---------|----|-----|-----|------|-------|
| Valence states | | 0 | +2 | +3 | +5 | +6 |
| | DLP-NPs | 7% | 52% | 41% | 8.5% | 91.5% |
| Samples | DP-NPs | 8% | 41% | 51% | 28% | 72% |
| | LP-NPs | 7% | 63% | 30% | 13% | 87% |

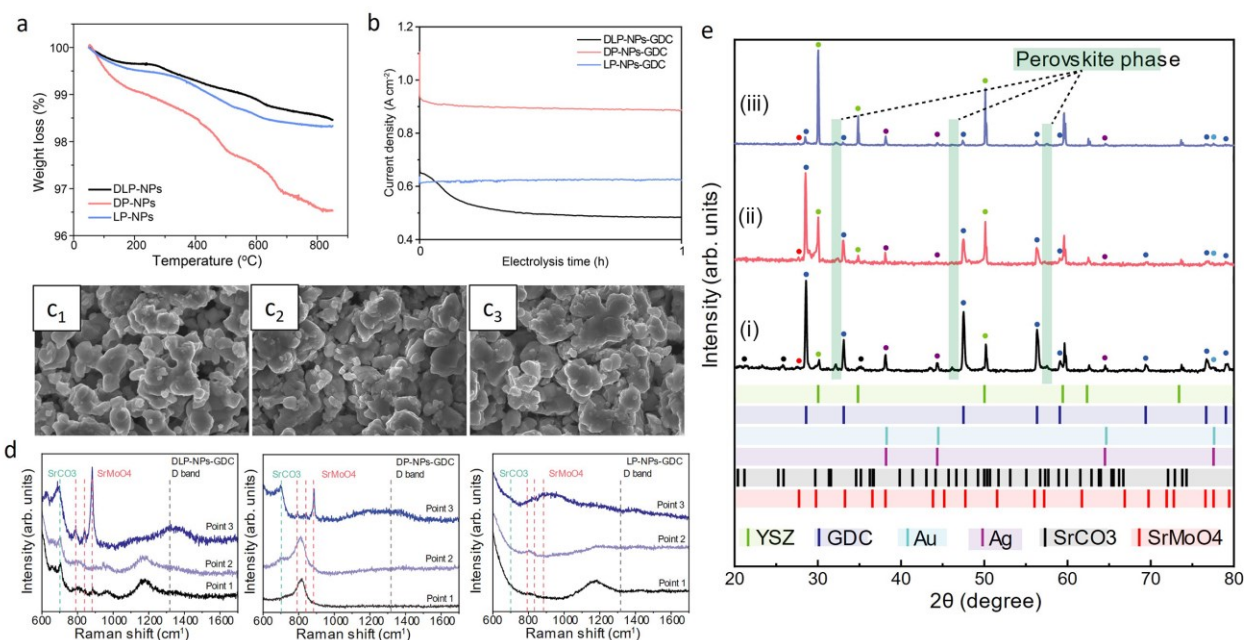


Figure S5.14 (a) TGA profiles of DP-NPs, DLP-NPs and LP-NPs. (b) Long-term stability performances (first hour) of DP-NPs-GDC, DLP-NPs-GDC and LP-NPs-GDC at 1.4 V and 850 °C. (c) SEM images of cathode surface microstructure of (c₁) DLP-NPs-GDC, (c₂) DP-NPs-GDC and (c₃) LP-NPs-GDC after long-term stability. (d) Repeated Raman results and (e) XRD results of cathode of (i) DLP-NPs-GDC, (ii) DP-NPs-GDC and (iii) LP-NPs-GDC after long-term stability.

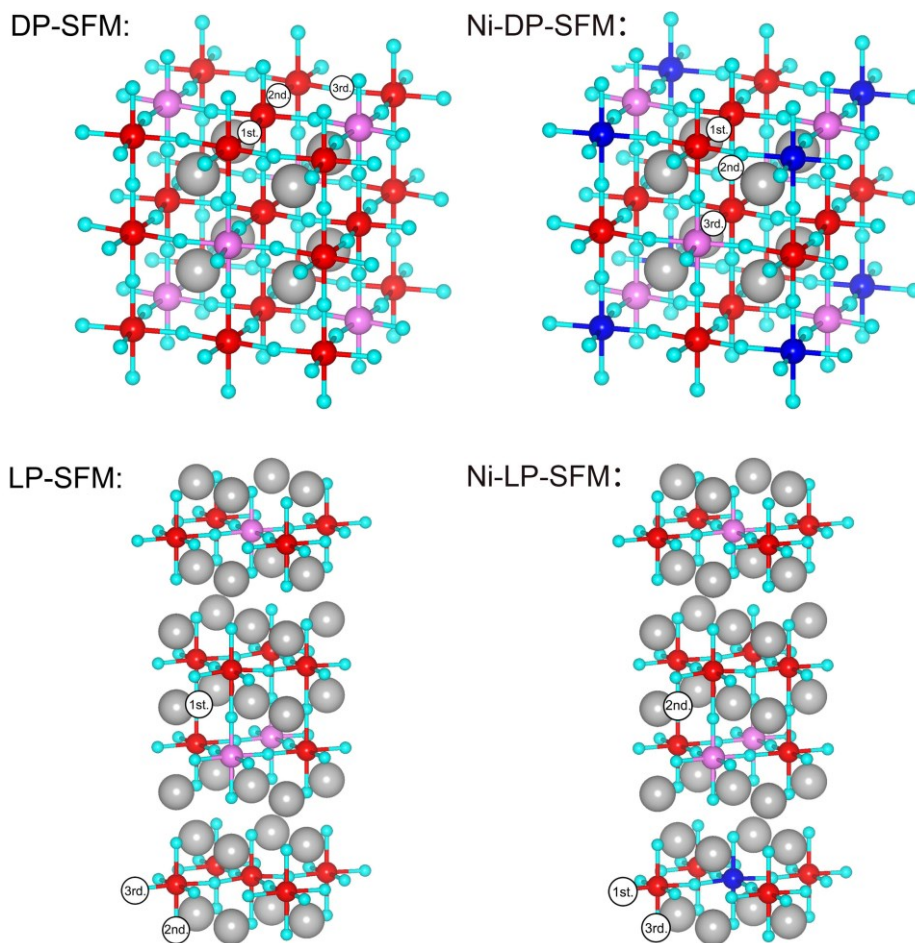


Figure S5.15 The most stable oxygen vacancy formation sites during the sequential formations of oxygen vacancy in the DP-SFM, Ni-DP-SFM, LP-SFM and Ni-LP-SFM models. In these DFT models, grey balls represent Sr atoms, red balls represent Fe atoms, dark blue balls represent Ni atoms, pink balls represent Mo atoms, light blue balls represent O atoms, the white balls represent oxygen vacancies, the 1st, 2nd, 3rd in the white balls represent the order in which the three oxygen vacancies are formed in these models.

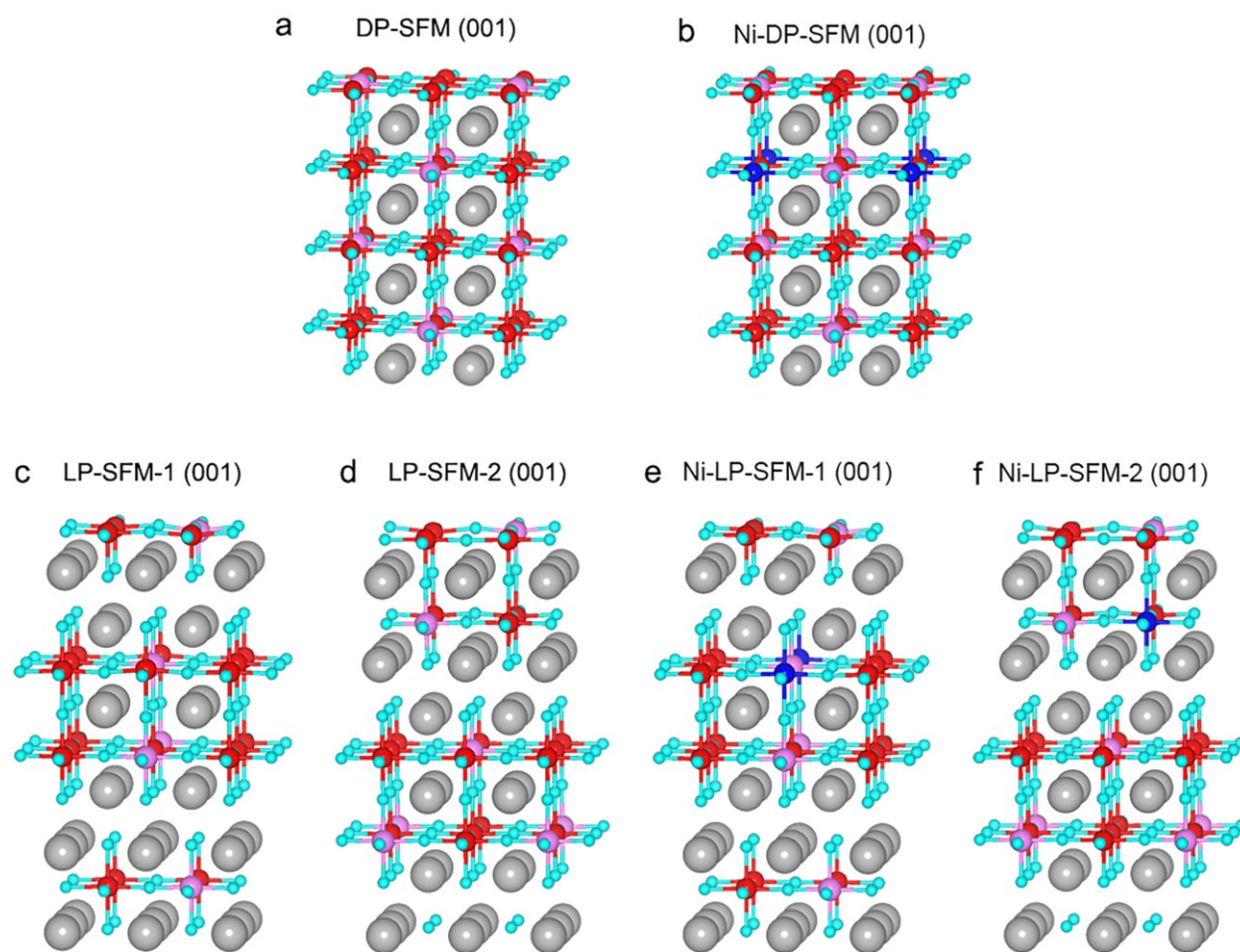


Figure S5.16 DP-based models and LP-based models for calculation of co-segregation energy.

The eight-layer metal-terminated (a) DP-SFM (001) and (b) Ni-DP-SFM (001) slabs based on the DP-Sr₈Fe₆Mo₂O₂₄ and DP-Sr₈Fe₅Ni₁Mo₂O₂₄ unit cells. The metal-terminated (c) LP-SFM-1 (001), (d) LP-SFM-2 (001), (e) Ni-LP-SFM-1 (001) and (f) Ni-LP-SFM-2 (001) slabs based on the LP-Sr₂₄Fe₁₂Mo₄O₅₆ and LP-Sr₂₄Fe₁₁Ni₁Mo₄O₅₆ unit cells. In these DFT models, the grey balls represent Sr atoms, the red balls represent Fe atoms, the dark blue balls represent Ni atoms, the pink balls represent Mo atoms, the light blue balls represent O atoms.

Table S5.6 Formation energy of oxygen vacancy (E_{V_O}) on models DP-SFM, DP-SFNM, LP-SFM and LP-SFNM.

| Models | 1st V_O | 2nd V_O | 3rd V_O |
|---------|-----------|-----------|-----------|
| DP-SFM | 0.98 | 2.22 | 3.14 |
| DP-SFNM | 0.62 | 1.77 | 2.32 |
| LP-SFM | 1.45 | 2.50 | 2.80 |
| LP-SFNM | 0.92 | 1.81 | 2.70 |

Table S5.7 Co-segregation energy of Fe and Ni ($E_{M_{co-seg}}$, where M is donated as B-site cations such as Ni, Fe) on slabs DP-SFM (001), LP-SFM-1 (001), LP-SFM-2 (001), DP-SFNM (001), LP-SFNM-1 (001) and LP-SFNM-2 (001).

| Models | Fe | Ni |
|-----------------|--------------|--------------|
| DP-SFM (001) | -0.39 | / |
| LP-SFM-1 (001) | -0.12 | / |
| LP-SFM-2 (001) | -0.34 | / |
| DP-SFNM (001) | -0.43 | -0.55 |
| LP-SFNM-1 (001) | -0.01 | -0.03 |
| LP-SFNM-2 (001) | -0.21 | -0.49 |

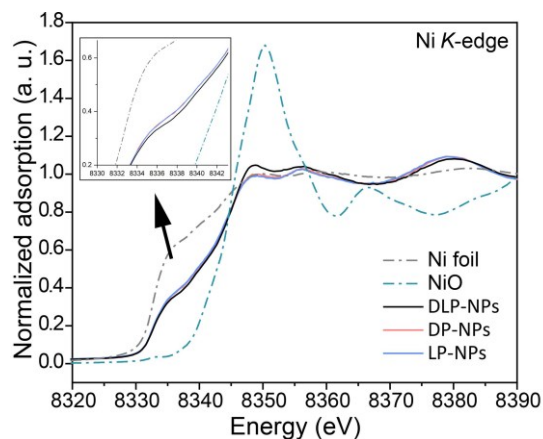


Figure S5.17 XANES results of DP-NPs, DLP-NPs and LP-NPs.

Chapter 6. Fluorine-stabilized BO_6 octahedron of host perovskites for robust CO_2 electrolysis on exsolved catalysts

6.1 Introduction

The significant enhancement in the catalytic activity of perovskites through *in-situ* exsolution technique has stimulated extensive studies to promote the exsolution of nanoparticles. [159, 170, 174, 183] Although the increased surface nanoparticles and oxygen vacancies significantly extend the TPB, [102, 184, 252, 253] it should also be pointed out that the facilitated process is at the cost of consuming the host perovskite, which accelerates A-site surface segregation, formation of B-site vacancies, and even phase reconstruction of host perovskite in the extreme case of promoting exsolution. [238, 242, 254, 255]

Taking the advantage of the phase evolution of the host perovskite during exsolution process, the P-eNs containing an optimized perovskite scaffold can be obtained by one-step *in-situ* reducing the pristine perovskite, thus facilitating the electrode kinetics. [105, 107, 241, 256] For example, the double perovskite $\text{PrBaMn}_{1.8}\text{Co}_{0.2}\text{O}_{4.99}$ with the higher oxygen ion conductivity can be formed accompanied with the exsolution of Co nanoparticles by one-step reducing simple perovskite $\text{Pr}_{0.5}\text{Ba}_{0.5}\text{Mn}_{0.9}\text{Co}_{0.1}\text{O}_{2.89}$, leading to the enhanced catalytic activity for CO_2 electrolysis. [167] However, for the cases where the pristine perovskites exhibit noticeably superior characteristics compared to their derived counterparts, the occurrence of the phase transition may undermine the catalytic performance. Typically, the double perovskite

$\text{Sr}_2\text{Fe}_{1.5}\text{Mo}_{0.5}\text{O}_{6-\delta}$, known for its good redox stability and catalytic activity, represents a prime illustration of a perovskite that holds more potential than its derived Ruddlesden-Popper structure. [257-259] Nonetheless, the potential negative impact of phase transition on catalytic performances is often overlooked in light of the overall performance enhancement from exsolution. [230, 260] Therefore, there is still ample opportunity for further improvement in reactivity by regulating exsolution process. In addition, we also need to acknowledge that the resistance of pristine perovskites to phase transition during exsolution can be considered as an indicator of their structural stability. Perovskites that exhibit greater susceptibility to phase transition during pre-reducing treatment may suggest that the initial structure is unstable, which is a great challenge for long-term stability in harsh reducing operating conditions. [177, 219, 251]

To address the aforementioned issues, it is imperative to boost the structural stability of such perovskites and enhance their resistance to unfavorable phase evolution and decomposition under reducing conditions. Based on the great promise of doping strategy in perovskites, a large number of work have concluded that the enhanced structural stability can be achieved by B-site substitution with highly redox-stable dopants, [127, 136, 200, 261] however, these stable B-site dopants inevitably occupy the active sites and possibly exhibit relatively passivating properties, eventually resulting in a trade-off between catalytic activity and stability. [262] Inspired by the studies on modifying the structures and properties of perovskites through O-site doping strategy that do not affect the occupation of B-site active sites, [139, 144, 145, 263] we speculate that the highly electronegative F anion can maintain the high oxidation state of the B-site cations, [263, 264] thereby enhancing the resistance of BO_6 octahedron to decomposition

under reducing conditions. Furthermore, F^- possesses an ionic radius similar to that of O^{2-} , [143, 265] so that a certain amount of F anions can occupy O-sites of perovskites, making this strategy applicable to a wide range of perovskite materials.

In this study, we demonstrate that the facile F doping strategy can suppress the phase transition of $Sr_2Fe_{1.2}Ni_{0.3}Mo_{0.5}O_{6-\delta}$ (SFN₃M) during pre-reduction treatment, and significantly enhance the robustness of the reduced SFN₃M with F doping (F-SFN₃M-red) for CO₂ electrolysis. Our experimental and theoretical findings reveal that the structural robustness of BO₆ octahedron can be improved by the partial substitution of O with F anions, thus inhibiting exsolution and phase transition. As a result, the surface of F-SFN₃M-red with the well-preserved double perovskite (DP) structure exhibits the stronger interactions with CO₂ in comparison to the partially reconstructed surface of the reduced SFN₃M (SFN₃M-red), which leads to the facilitated cathode kinetics. Furthermore, F-SFN₃M-red shows superior electrolytic stability than SFN₃M-red, especially at high voltages (≥ 1.4 V). This results in a continuous increase in CO productivity as a function of voltage. In contrast, SFN₃M-red experiences a significant decline in CO productivity at 1.8 V due to the phase decomposition under harsh reducing conditions. These findings highlight that F-doping strategy can aid in designing the P-eNs with high catalytic activity and stability for a wider range of operating conditions and catalytic reactions.

6.2 Results and discussion

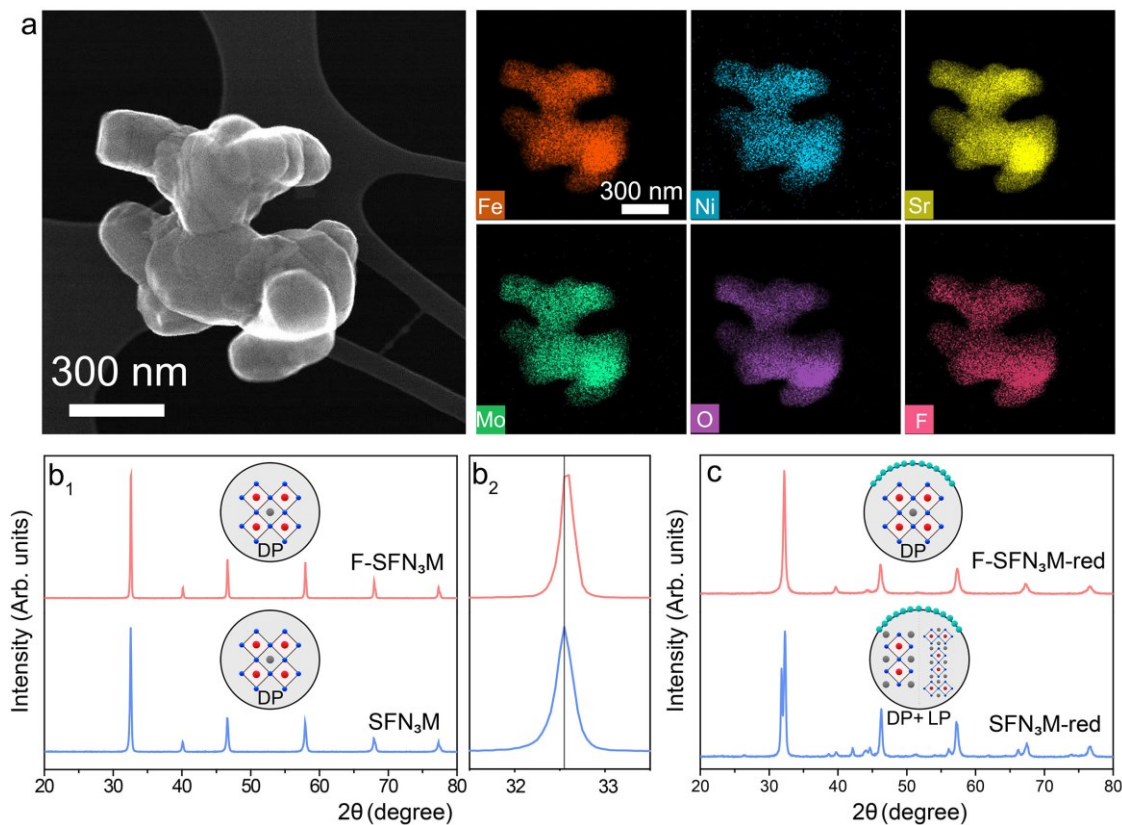


Figure 6.1 (a) Secondary electron-scanning transmission electron microscopy (SE-STEM) and STEM with energy-dispersive X-ray spectroscopy (STEM-EDS) results of F-SFN₃M. (b₁-b₂) XRD patterns of air-sintered SFN₃M and F-SFN₃M. (c) XRD patterns of SFN₃M-red and F-SFN₃M-red. (In the 2D models, the grey balls represent Sr/F atoms, the red balls represent Fe/Ni/Mo atoms, the blue balls represent O atoms, the light blue balls represent Fe-Ni nanoparticles).

Inhibition of phase transition by F doping. SFN₃M and F-doped SFN₃M (F-SFN₃M) was prepared by a sol-gel synthesis process, [194] followed by sintering in air. The external fluorine source was introduced by incorporating FeF₃ into the nitrate solvents in preparation of complexing agent. Using the secondary electron-scanning transmission electron microscopy (SE-STEM) and

STEM with energy-dispersive X-ray spectroscopy (STEM-EDS), we confirmed the uniform distribution of F anion throughout the SFN₃M perovskite matrix (Figure 6.1a). [144] Figure 6.1b₁ illustrates that the X-ray diffraction (XRD) patterns of both sintered samples match well with the DP-typed Sr₂FeMoO₆ (SFM) (PDF#00-060-0459) without any discernible second phase. The magnified diffraction peak at about 32° of F-SFN₃M shifts slightly to a higher angle with regard to SFN₃M (Figure 6.1b₂), indicative of the lattice shrinkage. It may be ascribed to the partial substitution of O anion (1.40 Å) with the smaller-sized F anion (1.33 Å), providing evidence of successful F doping into the SFN₃M lattice. [144, 266]

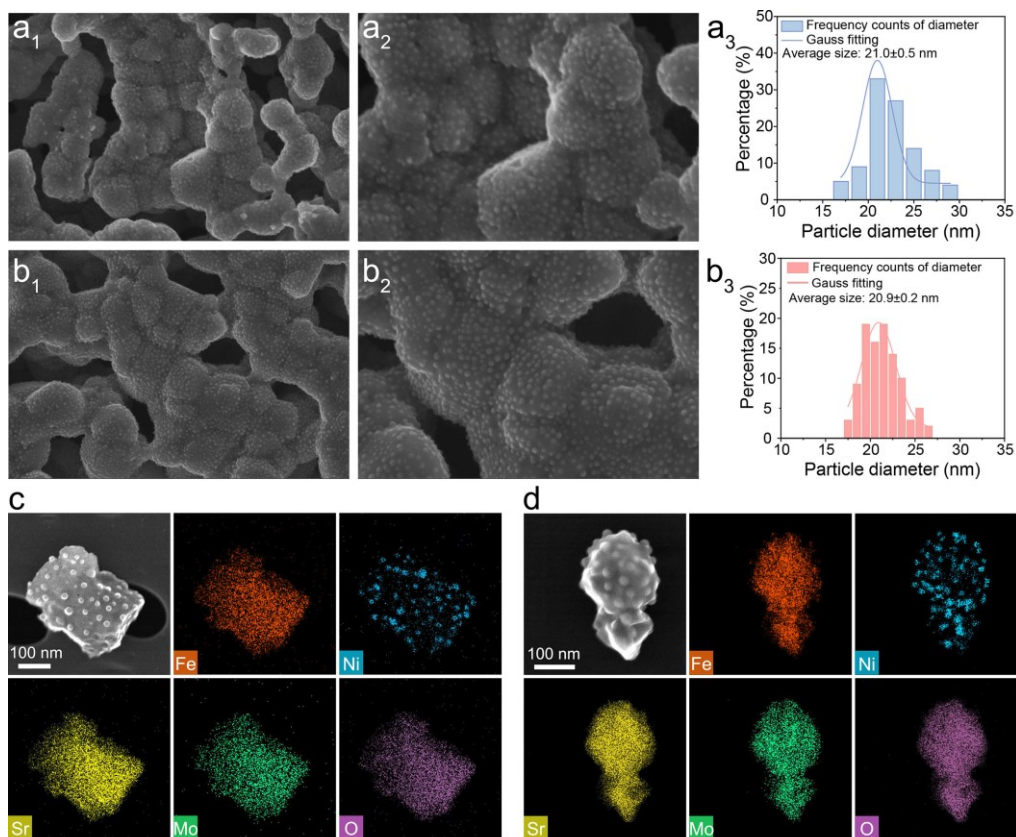


Figure 6.2 SEM images and size distribution histograms of the exsolved nanoparticles on (a₁-a₃) SFN₃M-red and (b₁-b₃) F-SFN₃M-red. STEM-EDS results of (c) SFN₃M-red and (d) F-SFN₃M-red.

To verify the capability of F doping to boost the structural robustness of SFN₃M, the as-prepared SFN₃M and F-SFN₃M were treated in a reducing condition containing 5% H₂/N₂ atmosphere at 850 °C for 2h. As shown in Figure 6.1c, a layered perovskite-typed (LP-typed) Sr₃FeMoO_{6.5} (PDF#00-052-1715) appears on the XRD pattern of SFN₃M-red. By contrast, only the pristine DP structure can be observed on the XRD pattern of F-SFN₃M-red. By tracking the structural evolutions of SFN₃M and F-SFN₃M throughout the reducing treatment (Figure S6.1), we identified that the pristine phase structures have been well-preserved on both samples when the temperature increases to 850 °C. However, SFN₃M undergoes a phase transformation toward LP structure following a 1 h reducing treatment at 850 °C, whereas the initial DP structure of F-SFN₃M remains unchanged. This suggests that the partial replacement of O with F contributes to the phase stabilization of the host perovskite under reducing conditions.

Insights into the enhanced structural stability of F-SFN₃M-red. The surface morphologies of exsolved nanoparticles on SFN₃M-red and F-SFN₃M-red were subsequently examined by field emission-scanning electron microscopy (FE-SEM). As can be seen from Figures 6.2a-b, the nanoparticles on both samples exhibit a uniform distribution and display a comparable size distribution in the range of 10-30 nm, with an average size of approximately 21 nm. Upon closer examination of individual nanoparticles using STEM-EDS, it is evident that the exsolved nanoparticles on both substrates are comprised of Fe and Ni (Figures 6.2c-d and S6.2).

Further analyses of the surface electronic structures of both P-eNs using X-ray photoelectron spectroscopy (XPS) reveal that the proportions of metallic Fe and Ni on the surface of SFN₃M-red are 8% and 38%, which are higher than 7% and 23% of F-SFN₃M-red, respectively (Figures

6.3a-b and Table S6.1). It suggests that the stripping amounts of reducible Fe and Ni cations in F-SFN₃M-red have been significantly reduced by F doping, below the threshold that triggers the structure collapse and reconstruction of the host perovskite. In addition, we have noticed that F-SFN₃M-red contains higher proportions of Fe and Mo in their higher oxidation states (+3 and +6) compared to SFN₃M-red (Figures 6.3b-c). Specifically, 56% of Fe³⁺ and 92% of Mo⁶⁺ exist in the host perovskite of F-SFN₃M-red, while in that of SFN₃M-red, the corresponding proportions are 44% and 90%, respectively (Table S6.1). It implies that the F anion in SFN₃M perovskite lattice is capable of maintaining the high valence state of B-site cations, thus enhancing the redox stability of F-SFN₃M-red.

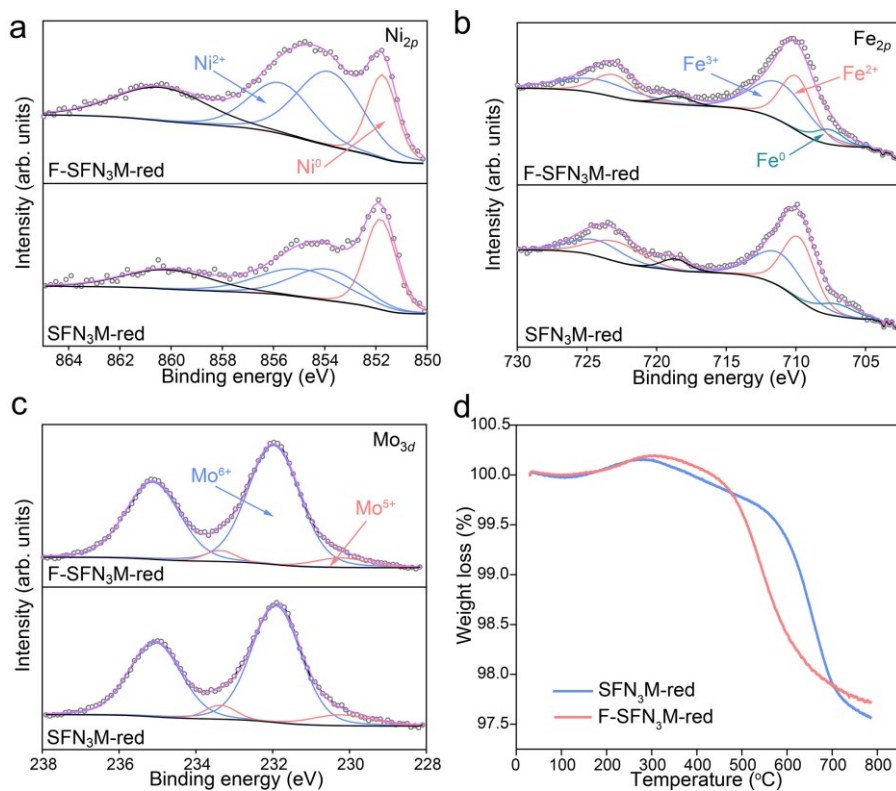


Figure 6.3 XPS of (a) Ni 2p, (b) Fe 2p, (c) Mo 3d for SFN₃M-red and F-SFN₃M-red. (d) TGA profiles of SFN₃M-red and F-SFN₃M-red in the 5% H₂/95% N₂ atmosphere.

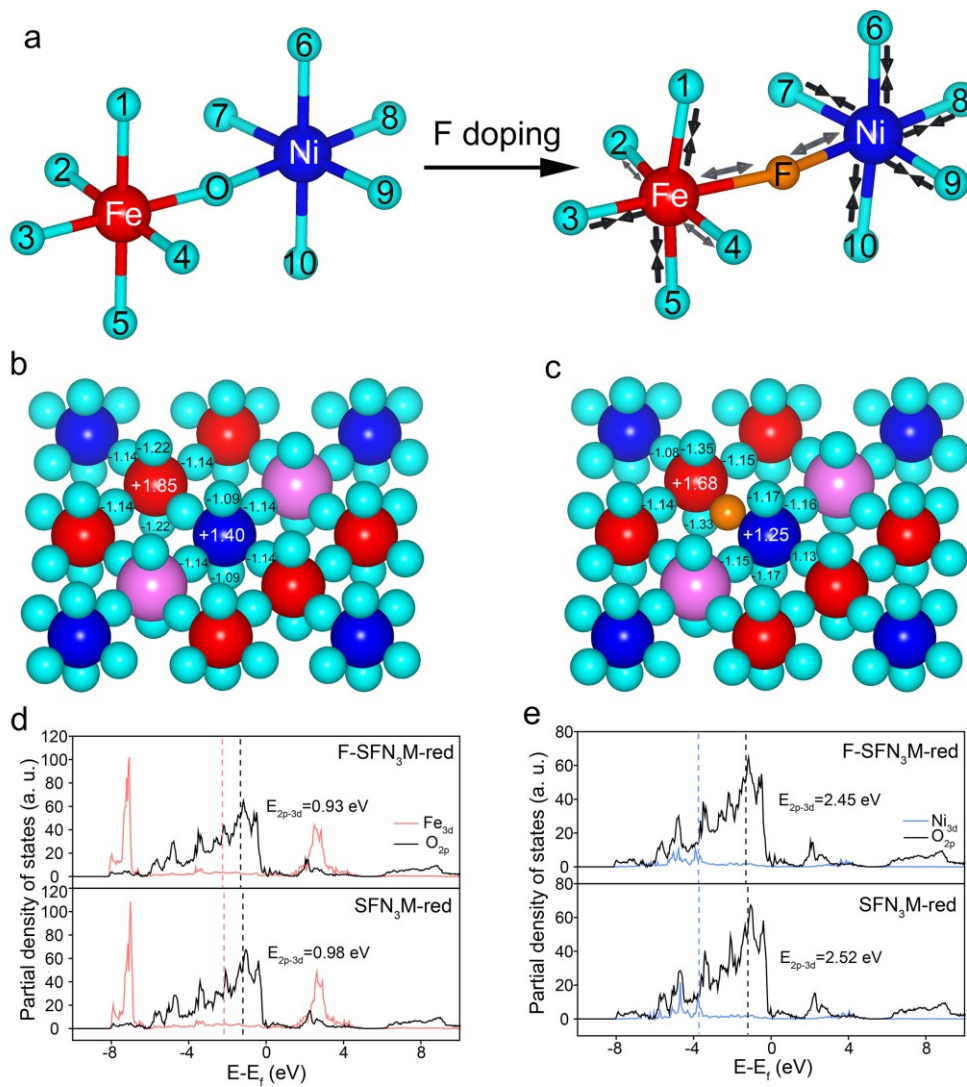


Figure 6.4 (a) Change of bond length of B-O after F doping in SFN₃M. Bader charge transfers on (b) SFN₃M and (c) F-SFN₃M models (In the DFT models, the grey balls represent Sr atoms, the red balls represent Fe atoms, the dark blue balls represent Ni atoms, the pink balls represent Mo atoms, the light blue balls represent O atoms, the orange balls represent F atoms). (d-e) Partial density of states analyses depicting the interaction between Fe/Ni 3d orbitals adjacent to F/O anions and the 2p orbitals of surrounding oxygen atoms.

To validate this point, we conducted thermogravimetric experiments in a reducing gas flow containing 5% H₂/N₂ to investigate the ability of two P-eNs to impede lattice oxygen loss under reducing conditions. As depicted from the weight loss profiles in Figure 6.3d, the initial weight loss of both samples below 200 °C can be assigned to the desorption of physically adsorbed species on the surface. [127, 137] Subsequently, both samples undergo a moderate weight increase starting at 200 °C, followed by another weight loss as the temperature reaches 300 °C. This unexpected weight gain could be explained by the adsorption of H₂ or other impurity gases from the feeding gas by the transition metals present on the surface. [267] Intriguingly, once the temperature reaches 500 °C, the weight loss profile of F-SFN₃M-red is steeper than that of SFN₃M-red, however, upon further increase in temperature to 780 °C, F-SFN₃M-red demonstrates a total weight loss of 2.28%, slightly lower than 2.44% recorded for SFN₃M-red. This observation highlights the ability of the F anion to impede the loss of lattice oxygen in the host perovskite.

To better understand the inhibitory effect of F-doping on exsolution and phase transformation at the atomic level, we performed density functional theory (DFT) calculations to investigate the effects of F anion on the BO₆ octahedral structure. During the optimization of the F-SFN₃M model, we found that the F anion manifests a preference for occupying the O-site that is shared by Fe and Ni cations, showing a minimum free energy of -539.22 eV across all possible F-SFN₃M models (Figure S6.3). Since bond length is an important geometric characteristic indicating the interactions between neighboring atoms, the B-O bond lengths from the optimized SFN₃M and F-SFN₃M models are depicted in Figures 6.4a, S6.4 and Table S6.2. These results indicate that upon F doping, a reduction in bond length occurs for all Ni-O bonds (oxygen number 6-10),

whereas three of the Fe-O bonds undergo compression (oxygen number 1, 3, 5), with the other two experience slight elongation (oxygen number 2, 4). This observation provides concrete evidence that the introduction of F dopants can reinforce the chemical stability of the BO_6 octahedron, thereby boosting the structural stability of the F-SFN₃M.

On the basis of the preliminary understanding of the effect of F doping on surrounding B-O bonds, the charge transfer within BO_6 octahedron was further investigated through Bader charge analyses (Figures 6.4b-c). In the SFN₃M model, the Fe and Ni atoms that share the same oxygen atom display a charge of +1.85 and +1.40, respectively (Table S6.3). However, upon replacing O with F, the charges of Fe and Ni atoms are reduced to +1.68 and +1.25, respectively. This suggests that the robust electrophilic nature of F anion is beneficial for preventing B-site elements from losing electrons. [188] Moreover, it can be observed that more electrons are transferred to the adjacent O atoms of Fe and Ni, as indicated by the overall decrease in Bader charges. We then performed partial density of states (PDOS) calculations to probe the *d-p* interaction between Fe/Ni 3*d* orbitals adjacent to the F/O anions and O 2*p* orbitals of the surrounding oxygen atoms (Figures 6.4d-e). It is evident that replacement of O with F causes an upward shift of the O 2*p* orbitals, which brings the O 2*p* orbitals closer in energy to the Fe/Ni 3*d* orbitals, thereby enhancing covalent bonding and Fe-O/Ni-O hybridizations. These results suggest that there is a stronger interaction between B-O, which is believed to play a pivotal role in inhibiting phase transition of F-SFN₃M during pre-reduction treatment.

Strengthened interaction between CO₂ and host perovskite. To gain a comprehensive understanding of the role of F-induced structural evolution in CO₂ electrolysis, CO₂

temperature-programmed desorption (CO₂-TPD) experiments were firstly performed to evaluate the CO₂ adsorption capacities of SFN₃M-red and F-SFN₃M-red. [127] As shown in Figure 6.5a, SFN₃M-red and F-SFN₃M-red display similar desorption process below 400 °C, which can be ascribed to the physical desorption of the dipole–dipole coupling of CO₂ molecules with the surface of perovskite substrates. [89, 137] Although both samples initiate the chemical desorption at 440 °C, their desorption behaviors remain dissimilar. SFN₃M-red displays a moderate desorption profile, where no observable desorption signals beyond 730 °C can be identified. On the other hand, F-SFN₃M-red exhibits a relatively intensive CO₂ chemical desorption peak alongside a wider range of desorption temperature up to 800 °C, indicative of a stronger interaction between the environmental CO₂ and the surface of F-SFN₃M-red at high temperatures. However, XPS spectra of O 1s results reveal that both samples display the similar surface concentration of chemisorbed oxygen species (O₂²⁻/O⁻, at the binding energy of ~531 eV), which act as the accommodation sites for the O atom of CO₂ molecules, with 70% of F-SFN₃M-red and 69% of SFN₃M-red, respectively (Figure 6.5b and Table S6.4). Therefore, the difference in CO₂ adsorption capacity between the two P-eNs is likely due to differences in the chemical environment of surface oxygen vacancies caused by different perovskite substrates. [138, 185, 268, 269] Consequently, maintaining a well-structured perovskite lattice *via* F-doping is more advantageous for surface CO₂ adsorption, which could greatly accelerate the surface kinetics of F-SFN₃M-red. Since a depletion layer of B-site reducible cations and a structure-restructured region appear near the surface within a few micrometers of host perovskites, [193] the high-activity interface formed between the perovskite scaffold and exsolved nanoparticles

in SFN₃M-red is primarily composed of LP structure and Fe-Ni alloy, thus leading to a relatively lower CO₂ surface exchange rate. [102, 230]

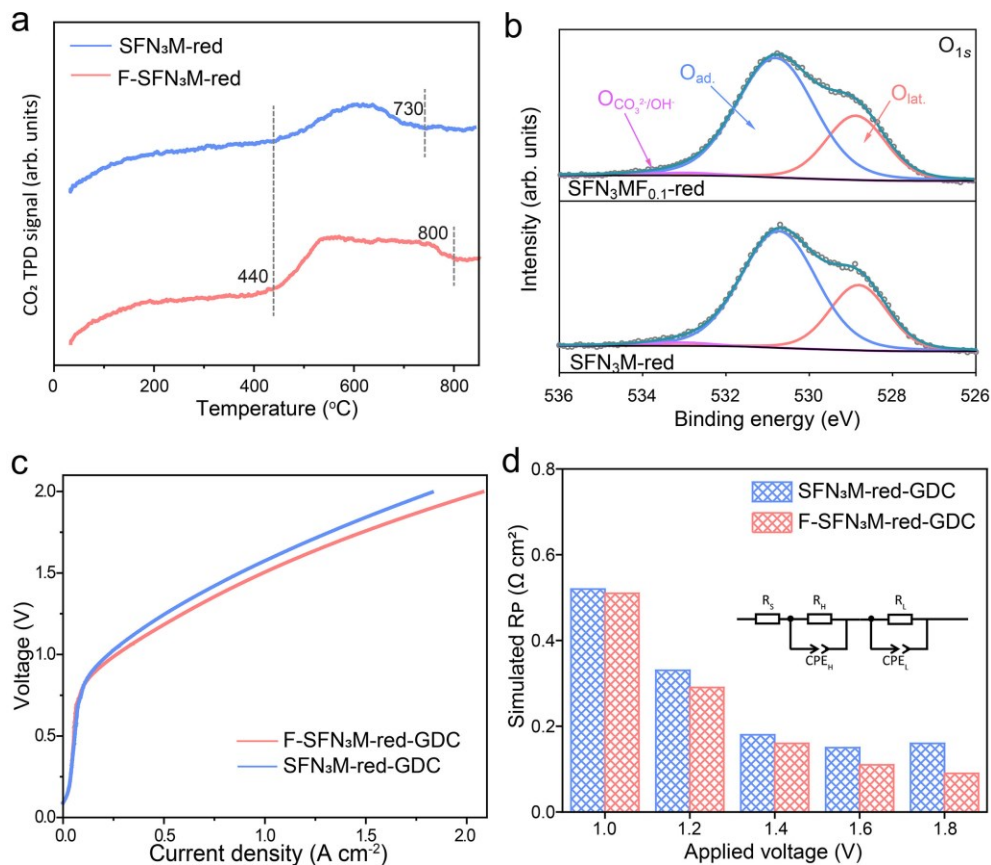


Figure 6.5 (a) CO₂-TPD results of SFN₃M-red and F-SFN₃M-red up to 800 °C. (b) XPS of O_{1s} for SFN₃M-red and F-SFN₃M-red. (c) Current density-voltage curves of SFN₃M-red-GDC and F-SFN₃M-red-GDC for pure CO₂ electrolysis at 850 °C. (d) Comparison of simulated polarization resistance of SFN₃M-red-GDC and F-SFN₃M-red-GDC using the equivalent circuit LR(CR)(QR).

After gaining initial understanding of the interaction between the two P-eNs and environmental CO₂, both P-eNs were subsequently mixed with the pure oxygen ion conductor gadolinium doped ceria (GDC) to fabricate the composite cathodes (SFN₃M-red-GDC and F-SFN₃M-red-GDC)

for CO₂ electrolysis at 850 °C. This allowed us to gain in-depth understanding of the impact of F-doping-induced structural evolution on the practical catalytic performances. The SOECs supported by YSZ electrolyte with GDC barrier layers on both sides (P-eNs-GDC|GDC|YSZ|GDC|(La_{0.6}Sr_{0.4})_{0.95}Co_{0.2}Fe_{0.8}O_{3-δ}-GDC) were well-assembled, which were simplified as SFN₃M-red-GDC and F-SFN₃M-red-GDC in following discussions. Figure 6.5c presents that the current density-voltage ($j - V$) curves of both SOECs for CO₂ electrolysis at 850 °C. It can be seen that F-SFN₃M-red-GDC exhibits the higher j compared to that of the SFN₃M-red-GDC at the same voltage. Specifically, the j of F-SFN₃M-red-GDC reaches 0.82 A cm⁻² at 1.4 V, slightly higher than 0.72 A cm⁻² for SFN₃M-red-GDC. Electrochemical impedance spectra (EIS) analysis was conducted to track the reactivity of two cathodes as a function of voltage. Using the equivalent circuit model LR(Q_HR_H)(Q_LR_L), we obtained the simulated polarization resistance (R_p) of both SOECs at 1 V, 1.2 V, 1.4 V, 1.6 V and 1.8 V (Figures 6.5d, S6.5 and Table S6.5). F-SFN₃M-red-GDC shows the smaller R_p than that with cathode SFN₃M-red-GDC at all monitored voltages, indicative of the facilitated CO₂ electrolysis process of F-SFN₃M-red-GDC than that of SFN₃M-red-GDC over a wide range of voltages. The enhancement of catalytic activity by F doping can be mainly attributed to the stronger CO₂ adsorption of on the DP structure compared to that on LP structure, as elucidated by the CO₂-TPD results.

Robust CO productivity of F-SFN₃M-red over a wide range of voltages. The robustness of P-eNs catalysts for CO₂ electrolysis is another crucial indicator for determining the efficiency of CO production over prolonged operation and evaluating their feasibility in further scale-up experiments and industrialization. Firstly, we conducted the 20 min potential step chronoamperometry tests ranging from 1.0 V to 1.8 V at 850 °C to obtain preliminary stability

information of both P-eNs. As shown in Figure 6.6a, both SOECs exhibit the satisfactory j response curves below 1.4 V. However, a notable difference is observed in the j curves of the two SOECs at and above 1.4 V, where the j of SFN₃M-red-GDC experienced a rapid decay, while F-SFN₃M-red-GDC maintains the appreciable j output up to 1.8 V. Myung *et al.* have demonstrated that external voltage can serve as a driving force for exsolution of nanoparticle, [165] the strong reducing conditions generated during electrolysis at high voltage may lead to the continued stripping of B-site reducible cations and lattice oxygen loss in the host perovskite. [177] Therefore, the superior short-term stability performances of F-SFN₃M-red can be attributed to the robust BO₆ octahedral framework conferred by the F anions.

Due to the near-unity Faraday efficiencies of both cells for producing CO (FE_{CO}) at all monitored voltages, the disparity in the capacity of both P-eNs to maintain stable j curves at high voltages results in an evidently distinct trend in CO production rate as a function of applied voltage (Figure 6.6b). In details, the CO productivity of SFN₃M-red-GDC displays a feeble CO output performance as the external voltage shifts more negatively, peaking at 1.6 V with a value of 5.00 mL min⁻¹ cm⁻², much inferior to the 7.09 mL min⁻¹ cm⁻² achieved on F-SFN₃M-red-GDC under the same condition. Furthermore, the stable j output of F-SFN₃M-red-GDC results in a monotonically increasing trend of the CO productivity as the applied voltage is increased, reaching 9.58 mL min⁻¹ cm⁻² at 1.8 V. This demonstrates a broad operational voltage suitability of F-SFN₃M-red-GDC for CO₂ electrolysis.

We proceeded to monitor the long-term stability of both SOECs at 1.4 V and 850 °C to investigate the degradation behaviors of both P-eNs. From Figure 6.6c, it is evident that SFN₃M-

red-GDC undergoes a j profile of “degradation-reactivation-degradation”, which was recently identified as the predominant degradation pattern of SFM-based P-eNs CO₂ electrolysis at 850 °C in our previous study. [177] Within expectations, such trend was absent in the j profile of F-SFN₃M-red-GDC, instead, it displays rather mild degradation throughout the electrolysis process. In particular, significant differences in the j profiles of the two cells were observed during the initial stage (0-4 h) (Figure S6.6). SFN₃M-red-GDC exhibits an extremely rapid degradation rate of 100 mA cm⁻² h⁻¹, which is nearly twice as fast as that of F-SFN₃M-red-GDC in the same period, the latter degraded at a rate of 52 mA cm⁻² h⁻¹. After an activation process, SFN₃M-red-GDC shows a peak j value of 0.5 A cm⁻² at 18 h, but the subsequent degradation leads to a j decline to 0.42 A cm⁻² after 90 h of electrolysis, which is significantly lower than 0.61 A cm⁻² for F-SFN₃M-red-GDC.

Raman analysis was then performed on the surface of the cathodes after long-term stability tests to investigate the presence of any post-reaction surface species. As shown in Figure 6.6d, the characteristic peaks of SrCO₃ (located at 701 cm⁻¹), SrMoO₄ (located at 795, 842, and 887 cm⁻¹) and carbon (D band, located at 1345 cm⁻¹, G band, located at 1590 cm⁻¹) can be detected on the cathode of SFN₃M-red-GDC, while only the specific peak of perovskite was found on that of F-SFN₃M-red-GDC. The emergence of Sr- and Mo-related species points to the occurrence of significant phase decomposition on the perovskite matrix of SFN₃M-red under the synergistic effects of high temperature and high voltage. [251, 270] For F-SFN₃M-red, on the other hand, the F anion doping unambiguously relieves the structural decomposition of host perovskite upon the high-voltage electrolysis by reinforcing the BO₆ octahedral structure. All the stability test results strongly suggest that F-SFN₃M-red-GDC demonstrates an outstanding performance

in improving CO productivity, and also highlights the great potential of F doping in achieving highly efficient CO₂ conversion of perovskite materials over a wide range of voltages.

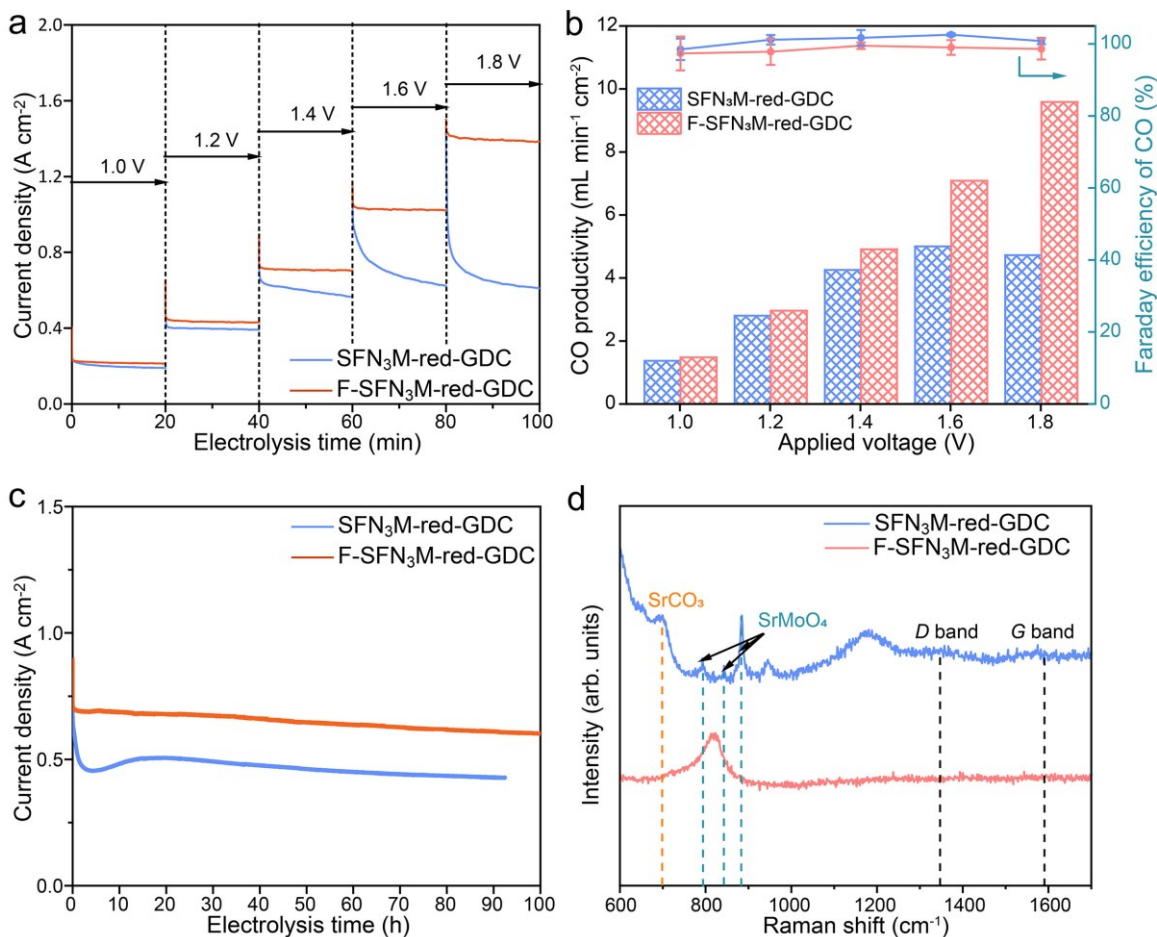


Figure 6.6 (a) The current density response curves for the 20 min potential step chronoamperometry and (b) the corresponding CO productivity (histogram) and FE_{CO} (markers) for SFN₃M-red-GDC and F-SFN₃M-red-GDC. (c) Long-term stability performances of SFN₃M-red and F-SFN₃M-red at 1.4 V and 850 °C. (d) Raman results of SFN₃M-red and F-SFN₃M-red after 100 h long-term stability tests.

6.3 Conclusions

In summary, we have demonstrated that the facile F doping strategy can prevent phase transformation and enhance the robustness of F-SFN₃M-red for CO₂ electrolysis. The well-preserved DP structure on the surface of F-SFN₃M-red displays more robust interactions with CO₂, leading to an enhanced catalytic activity. In addition, the higher resistance of host perovskite to decomposition is responsible for the stable *j* output of F-SFN₃M-red-GDC and consequently, an exceptional CO productivity over a broad range of voltages, particularly above 1.4 V. SFN₃M-red-GDC, on the other hand, displays a feeble CO output performance as a result of its rapid degradation above 1.4 V. By a combination of experimental characterizations and DFT calculations, we have discovered that F anion occupying O-site is capable of preserving the high oxidation states of B-site reducible cations and hindering the lattice oxygen loss, which can be ascribed to the enhanced robustness of BO₆ octahedron in host perovskite. These findings highlight a simple yet effective F doping approach to engineering perovskite-based catalysts with high catalytic activity and stability, which is of great significance to realize the commercial applications of P-eNs for the large-scale energy storage and conversion in SOCs.

6.4 Supporting information

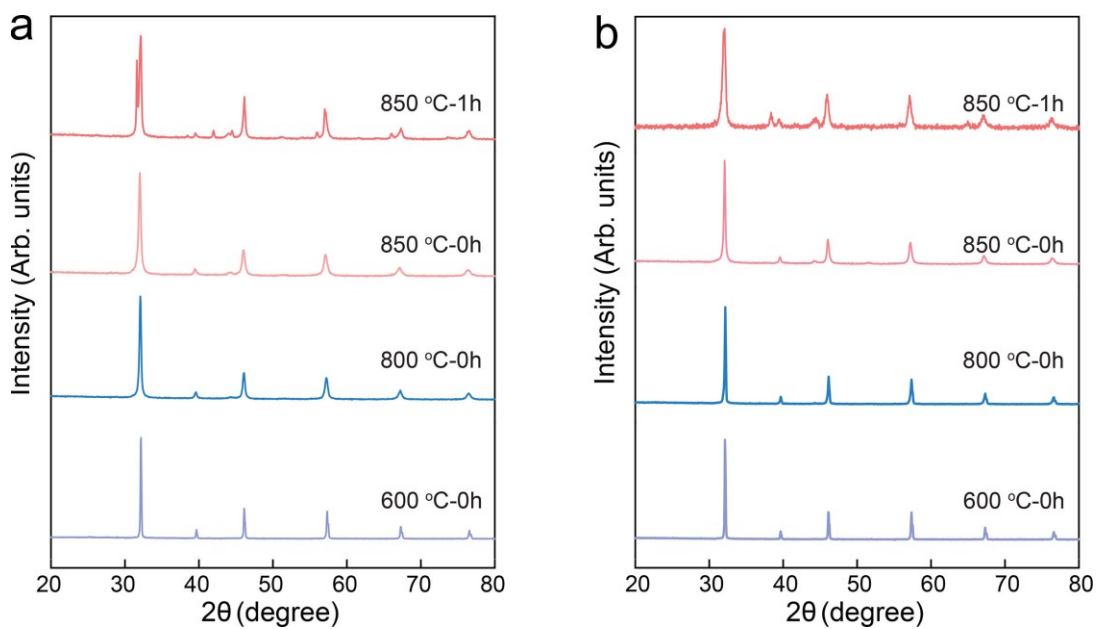


Figure S6.1 Ex situ XRD patterns of (a) SFN₃M and (b) F-SFN₃M after reduction at different temperatures and time.

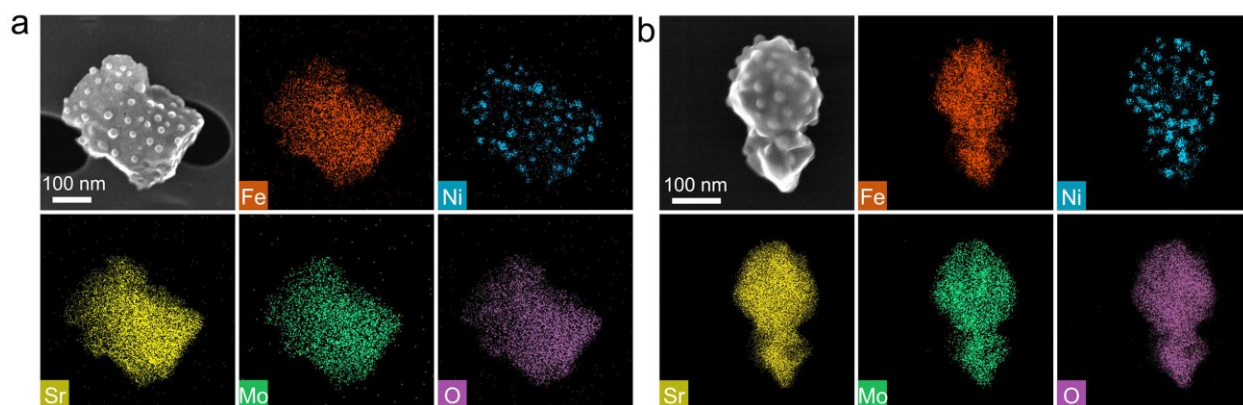


Figure S6.2 Secondary electron-scanning transmission electron microscopy (SE-STEM) and STEM with energy-dispersive X-ray spectroscopy (STEM-EDS) results of (a) SFN₃M-red (b) F-SFN₃M-red.

Table S6.1 Relative composition of Fe, Ni and Mo on SFN₃M-red and F-SFN₃M-red calculated from respective XPS spectra.

| B-site cations | | Ni | | Fe | | Mo | | |
|----------------|--------------------------|----|----|----|----|----|----|----|
| Valence states | | 0 | 2 | 0 | 2 | 3 | 5 | 6 |
| Samples | SFN ₃ M-red | 38 | 62 | 8 | 51 | 41 | 10 | 90 |
| | F-SFN ₃ M-red | 23 | 77 | 7 | 41 | 52 | 8 | 92 |

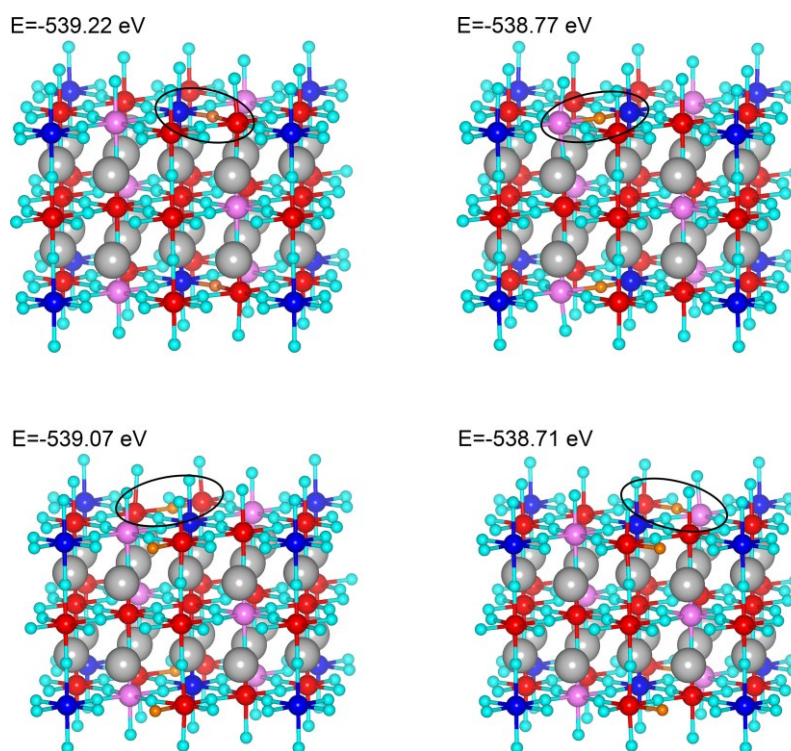


Figure S6.3 Possible configurations and corresponding free energies of F-SFN₃M based DFT-models. (In the DFT models, the grey balls represent Sr atoms, the red balls represent Fe atoms, the dark blue balls represent Ni atoms, the pink balls represent Mo atoms, the light blue balls represent O atoms, the orange balls represent F atoms)

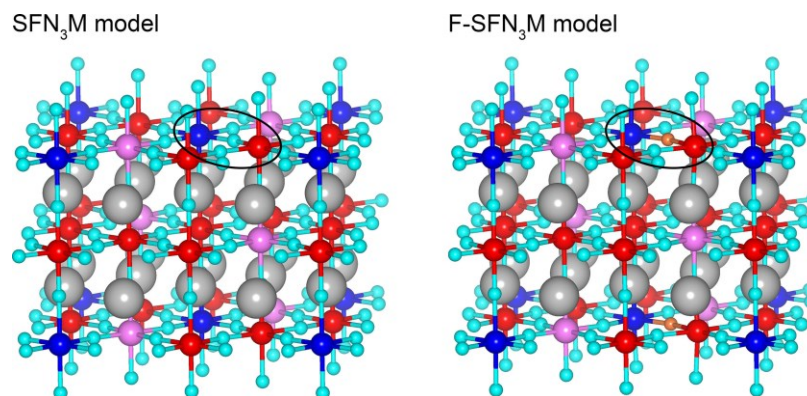


Figure S6.4 DFT models of SFN₃M and F-SFN₃M. (In the DFT models, the grey balls represent Sr atoms, the red balls represent Fe atoms, the dark blue balls represent Ni atoms, the pink balls represent Mo atoms, the light blue balls represent O atoms, the orange balls represent F atoms).

Table S6.2 Calculated B-O bond length in SFN₃M and F-SFN₃M models.

| Bonds | SFN ₃ M | F-SFN ₃ M | Change of bond length (Å) with substitution of O with F |
|---------------|--------------------|----------------------|---|
| | Bond length (Å) | | |
| Fe-O1 | 2.07324 | 2.05698 | -0.016(26) |
| Fe-O2 | 1.97143 | 1.97172 | +0.000(29) |
| Fe-O3 | 1.90281 | 1.87242 | -0.030(39) |
| Fe-O4 | 1.97136 | 1.97418 | +0.002(8) |
| Fe-O5 | 2.07324 | 2.05698 | -0.016(26) |
| Ni-O6 | 2.07412 | 2.07015 | -0.003(97) |
| Ni-O7 | 2.03984 | 2.03514 | -0.004(7) |
| Ni-O8 | 2.06072 | 2.00297 | -0.057(75) |
| Ni-O9 | 2.03984 | 2.02631 | -0.013(53) |
| Ni-O10 | 2.07412 | 2.07015 | -0.003(97) |

Table S6.3 Local Bader charge analysis on SFN₃M and F-SFN₃M models.

| Atom | SFN ₃ M | F-SFN ₃ M |
|------|--------------------|----------------------|
| O1 | -1.22 | -1.35 |
| O2 | -1.14 | -1.15 |
| O3 | -1.14 | -1.08 |
| O4 | -1.14 | -1.14 |
| O5 | -1.22 | -1.33 |
| Fe | +1.85 | +1.68 |
| Ni | +1.40 | +1.25 |
| O6 | -1.09 | -1.17 |
| O7 | -1.14 | -1.16 |
| O8 | -1.14 | -1.13 |
| O9 | -1.14 | -1.15 |
| O10 | -1.09 | -1.17 |

Table S6.4 Relative composition of O on SFN₃M-red and F-SFN₃M-red calculated from respective XPS spectra.

| Species | O | | |
|--------------------------|--|--|-----------------|
| | CO ₃ ²⁻ /OH ⁻ | O ₂ ²⁻ /O ⁻ | O ²⁻ |
| SFN ₃ M-red | 1 | 69 | 30 |
| F-SFN ₃ M-red | 1 | 70 | 28 |

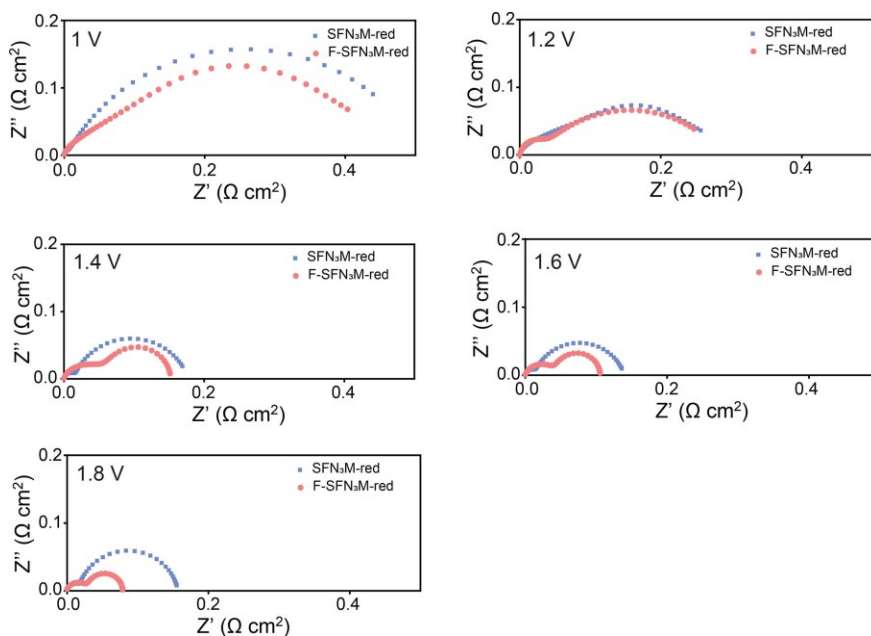


Figure S6.5 Simulated electrochemical impedance spectra of SFN₃M-red-GDC and F-SFN₃M-red-GDC with removing the ohmic resistance part.

Table S6.5 EIS fitting values of R_s , $R_p (=R_H+R_L)$ for SOECs with SFN₃M-red-GDC and F-SFN₃M-red-GDC as cathodes.

| Potential (V) | SOECs | R_H ($\Omega \text{ cm}^2$) | R_L ($\Omega \text{ cm}^2$) | R_p ($\Omega \text{ cm}^2$) |
|---------------|------------------------------|---------------------------------|---------------------------------|---------------------------------|
| 1 | SFN ₃ M-red-GDC | 0.1607 | 0.413 | 0.5737 |
| | F-SFN ₃ M-red-GDC | 0.12 | 0.39 | 0.51 |
| 1.2 | SFN ₃ M-red-GDC | 0.05994 | 0.2741 | 0.33404 |
| | F-SFN ₃ M-red-GDC | 0.03 | 0.26 | 0.29 |
| 1.4 | SFN ₃ M-red-GDC | 0.02 | 0.16 | 0.18 |
| | F-SFN ₃ M-red-GDC | 0.08 | 0.08 | 0.16 |
| 1.6 | SFN ₃ M-red-GDC | 0.02 | 0.13 | 0.15 |
| | F-SFN ₃ M-red-GDC | 0.06 | 0.05 | 0.11 |
| 1.8 | SFN ₃ M-red-GDC | 0.02 | 0.14 | 0.16 |
| | F-SFN ₃ M-red-GDC | 0.05 | 0.04 | 0.09 |

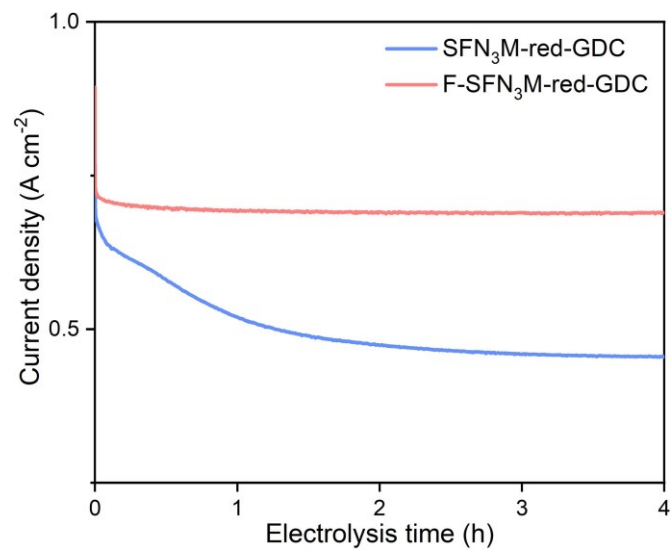


Figure S6.6 0-4 h long-term stability performances of SFN₃M-red and F-SFN₃M-red at 1.4 V and 850 °C.

Chapter 7. Summary and prospects

This thesis focuses on designing P-eNs materials with high catalytic activity and high stability for CO₂ electrolysis in SOEC, and investigating the electrolysis mechanisms and degradation mechanisms on P-eNs-based electrodes. In recent decades, tremendous efforts have been devoted to regulating the features of exsolved nanoparticles on the various perovskite scaffolds, including the size, distribution density, composition, and morphology, to meet the demands of various catalytic reactions and improve the catalytic activity. However, the host perovskite substrate, which is responsible for preserving the highly active sites and extending the TPB, has received relatively little attention. We still have insufficient comprehension of the effects of the host perovskite's phase evolution on catalytic reactions occurring on P-eNs, including the catalytic activity and stability. In my thesis, I focused on the structural evolution of perovskite substrate during exsolution and its effects on the overall performances of P-eNs based catalysts. Firstly, I found that although the catalytic activity of P-eNs has been improved compared to their counterparts without exsolution, there are still serious degradation problems on P-eNs-based materials, especially when working at high voltages. By analyzing the common exsolution process, I identified the B-site vacancies in the perovskite substrate as the main cause of the rapid degradation. To verify this point, a promising perovskite, SFNM, was selected as prototype due to its satisfactory redox stability and conductivity under both reducing and oxidizing conditions. Then, I used ion exchange to achieve B-site supplement to maintain the B-site saturation during the exsolution process. In terms of CO₂ reactivity improvement, B-site supplement significantly circumvents Sr segregation, facilitates the charge conductivity by

liberalizing oxygen vacancy distribution and offering more $B^{(n-1)+}-O-B^{n+}$ pathways within perovskite lattice. Combining with the promoted exsolution, excellent catalytic performance can be achieved even at high potentials. In terms of stability, in addition to the stable anchored nanoparticles, transformation of reduced perovskite SFNM into a delicate substrate SFM with negligible B-site vacancy and Ni incorporation renders robust structural stability of nanoparticle support under harsh reducing conditions. Furthermore, the degradation mechanisms on SFM-based P-eNs with and without B-site supplement at high voltages have been proposed from the perspective of structural evolution of parent perovskite. It reveals that the structural integrity of perovskite scaffold is of great significance to the overall durability of P-eNs.

Consequently, I aimed to regulate the structural evolution of parent perovskite without compromising the exsolution of nanoparticles, and gain insights into the reaction mechanisms on P-eNs, thus providing guidance on designing P-eNs-based materials for CO_2 electrolysis and even a wider range of applications. Firstly, I successfully suppressed and accelerated the phase transformation of SFN₃M by B-site supplement and prolonged exsolution strategies, without compromising exsolution. This has resulted in the production of three P-eNs, each possessing distinct metal supports, including pure double perovskite (DP-NPs), pure layered perovskite (LP-NPs) and their composite perovskite (DLP-NPs). In CO_2 electrolysis, DP-NPs exhibit the highest catalytic activity, whereas LP-NPs demonstrate remarkable stability performance over a broad range of operating voltages. The results show that the chemical environments of oxygen vacancies on the surface of perovskite substrates, as well as the structures of host perovskite, play an important role in determining the CO_2 adsorption capacity of P-eNs. Furthermore, the electronic structure of the perovskite scaffold not only dominates the activation of surface-

adsorbed CO₂ and the subsequent reduction of carbonate intermediate, but also determines the surface relaxation and preservation of high reactivity at high voltages. By DFT calculation, I demonstrated the switching of the rate-limiting step is thermodynamically unfavorable on DLP-NPs when phase transformed from double perovskite to layered perovskite. Lastly, I have revealed that the structural configuration and reducibility of perovskite substrate are responsible for the decomposition of P-eNs during CO₂ electrolysis. This work contributes to an in-depth understanding of the reaction mechanisms occurring on the P-eNs catalysts, and provides the guidance of rational design of P-eN-based catalysts for a variety of applications.

Based on the studies in this thesis, the suggestions of future work are listed below for researchers who are dedicated to the development of P-eNs-based materials for CO₂ electrolysis and other reactions in SOCs.

(1) Mechanism investigation of the exsolution process. Since exsolution is a decomposition process of perovskite, the growth of nanoparticles via exsolution will inevitably lead to the structural collapse of parent perovskite. A comprehensive understanding of the exsolution process and the reasons behind the improved performance of P-eNs-based materials compared to those without exsolution can provide valuable insights for the advancement of P-eNs-based materials.

(2) Investigation of in-situ electrolytic characterization techniques. Since exsolution results in many defects on the surface of perovskites, it complicates the surface chemical environments of perovskites. Furthermore, the harsh reducing environment under the electrolysis conditions leads to the dynamic alteration of the chemical surroundings on the surface of perovskites.

Hence, in-situ exploration of the electrolysis reaction on P-eNs can facilitate an understanding of the underlying reaction mechanisms. This, in turn, enables the optimization of electrolysis conditions to enhance the yield of CO and extend the operational duration, which holds significant implications for commercialization.

Bibliography

1. Friedlingstein P, O'Sullivan M, Jones MW, et al., Global Carbon Budget 2022, *Earth Syst Sci Data*. 14 (2022) 4811-900.
2. Aresta M, Dibenedetto A, Angelini A, Catalysis for the valorization of exhaust carbon: from CO₂ to chemicals, materials, and fuels. technological use of CO₂, *Chem Rev*. 114 (2014) 1709-42.
3. Nejat P, Jomehzadeh F, Taheri MM, et al., A global review of energy consumption, CO₂ emissions and policy in the residential sector (with an overview of the top ten CO₂ emitting countries), *Renewable Sustainable Energy Rev*. 43 (2015) 843-62.
4. Peters GP, Marland G, Le Quéré C, et al., Rapid growth in CO₂ emissions after the 2008–2009 global financial crisis, *Nat Clim Change*. 2 (2011) 2-4.
5. Jiang X, Guan D, Determinants of global CO₂ emissions growth, *Appl Energy*. 184 (2016) 1132-41.
6. Bréon FM, Broquet G, Puygrenier V, et al., An attempt at estimating Paris area CO₂ emissions from atmospheric concentration measurements, *Atmos Chem Phys*. 15 (2015) 1707-24.
7. Lauvaux T, Gurney KR, Miles NL, et al., Policy-Relevant Assessment of Urban CO₂ Emissions, *Environ Sci Technol*. 54 (2020) 10237-45.
8. Rezaei Sadr N, Bahrdo T, Taghizadeh R, Impacts of Paris agreement, fossil fuel consumption, and net energy imports on CO₂ emissions: a panel data approach for three West European countries, *Clean Technologies and Environmental Policy*. 24 (2022) 1521-34.
9. L'Orange Seigo S, Dohle S, Siegrist M, Public perception of carbon capture and storage (CCS): A review, *Renewable and Sustainable Energy Reviews*. 38 (2014) 848-63.
10. Schrag DP, Preparing to Capture Carbon, *Science*. 315 (2007) 812-3.
11. Whipple DT, Kenis PJA, Prospects of CO₂ Utilization via Direct Heterogeneous Electrochemical Reduction, *J Phys Chem Lett*. 1 (2010) 3451-8.
12. Zheng Y, Wang J, Yu B, et al., A review of high temperature co-electrolysis of H₂O and CO₂ to produce sustainable fuels using solid oxide electrolysis cells (SOECs): advanced materials and technology, *Chem Soc Rev*. 46 (2017) 1427-63.
13. Tan Y, Nookuea W, Li H, et al., Property impacts on Carbon Capture and Storage (CCS) processes: A review, *Energy Conversion and Management*. 118 (2016) 204-22.

14. Spinner NS, Vega JA, Mustain WE, Recent progress in the electrochemical conversion and utilization of CO₂, *Catal Sci Technol.* 2 (2012) 19-28.
15. Rafiee A, Rajab Khalilpour K, Milani D, et al., Trends in CO₂ conversion and utilization: A review from process systems perspective, *J Environ Chem Eng.* 6 (2018) 5771-94.
16. Zheng Y, Zhang W, Li Y, et al., Energy related CO₂ conversion and utilization: Advanced materials/nanomaterials, reaction mechanisms and technologies, *Nano Energy.* 40 (2017) 512-39.
17. Zain MM, Mohamed AR, An overview on conversion technologies to produce value added products from CH₄ and CO₂ as major biogas constituents, *Renewable Sustainable Energy Rev.* 98 (2018) 56-63.
18. Wang Y, Han P, Lv X, et al., Defect and Interface Engineering for Aqueous Electrocatalytic CO₂ Reduction, *Joule.* 2 (2018) 2551-82.
19. Jhong H-RM, Ma S, Kenis PJA, Electrochemical conversion of CO₂ to useful chemicals: current status, remaining challenges, and future opportunities, *Curr Opin Chem Eng.* 2 (2013) 191-9.
20. Agarwal AS, Zhai Y, Hill D, et al., The electrochemical reduction of carbon dioxide to formate/formic acid: engineering and economic feasibility, *ChemSusChem.* 4 (2011) 1301-10.
21. Zhao G, Huang X, Wang X, et al., Progress in catalyst exploration for heterogeneous CO₂ reduction and utilization: a critical review, *J Mater Chem A.* 5 (2017) 21625-49.
22. Razmjoo A, Gakenia Kaigutha L, Vaziri Rad MA, et al., A Technical analysis investigating energy sustainability utilizing reliable renewable energy sources to reduce CO₂ emissions in a high potential area, *Renew Energ.* 164 (2021) 46-57.
23. Qudrat-Ullah H, A review and analysis of renewable energy policies and CO₂ emissions of Pakistan, *Energy.* 238 (2022) 121849.
24. Tan X, Yu C, Ren Y, et al., Recent Advance in Innovative Strategies for CO₂ Electroreduction Reaction, *Energy Environ Sci.* 14 (2021) 765-80.
25. Sharifian R, Wagterveld M, Digdaya IA, et al., Electrochemical carbon dioxide capture to close the carbon cycle, *Energy & Environmental Science.* 14 (2021) 781-814.
26. Maiti D, Hare BJ, Daza YA, et al., Earth abundant perovskite oxides for low temperature CO₂ conversion, *Energy Environ Sci.* 11 (2018) 648-59.

27. Li T, Lees EW, Zhang Z, et al., Conversion of Bicarbonate to Formate in an Electrochemical Flow Reactor, *ACS Energy Lett.* 5 (2020) 2624-30.
28. Wang G, Chen J, Ding Y, et al., Electrocatalysis for CO₂ conversion: from fundamentals to value-added products, *Chem Soc Rev.* 50 (2021) 4993-5061.
29. De S, Dokania A, Ramirez A, et al., Advances in the Design of Heterogeneous Catalysts and Thermocatalytic Processes for CO₂ Utilization, *ACS Catalysis.* (2020) 14147-85.
30. Ganji P, Borse RA, Xie J, et al., Toward Commercial Carbon Dioxide Electrolysis, *Adv Sustain Syst.* 4 (2020) 2000096.
31. Song Y, Zhang X, Xie K, et al., High-temperature CO₂ electrolysis in solid oxide electrolysis cells: developments, challenges, and prospects, *Adv Mater.* 31 (2019) e1902033.
32. Stempien JP, Ding OL, Sun Q, et al., Energy and exergy analysis of Solid Oxide Electrolyser Cell (SOEC) working as a CO₂ mitigation device, *Int J Hydrog Energy.* 37 (2012) 14518-27.
33. Kungas R, Review—Electrochemical CO₂ Reduction for CO Production: Comparison of Low- and High-Temperature Electrolysis Technologies, *J Electrochem Soc.* 167 (2020) 044508.
34. Ebbesen SD, Jensen SH, Hauch A, et al., High temperature electrolysis in alkaline cells, solid proton conducting cells, and solid oxide cells, *Chem Rev.* 114 (2014) 10697-734.
35. Irvine JTS, Neagu D, Verbraeken MC, et al., Evolution of the electrochemical interface in high-temperature fuel cells and electrolyzers, *Nat Energy.* 1 (2016) 15014.
36. Deka DJ, Gunduz S, Fitzgerald T, et al., Production of syngas with controllable H₂/CO ratio by high temperature co-electrolysis of CO₂ and H₂O over Ni and Co- doped lanthanum strontium ferrite perovskite cathodes, *Appl Catal B.* 248 (2019) 487-503.
37. Lee D-Y, Mehran MT, Kim J, et al., Scaling up syngas production with controllable H₂/CO ratio in a highly efficient, compact, and durable solid oxide coelectrolysis cell unit-bundle, *Appl Energy.* 257 (2020) 114036.
38. Hauch A, Kungas R, Blennow P, et al., Recent advances in solid oxide cell technology for electrolysis, *Science.* 370 (2020) 186.
39. Venkataraman V, Pérez-Fortes M, Wang L, et al., Reversible solid oxide systems for energy and chemical applications-Review & perspectives, *J Energy Storage.* 24 (2019) 100782.

40. Gómez SY, Hotza D, Current developments in reversible solid oxide fuel cells, *Renewable Sustainable Energy Rev.* 61 (2016) 155-74.
41. Zamudio-García J, Caizán-Juanarena L, Porras-Vázquez JM, et al., A review on recent advances and trends in symmetrical electrodes for solid oxide cells, *J Power Sources.* 520 (2022).
42. Shen M, Ai F, Ma H, et al., Progress and prospects of reversible solid oxide fuel cell materials, *iScience.* 24 (2021) 103464.
43. R.L Ash WLD, G Varsi, Feasibility of rocket propellant production on Mars, *Acta Astronaut.* 5 (1978).
44. Richter R. Basic investigation into the production of oxygen in a solid electrolyte process. 16th Thermophysics Conference 1981.
45. Oxygen production on Mars using solid oxide electrolysis, *Solid State Ion.* 93 (1997) 321-8.
46. Sridhar KR, Iacomini CS, Finn JE, Combined H₂O/CO₂ Solid Oxide Electrolysis for Mars In Situ Resource Utilization, *J Propuls Power.* 20 (2004) 892-901.
47. Starr SO, Muscatello AC, Mars in situ resource utilization: a review, *Planet Space Sci.* 182 (2020) 104824.
48. Kim SJ, Choi GM, Stability of LSCF electrode with GDC interlayer in YSZ-based solid oxide electrolysis cell, *Solid State Ion.* 262 (2014) 303-6.
49. Goodenough JB, Oxide-Ion Electrolytes, *Annu Rev Mater Res.* 33 (2003) 91-128.
50. Ishihara T, Tabuchi J, Ishikawa S, et al., Recent progress in LaGaO₃ based solid electrolyte for intermediate temperature SOFCs, *Solid State Ion.* 177 (2006) 1949-53.
51. Tatsumi Ishihara HM, and Yusaku Takita, Doped LaGaO₃ Perovskite Type Oxide as a New Oxide Ionic Conductor, *J Am Chem Soc.* 116 (1994) 3801-3.
52. Opitz AK, Nenning A, Rameshan C, et al., Surface chemistry of perovskite-type electrodes during high temperature CO₂ electrolysis investigated by operando photoelectron spectroscopy, *ACS Appl Mater Interfaces.* 9 (2017) 35847-60.
53. Song Y, Zhou Z, Zhang X, et al., Pure CO₂ electrolysis over an Ni/YSZ cathode in a solid oxide electrolysis cell, *J Mater Chem A.* 6 (2018) 13661-7.
54. O'hayre R, Cha S-W, Colella W, et al. *Fuel cell fundamentals: John Wiley & Sons; 2016.*

55. Jiang Y, Chen F, Xia C, A review on cathode processes and materials for electro-reduction of carbon dioxide in solid oxide electrolysis cells, *J Power Sources*. 493 (2021) 229713.
56. Ma W, Xie S, Zhang XG, et al., Promoting electrocatalytic CO₂ reduction to formate via sulfur-boosting water activation on indium surfaces, *Nat Commun*. 10 (2019) 892.
57. Shao-horn Y, Perovskites in catalysis and electrocatalysis, *Science*. 358 (2017) 751-6.
58. Wang S, Inoishi A, Hong J-e, et al., Ni-Fe bimetallic cathodes for intermediate temperature CO₂ electrolyzers using a La_{0.9}Sr_{0.1}Ga_{0.8}Mg_{0.2}O₃ electrolyte, *J Mater Chem A*. 1 (2013) 12455-61.
59. Yu J, Men HJ, Qu YM, et al., Performance of Ni-Fe bimetal based cathode for intermediate temperature solid oxide electrolysis cell, *Solid State Ion*. 346 (2020) 115203.
60. Zhao C, Li Y, Zhang W, et al., Heterointerface engineering for enhancing the electrochemical performance of solid oxide cells, *Energy Environ Sci*. 13 (2020) 53-85.
61. Gao Y, Wang J, Lyu Y-Q, et al., In situ growth of Pt₃Ni nanoparticles on an A-site deficient perovskite with enhanced activity for the oxygen reduction reaction, *J Mater Chem A*. 5 (2017) 6399-404.
62. Morales-Zapata MA, Larrea A, Laguna-Bercero MA, Reversible operation performance of microtubular solid oxide cells with a nickelate-based oxygen electrode, *Int J Hydrog Energy*. 45 (2019) 5535-42.
63. Shin JW, Go D, Kye SH, et al., Review on process-microstructure-performance relationship in ALD-engineered SOFCs, *J phys energy*. 1 (2019) 042002.
64. Tucker MC, Progress in metal-supported solid oxide electrolysis cells: A review, *Int J Hydrog Energy*. 45 (2020) 24203-18.
65. Park BK, Cox D, Barnett SA, Effect of Nanoscale Ce_{0.8}Gd_{0.2}O_{2-δ} Infiltrant and Steam Content on Ni-(Y₂O₃)_{0.08}(ZrO₂)_{0.92} Fuel Electrode Degradation during High-Temperature Electrolysis, *Nano Lett*. 21 (2021) 8363-9.
66. Jiang Y, Ye L, Zhang S, et al., Doped ceria with exsolved Fe⁰ nanoparticles as a Sr-free cathode for CO₂ electrolysis in SOECs at reduced temperatures, *J Mater Chem A*. 10 (2022) 9380-3.
67. Yue X, Irvine JTS, Alternative Cathode Material for CO₂Reduction by High Temperature Solid Oxide Electrolysis Cells, *J Electrochem Soc*. 159 (2012) F442-F8.

68. Singh V, Muroyama H, Matsui T, et al., Feasibility of alternative electrode materials for high temperature CO₂ reduction on solid oxide electrolysis cell, *J Power Sources*. 293 (2015) 642-8.
69. Green R, Liu C, Adler S, Carbon dioxide reduction on gadolinia-doped ceria cathodes, *Solid State Ion*. 179 (2008) 647-60.
70. Tan Z, Song JT, Takagaki A, et al., Infiltration of cerium into a NiO–YSZ tubular substrate for solid oxide reversible cells using a LSGM electrolyte film, *J Mater Chem A*. 9 (2021) 1530-40.
71. Litzelman SJ, Tuller HL, Measurement of mixed conductivity in thin films with microstructured Hebb–Wagner blocking electrodes, *Solid State Ion*. 180 (2009) 1190-7.
72. Xie Y, Xiao J, Liu D, et al., Electrolysis of carbon dioxide in a solid oxide electrolyzer with silver-gadolinium-doped ceria cathode, *J Electrochem Soc*. 162 (2015) F397-F402.
73. F. Bidrawn GK, J. T. S. Irvine, Efficient reduction of CO₂ in a solid oxide electrolyzer, *Electrochem solid-state lett*. 11 (2008) B167-B70.
74. HOLTAPPELS P, Reaction of CO CO₂ gas mixtures on Ni±YSZ cermet electrodes, *J Appl Electrochem*. 29 (1999) 561–8.
75. Pihlatie M, Kaiser A, Mogensen M, Redox stability of SOFC: Thermal analysis of Ni–YSZ composites, *Solid State Ion*. 180 (2009) 1100-12.
76. Chen M, Liu Y-L, Bentzen JJ, et al., Microstructural Degradation of Ni/YSZ Electrodes in Solid Oxide Electrolysis Cells under High Current, *Journal of The Electrochemical Society*. 160 (2013) F883-F91.
77. Yue X, Irvine JTS, Alternative Cathode Material for CO₂ Reduction by High Temperature Solid Oxide Electrolysis Cells, *J Electrochem Soc*. 159 (2012) F442-F8.
78. Toebes ML, Impact of the structure and reactivity of nickel particles on the catalytic growth of carbon nanofibers, *Catal today*. 76 (2002) 33-42.
79. Gaudillere C, Navarrete L, Serra JM, Syngas production at intermediate temperature through H₂O and CO₂ electrolysis with a Cu-based solid oxide electrolyzer cell, *Int J Hydrog Energy*. 39 (2014) 3047-54.
80. Kim-Lohsoontorn P, Bae J, Electrochemical performance of solid oxide electrolysis cell electrodes under high-temperature coelectrolysis of steam and carbon dioxide, *J Power Sources*. 196 (2011) 7161-8.

81. Junjiang Zhu HL, Linyun Zhong, Ping Xiao, Xuelian Xu, Xiangguang Yang, Zhen Zhao, and Jinlin Li, Perovskite oxides preparation, characterizations, and applications in heterogeneous catalysis, *ACS catalysis*. 4 (2014) 2917–40.
82. Ishihara T. *Perovskite oxide for solid oxide fuel cells*: Springer Science & Business Media; 2009.
83. Sunarso J, Hashim SS, Zhu N, et al., Perovskite oxides applications in high temperature oxygen separation, solid oxide fuel cell and membrane reactor A review, *Prog Energy Combust Sci*. 61 (2017) 57-77.
84. Papac M, Stevanovic V, Zakutayev A, et al., Triple ionic-electronic conducting oxides for next-generation electrochemical devices, *Nat Mater*. 20 (2021) 301-13.
85. Jun A, Kim J, Shin J, et al., Perovskite as a Cathode Material: A Review of its Role in Solid-Oxide Fuel Cell Technology, *ChemElectroChem*. 3 (2016) 511-30.
86. Bhalla AS, Guo R, Roy R, The perovskite structure—a review of its role in ceramic science and technology, *Mater Res Innov*. 4 (2016) 3-26.
87. Dogu D, Meyer KE, Fuller A, et al., Effect of lanthanum and chlorine doping on strontium titanates for the electrocatalytically-assisted oxidative dehydrogenation of ethane, *Appl Catal B*. 227 (2018) 90-101.
88. Li Z, Xue KH, Wang J, et al., Cation and Anion Co-doped Perovskite Nanofibers for Highly Efficient Electrocatalytic Oxygen Evolution, *ACS Appl Mater Interfaces*. 12 (2020) 41259-68.
89. Ye L, Zhang M, Huang P, et al., Enhancing CO₂ electrolysis through synergistic control of non-stoichiometry and doping to tune cathode surface structures, *Nat Commun*. 8 (2017) 14785.
90. Christopher J. Bartel CS, Bryan R. Goldsmith, Runhai Ouyang, Charles B. Musgrave, Luca M. Ghiringhelli, Matthias Scheffler, New tolerance factor to predict the stability of perovskite oxides and halides, *Science*. 5 (2019) eaav0693.
91. Liang F, Partovi K, Jiang H, et al., B-site La-doped BaFe_{0.95-x}La_xZr_{0.05}O_{3-δ} perovskite-type membranes for oxygen separation, *J Mater Chem A*. 1 (2013) 746-51.
92. Xu X, Zhong Y, Shao Z, Double Perovskites in Catalysis, Electrocatalysis, and Photo(electro)catalysis, *Trends in Chemistry*. 1 (2019) 410-24.
93. Klyndyuk AI, Chizhova EA, Kharytonau DS, et al., Layered Oxygen-Deficient Double Perovskites as Promising Cathode Materials for Solid Oxide Fuel Cells, *Mater*. 15 (2021) 141.

94. Xu X, Pan Y, Zhong Y, et al., Ruddlesden–Popper perovskites in electrocatalysis, *Mater Horiz.* 7 (2020) 2519-65.
95. Ding P, Li W, Zhao H, et al., Review on Ruddlesden–Popper perovskites as cathode for solid oxide fuel cells, *J phys chem mater.* 4 (2021) 022002.
96. Druce J, Téllez H, Burriel M, et al., Surface termination and subsurface restructuring of perovskite-based solid oxide electrode materials, *Energy Environ Sci.* 7 (2014) 3593-9.
97. Su C, Wang W, Liu M, et al., Progress and Prospects in Symmetrical Solid Oxide Fuel Cells with Two Identical Electrodes, *Advanced Energy Materials.* 5 (2015) 1500188.
98. Hansen KK, Wandel M, Liu YL, et al., Effect of impregnation of $\text{La}_{0.85}\text{Sr}_{0.15}\text{MnO}_3$ /yttria stabilized zirconia solid oxide fuel cell cathodes with $\text{La}_{0.85}\text{Sr}_{0.15}\text{MnO}_3$ or Al_2O_3 nano-particles, *Electrochim Acta.* 55 (2010) 4606-9.
99. Munoz-Garcia AB, Bugaris DE, Pavone M, et al., Unveiling structure-property relationships in $\text{Sr}_2\text{Fe}_{1.5}\text{Mo}_{0.5}\text{O}_{6-\delta}$, an electrode material for symmetric solid oxide fuel cells, *J Am Chem Soc.* 134 (2012) 6826-33.
100. Xu X, Zhong Y, Shao Z, Double Perovskites in Catalysis, Electrocatalysis, and Photo(electro)catalysis, *Trends in Chemistry.* (2019).
101. Akande SO, Boulfrad S, Schwingenschlögl U, Intrinsic defect processes and O migration in $\text{PrBa}(\text{Co}/\text{Fe})_2\text{O}_{5.5}$, *J Mater Chem A.* 4 (2016) 3560-4.
102. Kim K, Joo S, Huang R, et al., Mechanistic insights into the phase transition and metal exsolution phenomena of $\text{Pr}_{0.5}\text{Ba}_{0.5}\text{Mn}_{0.85}\text{Co}_{0.15}\text{O}_{3-\delta}$ from simple to layered perovskite under reducing conditions and enhanced catalytic activity, *Energy Environ Sci.* 14 (2021) 873-82.
103. Kim H, Lim C, Kwon O, et al., Unveiling the key factor for the phase reconstruction and exsolved metallic particle distribution in perovskites, *Nat Commun.* 12 (2021) 6814.
104. Kwon O, Kim YI, Kim K, et al., Probing One-Dimensional Oxygen Vacancy Channels Driven by Cation-Anion Double Ordering in Perovskites, *Nano Lett.* 20 (2020) 8353-9.
105. Bahout M, Managutti PB, Dorcet V, et al., In situ exsolution of Ni particles on the $\text{PrBaMn}_2\text{O}_5$ SOFC electrode material monitored by high temperature neutron powder diffraction under hydrogen, *J Mater Chem A.* 8 (2020) 3590-7.

106. Gou Y, Li G, Ren R, et al., Pr-Doping Motivating the Phase Transformation of the BaFeO_{3-δ} Perovskite as a High-Performance Solid Oxide Fuel Cell Cathode, ACS Appl Mater Interfaces. (2021).
107. Sengodan S, Choi S, Jun A, et al., Layered oxygen-deficient double perovskite as an efficient and stable anode for direct hydrocarbon solid oxide fuel cells, Nat Mater. 14 (2015) 205-9.
108. Tarancón A, Burriel M, Santiso J, et al., Advances in layered oxide cathodes for intermediate temperature solid oxide fuel cells, J Mater Chem. 20 (2010).
109. Tong X, Zhou F, Yang S, et al., Performance and stability of Ruddlesden-Popper La₂NiO_{4+δ} oxygen electrodes under solid oxide electrolysis cell operation conditions, Ceram Int. 43 (2017) 10927-33.
110. Jorgensen JD, Dabrowski B, Pei S, et al., Structure of the interstitial oxygen defect in La₂NiO_{4+δ}, Phys Rev B. 40 (1989) 2187-99.
111. Chroneos A, Parfitt D, Kilner JA, et al., Anisotropic oxygen diffusion in tetragonal La₂NiO_{4+δ}: molecular dynamics calculations, J Mater Chem. 20 (2010) 266-70.
112. Beppu K, Hosokawa S, Teramura K, et al., Oxygen storage capacity of Sr₃Fe₂O_{7-δ} having high structural stability, J Mater Chem A. 3 (2015) 13540-5.
113. Huan D, Zhang L, Zhang S, et al., Ruddlesden–Popper oxide SrEu₂Fe₂O₇ as a promising symmetrical electrode for pure CO₂ electrolysis, J Mater Chem A. 9 (2021) 2706-13.
114. Zhang X, Tong Y, Liu T, et al., Robust Ruddlesden-Popper phase Sr₃Fe_{1.3}Mo_{0.5}Ni_{0.2}O_{7-δ} decorated with in-situ exsolved Ni nanoparticles as an efficient anode for hydrocarbon fueled solid oxide fuel cells, SusMat. (2022).
115. Zhang S-L, Cox D, Yang H, et al., High stability SrTi_{1-x}Fe_xO_{3-δ} electrodes for oxygen reduction and oxygen evolution reactions, J Mater Chem A. 7 (2019) 21447-58.
116. Li Y, Chen X, Yang Y, et al., Mixed-Conductor Sr₂Fe_{1.5}Mo_{0.5}O_{6-δ} as Robust Fuel Electrode for Pure CO₂ Reduction in Solid Oxide Electrolysis Cell, ACS Sustain Chem Eng. 5 (2017) 11403-12.
117. Liu S, Liu Q, Luo J-L, The excellence of La(Sr)Fe(Ni)O₃ as an active and efficient cathode for direct CO₂ electrochemical reduction at elevated temperatures, J Mater Chem A. 5 (2017) 2673-80.
118. Velraj S, Daramola DA, Tremblay JP, A novel solid oxide electrolytic cell with reduced endothermic load for CO₂ electrolysis using (La_{0.8}OSr_{0.2})_{0.95}MnO_{3-δ} cathode, J CO₂ Util. 48 (2021).

119. Li S, Li Y, Gan Y, et al., Electrolysis of H₂O and CO₂ in an oxygen-ion conducting solid oxide electrolyzer with a La_{0.2}Sr_{0.8}TiO_{3+δ} composite cathode, *J Power Sources*. 218 (2012) 244-9.
120. Pidburtnyi M, Zanca B, Coppex C, et al., A review on perovskite-type LaFeO₃ based electrodes for CO₂ reduction in solid oxide electrolysis cells: current understanding of structure–functional property relationships, *Chem Mater*. 33 (2021) 4249–68.
121. Ni C, Zhou J, Zhang Z, et al., Iron-based electrode materials for solid oxide fuel cells and electrolyzers, *Energy Environ Sci*. 14 (2021) 6287-319.
122. Zhang L, Xu C, Sun W, et al., Constructing perovskite/alkaline-earth metal composite heterostructure by infiltration to revitalize CO₂ electrolysis, *Sep Purif Technol*. 298 (2022).
123. Tian Y, Wang W, Liu Y, et al., Achieving Strong Coherency for a Composite Electrode via One-Pot Method with Enhanced Electrochemical Performance in Reversible Solid Oxide Cells, *ACS Catal*. (2021) 3704-14.
124. Lee S, Woo SH, Shin TH, et al., Pd and GDC Co-infiltrated LSCM cathode for high-temperature CO₂ electrolysis using solid oxide electrolysis cells, *J Chem Eng*. (2020).
125. Lv H, Zhou Y, Zhang X, et al., Infiltration of Ce_{0.8}Gd_{0.2}O_{1.9} nanoparticles on Sr₂Fe_{1.5}Mo_{0.5}O_{6-δ} cathode for CO₂ electroreduction in solid oxide electrolysis cell, *J Energy Chem*. 35 (2019) 71-8.
126. Yue X, Irvine JTS, Impedance Studies on LSCM/GDC Cathode for High Temperature CO₂ Electrolysis, *Electrochem Solid St*. 15 (2012).
127. Zhou Y, Zhou Z, Song Y, et al., Enhancing CO₂ electrolysis performance with vanadium-doped perovskite cathode in solid oxide electrolysis cell, *Nano Energy*. 50 (2018) 43-51.
128. Feng J, Yang G, Dai N, et al., Investigation into the effect of Fe-site substitution on the performance of Sr₂Fe_{1.5}Mo_{0.5}O_{6-δ} anodes for SOFCs, *J Mater Chem A*. 2 (2014) 17628-34.
129. Wentao Q YG, Di Yin, Zhenyu Li, Guojian Wu, Kui Xie, Yucheng Wu, Remarkable chemical adsorption of manganese-doped titanate for direct carbon dioxide electrolysis, *J Mater Chem A*. 2 (2014) 6904-15.
130. Hu S, Zhang L, Liu H, et al., Alkaline-earth elements (Ca, Sr and Ba) doped LaFeO_{3-δ} cathodes for CO₂ electroreduction, *J Power Sources*. 443 (2019) 227268.
131. Zhang Z, Zhu Y, Zhong Y, et al., Anion Doping: A New Strategy for Developing High-Performance Perovskite-Type Cathode Materials of Solid Oxide Fuel Cells, *Adv Energy Mater*. 7 (2017).

132. Ye L, Hu X, Wang X, et al., Enhanced CO₂ electrolysis with a SrTiO₃ cathode through a dual doping strategy, *J Mater Chem A*. 7 (2019) 2764-72.
133. He D, Ruan W, Li J, et al., Heterogeneity in the Mo doped La_{0.55}Sr_{0.45}FeO₃ cathode for direct CO₂ electrolysis, *Chemical Engineering Journal*. (2021).
134. Sun C, Bian L, Qi J, et al., Boosting CO₂ directly electrolysis by electron doping in Sr₂Fe_{1.5}Mo_{0.5}O_{6-δ} double perovskite cathode, *J Power Sources*. 521 (2022).
135. Xi X, Liu J, Fan Y, et al., Reducing d-p band coupling to enhance CO₂ electrocatalytic activity by Mg-doping in Sr₂FeMoO_{6-δ} double perovskite for high performance solid oxide electrolysis cells, *Nano Energy*. 82 (2021).
136. Xi X, Liu J, Luo W, et al., Unraveling the enhanced kinetics of Sr₂Fe_{1+x}Mo_{1-x}O_{6-δ} electrocatalysts for high-performance solid oxide cells, *Adv Energy Mater*. 11 (2021) 2102845.
137. Zhang YQ, Li JH, Sun YF, et al., Highly Active and Redox-Stable Ce-Doped LaSrCrFeO-Based Cathode Catalyst for CO₂ SOECs, *ACS Appl Mater Interfaces*. 8 (2016) 6457-63.
138. Li Y, Li Y, Yu L, et al., Achieving excellent and durable CO₂ electrolysis performance on a dual-phase fuel electrode in solid oxide electrolysis cells, *J Power Sources*. 491 (2021).
139. Li Y, Li Y, Wan Y, et al., Perovskite oxyfluoride electrode enabling direct electrolyzing carbon dioxide with excellent electrochemical performances, *Adv Energy Mater*. 9 (2019) 1803156.
140. Zhu J, Liu G, Liu Z, et al., Unprecedented Perovskite Oxyfluoride Membranes with High-Efficiency Oxygen Ion Transport Paths for Low-Temperature Oxygen Permeation, *Adv Mater*. 28 (2016) 3511-5.
141. Zhang Y, Zhu Z, Gu Y, et al., Effect of Cl doping on the electrochemical performance of Sr₂Fe_{1.5}Mo_{0.5}O_{6-δ} cathode material for solid oxide fuel cells, *Ceram Int*. (2020).
142. Gao J, Zhang Y, Wang X, et al., Nitrogen-doped Sr₂Fe_{1.5}Mo_{0.5}O_{6-δ} perovskite as an efficient and stable catalyst for hydrogen evolution reaction, *Mater Today Energy*. 20 (2021).
143. Park S, Han H, Yoon W, et al., Improving a Sulfur-Tolerant Ruddlesden–Popper Catalyst by Fluorine Doping for CO₂ Electrolysis Reaction, *ACS Sustain Chem Eng*. 8 (2020) 6564-71.
144. Zhang S, Jiang Y, Han H, et al., Perovskite Oxyfluoride Ceramic with In Situ Exsolved Ni-Fe Nanoparticles for Direct CO₂ Electrolysis in Solid Oxide Electrolysis Cells, *ACS Appl Mater Interfaces*. (2022).

145. Yang C, Tian Y, Pu J, et al., Anion Fluorine-Doped $\text{La}_{0.6}\text{Sr}_{0.4}\text{Fe}_{0.8}\text{Ni}_{0.2}\text{O}_{3-\delta}$ Perovskite Cathodes with Enhanced Electrocatalytic Activity for Solid Oxide Electrolysis Cell Direct CO_2 Electrolysis, *ACS Sustain Chem Eng.* 10 (2022) 1047–58.
146. Xiong J, Zhong H, Li J, et al., Engineering highly active oxygen sites in perovskite oxides for stable and efficient oxygen evolution, *Appl Catal B.* 256 (2019).
147. Kim JK, Jo YR, Kim S, et al., Exceptional Tunability over Size and Density of Spontaneously Formed Nanoparticles via Nucleation Dynamics, *ACS Appl Mater Interfaces.* 12 (2020) 24039-47.
148. Kousi K, Tang C, Metcalfe IS, et al., Emergence and Future of Exsolved Materials, *Small.* 17 (2021) e2006479.
149. Oh TS, Rahani EK, Neagu D, et al., Evidence and model for strain-driven release of metal nanocatalysts from perovskites during exsolution, *J Phys Chem Lett.* 6 (2015) 5106-10.
150. Neagu D, Oh TS, Miller DN, et al., Nano-socketed nickel particles with enhanced coking resistance grown in situ by redox exsolution, *Nat Commun.* 6 (2015) 8120.
151. Weber ML, Wilhelm M, Jin L, et al., Exsolution of Embedded Nanoparticles in Defect Engineered Perovskite Layers, *ACS Nano.* 15 (2021) 4546-60.
152. Lai K-Y, Manthiram A, Evolution of exsolved nanoparticles on a perovskite oxide surface during a redox process, *Chem Mater.* 30 (2018) 2838-47.
153. Lai K-Y, Manthiram A, Self-Regenerating Co–Fe Nanoparticles on Perovskite Oxides as a Hydrocarbon Fuel Oxidation Catalyst in Solid Oxide Fuel Cells, *Chem Mater.* 30 (2018) 2515-25.
154. Rosen BA, Progress and Opportunities for Exsolution in Electrochemistry, *Electrochem.* 1 (2020) 32-43.
155. Zhou J, Shin T-H, Ni C, et al., In Situ Growth of Nanoparticles in Layered Perovskite $\text{La}_{0.8}\text{Sr}_{1.2}\text{Fe}_{0.9}\text{Co}_{0.1}\text{O}_{4-\delta}$ as an Active and Stable Electrode for Symmetrical Solid Oxide Fuel Cells, *Chem Mater.* 28 (2016) 2981-93.
156. Y. Nishihata JM, T. Akao, H. Tana, Self-regeneration of a Pd-perovskite catalyst for automotive emissions control, *Nature.* 418 (2002) 162-4.
157. Carrillo AJ, Kim KJ, Hood ZD, et al., $\text{La}_{0.6}\text{Sr}_{0.4}\text{Cr}_{0.8}\text{Co}_{0.2}\text{O}_3$ Perovskite Decorated with Exsolved Co Nanoparticles for Stable CO_2 Splitting and Syngas Production, *ACS Appl Energy Mater.* (2020).

158. Burnat D, Kontic R, Holzer L, et al., Smart material concept: reversible microstructural self-regeneration for catalytic applications, *J Mater Chem A*. 4 (2016) 11939-48.
159. Liu S, Liu Q, Luo J-L, Highly Stable and Efficient Catalyst with In Situ Exsolved Fe–Ni Alloy Nanospheres Socketed on an Oxygen Deficient Perovskite for Direct CO₂ Electrolysis, *ACS Catal*. 6 (2016) 6219-28.
160. Hua B, Li M, Zhang Y-Q, et al., Facile Synthesis of Highly Active and Robust Ni–Mo Bimetallic Electrocatalyst for Hydrocarbon Oxidation in Solid Oxide Fuel Cells, *ACS Energy Lett*. 1 (2016) 225-30.
161. Zhang J, Gao M-R, Luo J-L, In Situ Exsolved Metal Nanoparticles: A Smart Approach for Optimization of Catalysts, *Chemistry of Materials*. 32 (2020) 5424-41.
162. Gao Y, Chen D, Saccoccio M, et al., From material design to mechanism study: Nanoscale Ni exsolution on a highly active A-site deficient anode material for solid oxide fuel cells, *Nano Energy*. 27 (2016) 499-508.
163. Liu F, Sommer F, Bos C, et al., Analysis of solid state phase transformation kinetics: models and recipes, *International Materials Reviews*. 52 (2013) 193-212.
164. Neagu D, Tsekouras G, Miller DN, et al., In situ growth of nanoparticles through control of non-stoichiometry, *Nat Chem*. 5 (2013) 916-23.
165. Myung JH, Neagu D, Miller DN, et al., Switching on electrocatalytic activity in solid oxide cells, *Nature*. 537 (2016) 528-31.
166. Han H, Park J, Nam SY, et al., Lattice strain-enhanced exsolution of nanoparticles in thin films, *Nat Commun*. 10 (2019) 1471.
167. Sun YF, Zhang YQ, Chen J, et al., New Opportunity for in Situ Exsolution of Metallic Nanoparticles on Perovskite Parent, *Nano Lett*. 16 (2016) 5303-9.
168. Chen Z, Hua B, Zhang X, et al., Organic photochemistry-assisted nanoparticle segregation on perovskites, *Cell Rep Phys Sci*. 1 (2020) 100243.
169. Joo S, Kwon O, Kim K, et al., Cation-swapped homogeneous nanoparticles in perovskite oxides for high power density, *Nat Commun*. 10 (2019) 697.
170. Kim JH, Kim JK, Liu J, et al., Nanoparticle Ex-solution for Supported Catalysts: Materials Design, Mechanism and Future Perspectives, *ACS Nano*. 15 (2021) 81-110.

171. Ding S, Li M, Pang W, et al., A-site deficient perovskite with nano-socketed Ni-Fe alloy particles as highly active and durable catalyst for high-temperature CO₂ electrolysis, *Electrochim Acta*. 335 (2020) 135683.
172. Kim J, Ferree M, Gunduz S, et al., Exsolution of nanoparticles on A-site-deficient lanthanum ferrite perovskites: its effect on co-electrolysis of CO₂ and H₂O, *J Mater Chem A*. (2022).
173. Managutti PB, Tymen S, Liu X, et al., Exsolution of Ni Nanoparticles from A-Site-Deficient Layered Double Perovskites for Dry Reforming of Methane and as an Anode Material for a Solid Oxide Fuel Cell, *ACS Appl Mater Interfaces*. 13 (2021) 35719-28.
174. Lv H, Lin L, Zhang X, et al., Promoting exsolution of RuFe alloy nanoparticles on Sr₂Fe_{1.4}Ru_{0.1}Mo_{0.5}O_{6-δ} via repeated redox manipulations for CO₂ electrolysis, *Nat Commun*. 12 (2021) 5665.
175. Jinhai Lu CZ, Changchang Pan, Wenlie Lin, John P. Lemmon, Fanglin Chen, Chunsen Li, Kui Xie, Highly efficient electrochemical reforming of CH₄/CO₂ in a solid oxide electrolyser, *Sci Adv*. 4 (2018) eaar5100.
176. Bak J, Bin Bae H, Chung SY, Atomic-scale perturbation of oxygen octahedra via surface ion exchange in perovskite nickelates boosts water oxidation, *Nat Commun*. 10 (2019) 2713.
177. Zhang BW, Zhu MN, Gao MR, et al., Boosting the stability of perovskites with exsolved nanoparticles by B-site supplement mechanism, *Nat Commun*. 13 (2022) 4618.
178. Opitz AK, Nenning A, Vonk V, et al., Understanding electrochemical switchability of perovskite-type exsolution catalysts, *Nat Commun*. 11 (2020) 4801.
179. Chen Z, Hua B, Zhang X, et al., Organic Photochemistry-Assisted Nanoparticle Segregation on Perovskites, *Cell Reports Physical Science*. 1 (2020).
180. Gao Y, Lu Z, You TL, et al., Energetics of Nanoparticle Exsolution from Perovskite Oxides, *J Phys Chem Lett*. 9 (2018) 3772-8.
181. Li X, Dai L, He Z, et al., In situ exsolution of PdO nanoparticles from non-stoichiometric LaFePd_{0.05}O_{3+δ} electrode for impedancemetric NO₂ sensor, *Sens Actuators B Chem*. 298 (2019).
182. Cao T, Kwon O, Gorte RJ, et al., Metal Exsolution to Enhance the Catalytic Activity of Electrodes in Solid Oxide Fuel Cells, *J Nanomater*. 10 (2020).

183. Kwon O, Sengodan S, Kim K, et al., Exsolution trends and co-segregation aspects of self-grown catalyst nanoparticles in perovskites, *Nat Commun.* 8 (2017) 15967.
184. Park S, Kim Y, Han H, et al., In situ exsolved Co nanoparticles on Ruddlesden-Popper material as highly active catalyst for CO₂ electrolysis to CO, *Appl Catal B.* 248 (2019) 147-56.
185. Lv H, Lin L, Zhang X, et al., In situ exsolved FeNi₃ nanoparticles on nickel doped Sr₂Fe_{1.5}Mo_{0.5}O_{6-δ} perovskite for efficient electrochemical CO₂ reduction reaction, *J Mater Chem A.* 7 (2019) 11967-75.
186. Lee JG, Myung JH, Naden AB, et al., Replacement of Ca by Ni in a Perovskite Titanate to Yield a Novel Perovskite Exsolution Architecture for Oxygen-Evolution Reactions, *Adv Energy Mater.* 10 (2020).
187. Sun X, Chen H, Yin Y, et al., Progress of exsolved metal nanoparticles on oxides as high performance (electro)catalysts for the conversion of small molecules, *Small.* 17 (2021) 2005383.
188. Lv H, Liu T, Zhang X, et al., Atomic-scale insight into exsolution of CoFe alloy nanoparticles in La_{0.4}Sr_{0.6}Co_{0.2}Fe_{0.7}Mo_{0.1}O_{3-δ} with Efficient CO₂ Electrolysis, *Angew Chem Int Ed.* 59 (2020) 15968-73.
189. Ansari HM, Bass AS, Ahmad N, et al., Unraveling the evolution of exsolved Fe–Ni alloy nanoparticles in Ni-doped La_{0.3}Ca_{0.7}Fe_{0.7}Cr_{0.3}O_{3-δ} and their role in enhancing CO₂–CO electrocatalysis, *J Mater Chem A.* 10 (2021) 2280-94.
190. Neagu D, Papaioannou EI, Ramli WKW, et al., Demonstration of chemistry at a point through restructuring and catalytic activation at anchored nanoparticles, *Nat Commun.* 8 (2017) 1855.
191. Neagu D, Kyriakou V, Roiban IL, et al., In situ observation of nanoparticle exsolution from perovskite oxides: from atomic scale mechanistic insight to nanostructure tailoring, *ACS Nano.* 13 (2019) 12996-3005.
192. Kalliopi Kousi DN, Leonidas Bekris, Evangelos I. Papaioannou and Ian S. Metcalfe, Endogenous nanoparticles strain perovskite host lattice providing oxygen capacity and driving oxygen exchange and CH₄ conversion to syngas, *Angew Chem Int Ed* 132 (2019) 2531-40.
193. Wang J, Kumar A, Wardini JL, et al., Exsolution-Driven Surface Transformation in the Host Oxide, *Nano Lett.* 22 (2022) 5401-8.

194. Liu S, Liu Q, Luo J-L, CO₂-to-CO conversion on layered perovskite with in situ exsolved Co-Fe alloy nanoparticles: an active and stable cathode for solid oxide electrolysis cells, *J Mater Chem A*. 4 (2016) 17521-8.
195. Kresse G, Furthmüller J, Hafner J, Theory of the crystal structures of selenium and tellurium: The effect of generalized-gradient corrections to the local-density approximation, *Phys Rev B*. 50 (1994) 13181-5.
196. Kresse G, Hafner J, Ab initio molecular dynamics for liquid metals, *Phys Rev B*. 47 (1993) 558-61.
197. Hammer B, Hansen LB, Nørskov JK, Improved adsorption energetics within density-functional theory using revised Perdew-Burke-Ernzerhof functionals, *Physical Review B*. 59 (1999) 7413-21.
198. Monkhorst HJ, Pack JD, Special points for Brillouin-zone integrations, *Phys Rev B*. 13 (1976) 5188-92.
199. Zhu K, Wu T, Li M, et al., Perovskites decorated with oxygen vacancies and Fe-Ni alloy nanoparticles as high-efficiency electrocatalysts for the oxygen evolution reaction, *J Mater Chem A*. 5 (2017) 19836-45.
200. Jiang Y, Yang Y, Xia C, et al., Sr₂Fe_{1.4}Mn_{0.1}Mo_{0.5}O_{6-δ} perovskite cathode for highly efficient CO₂ electrolysis, *J Mater Chem A*. 7 (2019) 22939-49.
201. Momma K, Izumi F, VESTA 3 for three-dimensional visualization of crystal, volumetric and morphology data, *J Appl Crystallogr*. 44 (2011) 1272-6.
202. Muñoz-García AB, Pavone M, Carter EA, Effect of Antisite Defects on the Formation of Oxygen Vacancies in Sr₂FeMoO₆: Implications for Ion and Electron Transport, *Chem Mater*. 23 (2011) 4525-36.
203. Grimme S, Antony J, Ehrlich S, et al., A consistent and accurate ab initio parametrization of density functional dispersion correction (DFT-D) for the 94 elements H-Pu, *J Chem Phys*. 132 (2010) 154104.
204. Wang V, Xu N, Liu J-C, et al., VASPKIT: A user-friendly interface facilitating high-throughput computing and analysis using VASP code, *Comput Phys Commun*. 267 (2021) 108033.
205. Muñoz-García AB, Pavone M, First-Principles Design of New Electrodes for Proton-Conducting Solid-Oxide Electrochemical Cells: A-Site Doped Sr₂Fe_{1.5}Mo_{0.5}O_{6-δ} Perovskite, *Chem Mater*. 28 (2016) 490-500.

206. Takamatsu A, Tamai K, Hosokawa S, et al., Oxidation and Storage Mechanisms for Nitrogen Oxides on Various Terminated (001) Surfaces of $\text{SrFeO}_{3-\delta}$ and $\text{Sr}_3\text{Fe}_2\text{O}_{7-\delta}$ Perovskites, *ACS Appl Mater Interfaces*. 13 (2021) 7216-26.
207. Li S, Yu D, Cheng S, et al., Recyclable Metal (Ni, Fe) Cluster Designed Catalyst for Cellulose Pyrolysis to Upgrade Bio-Oil, *Catal*. 10 (2020) 1160.
208. Arandiyana H, S. Mofarah S, Sorrell CC, et al., Defect engineering of oxide perovskites for catalysis and energy storage: synthesis of chemistry and materials science, *Chem Soc Rev*. 50 (2021) 10116-211.
209. Kim JH, Kim JK, Liu J, et al., Nanoparticle ex-solution for supported catalysts: materials design, mechanism and future perspectives, *ACS Nano*. 15 (2020) 81-110.
210. Kousi K, Tang C, Metcalfe IS, et al., Emergence and future of exsolved materials, *Small*. 17 (2021) 2006479.
211. Zhang T, Zhao Y, Zhang X, et al., Thermal stability of an in situ exsolved metallic nanoparticle structured perovskite type hydrogen electrode for solid oxide cells, *ACS Sustainable Chem Eng*. 7 (2019) 17834-44.
212. Skafte TL, Blennow P, Hjelm J, et al., Carbon deposition and sulfur poisoning during CO_2 electrolysis in nickel-based solid oxide cell electrodes, *J Power Sources*. 373 (2018) 54-60.
213. Hauch A, Kungas R, Blennow P, et al., Recent advances in solid oxide cell technology for electrolysis, *Science*. 370 (2020) eaba6118.
214. Thalinger R, Gocyla M, Heggen M, et al., Exsolution of Fe and SrO nanorods and nanoparticles from lanthanum strontium ferrite $\text{La}_{0.6}\text{Sr}_{0.4}\text{FeO}_{3-\delta}$ materials by hydrogen reduction, *J Phys Chem C*. 119 (2015) 22050-6.
215. Neagu D, Irvine JTS, Enhancing electronic conductivity in strontium titanates through correlated A and B-site doping, *Chem Mater*. 23 (2011) 1607-17.
216. Joo S, Seong A, Kwon O, et al., Highly active dry methane reforming catalysts with boosted in situ grown Ni-Fe nanoparticles on perovskite via atomic layer deposition, *Sci Adv*. 6 (2020) eabb1573.

217. Yu N, Jiang G, Liu T, et al., Understanding the A-site non-stoichiometry in perovskites: promotion of exsolution of metallic nanoparticles and the hydrogen oxidation reaction in solid oxide fuel cells, *Sustain Energy Fuels*. 5 (2021) 401-11.
218. Lv H, Lin L, Zhang X, et al., In situ investigation of reversible exsolution/dissolution of CoFe alloy nanoparticles in a Co-doped $\text{Sr}_2\text{Fe}_{1.5}\text{Mo}_{0.5}\text{O}_{6-\delta}$ Cathode for CO_2 Electrolysis, *Adv Mater*. 32 (2020) e1906193.
219. Hu S, Zhang L, Liu H, et al., Detrimental phase evolution triggered by Ni in perovskite-type cathodes for CO_2 electroreduction, *J Energy Chem*. 36 (2019) 87-94.
220. Meng X, Wang Y, Zhao Y, et al., In-situ exsolution of nanoparticles from Ni substituted $\text{Sr}_2\text{Fe}_{1.5}\text{Mo}_{0.5}\text{O}_6$ perovskite oxides with different Ni doping contents, *Electrochim Acta*. 348 (2020) 136351.
221. Chen X, Ni W, Wang J, et al., Exploration of Co-Fe alloy precipitation and electrochemical behavior hysteresis using Lanthanum and Cobalt co-substituted $\text{SrFeO}_{3-\delta}$ SOFC anode, *Electrochim Acta*. 277 (2018) 226-34.
222. Yao T, Hou N, Gan J, et al., Enhanced activity and stability of $\text{Sr}_2\text{FeMo}_{0.65}\text{Ni}_{0.35}\text{O}_{6-\delta}$ anode for solid oxide fuel cells with Na doping, *J Power Sources*. 425 (2019) 103-9.
223. Xi X, Liu J, Fan Y, et al., Reducing d-p band coupling to enhance CO_2 electrocatalytic activity by Mg-doping in $\text{Sr}_2\text{FeMoO}_{6-\delta}$ double perovskite, *Nano Energy*. 82 (2020) 105707.
224. Wan TH, Saccoccio M, Chen C, et al., Influence of the discretization methods on the distribution of relaxation times deconvolution: implementing radial basis functions with DRT tools, *Electrochim Acta*. 184 (2015) 483-99.
225. Deka DJ, Kim J, Gunduz S, et al., Coke formation during high-temperature CO_2 electrolysis over AFeO_3 (A = La/Sr) cathode: Effect of A-site metal segregation, *Appl Catal, B*. 283 (2021) 119642.
226. Na BT, Yang T, Liu J, et al., Enhanced accuracy of electrochemical kinetic parameters determined by electrical conductivity relaxation, *Solid State Ion*. 361 (2021) 115561.
227. Fairley N, Fernandez V, Richard-Plouet M, et al., Systematic and collaborative approach to problem solving using X-ray photoelectron spectroscopy, *Appl Surf Sci*. 5 (2021) 100112.
228. Ravel B, Newville M, ATHENA, ARTEMIS, HEPHAESTUS: data analysis for X-ray absorption spectroscopy using IFEFFIT, *J Synchrotron Rad*. 12 (2005) 537-41.

229. D’Orazio AC, Marshall T, Sultana T, et al., High temperature X-ray absorption spectroscopy of the local electronic structure and oxide vacancy formation in the $\text{Sr}_2\text{Fe}_{1.5}\text{Mo}_{0.5}\text{O}_{6-\delta}$ solid oxide fuel cell anode catalyst, *ACS Appl Energy Mater.* 2 (2019) 3061-70.
230. Du Z, Zhao H, Yi S, et al., High-Performance Anode Material $\text{Sr}_2\text{FeMo}_{0.65}\text{Ni}_{0.35}\text{O}_{6-\delta}$ with In Situ Exsolved Nanoparticle Catalyst, *ACS Nano.* 10 (2016) 8660-9.
231. Kim M, Park J, Ju H, et al., Understanding synergistic metal–oxide interactions of in situ exsolved metal nanoparticles on pyrochlore oxide support for enhanced water splitting, *Energy Environ Sci.* 14 (2021) 3053-63.
232. Hong J, Heo SJ, Singh P, Water mediated growth of oriented single crystalline SrCO_3 nanorod arrays on strontium compounds, *Sci Rep.* 11 (2021) 3368.
233. Jena P, Gupta SK, Natarajan V, et al., On the photo-luminescence properties of sol–gel derived undoped and Dy^{3+} ion doped nanocrystalline Scheelite type AMoO_4 (A = Ca, Sr and Ba), *Mater Res Bull.* 64 (2015) 223-32.
234. Chen L, Xu J, Wang X, et al., $\text{Sr}_2\text{Fe}_{1.5+x}\text{Mo}_{0.5}\text{O}_{6-\delta}$ cathode with exsolved Fe nanoparticles for enhanced CO_2 electrolysis, *Int J Hydrog Energy.* 45 (2020) 11901-7.
235. Bai L, Li H, Yan Z, et al., New insight into the doped strontium titanate cathode with in situ exsolved nickel nanoparticles for electrolysis of carbon dioxide, *Adv Mater Interfaces.* 8 (2020) 2001598.
236. Choi J, Park S, Han H, et al., Highly efficient CO_2 electrolysis to CO on Ruddlesden–Popper perovskite oxide with in situ exsolved Fe nanoparticles, *J Mater Chem A.* 9 (2021) 8740-8.
237. Tian Y, Liu Y, Naden A, et al., Boosting CO_2 electrolysis performance by calcium oxide-looping combined with in situ exsolved Ni-Fe nanoparticles based on symmetrical solid oxide electrolysis cell, *J Mater Chem A.* 8 (2020) 14895-9.
238. Xi X, Fan Y, Zhang J, et al., In situ construction of hetero-structured perovskite composites with exsolved Fe and Cu metallic nanoparticles as efficient CO_2 reduction electrocatalysts for high performance solid oxide electrolysis cells, *J Mater Chem A.* 10 (2022) 2509-18.
239. Su C, Wang W, Shao Z, Cation-Deficient Perovskites for Clean Energy Conversion, *Acc Mater Res.* 2 (2021) 477-88.

240. Zhu M-N, Zhang B-W, Gao M-R, et al., Electrochemically reconstructed perovskite with cooperative catalytic sites for CO₂-to-formate conversion, *Appl Catal B*. 306 (2022) 121101.
241. Tian Y, Yang C, Wang Y, et al., Phase transition with in situ exsolution nanoparticles in the reduced Pr_{0.5}Ba_{0.5}Fe_{0.8}Ni_{0.2}O_{3-δ} electrode for symmetric solid oxide cells, *J Mater Chem A*. 10 (2022) 16490-6.
242. Deka DJ, Kim J, Gunduz S, et al., Investigation of hetero-phases grown via in-situ exsolution on a Ni-doped (La,Sr)FeO₃ cathode and the resultant activity enhancement in CO₂ reduction, *Appl Catal B*. 286 (2021) 119917.
243. Kim JK, Kim S, Kim S, et al., Dynamic Surface Evolution of Metal Oxides for Autonomous Adaptation to Catalytic Reaction Environments, *Adv Mater*. 35 (2022) 2203370.
244. Ning Han XG, Junling Cheng, Pengyun Liu, Shuguang Zhang, Shiping Huang, Matthew R. Rowles, Jan Fransaer, Shaomin Liu, Inhibiting in situ phase transition in Ruddlesden-Popper perovskite via tailoring bond hybridization and its application in oxygen permeation, *Matter*. 4 (2021) 1720-34.
245. Eum D, Kim B, Song J-H, et al., Coupling structural evolution and oxygen-redox electrochemistry in layered transition metal oxides, *Nat Mater*. 21 (2022) 664–72.
246. Xi X, Wang X-W, Fan Y, et al., Efficient bifunctional electrocatalysts for solid oxide cells based on the structural evolution of perovskites with abundant defects and exsolved CoFe nanoparticles, *J Power Sources*. 482 (2021) 228981.
247. Zhi M, Zhou G, Hong Z, et al., Single crystalline La_{0.5}Sr_{0.5}MnO₃ microcubes as cathode of solid oxidefuel cell, *Energy Environ Sci*. 4 (2011) 139-44.
248. Nechache A, Cassir M, Ringuedé A, Solid oxide electrolysis cell analysis by means of electrochemical impedance spectroscopy: A review, *J Power Sources*. 258 (2014) 164-81.
249. Cowin PI, Lan R, Petit CTG, et al., Conductivity and redox stability of new double perovskite oxide Sr_{1.6}K_{0.4}Fe_{1+x}Mo_{1-x}O_{6-δ} (x=0.2, 0.4, 0.6), *J Mater Sci*. 51 (2016) 4115-24.
250. Kim M, Park J, Ju H, et al., Understanding synergistic metal–oxide interactions of in situ exsolved metal nanoparticles on a pyrochlore oxide support for enhanced water splitting, *Energy Environ Sci*. 14 (2021) 3053-63.

251. Li J, Liu Q, Song Y, et al., In-situ exsolution of cobalt nanoparticles from $\text{La}_{0.5}\text{Sr}_{0.5}\text{Fe}_{0.8}\text{Co}_{0.2}\text{O}_{3-\delta}$ cathode for enhanced CO_2 electrolysis performance, *GreenChE*. 3 (2021) 250-8.
252. Wang J, Kalaev D, Yang J, et al., Fast Surface Oxygen Release Kinetics Accelerate Nanoparticle Exsolution in Perovskite Oxides, *J Am Chem Soc*. 145 (2023) 1714-27.
253. Oh J, Joo S, Lim C, et al., Precise Modulation of Triple-Phase Boundaries towards a Highly Functional Exsolved Catalyst for Dry Reforming of Methane under a Dilution-Free System, *Angew Chem Int Ed Engl*. 61 (2022) e202204990.
254. Ju Y-W, Lee S, Kang BS, et al., Phase transition of doped LaFeO_3 anode in reducing atmosphere and their power generation property in intermediate temperature solid oxide fuel cell, *Int J Hydrog Energy*. 44 (2019) 29641-7.
255. Götsch T, Schlicker L, Bekheet MF, et al., Structural investigations of $\text{La}_{0.6}\text{Sr}_{0.4}\text{FeO}_{3-\delta}$ under reducing conditions: kinetic and thermodynamic limitations for phase transformations and iron exsolution phenomena, *RSC Advances*. 8 (2018) 3120-31.
256. Tan T, Wang Z, Qin M, et al., In Situ Exsolution of Core-Shell Structured NiFe/FeOx Nanoparticles on $\text{Pr}_{0.4}\text{Sr}_{1.6}(\text{NiFe})_{1.5}\text{Mo}_{0.5}\text{O}_{6-\delta}$ for CO_2 Electrolysis, *Adv Funct Mater*. 32 (2022).
257. Ding H, Tao Z, Liu S, et al., A redox-stable direct-methane solid oxide fuel cell (SOFC) with $\text{Sr}_2\text{FeNb}_{0.2}\text{Mo}_{0.8}\text{O}_{6-\delta}$ double perovskite as anode material, *Journal of Power Sources*. 327 (2016) 573-9.
258. Guo Y, Guo T, Zhou S, et al., Characterization of $\text{Sr}_2\text{Fe}_{1.5}\text{Mo}_{0.5}\text{O}_{6-\delta}$ - $\text{Gd}_{0.1}\text{Ce}_{0.9}\text{O}_{1.95}$ symmetrical electrode for reversible solid oxide cells, *Ceramics International*. 45 (2019) 10969-75.
259. Liu T, Zhao Y, Zhang X, et al., Robust redox-reversible perovskite type steam electrolyser electrode decorated with in situ exsolved metallic nanoparticles, *Journal of Materials Chemistry A*. 8 (2020) 582-91.
260. He F, Hou M, Zhu F, et al., Building Efficient and Durable Hetero-Interfaces on a Perovskite-Based Electrode for Electrochemical CO_2 Reduction, *Adv Energy Mater*. (2022).
261. Tezel E, Guo D, Whitten A, et al., Elucidating the Role of B-Site Cations toward CO_2 Reduction in Perovskite-Based Solid Oxide Electrolysis Cells, *J Electrochem Soc*. 169 (2022).

262. Li P, Yang P, Shao T, et al., Evaluating the Effect of B-Site Cation Doping on the Properties of $\text{Pr}_{0.4}\text{Sr}_{0.5}\text{Fe}_{0.9}\text{Mo}_{0.1}\text{O}_3$ for Reversible Single-Component Cells, *Industrial & Engineering Chemistry Research*. (2022).
263. Liu Y, Wang W, Xu X, et al., Recent advances in anion-doped metal oxides for catalytic applications, *Journal of Materials Chemistry A*. 7 (2019) 7280-300.
264. Ko YJ, Kim JY, Lee WH, et al., Exploring dopant effects in stannic oxide nanoparticles for CO_2 electro-reduction to formate, *Nat Commun*. 13 (2022) 2205.
265. Zhang S, Yang C, Jiang Y, et al., A robust fluorine-containing ceramic cathode for direct CO_2 electrolysis in solid oxide electrolysis cells, *J Energy Chem*. 77 (2023) 300-9.
266. Zhang L, Sun W, Xu C, et al., Attenuating a metal–oxygen bond of a double perovskite oxide via anion doping to enhance its catalytic activity for the oxygen reduction reaction, *Journal of Materials Chemistry A*. 8 (2020) 14091-8.
267. Ingmar Swart FMFdG, Bert M. Weckhuysen, Philipp Gruene, Gerard Meijer, and André Fielicke, H_2 Adsorption on 3d Transition Metal Clusters: A Combined Infrared Spectroscopy and Density Functional Study, *J Phys Chem A*. 112 (2008) 1139–49.
268. Zhu K, Wu T, Li M, et al., Perovskites decorated with oxygen vacancies and Fe–Ni alloy nanoparticles as high-efficiency electrocatalysts for the oxygen evolution reaction, *Journal of Materials Chemistry A*. 5 (2017) 19836-45.
269. Hu S, Zhang L, Cai L, et al., Iron stabilized 1/3 A-site deficient La–Ti–O perovskite cathodes for efficient CO_2 electroreduction, *J Mater Chem A*. 8 (2020) 21053-61.
270. Yang Y, Tong X, Hauch A, et al., Study of solid oxide electrolysis cells operated in potentiostatic mode: Effect of operating temperature on durability, *Chemical Engineering Journal*. (2021).